THE UNIVERSITY *of* EDINBURGH

Design and Performance Analysis of Optical Attocell Networks

Liang Yin

A thesis submitted for the degree of Doctor of Philosophy.
The University of Edinburgh.
May 2018

Abstract

The exponentially increasing demand for high-speed wireless communications will no longer be satisfied by the traditional radio frequency (RF) in the near future due to its limited spectrum and overutilization. To resolve this imminent issue, industrial and research communities have been looking into alternative technologies for communication. Among them, visible light communication (VLC) has attracted much attention because it utilizes the unlicensed, free and safe spectrum, whose bandwidth is thousand times larger than the entire RF spectrum. Moreover, VLC can be integrated into existing lighting systems to offer a dual-purpose, cost-effective and energy-efficient solution for next-generation small-cell networks (SCNs), giving birth to the concept of optical attocell networks.

Most relevant works in the literature rely on system simulations to quantify the performance of attocell networks, which suffer from high computational complexity and provide limited insights about the network. Mathematical tools, on the other hand, are more tractable and scalable and are shown to closely approximate practical systems. The presented work utilizes stochastic geometry for downlink evaluation of optical attocell networks, where the co-channel interference (CCI) surpasses noise and becomes the limiting factor of the link throughput. By studying the moment generating function (MGF) of the aggregate interference, a theoretical framework for modeling the distribution of signal-to-interference-plus-noise ratio (SINR) is presented, which allows important performance metrics such as the coverage probability and link throughput to be derived. Depending on the source of interference, CCI can be classified into two categories: inter-cell interference (ICI) and intra-cell interference. In this work, both types of interference are characterized, based on which effective interference mitigation techniques such as the coordinated multipoint (CoMP), power-domain multiplexing and successive interference cancellation (SIC) are devised. The proposed mathematical framework is applicable to attocell networks with and without such interference mitigation techniques.

Compared to RF networks, optical attocell networks are inherently more secure in the physical layer because visible light does not penetrate through opaque walls. This work analytically quantifies the physical-layer security of attocell networks from an information-theoretic point of view. Secrecy enhancement techniques such as AP cooperation and eavesdropper-free protected zones are also discussed. It is shown that compared to AP cooperation, implementing secrecy protected zones is more effective and it can contribute significantly to the network security.

Lay Summary

Current wireless networks are designed to operate in the radio frequency (RF) band below 300 gigahertz (GHz). Since this GHz-wide spectrum has been extensively used for commercial, medical and military applications, it will no longer be able to accommodate the exponentially increasing demand for high-speed wireless communications in the near future. Such an imminent issue has motivated industrial and research communities to seek new technologies and even-higher frequency bands for communication. The presented work investigating the use of visible light for wireless networking falls into this category.

Integrating visible light communication (VLC) into existing lighting systems has recently been proposed as a dual-purpose, cost-effective and energy-efficient solution to the spectrum crunch. The current work focuses primarily on evaluating the link-layer performance of indoor VLC networks, where interference surpasses noise and becomes one of the key limiting factors. By investigating the distribution of interference, fundamental performance indicators such as the link quality, throughput and information security are characterized.

VLC-enabled optical attocell networks are an example of small-cell networks (SCNs), which can provide significant improvements to indoor data coverage. The benefits of such networks originate from the reduced cell size, which in turn allows communication resources such as time and frequency to be more efficiently shared and reused. In this work, advanced signal processing techniques as well as light cooperation schemes are designed and investigated as methods to enhance the network performance. Utilizing the presented results, this work deepens the understanding of interference, its impact on the network performance and the effectiveness of the proposed interference mitigation techniques.

Declaration of Originality

I hereby declare that the research recorded in this thesis and the thesis itself were composed and originated entirely by myself in the Institute for Digital Communications (IDCOM) at The University of Edinburgh.

I declare that concepts presented in this thesis have not been used for the purpose of obtaining another degree or professional qualification.

Liang Yin

Acknowledgements

My deepest gratitude goes to my parents for their love and support. They have shaped me into who I am today and this thesis would not have been possible without their constant encouragement.

I would like to express my sincere gratitude to my supervisor, Professor Harald Haas, for his support, encouragement and advice throughout my PhD. His academic proficiency and enthusiasm for research have deeply inspired me and made this journey much enjoyable. It has been a privilege and honor working with him. I am also grateful to Dr Majid Safari, Dr David Laurenson and Dr James R. Hopgood for their engaging lectures before my PhD. My thanks also go to Ms Hannah Brown for proof-reading this thesis.

Last but not least, I would like to thank my dear friends who have made my life more delightful in Edinburgh. A special thank-you to my lovely girlfriend. They have all contributed to this thesis in a magic way. I also thank my colleagues at IDCOM for exchanging ideas and sharing the coffee room.

Contents

List of Figures

List of Tables

Acronyms and Abbreviations

AC	alternating current
ACO-OFDM	asymmetrically clipped optical OFDM
AD	angle diversity
AGC	automatic gain control
AP	access point
APD	avalanche photodiode
AR	augmented reality
ASE	area spectral efficiency
AWGN	additive white Gaussian noise
BB	busy burst
BJT	bipolar-junction transistor
bpcu	bit per channel use
BPP	binomial point process
BS	base station
CB	coordinated beamforming
CCDF	complementary cumulative distribution function
CCI	co-channel interference
CDF	cumulative distribution function
CDMA	code division multiple access
CLT	central limit theorem
CoMP	coordinated multipoint
CP	cyclic prefix
CPC	compound parabolic concentrator
CS	coordinated scheduling
CSI	channel state information
CSK	color-shift keying
DC	direct current
DCO-OFDM	direct current biased optical OFDM
DD	direct detection

DPS	dynamic point selection
DSL	digital subscriber line
DSSS	direct-sequence spread spectrum
dB	decibel
EM	electromagnetic
ES	exhaustive search
FDMA	frequency division multiple access
FET	field-effect transistor
FFR	fractional frequency reuse
FFT	fast Fourier transform
FOV	field-of-view
FPA	fixed power allocation
FSPL	free-space path loss
GPP	Ginibre point process
HetNet	heterogeneous network
ICI	inter-cell interference
IEEE	Institute of Electrical and Electronics Engineers
IFFT	inverse fast Fourier transform
IM	intensity modulation
IoT	Internet of things
IP	Internet protocol
IR	infrared
ISI	intersymbol interference
JT	joint transmission
LAN	local area network
LED	light-emitting diode
LD	laser diode
LDS	low-density signature
LOS	line-of-sight
LTE	long-term evolution
LTE-A	long-term evolution advanced
GHz	gigahertz
GRPA	gain ratio power allocation

GSM	global system of mobile
kHz	kilohertz
MA	multiple access
MAC	medium access control
MAN	metropolitan area network
MCM	multi-carrier modulation
MCP	Matérn cluster process
MGF	moment generating function
MHCPP	Matérn hard-core point process
MHz	megahertz
MIMO	multiple-input multiple-output
MISO	multiple-input single-output
nm	nanometer
NOMA	non-orthogonal multiple access
OFDM	orthogonal frequency division multiplxing
OFDMA	orthogonal frequency division multiple access
OMA	orthogonal multiple access
O-OFDM	optical orthogonal frequency division multiplxing
OOK	on-off keying
OSI	Open Systems Interconnect
OWC	optical wireless communication
PAPR	peak-to-average power ratio
PAM	pulse amplitude modulation
PCP	Poisson cluster process
PD	photodiode
PDF	probability density function
PDU	protocol data unit
PGFL	probability generating functional
PIN	positive-intrinsic-negative
PLC	power line communication
PMF	probability mass function
p-n	positive-negative
PPP	Poisson point process

PPM	pulse position modulation
PSD	power spectral density
PWM	pulse width modulation
P2P	point-to-point
QAM	quadrature amplitude modulation
QoS	quality of service
RB	resource block
RF	radio frequency
RGB	red, green and blue
RMS	root-mean-square
RSS	received signal strength
SC	superposition coding
SC-FDMA	single carrier frequency division multiple access
SCM	single-carrier modulation
SCN	small-cell network
SIC	successive interference cancellation
SINR	signal-to-interference-plus-noise ratio
SIR	signal-to-interference ratio
SISO	single-input single-output
SNR	signal-to-noise ratio
TIA	transimpedance amplifier
TIG	topic interest group
TCP	Thomas cluster process
TDMA	time division multiple access
TF	time-frequency
THz	terahertz
TOV	turn-on voltage
VLC	visible light communication
VNI	Visual Networking Index
VR	virtual reality
5G	fifth generation

Nomenclature

a	scale parameter of a generalized gamma distribution
a_i	power coefficient for user i
A_{PD}	detection area of the PD
$A_{\square}$	surface pixel area
$\mathcal{A}_i$	event of LED i transmitting signals
b	number of bounces
b_k	bandwidth coefficient for user k
$\mathcal{B}$	a two-dimensional ball
B	modulation bandwidth
c	speed of light
C	information-theoretic capacity
C_{b}	channel capacity of the legitimate link
C_{e}	channel capacity of the eavesdropping link
C_{PD}	PD capacitance per unit area
C_{s}	secrecy capacity
$\bar{C}_{\mathrm{s}}$	target secrecy rate
$C_{\mathrm{s}}^{\mathrm{UB}}$	upper bound on the secrecy capacity
$d_{(i,j)}$	Euclidean distance between elements i and j
D	radius of the secrecy protected zone
$\mathcal{D}$	integration domain
$\mathbb{E}$	expectation operator
E	a random event
Ei	exponential integral function
f	frequency
f_X	PDF of a random variable X
F_X	CDF of a random variable X
$\mathcal{F}_X$	characteristic function of a random variable X
${}_2F_1(\cdot,\cdot;\cdot;\cdot)$	Gauss hypergeometric function
${}_2F_2(\cdot,\cdot;\cdot,\cdot;\cdot)$	generalized hypergeometric series

g_{FET}	transconductance of the FET
G_{TIA}	open-loop voltage gain of the TIA
G_{c}	optical concentrator gain
G_{f}	optical filter gain
h	channel impulse response
$\mathbf{h}_i$	true channel coefficient vector at AP i
$\hat{\mathbf{h}}_i$	channel estimation vector at AP i
H	channel frequency response
$\mathsf{I}_{\mathrm{agg}}$	(unitless) normalized aggregate interference power
I_{bg}	background current
I_{bottom}	bottom clipping level
I_{DC}	DC bias current
I_2	noise bandwidth factor
I_{f}	aggregate interference outside the cancellation region
I_{FET}	channel-noise factor of the FET
I_{n}	aggregate interference side the cancellation region
I_{top}	top clipping level
$\Im$	imaginary part of a complex number
$\jmath$	imaginary number $\left(\jmath = \sqrt{-1}\right)$
k	shape parameter of a gamma distribution
k_{B}	Boltzmann constant
K	number of users
L	vertical distance between the ceiling and the user plane
m	LED Lambertian order
$\mathcal{M}$	moment generating function
n	number of dimensions
n_{c}	reflective index of optical concentrators
n_{clip}	clipping noise
N_{IFFT}	size of IFFT
N_{LED}	number of LEDs
$\mathbb{P}$	probability operator
p_{active}	probability that an LED is actively transmitting signals
p_{e}	eavesdropping probability

p_{so}	secrecy outage probability
$\bar{p}_{\mathrm{so}}$	target secrecy outage probability
$p_{\mathrm{so}}^{\mathrm{LB}}$	lower bound on the secrecy outage probability
$p_{\mathrm{so}}^{\mathrm{UB}}$	upper bound on the secrecy outage probability
P_{o}	optical power of the LED
P_{rx}	received optical power
P_{tx}	transmit (electrical) signal power
$\mathrm{P}_k^{\mathrm{out}}$	outage probability of user k
$\mathrm{P}^{\mathrm{cov}}$	system coverage probability
q_{e}	elementary charge
$Q(\cdot)$	Q function
Q_k	ergodic data rate for user k ($k \neq K$)
Q_K	ergodic data rate for user K
r_{c}	radius of the cooperation region
r_{e}	radius of the attocell
r_{I}	radius of the cancellable interference region
$\mathbb{R}$	the real-coordinate space
R_k	data rate of the k-th user (NOMA)
$\bar{R}_k$	data rate of the k-th user (OFDMA)
$\tilde{R}_k$	target data of the k-th user (NOMA)
$R_{k\to j}$	required rate for user k to detect the message for user j
R^{NOMA}	ergodic sum rate of NOMA
R^{OFDMA}	ergodic sum rate of OFDMA
$\Re$	real part of a complex number
$s(t)$	time-domain bipolar signal
$\tilde{s}(t)$	time-domain unipolar signal (after clipping)
s_i	time-domain bipolar signal for user i
s^+	superposed signal for NOMA
S_{LED}	normalized radiant intensity function of a white LED
S	(unitless) normalized signal power
$\mathcal{S}$	reflection surfaces
SINR	SINR
t	time index

T	SINR target
T_{K}	absolute temperature
$U(\cdot,\cdot,\cdot)$	confluent hypergeometric function
v_k	power coefficient for user k (OFDMA)
x_i	horizontal distance between node i and the reference point
x_0	the nearest AP to the origin
X_k	QAM symbol on subcarrier k
y_k	received signal at user k
Y	(unitless) normalized signal amplitude
z_k	noise at user k
α_{clip}	clipping attenuation factor
χ	a Bernoulli random variable
δ	Dirac delta function
$\boldsymbol{\epsilon}_i$	channel estimation error vector at AP i
η	effective responsivity of the PD
η_{I}	residual interference factor
η_{PD}	responsivity function of the PD
$\Gamma(\cdot)$	standard gamma function
$\Gamma(\cdot,\cdot)$	incomplete gamma function
λ_{a}	density of APs
λ_{u}	density of mobile users
μ	standard Lebesgue measure
$\phi(\cdot)$	PDF of the standard Gaussian distribution
φ_i	polar angle between node i and the reference point
Φ	point process
Φ_{a}	point process for VLC APs
Φ_{e}	point process for eavesdroppers
Φ_{LED}	point process for indoor LEDs
Φ_{u}	point process for mobile users
Ψ_{FOV}	FOV of optical concentrators
$\Psi_{1/2}$	LED semiangle
$\mathfrak{r}$	spectral reflectance
ρ	transmit SNR

σ^2_{clip}	clipping noise variance
σ^2_{QAM}	QAM symbol variance
σ^2_s	variance of the time-domain signal $s(t)$
σ^2_{shot}	variance of the shot noise
$\sigma^2_{\text{thermal}}$	variance of the thermal noise
σ^2_{n}	total noise variance
σ^2_{nb}	noise variance at the legitimate user
σ^2_{ne}	noise variance at the eavesdropper
$\bar{\sigma}^2_{\text{n}}$	normalized noise variance
τ_{RMS}	RMS delay spread of the channel
$\bar{\tau}$	mean channel delay
θ	scale parameter of a Gamma distribution
$\theta_{\text{rx},(i,j)}$	angle of incidence between elements i and j
$\theta_{\text{tx},(i,j)}$	angle of irradiance between elements i and j

Chapter 1
Introduction

The rapid development of cloud computing and data-hungry applications such as augmented reality (AR) and virtual reality (VR) has led to the tremendous and continuously increasing wireless data traffic over the the past five years. According to the Cisco Visual Networking Index (VNI): Global Mobile Data Traffic Forecast Update [7], global mobile data traffic is expected to increase sevenfold between 2016 and 2021, reaching 49 exabytes per month by 2021. However, the total radio frequency (RF) spectrum that can be used for wireless communication is limited, and almost every spectrum band is currently occupied for commercial or military applications. In order to keep pace with the tremendous demand for wireless services, new technologies and means of communication are of great research interest. Among many candidate approaches, one option is to use the higher electromagnetic (EM) spectrum, such as millimeter wave and visible light, for communication.

The technology of using visible light for wireless communication is termed as visible light communication (VLC) [4, 8]. Compared to the entire RF spectrum, which ranges from 3 kilohertz (kHz) to 300 gigahertz (GHz), visible light corresponds to the frequency band from 430 to 770 terahertz (THz). According to the Friis equation [9], increasing the signal frequency from 300 GHz to 300 THz results in an extra 60 decibels (dB) of free-space path loss (FSPL) in the received power. Therefore, VLC is ideal for the application of short-range local and metropolitan area networks (LANs/WANs), as is suggested by the Institute of Electrical and Electronics Engineers (IEEE) 802.15.7 standard[1] [11]. When signals are transmitted at a higher frequency, the effect of signal blockage and shadowing becomes more evident. As a result, for the application of high-speed wireless communication, VLC systems should be designed to reduce the probability of link blockage and shadowing. This requirement can be achieved by using the small cell concept such as the optical attocell [12] in conjunction with optical beamforming techniques [13, 14].

[1] A new topic interest group (TIG) has recently been established within the IEEE 802.11 working group aiming to develop a potential new standard on light communication [10].

The use of visible light for communication offers a number of advantages over traditional RF communications. First, the unlicensed visible light spectrum in the order of THz poses a great opportunity for low-cost broadband communication, and it could effectively alleviate the spectrum congestion currently evident in RF systems. Second, visible light does not penetrate through opaque walls. Therefore, VLC by nature exhibits higher data security at the physical layer. Third, light signals sharing the same frequency blocks but in different rooms do not interfere with each other. This yields a high frequency reuse factor and area spectral efficiency (ASE) [15]. Fourth, the absence of electromagnetic interference to existing RF systems makes VLC applicable in electromagnetic sensitive areas such as aircraft cabins, hospitals and intrinsically safe environments. Fifth, VLC is more energy-efficient because its deployment can build upon existing lighting infrastructures, where energy consumed for typical illumination is reused for wireless communication purposes.

Over the past decade, significant research efforts have been devoted to the study and exploration of point-to-point (P2P) VLC transmission and reception techniques. While link-level investigations are necessary towards understanding the capability of VLC as a suitable candidate for high-speed wireless solutions, it is also of paramount importance to study the performance of a fully fledged VLC network with simultaneous multiuser access. Such a network is also called the optical attocell network [12]. Focusing on various multiple access techniques, this work investigates the theoretical performance limits in the context of random attocell networks with the presence of multiple transmitters and receivers. The derived results can serve as an analytical framework to devise constructive insights for the design of future attocell networks.

1.1 Motivation

In the context of RF wireless networks, one of the mainstream technologies to enhance the ASE is network densification [16, 17]. The idea is to maximize the utilization of the available spectrum resources by deploying an increased number of cells. It has the benefit of reducing path loss, which increases both the desired signal power and interference, effectively reducing the impact of noise. Therefore, interference mitigation techniques are paramount for the performance enhancement of dense wireless networks. To achieves this, adaptive resource allocation and advanced signal processing techniques are necessary. The effectiveness of this approach has been demonstrated through several past generations of cellular technologies [18, 19]. During the last three decades, accompanied by increased number of cells, the cell size has also

shrunk progressively. Compared to traditional high-power macrocells, whose radius is typically greater than 1 km, small cells include picocells, with a radius of hundreds of meters, and femtocells, with an even smaller radius of tens of meters. Apart from its advantages, network densification also has a bottleneck: backhaul [16]. The backhaul is a wired or wireless backbone network which connects base stations (BSs) or access points (APs) to the core network for data transfer and information sharing. It needs to meet stringent requirements in terms of capacity, latency, availability, energy efficiency and cost [20]. Such requirements become especially demanding for dense networks with the cooperation of BSs or APs. For example, with a finite backhaul capacity, the number of feedback bits that can be conveyed per transmission block is limited.

The concept of optical attocells [12] follows the continuing trend of cell densification and it aims to provide significant throughput improvements to indoor data coverage. In fact, optical attocells can be designed as an additional layer to existing heterogeneous networks (HetNets) and help offload the continuously increasing mobile data traffic [21]. In doing so, optical attocells receive zero interference from, and generate zero interference to, their RF counterparts due to the use of distinct frequency bands. Initial results have shown that with advanced LED technologies attocell networks are estimated to deliver $40-1800$ higher ASE than RF femtocell networks [21].

Unlike RF networks, whose deployment typically requires the physical implementation of antennas, optical attocells can build upon existing lighting infrastructures such as light-emitting diodes (LEDs). In this case, energy that is typically used by lighting devices to provide illumination is reused for wireless data transfer. Considering a modern office, which is illuminated by a number of lighting devices, each light can be integrated with VLC and functions additionally as an optical AP. As information can be sent from a central hub to each AP via power cables or dedicated optical fibre links, backhaul implementation in attocell networks seems more feasible than that in RF networks. Since the light source typically has limited power and directionality, it also has a confined coverage area whose radius is in the range of meters. Therefore, as mobile users roam across the indoor space, frequent handovers among different optical attocells are expected to take place [22].

As an emerging technology, VLC is still faced with many challenges that need to be addressed before it can be deployed network-wide. One of the fundamental factors that limit the throughput of VLC networks is interference. Interference typically does not exist in a P2P VLC link

because there is only one transmitter-receiver pair. In an attocell network, interference could originate from multiple APs communicating with a common user, from a single AP communicating with multiple users, or from multiple APs communicating with multiple users. On the one hand, similar to the receiver noise, interference has a direct influence on the signal-to-interference-plus-noise ratio (SINR), which serves as a fundamental indicator of the link quality. On the other hand, interference differs from noise in that it is composed of signals transmitted from other APs and thus possesses a certain structure and property. In this sense, interference can be further exploited to better understand the performance limit of VLC networks and help devise efficient design insights.

In a general wireless network, multiple access (MA) is the technology that allows multiple transmitter-receiver pairs to communicate in a regulated manner. An efficient MA technology should be designed so that the network can support a sufficiently large number of users without severe interference, and the aggregate information capacity of communication channels are maximized. The earliest cellular network is an analog system relying on the frequency division multiple access (FDMA) [23], where users are allocated separated portions of the frequency band to transmit data. In the global system of mobile (GSM), digital modulation replaces analog modulation, and the multiuser capability of the network is supported by time division multiple access (TDMA)[2] [23]. The use of TDMA allows users to share the same frequency resource by transmitting signals in rapid succession. Moving to the next generation of cellular network, the industry standard for MA is the code division multiple access (CDMA) [23, 24], in which users can share the same frequency bands and transmit information simultaneously. To avoid undue interference among users, CDMA uses the direct-sequence spread spectrum (DSSS) technique, where each user is assigned a unique code sequence to spread the signal spectrum over the entire communication bandwidth. In this way, when each user demodulates its data, the signals transmitted by other users would appear as pseudo noise. In current cellular networks, the most popular digital modulation technique is the orthogonal frequency division multiplexing (OFDM) [25, 26]. OFDM is one of the most widely used forms of multicarrier modulation, in which the data is modulated onto a set of orthogonal subcarriers and transmitted in parallel. By partitioning the available frequency bands into a collection of narrow subbands, OFDM is more immune to frequency selective fading, and the capacity of an OFDM-based system can be readily maximized with adaptive modulation techniques [27]. Orthogonal

[2] Although the actual implementation of MA in GSM involves both FDMA and TDMA, it is generally known as TDMA due to the added novelty of time multiplexing.

frequency division multiple access (OFDMA) [25, 26] is the multiuser version of OFDM, where orthogonal subcarriers are allocated to multiple users for MA. FDMA, TDMA and OFDMA all belong to the category of the orthogonal multiple access (OMA), where resource blocks (RBs) such as frequency bands and time slots are uniquely allocated to multiple users as a means of interference avoidance. By contrast, CDMA does not belong to the OMA category because it allows users to share the available RBs and the effect of interference is minimized through user-specific spreading sequences.

In addition to the unprecedented increase in the sheer volume of wireless data, the number of wireless devices, including the Internet of Things (IoT), is also expected to grow exponentially in the fifth generation (5G) wireless network [7, 19]. As a result, novel MA techniques that are capable of providing the massive connectivity for users and devices are required for 5G. To meet this target, substantial research efforts have been devoted to the concept of non-orthogonal multiple access (NOMA) [28, 29], which is proven to yield a higher spectral efficiency than traditional OMA techniques. In general, NOMA techniques can be classified into two main categories: power-domain multiplexing based NOMA [30–33] and code-domain multiplexing based NOMA [34–36]. The power-domain multiplexing based NOMA allows multiple users to share the same RBs by using superposition coding (SC) [37, 38] at the transmitter side and successive interference cancellation (SIC) [37–41] at the receiver side. The rationale is to exploit the spatial diversity of wireless channels so that interference can be efficiently mitigated through SIC. The code-domain multiplexing based NOMA, on the other hand, relies on spreading sequences such as low-density signature (LDS) sequences and trellis codes to realize MA.

1.2 Contributions

It is envisaged that VLC networks will become one of the major contributors to future HetNets of 5G and beyond, which will help handle a large portion of indoor wireless connectivity. In this context, the current work aims to provide a set of analytical tools that would allow network operators and designers to quickly assess the downlink performance of an indoor attocell network. The main performance metrics under consideration are the SINR, coverage (or outage) probability, the network capacity and the secrecy capacity[3]. Based on the proposed analytical framework, performance limitations of attocell networks can be identified, thus allowing

[3]The definitions of these performance metrics will be made clear in latter chapters.

efficient MA solutions to be suggested. The derived theoretical results are validated against extensive Monte Carlo simulations with various network parameters. Moreover, the proposed analytical framework is extended so that with modification it is also applicable to attocell networks with advanced signal processing techniques such as the coordinated multipoint (CoMP) transmission and SIC.

The SINR characteristics are investigated as a fundamental and necessary step towards understanding the MA performance of an optical attocell network. The SINR is primarily affected by the orientation of the optical transmitter and receiver devices and the physical distance in between. Although the alignment of a transmitter-receiver pair can be optimized through techniques such as angle diversity (AD) [42–44], the link distance is user-specific and hence cannot be optimized. The link distance between a transmitter-receiver pair depends on their spatial locations in the network, which are generally modeled either deterministically or stochastically. On the one hand, the deterministic spatial model is from the transmitter's point of view, and it assumes that the location of the transmitter is fixed and known *a priori*. A typical example is the grid model, where APs are regularly placed in the shape of a grid while users can be at either fixed or random locations. On the other hand, the stochastic spatial model is from the receiver's point of view. More specifically, it places the receiver of interest at the origin and uses stochastic processes [45–49] to model the locations of transmitters. Both models have their advantages and limitations and they are discussed and compared in this work. Note that although stochastic processes have been extensively studies for RF networks, the results are not directly applicable to attocell networks. This is because, apart from their distinctive channel characteristics, link modeling in VLC involves both horizontal and vertical separations between the transmitter and receiver while modeling the link distance in RF involves only the horizontal distance.

The idle probability of APs is evident, especially in underloaded networks as well as general networks that operate with an AP sleep strategy in order to save energy and/or reduce the level of interference. In these scenarios, it is inaccurate to assume that all APs, except the serving AP that transmits useful signals to the user of interest, are the source of interference. Motivated by this, the Poisson point process (PPP) model is utilized to characterize the SINR statistics in attocell networks using a novel approach based on the moment generating function (MGF). The MGF-based approach allows fast computation of the statistical moments of the SINR without the need to calculate the cumulative distribution function (CDF) beforehand. More specifically, the MGF is utilized to find positive moments of the SINR, which are then used to facilitate the

computation of the mean, variance of the SINR and the ergodic link capacity. The proposed analytical framework is also extended to include SIC as a means to enhance the link performance. In the analysis, a general model is considered for SIC, which takes into account the residual interference that is caused by imperfect SIC processes.

In an attocell network, the link quality is generally limited by both interference and noise. Compared to using expensive receivers with a low noise figure, utilizing interference mitigation techniques to improve the network performance is more cost-effective. CoMP with joint transmission (JT) is considered as an interference mitigation technique in this work, where the cooperation among APs can be realized using existing power lines [50] or additional communication cables. The performance of a VLC network with both noncoherent JT and coherent JT[4] is investigated based on a newly proposed analytical model, whose accuracy is verified through extensive Monte Carlo simulations. It is demonstrated that coherent JT yields superior coverage performance than noncoherent JT, however, at the cost of requiring a more stringent signal synchronization and incurring a higher implementation complexity. Results also indicate that coherent JT is more advantageous than its noncoherent counterpart in an attocell network with a dense deployment of APs and high rate demands.

In order to further enhance the system capacity, the concept of NOMA is applied to attocell networks, whose performance is analytically characterized for two separate cases. In the case of guaranteed quality of service (QoS) provisioning, an analytical expression for the system coverage probability is derived. The existence of optimal power allocation coefficients for the two-user paired NOMA is also shown. In the case of opportunistic best-effort service provisioning, a closed-form expression for the ergodic sum rate is formulated, which is applicable for arbitrary power allocation strategies. The probability that NOMA achieves higher individual rates than OMA is derived. Also, an upper bound on the sum rate gain of NOMA over OMA in high SNR regimes is given. Moving on, the proposed analytical framework is then used to devise user pairing strategies to further improve the system throughput. The results confirm the superiority of NOMA over conventional OMA techniques when applied to attocell networks.

The broadcasting nature of LED lights allows concurrent signal transmission to realize MA. However, it also brings potential concerns to network administrators regarding information privacy and confidentiality. Focusing on the physical layer, analytical expressions for the link

[4]Note that the noncoherent and coherent JT schemes discussed in this work are related to electrical signals. Detailed definitions will be given in Chapter 4.

secrecy outage probability, which is defined as the probability that the achievable secrecy rate is below a certain threshold, the ergodic secrecy rate and their lower and upper bounds are derived. Impacts of AP cooperation and the implementation of a secrecy protected zone are also investigated. Results show that cooperating neighboring APs can enhance the secrecy performance of indoor attocell networks, but only to a limited extent. In contrast, building secrecy protected zones around APs can significantly improve the network security.

1.3 Thesis Layout

The remainder of this thesis is organized as follows. Chapter 2 introduces the concept of optical attocells and their implementation based on existing indoor lighting infrastructures. A brief review of relevant topics are provided therein, including deterministic and stochastic network modeling techniques and physical-layer aspects of VLC.

Chapter 3 describes in detail the deterministic and stochastic models for abstracting indoor attocell networks. Both models are compared in terms of the distribution functions of signal, interference and SINR based on the user-centric cell association principle. Following this, the MGF is applied to analytically characterize the distribution of interference and statistical moments of the SINR. The analytical framework is then generalized to incorporate the SIC capability of mobile users.

In Chapter 4, CoMP-JT is considered as an interference mitigation technique to enhance the performance of attocell networks. The level of interference is reduced by coordinating a cluster of APs for noncoherent or coherent JT. By finding the approximate distribution of the interference using second-order moment matching, a simple analytical model to evaluate the coverage performance of cooperative VLC networks is provided. The performance gap between noncoherent and coherent JT schemes is also quantified.

Chapter 5 discusses the concept and implementation of NOMA in attocell VLC networks, where a theoretical framework is presented to aid the performance analysis. The performance of NOMA is compared to that provided by traditional OMA techniques. Closed-form expressions for the link coverage probability and the ergodic sum rate are derived. Results illustrate that compared with OMA, NOMA can offer a high performance gain by utilizing power-domain multiplexing, and this performance gain can be further enlarged by pairing users with more distinctive channel conditions. The impact of various network parameters are also discussed.

Chapter 6 investigates the physical-layer security of attocell networks from an information theoretic perspective. Analytical expressions for the secrecy outage probability and the ergodic secrecy rate are derived using the stochastic PPP model. By introducing AP cooperation, tight lower and upper bounds on the secrecy performance are given in simple forms. It is shown that implementing eavesdropper-free protected zones can significantly improve the network security.

Finally, Chapter 7 summaries the key findings of this work, identifies some of its limitations and suggests possible directions for further research. It is the author's hope that this thesis can contribute to the research, development and real implementation of future optical attocell networks.

1.4 Summary

Along with many other technologies, optical attocell networking will complement and contribute substantially to future HetNets of 5G and beyond. Despite the tremendous research efforts on the topic of P2P VLC, only limited research attention has been paid to the networking perspective. The presented work attempts to fill this gap with analytical characterizations of the downlink performance of attocell networks via a systematic approach. The motivations, contributions and the thesis layout have been presented in this chapter.

Chapter 2
Background

2.1 Network Geometry

Wireless communications have been regarded as one of the most influential and phenomenal technologies for the past three decades as they have dramatically changed the way modern people communicate, work and entertain. The oldest formats of wireless communications can be traced back to the prehistory era, when smoke signals, fires, drums and beacons were used to send messages over long distances. In contrast, modern wireless communications as we know them today are built upon the fundamental works from Maxwell, Hertz and Tesla [51]. Broadly speaking, wireless communications are defined as the transfer of information or power from one place to another by means of electromagnetic (EM) waves [23]. Since the first successful demonstration of the wireless telegraph by Marconi in 1897, different types of wireless systems have made their appearances. By the late 1930s, radio had become one of the most widely used technologies for commercial and military applications.

A wireless network can be abstracted into a collection of transmitting and receiving nodes, that are located within a confined geographical region. For unidirectional wireless networks, the transmission mode is simplex and signals can only flow in one direction: from the transmitting node to the receiving node. Examples of this kind are TV and radio broadcasting. For bidirectional wireless networks, a transmitting node can also function as a receiving node, allowing signals to flow in both directions. A bidirectional wireless network can be either half-duplex or full-duplex, depending on whether signal transmission and reception take place in sequence or simultaneously. Typical examples include the walkie-talkie for half-duplex communication and the telephone for full-duplex communication. The direction in which signals flow from base stations (BSs) or access points (APs) to mobile users is called the downlink, while the uplink represents the direction of signals flowing from mobile users to BSs or APs. A transmitter-receiver pair is formed when a transmitter has agreed to send the information that is requested by a receiver, possibly through a router or a central unit. As the name “wireless” represents, signals are typically transmitted without dedicated cables, and the communication medium can

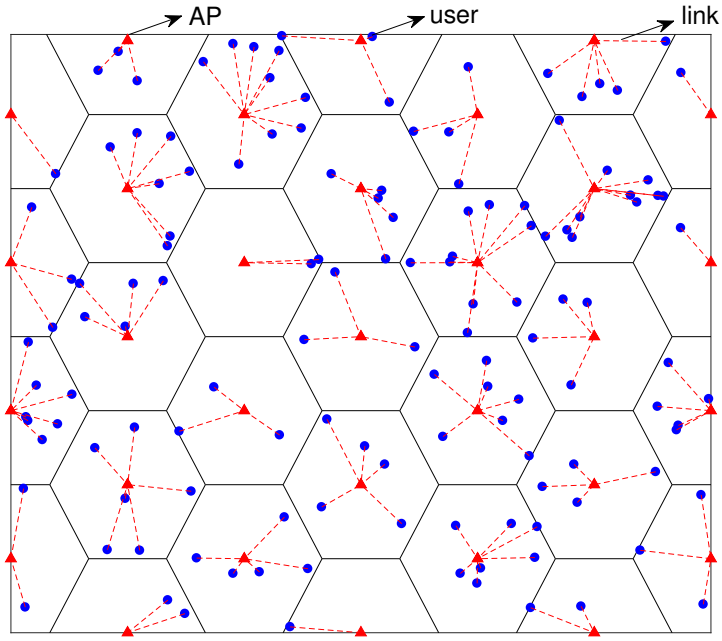

Figure 2.1: *An example of the hexagonal grid model for wireless networks. In this figure, mobile users follow a PPP and they are associated with the nearest AP.*

be vacuum, air, water, *etc.* Whatever the medium, the geometry of transmitting and receiving nodes has a significant impact on the communication link performance since it directly affects the signal-to-interference-plus-noise ratio (SINR) and hence the achievable data rate.

Broadly speaking, geometric modeling of wireless nodes can be classified into two groups: the deterministic approach and the stochastic approach. On the one hand, the deterministic approach assumes a fixed number of APs, whose locations are known *a priori*. The most common example of this kind is the hexagonal grid model, as shown in Figure 2.1. The stochastic approach [45–49], on the other hand, focuses on the macroscopic characteristic of wireless networks and assumes the locations of nodes are subject to uncertainty. More specifically, it calculates the statistical performance of the network by averaging the results over a large number of snapshots, with each snapshot being a realization of the point process. Therefore, different point processes can be used to simulate various types of wireless networks and the obtained results can serve as a spatial-average indicator.

Consider the n-dimensional Euclidean space $\mathbb{R}^n$. A spatial point process Φ, either deterministic or stochastic, is a collection of points that reside inside the space $\mathbb{R}^n$ without accumulation. Typical point processes that are widely used for modeling wireless networks include the Poisson point process (PPP) [52], the binomial point process (BPP) [53], the Matérn hard-core point

process (MHCPP) [54] and the Poisson cluster process (PCP) [55], to name just a few. Brief definitions of these common point processes are described in the following.

- **PPP:** The PPP is defined as the point process in which the number of points in a bounded closed set is a Poisson random variable, and the number of points in disjoint sets are independent.
- **BPP:** Given a point process with a fixed total number of points in a bounded closed set, this point process is a BPP if the number of points inside a subset is a binomial random variable. As a result, the numbers of points in disjoint subsets are related by a multinomial distribution.
- **MHCPP:** The MHCPP is a repulsive point process based on a parent PPP, where constituent points are forbidden to be closer together than a predefined hard-core distance. There are two common types of MHCPP. For type I, all nodes are removed if they have a neighboring node within the hard-core distance. For type II, each node is allocated with a random mark, and a node is removed if another node with a smaller mask exists within the hard-core distance.
- **PCP:** The PCP is a clustered point process. It can be constructed by replacing each point in a parent PPP with a cluster of points based on a specific mechanism. Two well-known examples of the PCP are the Matérn cluster process (MCP) and the Thomas cluster process (TCP). In MCP, each parent node is replaced by a cluster of nodes, whose size is a Poisson random variable. Each node in the cluster is independently and uniformly distributed within a disc of fixed radius around the parent node. In TCP, each parent node is replaced by a cluster of nodes, whose size is a Poisson random variable. Each node in the cluster has an isotropic Gaussian displacement from its parent node.

Examples of these common point processes on the two-dimensional (2D) plane are given in Figure 2.2. From both Figure 2.1 and Figure 2.2, it can be seen that according to the nearest AP association rule, cells are formulated into different shapes. The lines that separate APs into different cells constitute the Voronoi tessellation [56]. It is worth noting that the modeling of APs for RF networks are mostly on the 2D plane. This is because in RF networks, the vertical distance between an AP and a mobile user is typically much smaller than the horizontal distance. However, in indoor attocell networks, the vertical distance between an AP and a mobile user is similar to the horizontal distance. As a result, a three-dimensional (3D) model

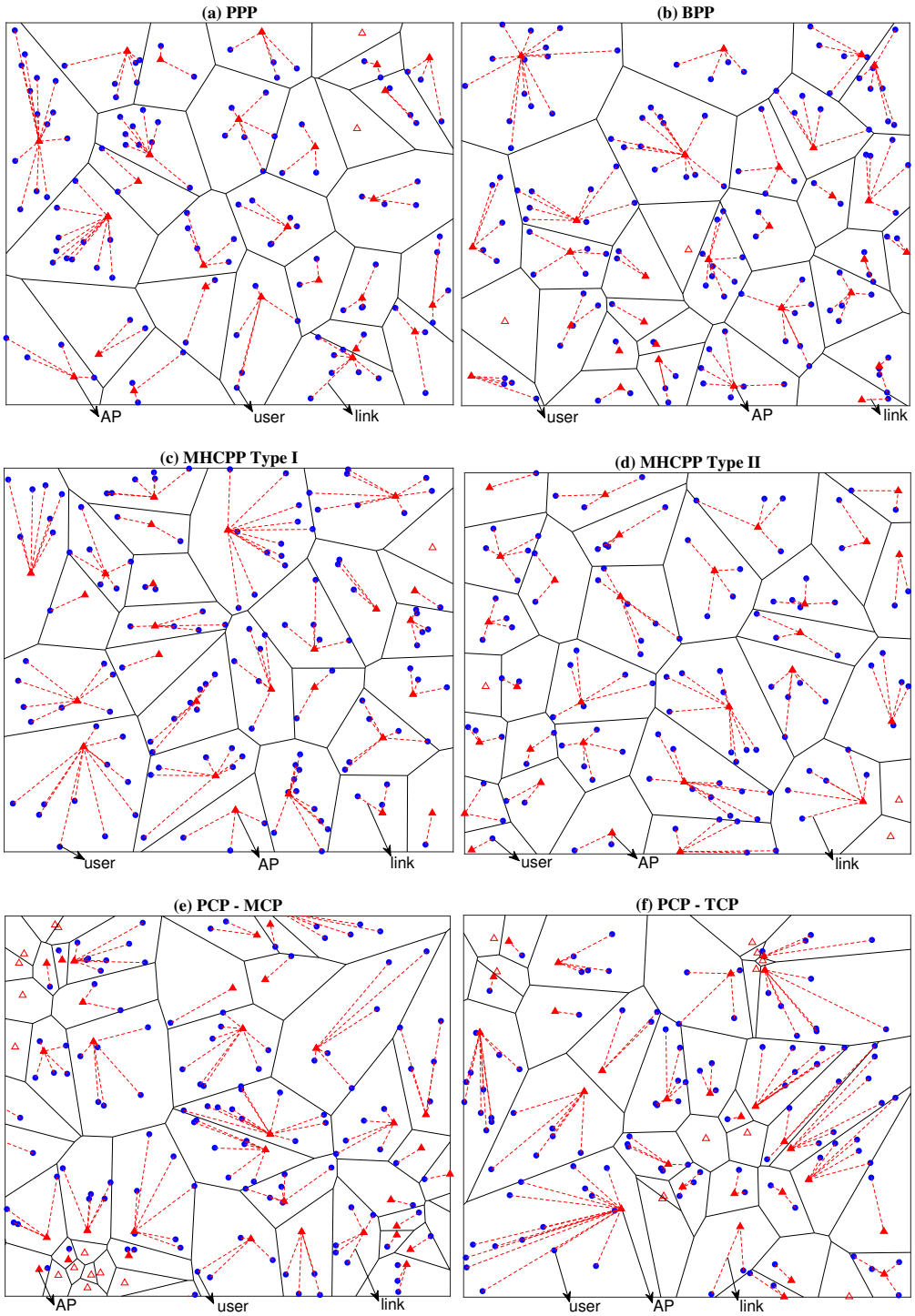

Figure 2.2: *Stochastic point processes for wireless networks: (a) the homogeneous PPP with intensity 0.12; (b) the BPP with a total number of 31 APs; (c) & (d) the MHCPP of type I & II with hard-core distance 1. The parent PPP has intensity 0.12; (e) & (f) the PCP obtained from a parent homogeneous PPP of intensity 0.024. The cluster radius is 2, and each cluster contains 5 nodes on average. For the TCP, the standard deviation of the Gaussian displacement is 2.*

is required for the performance analysis. In reality, both horizontal and vertical distances of a VLC link should be modeled as random variables. However, accurate modeling of the vertical distance of indoor mobile users is yet to be defined. To simplify the analysis, this work assumes that the vertical distance of a VLC link is a constant, but its value can be adjusted to reflect different scenarios. Furthermore, this model can be generalized to include vertical uncertainty by averaging the result with respect to the distribution of the vertical distance.

2.2 Visible Light Communication

Visible light communication (VLC) [4, 8], belonging to the field of optical wireless communication (OWC), is a technology that uses visible light, whose spectrum ranges from 430 to 770 THz, for wireless communication. This tremendous and unlicensed bandwidth makes VLC a promising technology for short-range indoor wireless communications. Compared to RF, visible light exhibits qualitatively different behaviors. For example, visible light is subject to absorption by dark objects and reflection and diffusion by light-colored objects. Also, visible light does not penetrate through opaque objects so that information signals transmitted by VLC are typically confined within the room. This unique property makes VLC inherently more secure against malicious eavesdropping than its RF counterpart.

As light-emitting diodes (LEDs) are rapidly replacing traditional incandescent and fluorescent light sources, they are also an economical and efficient candidate for VLC transmitting devices [4, 8]. Apart from LEDs, laser diodes (LDs) with a much higher current density and optical efficiency can also be used for VLC [57–59]. One of the major differences between LEDs and LDs is that the former is an incoherent light source where photons are emitted spontaneously with different phases, while the latter is a coherent light source where photons are emitted with their wave fronts launched in unison. In contrast to RF systems, where the information is modulated onto the complex-valued bipolar EM signal and transmitted by the antenna, it is impractical to detect optical signals with appreciable signal power in a single electromagnetic mode for VLC systems. As a result, it is extremely difficult to implement a coherent receiver for VLC. Instead, a viable and practical solution is to use intensity modulation and direct detection (IM/DD) with cost-effective devices such as LEDs and photodiodes (PDs) [60]. In IM/DD, information is modulated onto the intensity of the emitted light, and a current signal, whose amplitude is proportional to the received light intensity, is used for signal detection without the need of local oscillators.

2.2.1 Light-Emitting Diode as the Transmitter

The LED is a positive-negative (p-n) junction based semiconductor device that is subject to spontaneous optical radiation when an electronic excitation is applied [61]. The use of LEDs as VLC transmitters is to convert the modulated electric signal into an optical signal. Among many other devices, the LED is the most favorable candidate for VLC because of its increasing popularity in the lighting industry. A complete LED package also includes a driver circuit, which is designed to control the current flowing through the LED to adjust the brightness of the emitted light. As is recommended by lighting manufacturers, it is preferable to drive LEDs using a constant current to provide the required illumination because this allows LEDs to operate at the optimized energy efficiency and hence reduces the carbon dioxide emission. In VLC, information is carried by the rapidly varying current signals that drive the LED. Although the switching frequency, usually in the order of megahertz (MHz), is high enough so that the fluctuation of the light intensity is not perceptible to the human eye, the varying current does cause a deviation in the illumination quality from its typical value [62]. However, by balancing the direct current (DC) to the modulated signal, the output light quality of LEDs can be successfully persevered [63].

Because of the p-n junction barrier, typical LEDs have a sigmoid characteristic function between the forward current and the applied voltage [61]. More specifically, the LED is not turned on unless a forward voltage above the turn-on voltage (TOV) is applied. As the forward voltage increases and exceeds the TOV threshold, the flowing current increases exponentially before it is saturated. The saturation occurs when the output current is primarily limited by the thermal aspects of the LED, which in turn cause the electrical-to-optical efficiency to drop. The exact values for the TOV and the saturation voltage vary from device to device, and they are dependent on parameters such as the diode type, packaging and ambient temperature. Signals that are directly transmitted using off-the-shelf LEDs are subject to nonlinear distortions. To resolve this unwanted effect, a piecewise polynomial-based predistorter [64, 65] can be used at the transmitter front-end to transfer the sigmoid characteristic function of the LED into a linear one.

White LEDs that can be used for both illumination and wireless data transfer can be produced in the following two ways.

- Phosphor-coated blue LED [66]: This method produces white light using a single blue

LED and a yellow phosphor coating. As blue photons traverse through the phosphor layer, some of them are converted into yellow photons. The combination of blue and yellow photons yields the perceived white light by the human eye. This method has been widely used in the production of white LEDs because it offers good color rendering and allows the color temperature of the produced light to be easily adjusted by changing the thickness of the phosphor coating. Unfortunately, blue LEDs and yellow phosphors degrade over time, which would cause a shift in the color of the delivered light.

- RGB-LED: In this method, white light is produced by mixing the red, green and blue (RGB) lights [66]. The RGB-LED is typically more expensive than the phosphor-coated blue LED since it requires three LEDs for a single package. However, it offers more control over the color quality of the produced light. More importantly, the bandwidth of the RGB-LED is not limited by the yellow phosphor, which generally has a slow response. Also, since RGB-LEDs can offer parallel communications, they potentially yield higher data rates than phosphor-coated blue LEDs.

Although LEDs are commercially available in many varieties and packages, the generalized Lambertian model has been found to be reasonably accurate for modeling the angular distribution of radiant output power [67, 68]. In the Lambertian model, the directionality of an LED is quantified by the Lambertian order m, and it can be calculated from $m = -1/\log_2(\cos(\Psi_{1/2}))$, where $\Psi_{1/2}$ represents the semiangle of the LED. By definition, a more directional LED has a larger Lambertian order, and integrating the angular distribution of the radiant power across a hemisphere yields the total power radiated by the LED.

2.2.2 Photodiode as the Receiver

LEDs have been so commonly used as light emitters and it is easy to forget that they are essentially diodes [69]. As a result, under reverse bias conditions, LEDs can be used as optical receivers whose equivalent model consists of a capacitor in parallel with a current source [70–72]. However, the achievable data rate is usually limited. In contrast, the PD is a preferable candidate for high-speed applications of VLC. PDs are optoelectronic devices that generate a current with amplitude proportional to the received instantaneous power [73]. In other words, the amplitude of the induced current is proportional to the square of the received electrical field impinging on the detector surface. A PD can be made from different materials, which intrinsically define the characteristics of the PD. For example, a silicon-made PD typically responds

to EM waves within the $190 - 1100$ nanometer (nm) spectrum while a Germanium-made PD is responsive to EM waves within the $400 - 1700$ nm spectrum [73]. The responsivity of a PD is defined as the ratio of the generated photocurrent to the amount of incident optical power [73]. It is commonly used to quantify the optoelectronic efficiency of a PD.

As the optical signal to be detected in VLC is generally weak, it is paramount that appropriate PDs are selected. Some important criteria that should be considered are listed as follows:

- cost and reliability
- usable bandwidth for signal detection
- high responsivity in the visible light spectrum and low/zero responsivity elsewhere
- low noise level
- physical specifications such as the detection area and the field-of-view (FOV)

Although there are many types of PDs that can be used for VLC, the most popular ones are the positive-intrinsic-negative (PIN) photodiode and the avalanche photodiode (APD) [60, 74]. As the name implies, a PIN PD is constructed by placing an intrinsic semiconductor material between the p-type doped and n-type doped regions. When a reverse bias is applied, the PIN PD converts the incident photons, whose power is larger than the band-gap energy of the semiconductor material, into a current signal. Different from a PIN PD, an APD operates at a very high reverse bias. This process results in the so-called avalanche multiplication effect [73], where a photogenerated carrier creates a secondary carrier by impact ionization, resulting in a very high photocurrent gain. Therefore, the responsivity of an APD can be greater than unity while the responsivity of a PIN PD is typically smaller than unity. APDs are preferable when the system is subject to little shot noise[1] and the APD's high internal gain can help overcome the preamplifier thermal noise at a latter stage of receiver circuits. [60] However, when the ambient-induced shot noise dominants thermal noise, the avalanche multiplication in APD increases the variance of shot noise, resulting in a net degradation of signal quality. Compared to PIN PDs, APDs have additional drawbacks such as their high cost, requirement for high reverse bias and temperature-dependent amplifying gain. For these reasons, PIN PDs are selected for the analysis in the following chapters.

[1] In bright sunlight, it is possible to reduce the shot noise with the use of optical filters.

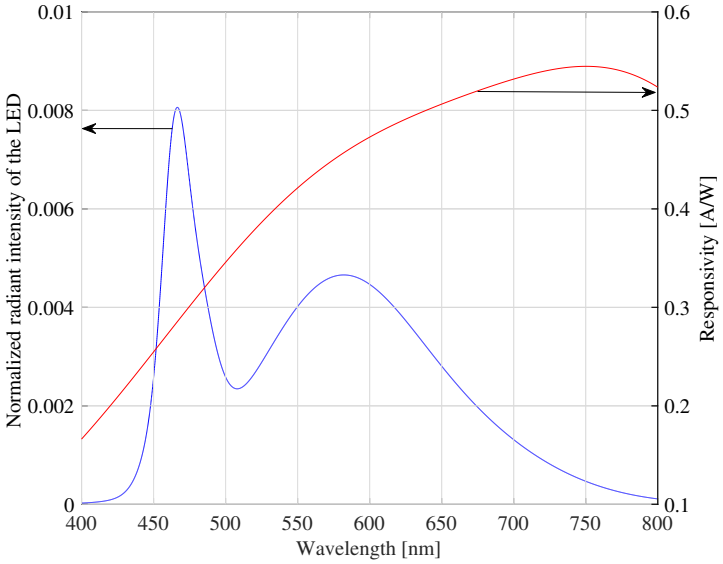

Figure 2.3: *Normalized radiant intensity of a commercially available white LED [1] and the responsivity function of a typical PIN PD [2] within the visible light spectrum.*

2.2.2.1 Equivalent Responsivity

Since PDs exhibit different responsivities across the visible light spectrum, it is necessary to calculate the effective responsivity that is weighed with respect to the radiant profile of the LED. Assume a white LED has a normalized radiant intensity $S_{\mathrm{LED}}(f)$ satisfying $\int_{380\mathrm{nm}}^{780\mathrm{nm}} S_{\mathrm{LED}}(f)\mathrm{d}f = 1$, where f represents the frequency and the integration region represents the visible light spectrum. Given that a PD has a responsivity function $\eta_{\mathrm{PD}}(f)$, the effective responsivity of the PD can be calculated as:

$$\eta = \int_{380\mathrm{nm}}^{780\mathrm{nm}} S_{\mathrm{LED}}(f)\eta_{\mathrm{PD}}(f)\mathrm{d}f. \tag{2.1}$$

In Figure 2.3, the radiant profile of a commercially available white LED from Vishay [1] and the responsivity curve of a commercially available PIN PD manufactured by First Sensor [2] are illustrated. It can be seen that the white LED has local peak power intensities at 470 nm and 580 nm while the PIN PD is the least sensitive to the blue light and the most sensitive to the red light, with a peak sensitivity at 750 nm. By applying (2.1), an equivalent responsivity of 0.41 A/W is obtained.

2.2.2.2 Receiver Noise

Along with many other specifications of a VLC link, the noise process also plays a critical role in determining the overall link performance. When a PD is used as the optical receiver for

VLC, the primary sources of noise are the shot noise and thermal noise.

Shot noise, which is usually the limiting source of noise in a well-designed optical receiver, originates from random fluctuations of photons in the induced photocurrent [73]. This randomness can be modeled by a Poisson process. Since the number of random photons is usually large, the discrete Poisson distribution approaches a Gaussian distribution with the same mean. In this case, the impact of elementary photons becomes negligible, making the actual shot noise process indistinguishable from the Gaussian distribution. Although shot noise originates from both information signals and the ambient light, the contribution of signal-dependent shot noise is comparatively small and hence can be neglected [60]. Therefore, the shot noise can be modeled as an addictive white Gaussian noise (AWGN), whose variance is [4, 60]:

$$\sigma_{\text{shot}}^2 = 2q_{\text{e}}I_{\text{bg}}I_2B, \tag{2.2}$$

where q_{e} is the elementary charge, I_{bg} is the background current induced by the ambient light, $I_2 = 0.562$ is the noise bandwidth factor [4] and B is the modulation bandwidth of the system.

To make the received signal more noise-tolerant, preamplifiers are commonly used at the receiver front-end to amplify the received signal. The three principal requirements when choosing a preamplifier for VLC are a large bandwidth, a wide dynamic range and the capability of rejecting ambient lights. A large bandwidth supports high data rates. A wide dynamic range ensures that signals with various link distances and hence attenuations can be accommodated. In the case of VLC with reflections and shadowing, signals coming from different paths may differ by orders of magnitude in power. The capability of rejecting ambient lights allows the receiver to operate in most practical environments, even in the presence of strong daylight [75]. There are many preamplifier designs, among which the most suitable one for VLC is the transimpedance amplifier (TIA), which converts a photocurrent into a voltage signal and is most often implemented with an operational amplifier because it offers a large bandwidth and a large dynamic range due to the use of feedback resistors and automatic gain control (AGC) [60, 76]. Compared to a bipolar-junction transistor (BJT), a field-effect transistor (FET) typically has lower noise [60, 76]. Therefore, an FET-based TIA is assumed in the following analysis. The thermal noise, also known as the Johnson noise, is caused by the thermal fluctuations of electrons in the receiver preamplifier circuit [77]. After neglecting noise contributions from the gate leakage current and the $1/f$ noise, the variance of the thermal noise, which can also be

modeled as the AWGN, is given by [4, 5, 76]:

$$\sigma^2_{\text{thermal}} = \frac{4.496\pi k_{\text{B}} T_{\text{K}}}{G_{\text{TIA}}} C_{\text{PD}} A_{\text{PD}} B^2 + \frac{1.389\pi^2 k_{\text{B}} T_{\text{K}} I_{\text{FET}}}{g_{\text{FET}}} C^2_{\text{PD}} A^2_{\text{PD}} B^3, \tag{2.3}$$

where A_{PD} is the detection area of the PD; k_{B} is the Boltzmann constant; T_{K} is the absolute temperature; G_{TIA} is the open-loop voltage gain of the TIA; C_{PD} is the fixed capacitance of the PD per unit area; I_{FET} is the channel-noise factor of the FET; and g_{FET} is the transconductance of the FET. In (2.3), the first term represents the thermal noise from the feedback resistor and the second term represents the thermal noise from the FET channel resistance. The variance of the overall noise process is therefore:

$$\sigma^2_{\text{n}} = \sigma^2_{\text{shot}} + \sigma^2_{\text{thermal}}. \tag{2.4}$$

The contributions of shot noise and thermal noise are compared in a numerical example shown in Figure 2.4. It can been seen that shot noise is the dominant noise source when the system bandwidth is smaller than 100 MHz. If a higher modulation bandwidth is used, thermal noise surpasses shot noise and becomes the limiting noise process at the receiver. Since the bandwidth of a typical LED is $5 \sim 60$ MHz [78], it is reasonable to neglect the impact of thermal noise and consider only the shot noise for a VLC system utilizing 30 MHz bandwidth.

Optical filters are widely used at the receiver front-end for the purpose of reducing the noise level and/or removing the slow-response yellow light to enhance the system bandwidth [79]. For example, bandpass filters are designed to allow signals within a particular range of wavelengths to pass while rejecting ambient lights outside the passband. The detectable signal power is proportional to the collection area of the PD, as is the noise variance. Moreover, increasing the collection area of the PD is expensive and would reduce the usable bandwidth [73]. As a result, it is preferable to employ optical concentrators as a means of increasing the effective collection area of the PD. The compound parabolic concentrator (CPC) is a type of nonimagining concentrator that is widely used for OWC [80]. Compared to a bare PD, which has a FOV of $90°$, a CPC exhibits a trade-off between the optical gain and its FOV. Specifically, a CPC with a FOV of Ψ_{FOV} can achieve an optical gain of G_{c} [60, 80]:

$$G_{\text{c}}(\theta_{\text{rx}}) = \begin{cases} \frac{n_{\text{c}}^2}{\sin^2(\Psi_{\text{FOV}})}, & 0 \le \theta_{\text{rx}} \le \Psi_{\text{FOV}} \\ 0, & \theta_{\text{rx}} > \Psi_{\text{FOV}} \end{cases}, \tag{2.5}$$

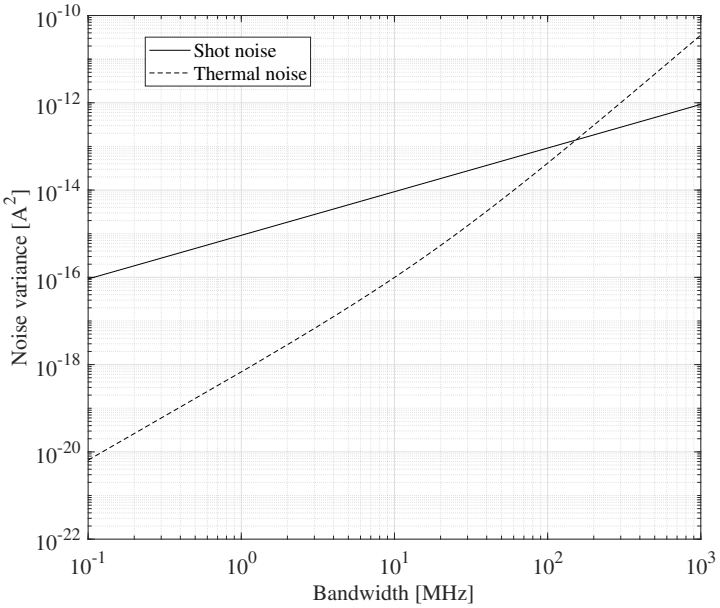

Figure 2.4: *A comparison between shot noise and thermal noise as a function of the modulation bandwidth. The background current $I_{\mathrm{bg}} = 5100\ \mu\mathrm{A}$ is measured from direct sun light without optical filter [3]. The remaining parameters are [4, 5]: $G_{\mathrm{TIA}} = 10$; $C_{\mathrm{PD}} = 112\ \mathrm{pF/cm^2}$; $A_{\mathrm{PD}} = 1\ \mathrm{cm^2}$; $I_{\mathrm{FET}} = 1.5$; and $g_{\mathrm{FET}} = 30\ \mathrm{mS}$.*

where θ_{rx} is the angle of the incident light and n_{c} is the reflective index of the optical concentrator, defined as the ratio of the speed of light in vacuum and the phase velocity of light in the optical concentrator. For visible light, typical values for n_{c} vary between 1 and 2.

2.2.3 Channel Model

The received electric field at the VLC receiver is subject to spatial variations of magnitude and phase, so that the "multipath fading" effect would exist at the optical detector. However, since the wavelength of visible light is hundreds of nanometers and the detection area of a typical PD is millions of square wavelengths, this spatial diversity effectively averages out the multipath fading effect [60]. In other words, the VLC channel would remain static if the location of the detector is offset by a distance that is in the order of a wavelength. Despite the absence of random fading, multipath channels still give rise to the intersymbol interference (ISI), especially for VLC systems utilizing a large modulation bandwidth.

VLC links can be implemented in various ways but they can be classified into two common categories. The classification criterion is related to whether the communication relies on the existence of an unblocked line-of-sight (LOS) between the transmitter-receiver pair. The LOS

link relies on the direct path while non-LOS or diffuse links rely on reflections of light from diffusive reflectors such as walls and ceilings. Compared to LOS links that typical yield higher data rates, diffuse links are more robust and easy to use and they allow signal transmission even in the presence of barriers. For both types of configuration, signal reception can be nondirectional when wide-angle transmitters and receivers are employed.

The VLC channel can be modeled as a baseband linear system. Denote by $h(t)$ the impulse response of the VLC channel, including both the LOS and diffuse links, where t is the time index. Alternatively, the VLC channel can also be characterized by its frequency response:

$$H(f) = \int_{-\infty}^{\infty} h(t) e^{-\jmath 2\pi f t} \mathrm{d}t, \tag{2.6}$$

where $\jmath = \sqrt{-1}$ is the imaginary number. When the system bandwidth does not exceed the 3-dB bandwidth of the channel, the VLC channel can be quantified by its DC gain because the frequency response is relatively flat near DC. Using the multi-bounce model, the channel impulse response can be written as:

$$h(t) = \sum_{b=0}^{\infty} h^{(b)}(t), \tag{2.7}$$

where $h^{(b)}(t)$ is the response after b bounces. When the direct link is unobstructed, the LOS channel gain (after zero bounce) is given by [60, 67]:

$$\begin{aligned} h^{(0)}(t) =& \frac{(m+1)A_{\mathrm{PD}}\eta}{2\pi d_{(\mathrm{LED,PD})}^2} \cos^m(\theta_{\mathrm{tx},(\mathrm{LED,PD})}) G_{\mathrm{f}}(\theta_{\mathrm{rx},(\mathrm{LED,PD})}) G_{\mathrm{c}}(\theta_{\mathrm{rx},(\mathrm{LED,PD})}) \\ & \times \cos(\theta_{\mathrm{rx},(\mathrm{LED,PD})}) \delta\left(t - \frac{d_{(\mathrm{LED,PD})}}{c}\right), \end{aligned} \tag{2.8}$$

where $d_{(\mathrm{LED,PD})}$ is the Euclidean distance between the transmitter and receiver; $\theta_{\mathrm{tx},(\mathrm{LED,PD})}$ and $\theta_{\mathrm{rx},(\mathrm{LED,PD})}$ are the angle of irradiance and the angle of incidence between the transmitter-receiver pair, respectively; G_{f} represents the transmission gain of the optical filter used at the receiver front end; $\delta(\cdot)$ is the Dirac delta function; and c is the speed of light.

Analytical modeling of the diffuse channel is more involved as the transmitted signal may experience multiple reflections before it arrives at the optical receiver. It should be mentioned that the diffuse channel models developed for infrared (IR) systems [60, 67, 81–84] cannot be applied directly to VLC. This is because IR signals are narrowband while VLC signals are

wideband in nature. This difference requires the wavelength-dependent properties of the LED, the PD and the spectral reflectance of interior materials to be considered [6, 85]. With a slight abuse of notation, the effective responsivity of the PD when receiving the VLC signal after b bounces is denoted by $\eta^{(b)}$. By definition, $\eta = \eta^{(0)}$. When the transmitted signal experiences $b > 0$ bounces, $\eta^{(b)}$ can be calculated by:

$$\eta^{(b)} = \int_{380\text{nm}}^{780\text{nm}} S_{\text{LED}}(f)\eta_{\text{PD}}(f) \prod_{i=1}^{b} \mathfrak{r}^{i}(f)\mathrm{d}f, \tag{2.9}$$

where $\mathfrak{r}^{i}(f)$ is the spectral reflectance function of the i-th reflector, which can be the walls, ceiling, floor and other interior finishing objects. The b-bounce $(b > 0)$ impulse response is given by [6]:

$$\begin{aligned} h^{(b)}(t) =& \eta^{(b)} G_{\text{f}}(\theta_{\text{rx},(b,\text{PD})}) G_{\text{c}}(\theta_{\text{rx},(b,\text{PD})}) \\ & \times \iint_{\mathcal{S}} \prod_{i=1}^{b+1} \Upsilon_i \delta\left(t - \frac{d_{(\text{LED},1)} + d_{(b,\text{PD})} + \sum_{j=1}^{b-1} d_{(j,j+1)}}{c}\right) \mathrm{d}A_{\square}, \end{aligned} \tag{2.10}$$

where $\theta_{\text{rx},(b,\text{PD})}$ denotes the incidence angle from the b-th reflector to the PD; $d_{(\text{LED},1)}$ denotes the Euclidean distance between the LED and the first reflecting element; $d_{(j,j+1)}$ denotes the Euclidean distance between the j-th reflecting element and the next reflecting element; and $d_{(b,\text{PD})}$ denotes the Euclidean distance between the b-th reflecting element to the PD. The geometry of the multipath channel is shown in Figure 2.5. In (2.10), the integration is performed with respect to all reflecting surface elements and $\mathrm{d}A_{\square}$ is the differential surface of area. Moreover, Υ_i are auxiliary variables, defined as [6]:

$$\begin{aligned} \Upsilon_1 =& \frac{A_{\square}(m+1)\cos^{m}(\theta_{\text{tx},(\text{LED},1)})\cos(\theta_{\text{rx},(\text{LED},1)})}{2\pi d_{(\text{LED},1)}^{2}}, \\ \Upsilon_2 =& \frac{A_{\square}\cos(\theta_{\text{tx},(1,2)})\cos(\theta_{\text{rx},(1,2)})}{\pi d_{(1,2)}^{2}}, \\ & \vdots \\ \Upsilon_{b+1} =& \frac{A_{\text{PD}}\cos(\theta_{\text{tx},(b,\text{PD})})\cos(\theta_{\text{rx},(b,\text{PD})})}{\pi d_{(b,\text{PD})}^{2}}. \end{aligned}$$

To evaluate the severity of ISI caused by multipath distortions, the channel root-mean-square

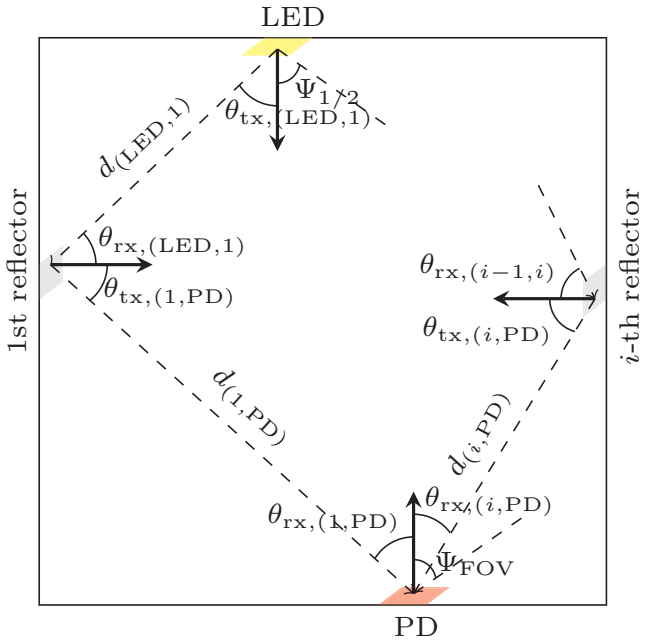

Figure 2.5: *Geometry of the multipath channel.*

(RMS) delay spread can be used as an efficient indicator [60]:

$$\tau_{\mathrm{RMS}} = \sqrt{\frac{\int_{-\infty}^{\infty}(t-\bar{\tau})^2 h^2(t)\mathrm{d}t}{\int_{-\infty}^{\infty} h^2(t)\mathrm{d}t}}, \tag{2.11}$$

where the mean delay $\bar{\tau}$ is given by:

$$\bar{\tau} = \frac{\int_{-\infty}^{\infty} t h^2(t)\mathrm{d}t}{\int_{-\infty}^{\infty} h^2(t)\mathrm{d}t}. \tag{2.12}$$

As a rule of thumb, the channel can be viewed as ISI-free if the symbol duration is more than ten times as large as the RMS delay spread [23].

A numerical study of the multipath channel is presented in Figure 2.6, where up to 3-bounce reflections are taken into consideration. In the simulation, the spatial resolution is set to 4, *i.e.,* the differential surface is a square of size 0.25×0.25 m^2. It can be seen that multipath channels have higher path losses and experience stronger fluctuations at higher frequencies. Also, Figure 2.6 shows that the overall frequency response is reasonably flat since it is dominated by the LOS channel. For example, the maximum fluctuation is less than 2 dB for frequencies between 0 and 200 MHz.

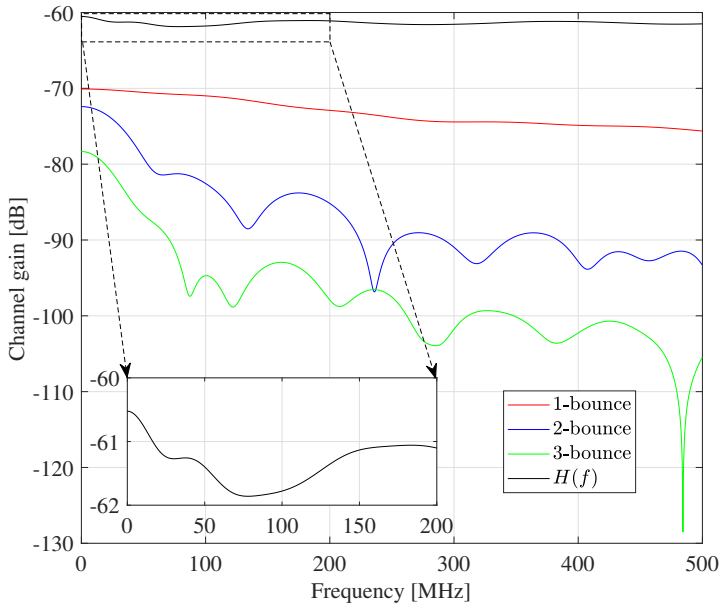

Figure 2.6: *Frequency response of a VLC channel. The simulation environment is of size* $5 \times 5 \times 3$ m^3. *The transmitter is a commercially available white LED [1] located at* $(2.5, 2.5, 3)$. *The receiver is a commercially available PIN PD [2] located at* $(1, 1, 1)$. *The spectral reflectance of the interior material (including walls, floor and ceiling) are obtained from [6].*

Figure 2.7 shows the cumulative distribution function (CDF) of the RMS delay spread of a VLC channel. It can be seen that in this setup the maximum RMS delay spread does not exceed 6.2 ns. The coherence bandwidth can be estimated from the inverse of RMS delay, yielding 161 MHz. Therefore, ISI-free signal transmission can be achieved in a VLC system with ~ 20 MHz bandwidth because of the strong LOS component. Nevertheless, even larger bandwidths are possible with the use of ISI cancellation techniques [86–88].

2.2.4 Optical Orthogonal Frequency Division Multiplexing

The use of IM for VLC systems requires the transmitted signal to be real and non-negative. Existing modulation techniques that can be adapted for VLC in a straightforward manner include on-off keying (OOK), pulse amplitude modulation (PAM), pulse width modulation (PWM), pulse position modulation (PPM) and their variants [89]. These single-carrier modulation (SCM) schemes are easy to implement and are ideal for low-speed applications. As the data rate increases, implementing these modulation schemes requires complex equalizers at the receiver front-end in order to combat the ISI over the dispersive channel.

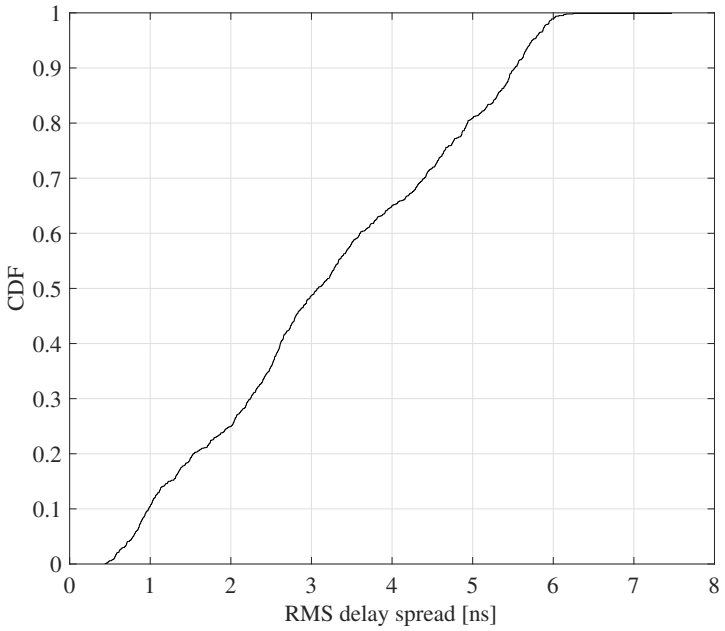

Figure 2.7: *RMS delay spread of a VLC channel based on 1,000 user locations drawn from a uniform distribution. The simulation setup is the same as described in Figure 2.6.*

In contrast to SCM, multi-carrier modulation (MCM) such as orthogonal frequency division multiplxing (OFDM) [90–92] has been widely used for high-speed VLC systems. OFDM uses a multiplicity of narrowband sub-carriers for parallel signal transmission. As a result, the symbol period becomes much longer than that of a serial system and the ISI can be effectively mitigated if the symbol period is long enough as the RMS delay of the channel. In most OFDM implementations, the residual ISI, if there is any, can be easily removed by using a form of guard interval named cyclic prefix (CP). The use of OFDM also enables low-complexity channel equalization via single-tap equalizers, as well as adaptive bit and power loading algorithms to further optimize the achievable data rate [78, 93–95].

Optical OFDM (O-OFDM) for VLC imposes Hermitian symmetry on the modulated subcarriers to obtain a real-valued signal. There are many variants of O-OFDM that can produce real and non-negative signals, with the most common ones being direct current biased optical OFDM (DCO-OFDM) [96] and asymmetrically clipped optical OFDM (ACO-OFDM) [97]. In DCO-OFDM, the modulated signal is made non-negative by adding a positive DC bias to the bipolar signal. In ACO-OFDM, symbols are carried by odd subcarriers only and the transmitted signal is ensured to be non-negative by hard clipping at the zero level. In this thesis, DCO-OFDM is assumed as the default modulation format because of its a high spectral efficiency and the ability to provide a constant illumination level [98, 99].

A DCO-OFDM transmitter converts parallel sequences of complex data symbols, which are mapped from quadrature amplitude modulation (QAM), into a discrete time-domain signal through the inverse fast Fourier transform (IFFT). Because of the Hermitian symmetry constraint, the QAM symbols need to satisfy $X_0 = X_{N_{\mathrm{IFFT}}/2} = 0$ and $X_k = X^*_{N_{\mathrm{IFFT}}-k}$, where N_{IFFT} is the size of IFFT, X_k is the QAM symbol to be transmitted on subcarrier k ($k = 1, \cdots, N_{\mathrm{IFFT}}/2 - 1$), and $[\cdot]^*$ denotes the complex conjugate operation. After IFFT, the time-domain signal is given by [92]:

$$s(t) = \frac{1}{\sqrt{N_{\mathrm{IFFT}}}} \sum_{k=0}^{N_{\mathrm{IFFT}}-1} X_k \exp\left(\frac{\jmath 2\pi k t}{N_{\mathrm{IFFT}}}\right). \tag{2.13}$$

Since subcarriers X_0 and $X_{N_{\mathrm{IFFT}}/2}$ carry no data, the number of unique data carrying subcarriers in DCO-OFDM is $N_{\mathrm{IFFT}}/2 - 1$. For M-QAM, the real and imaginary parts of modulated symbols are independent variables with zero mean and variance $\sigma^2_{\mathrm{QAM}}/2$, yielding complex symbols of variance σ^2_{QAM}. According to the central limit theorem (CLT) [100–102], $s(t)$ approaches a Gaussian distribution for a large number of subcarriers, *e.g.,* $N_{\mathrm{IFFT}} > 64$. Based on (2.13), the variance of $s(t)$ can be calculated as:

$$\sigma_s^2 = \mathbb{E}\left[s^2(t)\right] = \frac{N_{\mathrm{IFFT}} - 2}{N_{\mathrm{IFFT}}} \sigma^2_{\mathrm{QAM}}. \tag{2.14}$$

The bipolar signal $s(t)$ can be converted to a unipolar signal by adding a DC bias I_{DC} and applying zero-level clipping. However, in order to accommodate the linear operation region of typical LEDs, the DC-biased signal needs to be clipped at both (positive) bottom and top levels. The clipped unipolar signal is:

$$\tilde{s}(t) = \begin{cases} I_{\mathrm{bottom}} & s(t) + I_{\mathrm{DC}} \leq I_{\mathrm{bottom}} \\ s(t) + I_{\mathrm{DC}} & I_{\mathrm{bottom}} < s(t) + I_{\mathrm{DC}} < I_{\mathrm{top}} \\ I_{\mathrm{top}} & s(t) + I_{\mathrm{DC}} \geq I_{\mathrm{top}} \end{cases}, \tag{2.15}$$

where I_{bottom} and I_{top} are the bottom and top clipping levels, respectively. The clipping operation modifies the mean of the time-domain signal and hence the radiated optical power, whose value is given by [65, 101]:

$$P_{\mathrm{o}} = \mathbb{E}\left[\tilde{s}(t)\right] = \sigma_s \left(\varrho_{\mathrm{top}} Q(\varrho_{\mathrm{top}}) - \varrho_{\mathrm{bottom}} Q(\varrho_{\mathrm{bottom}}) - \phi(\varrho_{\mathrm{top}}) + \phi(\varrho_{\mathrm{bottom}})\right) + I_{\mathrm{bottom}}, \tag{2.16}$$

where $\varrho_{\text{top}} = (I_{\text{top}} - I_{\text{DC}})/\sigma_s$, $\varrho_{\text{bottom}} = (I_{\text{bottom}} - I_{\text{DC}})/\sigma_s$, $\phi(\cdot)$ is the probability density function (PDF) of the standard Gaussian distribution, and $Q(\cdot)$ is the well-known Q function. To better understand the effect of double-sided clipping, the clipped signal can be modeled by the Bussgang theorem [65, 101, 103]:

$$\tilde{s}(t) = \alpha_{\text{clip}} \left(s(t) + I_{\text{DC}}\right) + n_{\text{clip}}, \tag{2.17}$$

where $\alpha_{\text{clip}} = Q(\varrho_{\text{bottom}}) - Q(\varrho_{\text{top}})$ is the clipping attenuation factor and n_{clip} is the uncorrelated clipping noise. Although n_{clip} is not necessarily Gaussian, when the fast Fourier transform (FFT) is applied at the system receiver, n_{clip} is transformed into addictive Gaussian noise in the frequency domain according to the CLT [100]. The variance of the clipping noise can be calculated as [65, 101]:

$$\begin{aligned}\sigma_{\text{clip}}^2 = &- \sigma_s^2 \left(\phi(\varrho_{\text{bottom}}) - \phi(\varrho_{\text{top}}) + \varrho_{\text{bottom}}(1 - Q(\varrho_{\text{bottom}})) + \varrho_{\text{top}} Q(\varrho_{\text{top}})\right)^2 \\ &+ \sigma_s^2 \left(\alpha_{\text{clip}} - \alpha_{\text{clip}}^2 + \varrho_{\text{bottom}}^2(1 - Q(\varrho_{\text{bottom}})) + \varrho_{\text{top}}^2 Q(\varrho_{\text{top}})\right) \\ &+ \sigma_s^2 \left(\varrho_{\text{bottom}}\phi(\varrho_{\text{bottom}}) - \varrho_{\text{top}}\phi(\varrho_{\text{top}})\right),\end{aligned} \tag{2.18}$$

and the useful signal power is scaled to

$$P_{\text{tx}} = \alpha_{\text{clip}}^2 \sigma_s^2. \tag{2.19}$$

According to the three-sigma rule of thumb, setting $\min(I_{\text{DC}} - I_{\text{bottom}}, I_{\text{top}} - I_{\text{DC}})/\sigma_s > 3$ ensures that at least 99.7% of the original signal remains unclipped [65, 95]. In this scenario, the clipping distortion in the system can be considered negligible.

2.3 Summary

This chapter briefly discusses the geometry and link configuration of an attocell network. In contrast to the deterministic grid model, stochastic models focus on the macroscopic property of the network, where the collection of APs and their geographical locations are subject to certain distributions. Although the topology of the deterministic model matches physical locations of indoor lighting devices, this model implicitly assumes that all light devices are active transmitters, which may not be true for networks with a low density of mobile users. Stochastic models, on the other hand, allow statistical evaluation of the network performance by averaging

over a large number of topology snapshots. Such models transform the randomness of mobile users to the random deployment of APs, yielding tractable results and providing useful design insights.

The physical layer of a VLC system involves a transmitter, a receiver and a communication channel. In most practical VLC systems, the transmitter is in the form of an LED since it can provide both illumination and wireless data transfer. White LEDs can be made of phosphor-coated blue LEDs or RGB LEDs. Phosphor-coated blue LEDs are generally cheaper, but their modulation bandwidth is limited by the slow-response yellow phosphor coating. RGB LEDs, on the other hand, produce white light by mixing the red, green and blue lights. Despite being more expensive than phosphor-coated blue LEDs, RGB LEDs offer more control over the color of the emitted light. Moreover, the bandwidth of RGB LEDs is larger than that of phosphor-coated blue LEDs, and parallel communication is achievable with a single package of RGB LEDs. The VLC receiver can be an image sensor or a PD. Being the most sensitive to incident photons and having a large bandwidth, the PD is most commonly used for high-speed VLC applications. Like many other optical receivers, PDs are subject to random fluctuations of photons in the detector, which give rise to the shot noise. The thermal noise is the result of thermal fluctuations of electrons in the receiver preamplifier circuit. Since the system bandwidth is typically limited to hundreds of MHz, shot noise dominates the receiver noise processes and it can be modeled as an AWGN. The communication channel of a VLC system contains both LOS (if unblocked) and diffuse components. Unlike RF channels, the VLC channel is deterministic due to the large detection area of the PD when compared to the wavelength of visible light. Accurate modeling of VLC channels requires the consideration of the radiant profile of white LEDs, the responsivity profile of PDs and the reflectance characteristic of surface reflectors, which are all wavelength-dependent functions.

O-OFDM has been increasingly used in VLC because of its resistance to ISI and the ability to offer high data rates. Before the modulated OFDM signal can be transmitted by the LED, it is double-sided clipped in order to fit the linear dynamic range of typical LEDs. Bussgang theorem allows accurate modeling of the clipped OFDM signal. Despite the existence of the unwanted clipping noise, its effect can be minimized when the clipping levels are set outside the three-sigma region.

Chapter 3
Signal, Interference and SINR Statistics: From Deterministic to Stochastic Models

3.1 Introduction

The topology of wireless networks, also known as the network geometry, refers to the geographical pattern formed by the transmitting and receiving devices therein. In indoor optical attocell networks, lighting-emitting diodes (LEDs) serve as both illumination devices as well as optical access points (APs). The frequently used deterministic model assumes fixed locations of APs inside an attocell network, which coincide with the locations of LEDs [4, 104–107]. However, considering real-time snapshots of an attocell network, not every LED operates as a signal transmitter due to the random movement of mobile users. This is evident for networks with a low density of users and networks operating with an AP-sleeping strategy. As a result, although the actual deployment of LEDs may be regular, the topology of operational APs can be irregular, which also changes dynamically as users roam freely inside the network coverage area [108]. Also, the regular deployment of APs, for example in a hexagonal shape, does not lead to elegant and tractable analytical results [109]. In fact, system-level performance analysis of such networks typically relies on computer-aided Monte Carlo simulations, which are often time-consuming and do not provide direct insights into how the performance scales with various parameters of the network.

To overcome these technical shortcomings, stochastic models have recently been proposed in attocell networks to abstract the locations of APs as random variables [108, 109]. By using mathematical tools from stochastic geometry [45–49], analytical frameworks are developed to capture the essential behavior and characteristics of the network. In this chapter, a connection between these two models in a three-dimensional (3D) attocell network is first made. Note that the vertical distance of a communication link also needs to be considered because it is comparable to the horizontal distance for indoor visible light communication (VLC) applications. The stochastic model selected for analysis in this thesis is the Poisson point process

(PPP) due to its simplicity and mathematical tractability. The key performance metrics under consideration are the signal power S, the aggregate interference power $\mathsf{I}_{\mathrm{agg}}$ and the signal-to-interference-plus-noise ratio (SINR) SINR. With the knowledge of these key metrics, one can easily compute the information-theoretic capacity, link coverage probability and spectral efficiency of the network. To accommodate random movements of mobile users, this chapter focuses on studying the statistics of these metrics rather than evaluating them based on fixed user locations. As the presented analysis does not assume particular parameter values, it is general enough and scalable for attocell networks with various sizes and parameters. Moreover, the theoretical framework is extended to include successive interference cancellation (SIC) as a means to enhance the network performance.

The remainder of this chapter is organized as follows. Section 3.2 presents a preliminary analysis and comparison between the hexagonal and PPP models. Since not all the available LEDs function as the signal transmitter, a thinning process is applied to the hexagonal model in order to closely reflect the real scenario. After justifying the applicability of the PPP model, mathematical expressions for the SINR statistics are formulated in Section 3.3. The results are further used for the derivation of link coverage probability and ergodic capacity. In the same section, a generalization of the mathematical framework to include the SIC and numerical examples are also presented. Simulation results are presented in Section 3.4. Finally, concluding remarks are given in Section 3.5.

3.2 System Models and Preliminary Analysis

Consider the downlink transmission of an indoor attocell network, with full frequency reuse, over a confined 3D indoor space. This network model is scalable and can be applied to practical scenarios such as homes, offices and conference halls.

3.2.1 Thinned Hexagonal Model

The top-view of the hexagonal model is shown in Figure 2.1, where each user is assumed to be associated with the AP that has the strongest SINR. Notice that indoor LEDs are typically installed facing vertically downward. By assuming that the optical receivers face vertically upward, the nearest AP yields the highest SINR. Based on the fact that indoor LEDs are installed in the ceiling, they have fixed vertical coordinates. For notational simplicity, only their horizon-

tal coordinates are modeled according to a deterministic point process $\Phi_{\mathrm{LED}} = \{(x_i, \varphi_i), i \in \{1, 2, \cdots, N_{\mathrm{LED}}\}\} \subset \mathbb{R}^2$, where N_{LED} is the total number of LEDs and x_i and φ_i denote the horizontal distance and the polar angle between LED i and the reference point, respectively. The vertical distance between the ceiling and the user plane is denoted by L. Because of the random movement of mobile users, only LEDs that are requested to send information serve as APs. Motivated by this, the distribution of APs is modeled by thinning the original hexagonal model. The thinning rule is modeled by a Bernoulli distribution:

$$\mathbb{P}\left[\mathcal{A}_i = \chi\right] = \begin{cases} p_{\mathrm{active}}, & \chi = 1 \\ 1 - p_{\mathrm{active}}, & \chi = 0 \end{cases}, \tag{3.1}$$

where $\mathcal{A}_i$ denotes the event that LED i is requested to transmit signals and p_{active} is the probability of that event. Based on this thinning procedure, the point process for APs can be obtained as $\Phi_{\mathrm{a}} = \{(x_i, \varphi_i) : (x_i, \varphi_i) \in \Phi_{\mathrm{LED}}, \mathcal{A}_i = 1\}$.

A random user following the uniform distribution is assumed to roam freely across the entire space without any particular preferences or restrictions. Therefore, this user is equally probable to be associated with any AP inside the network. The coordinates of the serving AP to this random user is denoted by (x^*, φ^*). Using the line-of-sight (LOS) channel model presented in Section 2.2.3, the channel gain can be rewritten as a function of AP location $h(x_i, \varphi_i)$. Based on this notation, the received electrical signal power is $\mathsf{S} = P_{\mathrm{tx}} h^2(x^*, \varphi^*)$ and the aggregate interference power is $\mathsf{I}_{\mathrm{agg}} = \sum_{(x_i,\varphi_i)\in\Phi_{\mathrm{a}}\setminus\{(x^*,\varphi^*)\}} P_{\mathrm{tx}} h^2(x_i, \varphi_i)$, with P_{tx} being the transmit electrical signal power of the AP, as defined in (2.19).

3.2.2 Poisson Point Process Model

The top-view of the PPP model is shown in Figure 2.2 (a). In this model, the horizontal positions of VLC APs are modeled by a 2D homogeneous PPP $\Phi_{\mathrm{a}} = \{x_i, i \in \mathbb{N}\} \subset \mathbb{R}^2$ with constant density λ_{a}, where x_i is the horizontal distance from AP i to the origin in the non-decreasing order, *i.e.,* $x_0 \leq x_1 \leq \cdots$. Similarly, mobile users are assumed to be at a lower plane and their horizontal positions are modeled by another independent 2D homogeneous PPP $\Phi_{\mathrm{u}} = \{y_i, i \in \mathbb{N}\} \subset \mathbb{R}^2$ with constant density λ_{u}, where y_i is the horizontal distance from user j to the origin. To facilitate the analysis, an additional user is placed at the room center

(origin)[1]. Now the new point process for mobile users becomes $\Phi_{\mathrm{u}} \bigcup \{0\}$. Slivnyak's theorem states that adding a user into Φ_{u} is equivalent to conditioning Φ_{u} on the added point, and this does not change the distribution of the original process [45]. Therefore, the added user at the origin can be treated as the *typical* user because it can reflect the spatially averaged performance of all users in the network. This is true for an infinite network. For a finite network, the obtained result also remains unchanged, as long as the typical user is far away from the room boundaries. This is justified by the power-scaling law, stating that the received power is inversely proportional to the link distance and quickly diminishes as the interfering AP is moved further away from the receiver. The impact of room boundaries has been investigated in [108] and it is omitted here.

Denote by x^* the serving AP that gives the highest channel gain to the typical user, whose detector is pointed vertically upward. It can be calculated by:

$$x^* = \arg \max_{x_i \in \Phi_{\mathrm{a}}} h(x_i). \tag{3.2}$$

Considering LOS channels without reflections or shadowing, the solution to (3.2) is $x^* = x_0$, It can be seen from (3.2) that the highest channel gain association is equivalent to the nearest AP association, resulting in coverage areas that form the Voronoi tessellation, as depicted in Figure 2.2 (a). In this model, the received electrical signal power is $\mathsf{S} = P_{\mathrm{tx}} h^2(x_0)$ and the aggregate interference power is $\mathsf{I}_{\mathrm{agg}} = \sum_{x_i \in \Phi_{\mathrm{a}} \setminus \{x_0\}} P_{\mathrm{tx}} h^2(x_i)$.

3.2.3 Preliminary Results

To compare the thinned hexagonal model with the stochastic PPP model, simulation-based preliminary results on the signal, interference and SINR statistics are presented. The SINR is defined as:

$$\mathsf{SINR} = \frac{\mathsf{S}}{\mathsf{I}_{\mathrm{agg}} + \sigma_{\mathrm{n}}^2}. \tag{3.3}$$

A quantitative comparison between the thinned hexagonal model and the PPP model is shown in Figure 3.1. The results are obtained from Monte Carlo simulations and they illustrate the empirical probability density function (PDF) of the signal power S, the aggregate interference power $\mathsf{I}_{\mathrm{agg}}$ and the SINR of a random user inside an attocell network. It can be seen from Fig-

[1] Both terminologies are used interchangeably throughout this chapter.

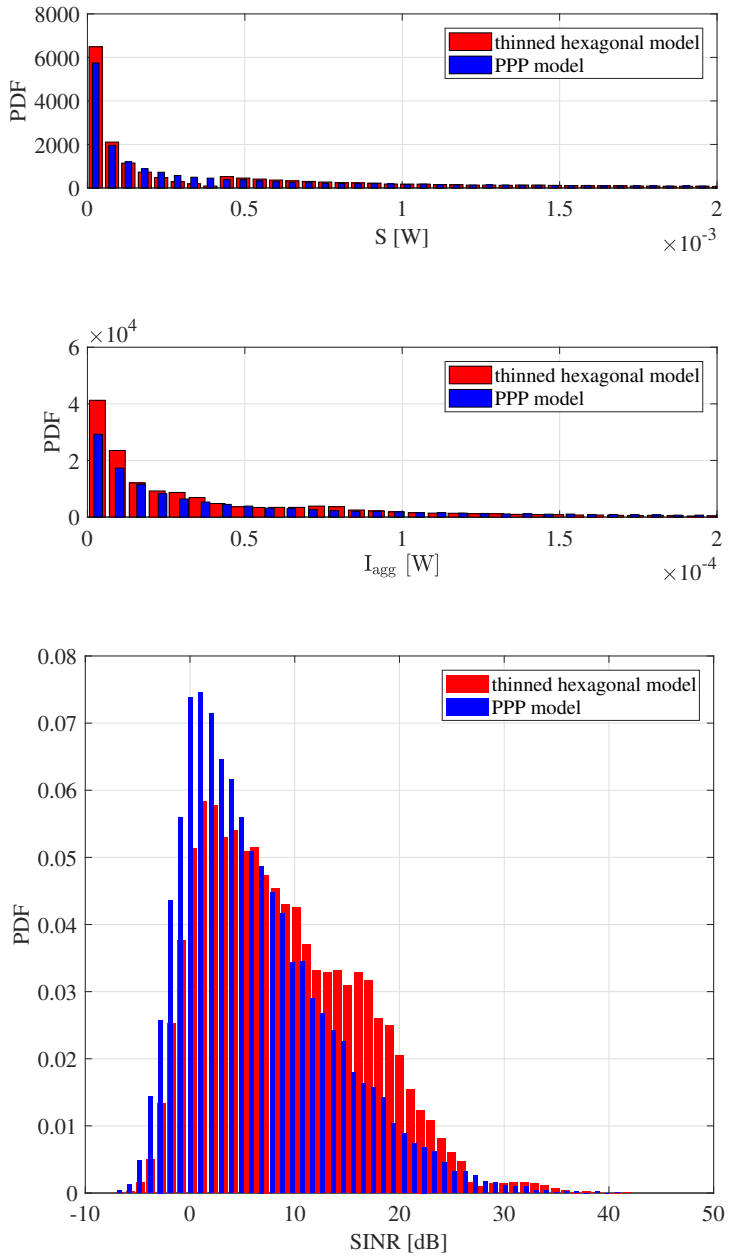

Figure 3.1: *Empirical PDFs of the signal (top), interference (middle) and SINR (bottom): a comparison between the thinned hexagonal model and the PPP model. In the simulation, a room of size* $18 \times 14 \times 3.5\ \mathrm{m}^3$ *is assumed. For the thinned hexagonal model, the LED layout is the same as shown in Figure 2.1 and* $p_{\mathrm{active}} = 0.4$*. For the PPP model,* $\lambda_{\mathrm{a}} = 0.12$*. For both models,* $P_{\mathrm{tx}} = 1\ \mathrm{W}$*;* $L = 2\ \mathrm{m}$*;* $\Psi_{1/2} = 60°$*;* $\Psi_{\mathrm{FOV}} = 90°$*; and the noise variance is neglected.*

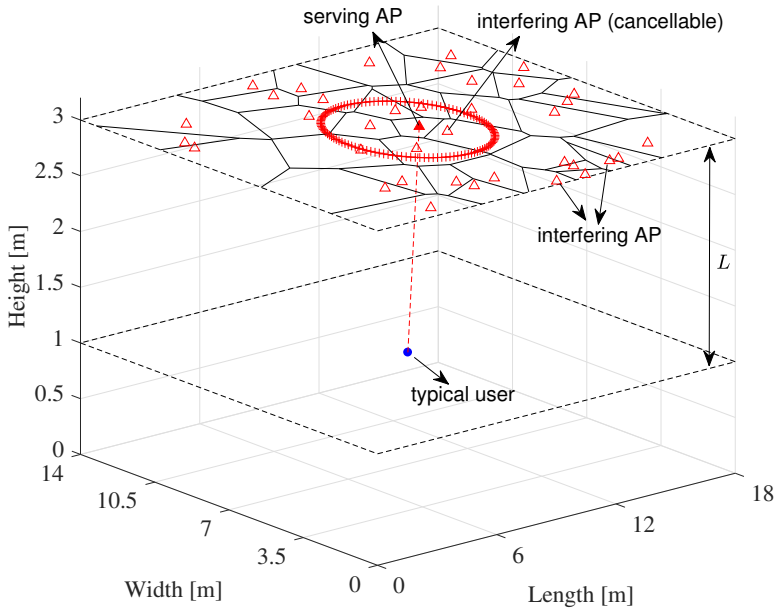

Figure 3.2: *Illustration of the PPP model for VLC networks. The typical user is served by the nearest AP in its vicinity while other APs act as interfering sources. The interference from APs inside ball $\mathcal{B}(o, r_{\mathrm{I}})$ is partially/completely cancellable if imperfect/perfect SIC receivers are used. A degenerated network model without SIC can be obtained by setting $r_{\mathrm{I}} = 0$ and/or $\eta_{\mathrm{I}} = 1$.*

ure 3.1 that the distributions of S and $\mathsf{I}_{\mathrm{agg}}$ both have long tails due to the power-law decaying characteristic of the VLC channel. Also, it is interesting to note that the PPP model yields similar results as the thinned hexagonal model in terms of signal, interference and SINR statistics. Therefore, the stochastic PPP model is selected for the performance evaluation of VLC networks in the remaining sections of this chapter. The use of the PPP model allows tractable analytical results to be derived and useful design insights to be obtained.

3.3 SINR Statistics

In this section, we formally study the PPP model and present an analytical framework based on the moment generating function (MGF) for fast and tractable computation of the SINR statistics in indoor attocell networks. The proposed framework is also generalized to incorporate SIC for advanced interference mitigation.

3.3.1 System Model

The PPP model described in Section 3.2.2 is used. To include SIC, an interference cancellation region is added to the network model. In particular, the interference cancellation region is represented by a 2D ball $\mathcal{B}(o, r_{\mathrm{I}})$, which is centered at the origin with radius r_{I}. Note that r_{I} is a tunable parameter, whose value can be chosen so that the average number of interfering APs that can be canceled corresponds to the SIC capability of the receiver [40]. For clarity, the VLC receiver without SIC capability is named the *nSIC receiver* while the VLC receiver with SIC capability is named the *SIC receiver*. Consider a practical (imperfect) SIC receiver and assume that it is capable of reducing the power of interference generated by the interfering nodes inside the cancellation region by a factor of $1 - \eta_{\mathrm{I}}$ (*i.e.,* leaving a residual interference with factor η_{I}). The analysis can also be applied to perfect SIC receivers by setting $\eta_{\mathrm{I}} = 0$. With these definitions, it is clear that a SIC receiver degenerates into a nSIC receiver when $r_{\mathrm{I}} = 0$ and/or $\eta_{\mathrm{I}} = 1$. The described system model is general enough for analyzing the interference distribution as well as the SINR statistics in attocell networks.

Considering the LOS channel model in (2.8), the channel gain from AP i to the typical user can be simplified to

$$h(x_i) = \alpha \left(x_i^2 + L^2\right)^{-\frac{m+3}{2}}, \tag{3.4}$$

where α is defined as $\alpha = (m+1)A_{\mathrm{PD}}\eta G_{\mathrm{f}}(\theta_{\mathrm{rx},(i,o)})G_{\mathrm{c}}(\theta_{\mathrm{rx},(i,o)})L^{m+1}/2\pi$. To simplify the analysis, the SINR in (3.3) can be rewritten as:

$$\mathsf{SINR} = \frac{\mathsf{S}}{\mathsf{I}_{\mathrm{agg}} + \bar{\sigma}_{\mathrm{n}}^2}, \tag{3.5}$$

where $\mathsf{S} = (x_0^2 + L^2)^{-(m+3)}$ is defined as the (unitless) normalized signal power, $\mathsf{I}_{\mathrm{agg}}$ as the (unitless) normalized aggregate interference and $\bar{\sigma}_{\mathrm{n}}^2 = \sigma_{\mathrm{n}}^2/P_{\mathrm{tx}}\alpha^2$ as the (unitless) normalized noise power. For different receiver types, the normalized aggregate interference can be formulated as:

$$\mathsf{I}_{\mathrm{agg}} = \begin{cases} \displaystyle\sum_{x_i \in \Phi_{\mathrm{a}} \setminus \{x_0\}} \left(x_i^2 + L^2\right)^{-(m+3)}, & \text{nSIC receiver} \\ \eta_{\mathrm{I}} \left(\displaystyle\sum_{x_i \in \Phi_{\mathrm{a}} \cap \mathcal{B}(o, r_{\mathrm{I}}) \setminus \{x_0\}} \left(x_i^2 + L^2\right)^{-(m+3)} \right) & \\ + \displaystyle\sum_{x_j \in \Phi_{\mathrm{a}} \setminus \mathcal{B}(o, r_{\mathrm{I}}) \setminus \{x_0\}} \left(x_j^2 + L^2\right)^{-(m+3)}, & \text{SIC receiver} \end{cases}. \tag{3.6}$$

3.3.2 nSIC Receiver

This subsection focuses on the analysis of the nSIC receiver. It can be seen from (3.5) that it is generally difficult to compute the statistics of SINR directly from its definition because it requires an infinite number of nested integrals due to the interdependency among variables x_i ($i \in \mathbb{N}$). In the following, an MGF-based approach to calculate the exact statistics of the SINR is proposed. The MGF of a random variable X is defined as $\mathcal{M}_X(t) = \mathbb{E}[\exp(tX)]$, $t \in \mathbb{R}$, provided that the expectation of variable $\exp(tX)$ exists in the interval of t of interest. To calculate $\mathcal{M}_X(t)$, the interdependency between S and I_{agg} is decoupled by first conditioning on x_0 and then using the conditional PDF of I_{agg} to derive the SINR. Before investigating the SINR statistics in detail, it is essential to obtain some knowledge of the conditional distribution of the aggregate interference.

The MGF of the conditional aggregate interference can be calculated with the probability generating functional (PGFL) of the PPP:

$$\begin{aligned}
\mathcal{M}_{\mathsf{I}_{\text{agg}}|x_0}(t) =& \mathbb{E}\left[\exp\left(t\mathsf{I}_{\text{agg}}\right)|x_0\right] \\
=& \mathbb{E}\left[\prod_{x_i\in\Phi_{\text{a}}\setminus\{x_0\}} \exp\left(t\left(x_i^2+L^2\right)^{-(m+3)}\right)\middle| x_0\right] \\
=& \exp\left(-2\pi\lambda_{\text{a}}\int_{x_0}^{\infty} x\left(1-\exp\left(t\left(x^2+L^2\right)^{-(m+3)}\right)\right)\mathrm{d}x\right) \\
=& \exp\left(-\pi\lambda_{\text{a}}\int_{x_0^2+L^2}^{\infty}\left(1-\exp\left(tu^{-(m+3)}\right)\right)\mathrm{d}u\right),
\end{aligned} \tag{3.7}$$

where the last step follows from a change of variable $u = x^2 + L^2$. Using the integral result of [110, (2.33.10)], the integration inside (3.7) can be calculated as:

$$\begin{aligned}
&\int_{x_0^2+L^2}^{\infty}\left(1-\exp\left(tu^{-(m+3)}\right)\right)\mathrm{d}u \\
=&\left(u-\frac{1}{m+3}(-t)^{\frac{1}{m+3}}\Gamma\left(-\frac{1}{m+3},-tu^{-(m+3)}\right)\right)\Bigg|_{x_0^2+L^2}^{\infty} \\
=&\left(u-u\exp\left(tu^{-(m+3)}\right)+(-t)^{\frac{1}{m+3}}\Gamma\left(\frac{m+2}{m+3},-tu^{-(m+3)}\right)\right)\Bigg|_{x_0^2+L^2}^{\infty},
\end{aligned} \tag{3.8}$$

where $\Gamma(\cdot,\cdot)$ represents the incomplete gamma function. Note that the function inside (3.8)

converges when u approaches infinity:

$$\lim_{u\to\infty}\left(u-u\exp\left(tu^{-(m+3)}\right)+(-t)^{\frac{1}{m+3}}\Gamma\left(\frac{m+2}{m+3},-tu^{-(m+3)}\right)\right)=(-t)^{\frac{1}{m+3}}\Gamma\left(\frac{m+2}{m+3}\right), \tag{3.9}$$

where $\Gamma(\cdot)$ is the standard gamma function. Combining (3.7) – (3.9) yields a closed-form expression for the MGF of the conditional aggregate interference:

$$\begin{aligned}\mathcal{M}_{\mathsf{I}_{\mathrm{agg}}|x_0}(t)=\exp\Bigg\{-\pi\lambda_{\mathrm{a}}\Bigg\{&\left(x_0^2+L^2\right)\left(-1+\exp\left(t\left(x_0^2+L^2\right)^{-(m+3)}\right)\right)\\&+(-t)^{\frac{1}{m+3}}\left(\Gamma\left(\frac{m+2}{m+3}\right)-\Gamma\left(\frac{m+2}{m+3},-t\left(x_0^2+L^2\right)^{-(m+3)}\right)\right)\Bigg\}\Bigg\}.\end{aligned} \tag{3.10}$$

From the series expansion of the MGF

$$\mathcal{M}_{\mathsf{I}_{\mathrm{agg}}|x_0}(t)=\sum_{n=0}^{\infty}\frac{t^n}{n!}\mathbb{E}\left[\mathsf{I}_{\mathrm{agg}}^n|x_0\right], \tag{3.11}$$

the n-th (positive) moment of $\mathsf{I}_{\mathrm{agg}}$, conditioned on distance x_0, can be obtained by differentiating its MGF:

$$\mathbb{E}\left[\mathsf{I}_{\mathrm{agg}}^n|x_0\right]=\left.\frac{\partial^n}{\partial t^n}\mathcal{M}_{\mathsf{I}_{\mathrm{agg}}|x_0}(t)\right|_{t=0}. \tag{3.12}$$

With the MGF given in (3.10), the PDF and cumulative distribution function (CDF) of $\mathsf{I}_{\mathrm{agg}}$ conditioned on x_0 can be computed efficiently using numerical methods, for example, through the Gil-Pelaez inversion formulae [111]:

$$f_{\mathsf{I}_{\mathrm{agg}}|x_0}(I)=\frac{1}{\pi}\int_0^{\infty}\Re\left\{\exp\left(-\jmath zI\right)\mathcal{M}_{\mathsf{I}_{\mathrm{agg}}|x_0}(\jmath z)\right\}\mathrm{d}z, \tag{3.13}$$

$$F_{\mathsf{I}_{\mathrm{agg}}|x_0}(I)=\frac{1}{2}-\frac{1}{\pi}\int_0^{\infty}\Im\left\{\frac{\exp\left(-\jmath zI\right)\mathcal{M}_{\mathsf{I}_{\mathrm{agg}}|x_0}(\jmath z)}{z}\right\}\mathrm{d}z, \tag{3.14}$$

where $\Re\{\cdot\}$ and $\Im\{\cdot\}$ denote the real and imaginary parts of a complex number, respectively. As an example, the empirical PDF and the analytical PDF of $\mathsf{I}_{\mathrm{agg}}|x_0$ is compared in Figure 3.3. It can be seen that the analytical results closely match the simulation data for different values of x_0.

The unconditioned PDF/CDF of the aggregate interference can be obtained by further averaging

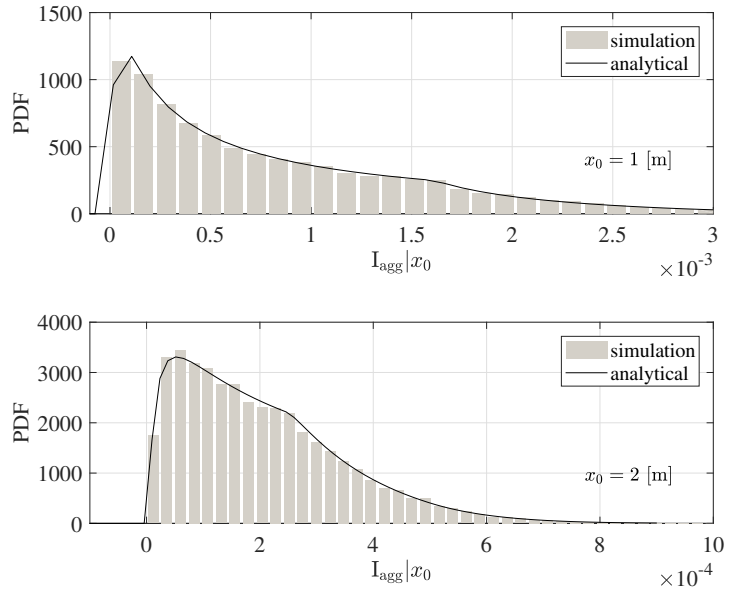

Figure 3.3: *Empirical and analytical PDFs of* $\mathsf{I}_{\mathrm{agg}}$ *conditioned on* x_0 *(without SIC). The network setup is illustrated in Figure 3.2. The following parameters are used:* $\Psi_{1/2} = 60°$, $\lambda_{\mathrm{a}} = 0.1$ *and* $L = 2$ m.

the conditional PDF/CDF with respect to x_0. However, it is the conditional PDF and CDF that are of interest because they enable the calculation of the complementary cumulative distribution function (CCDF) of the SINR, or equivalently the coverage probability. More specifically, the link coverage probability is defined as the probability that SINR exceeds a given threshold T:

$$\begin{aligned}\mathbb{P}\left[\mathsf{SINR} > T\right] =& \mathbb{E}_{x_0}\left[\mathbb{P}\left[\frac{\mathsf{S}}{\mathsf{I}_{\mathrm{agg}} + \bar{\sigma}_{\mathrm{n}}^2} > T \middle| x_0\right]\right] \\ =& \mathbb{E}_{x_0}\left[\mathbb{P}\left[\mathsf{I}_{\mathrm{agg}} < \frac{1}{T}\left(x_0^2 + L^2\right)^{-(m+3)} - \bar{\sigma}_{\mathrm{n}}^2 \middle| x_0\right]\right] \\ =& \int_0^{\infty} 2\pi\lambda_{\mathrm{a}} x_0 \exp\left(-\pi\lambda_{\mathrm{a}} x_0^2\right) F_{\mathsf{I}_{\mathrm{agg}}|x_0}\left(\frac{1}{T}\left(x_0^2 + L^2\right)^{-(m+3)} - \bar{\sigma}_{\mathrm{n}}^2\right) \mathrm{d}x_0,\end{aligned} \tag{3.15}$$

where the nearest distance distribution of the PPP $f_{x_0}(x_0) = 2\pi\lambda_{\mathrm{a}} x_0 \exp\left(-\pi\lambda_{\mathrm{a}} x_0^2\right)$ [112] has been applied in the last step.

To simplify the calculation, an analytical upper bound on the coverage probability can be derived. Revisiting the SINR expression in (3.5), the coverage probability can be formulated in a brute-force way:

$$\mathbb{P}\left[\mathsf{SINR} > T\right] = \int \cdots \int \int_{\mathcal{D}(T)} f_{x_0, x_1, \cdots, x_n}(x_0, x_1, \cdots, x_n) \mathrm{d}x_0 \mathrm{d}x_1 \cdots \mathrm{d}x_n, \tag{3.16}$$

where $\mathcal{D}(T)$, as a function of the SINR threshold T, is the domain of integration formed by the $n+1$ variables satisfying inequality $\mathsf{SINR} > T$, and $f_{x_0,x_1,\cdots,x_n}(x_0,x_1,\cdots,x_n)$ is the joint distance distribution of the nearest $n+1$ APs in the PPP [112]. Since the domain of integration is highly coupled by $x_0,x_1,\cdots,x_n$, it is typically hard to compute the coverage probability directly with (3.16). To simplify the problem, only the serving AP (x_0) and the nearest interfering AP to the typical user (x_1) are considered. The obtained result thus serves as an upper bound on the coverage probability because it ignores the effect of receiver noise and underestimates the interference level. Because $\mathsf{SINR} \leq (x_0^2+L^2)^{-(m+3)}/(x_1^2+L^2)^{-(m+3)}$, it immediately follows that $\mathbb{P}[\mathsf{SINR} > T] \leq \mathbb{P}\left[(x_0^2+L^2)^{-(m+3)}/(x_1^2+L^2)^{-(m+3)} > T\right] = \mathbb{P}\left[x_1 > \sqrt{T^{\frac{1}{m+3}}(x_0^2+L^2)-L^2}\right]$. Given that the joint PDF of x_0 and x_1 is $f_{x_0,x_1}(x_0,x_1) = \exp(-\pi\lambda_{\mathrm{a}}x_1^2)(2\pi\lambda_{\mathrm{a}})^2x_0x_1$ [112], the upper bound on the coverage probability can be calculated as:

$$\begin{aligned}\mathbb{P}\left[\mathsf{SINR} > T\right] \leq & \mathbb{P}\left[x_1 > \sqrt{T^{\frac{1}{m+3}}(x_0^2+L^2)-L^2}\right] \\ = & \int_0^\infty \int_{\sqrt{T^{\frac{1}{m+3}}(x_0^2+L^2)-L^2}}^\infty f_{x_0,x_1}(x_0,x_1)\mathrm{d}x_1\mathrm{d}x_0 \\ = & T^{-\frac{1}{m+3}} \exp\left(-\pi\lambda_{\mathrm{a}}L^2\left(T^{\frac{1}{m+3}}-1\right)\right). \end{aligned} \tag{3.17}$$

The exact coverage probability and its analytical upper bound are compared in Figure 3.4 as a function of parameter L. In general, the coverage probability at a typical user decreases as L increases. The decay of the coverage probability is observed to be steady at small values of L and rapid for large values of L. The derived analytical expression closely matches the simulation results while the upper bound exhibits a positive gap from the exact one. For larger values of T, the gap between the upper bound and the exact result becomes smaller.

With the CCDF expression given in (3.15), the expectation of the n-th moment of the SINR can be expressed as:

$$\mathbb{E}\left[\mathsf{SINR}^n\right] = n\int_0^\infty T^{n-1}\mathbb{P}\left[\mathsf{SINR} > T\right]\mathrm{d}T, \tag{3.18}$$

whose calculation requires three numerical integrations. Based on the derivation in (3.15), it is interesting to note that when conditioned on distance x_0, the normalized signal power S and the sum of the normalized aggregate interference plus the normalized noise power $\mathsf{I}_{\mathrm{agg}} + \bar{\sigma}_{\mathrm{n}}^2$ are decoupled in the SINR expression. Therefore, results derived for the negative integer moments

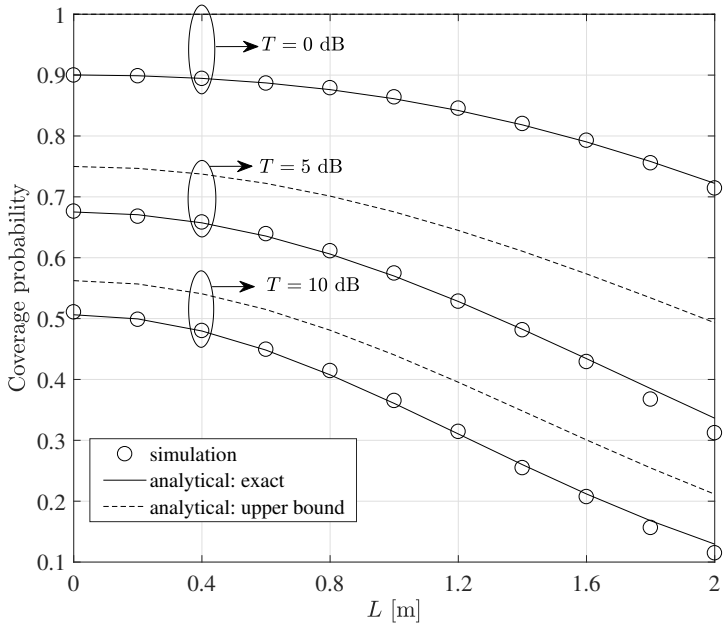

Figure 3.4: *Coverage probability and its upper bound. The network setup is illustrated in Figure 3.2 with* $\lambda_{\mathrm{a}} = 0.1$.

of positive random variables can be applied [113]. This leads to a simplified expression for the n-th moment of the SINR, whose calculation is reduced to only one double integral. More specifically, given x_0, the n-th moment of the SINR can be calculated as:

$$\mathbb{E}\left[\mathsf{SINR}^n\right] = \mathbb{E}_{x_0}\left[\left(x_0^2 + L^2\right)^{-(m+3)n} \mathbb{E}\left[\left(\mathsf{I}_{\mathrm{agg}} + \bar{\sigma}_{\mathrm{n}}^2\right)^{-n} \middle| x_0\right]\right], \tag{3.19}$$

where the inner expectation, being a negative integer moment of a positive random variable, can be written as a function of the MGF [113]:

$$\mathbb{E}\left[\left(\mathsf{I}_{\mathrm{agg}} + \bar{\sigma}_{\mathrm{n}}^2\right)^{-n} \middle| x_0\right] = \Gamma^{-1}(n) \int_0^{\infty} t^{n-1} \mathcal{M}_{\mathsf{I}_{\mathrm{agg}}+\bar{\sigma}_{\mathrm{n}}^2|x_0}(-t)\mathrm{d}t. \tag{3.20}$$

Based on the definition of MGF, it is straightforward to show that

$$\mathcal{M}_{\mathsf{I}_{\mathrm{agg}}+\bar{\sigma}_{\mathrm{n}}^2|x_0}(-t) = \mathbb{E}\left[\exp\left(-t(\mathsf{I}_{\mathrm{agg}} + \bar{\sigma}_{\mathrm{n}}^2)\right)|x_0\right] = \mathcal{M}_{\mathsf{I}_{\mathrm{agg}}|x_0}(-t)\exp\left(-t\bar{\sigma}_{\mathrm{n}}^2\right). \tag{3.21}$$

Combining (3.19) – (3.20), the following result is obtained:

$$\begin{aligned}\mathbb{E}\left[\mathsf{SINR}^n\right] =& \Gamma^{-1}(n) \int_0^{\infty} 2\pi\lambda_{\mathrm{a}} x_0 \exp\left(-\pi\lambda_{\mathrm{a}} x_0^2\right)\left(x_0^2 + L^2\right)^{-(m+3)n} \\ &\times \int_0^{\infty} t^{n-1} \mathcal{M}_{\mathsf{I}_{\mathrm{agg}}|x_0}(-t)\exp\left(-t\bar{\sigma}_{\mathrm{n}}^2\right)\mathrm{d}t\mathrm{d}x_0,\end{aligned} \tag{3.22}$$

The statistical moments of the SINR are useful for studying the characteristics of the SINR, such as the mean, variance and skewness, without knowing its exact distribution functions. More importantly, the MGF can also be used to simplify the derivation of some important performance metrics of the network. For example, the information-theoretic capacity of VLC systems has been derived as $C = 1/2 \log_2 (1 + \mathsf{SINR})$ [65]. In the expression, the scaling factor $1/2$ represents the spectrum efficiency loss due to the Hermitian symmetry constraint on real-valued VLC channels. A general method to calculate the ergodic capacity of the typical user involves the integration of the product of the capacity expression and the density function of the SINR:

$$\begin{aligned}\mathbb{E}[C] =& \int_0^\infty \frac{1}{2} \log_2 (1+T) \, \mathrm{d}\mathbb{P}[\mathsf{SINR} < T] \\ =& \frac{1}{2\ln(2)} \int_0^\infty \frac{1}{1+T} \mathbb{P}[\mathsf{SINR} > T] \, \mathrm{d}T. \end{aligned} \tag{3.23}$$

The computation of (3.23) requires three integrations as well as one inversion of the MGF of the aggregate interference conditioned on x_0. In the following, a new method is proposed to calculate the statistical average of the capacity function. The new method is simpler than (3.23) in that it does not require the knowledge of the CCDF of the SINR. Instead, it is based on rewriting the capacity expression with a series representation. From the definition of the SINR, it holds that $\mathsf{SINR} > 0$. As a result, the capacity function can be rewritten as [110, (1.512.3)]:

$$C = \frac{1}{2\ln(2)} \sum_{n=1}^{\infty} \frac{1}{n} \left(\frac{\mathsf{SINR}}{1+\mathsf{SINR}} \right)^n. \tag{3.24}$$

Since the integral representation of the Gamma function satisfies the following equality [110, (8.312.2)]:

$$\left(\frac{\mathsf{SINR}}{1+\mathsf{SINR}} \right)^n = \mathsf{SINR}^n \int_0^\infty \frac{t^{n-1}}{\Gamma(n)} \exp\left(-z(1+\mathsf{SINR})\right) \mathrm{d}z, \tag{3.25}$$

combining (3.24) and (3.25), the capacity function simplifies to:

$$\begin{aligned} C =& \frac{1}{2\ln(2)} \sum_{n=1}^{\infty} \frac{1}{n} \mathsf{SINR}^n \int_0^\infty \frac{z^{n-1}}{\Gamma(n)} \exp\left(-z(1+\mathsf{SINR})\right) \mathrm{d}z \\ =& \frac{1}{2\ln(2)} \int_0^\infty \frac{1-\exp(-z\mathsf{SINR})}{z} \exp(-z) \mathrm{d}z \\ =& \frac{1}{2\ln(2)} \int_0^\infty \left(1-\exp(-t\mathsf{S})\right) \frac{\exp\left(-t\left(\mathsf{I}_{\mathrm{agg}} + \bar{\sigma}_{\mathrm{n}}^2\right)\right)}{t} \mathrm{d}t, \end{aligned} \tag{3.26}$$

where the second step follows from interpreting the Taylor series of the exponential function

$\sum_{n=1}^{\infty}(t\mathsf{SINR})^n/n\Gamma(n) = \exp(t\mathsf{SINR}) - 1$, and the last step follows from a change of variable $t = z\left(\mathsf{I}_{\text{agg}} + \bar{\sigma}_{\text{n}}^2\right)^{-1}$. Note that the new capacity expression shown in (3.26) contains exponential functions of S and $\mathsf{I}_{\text{agg}} + \bar{\sigma}_{\text{n}}^2$. It also involves an integration over non-negative values of t. Therefore, after taking the expectation on both sides of (3.26), the expectation operator can be moved inside the integral. Mathematically, this yields:

$$\mathbb{E}[C] = \frac{1}{2\ln(2)} \int_0^{\infty} \mathbb{E}\left[(1 - \exp(-t\mathsf{S})) \frac{\exp\left(-t\left(\mathsf{I}_{\text{agg}} + \bar{\sigma}_{\text{n}}^2\right)\right)}{t} \right] \mathrm{d}t. \tag{3.27}$$

The calculation of the inner expectation of (3.27) can be simplified by first conditioning on distance x_0 to decouple S and $\mathsf{I}_{\text{agg}} + \bar{\sigma}_{\text{n}}^2$ and then calculating the expectation over x_0:

$$\begin{aligned} &\mathbb{E}\left[(1 - \exp(-t\mathsf{S})) \frac{\exp\left(-t\left(\mathsf{I}_{\text{agg}} + \bar{\sigma}_{\text{n}}^2\right)\right)}{t} \right] \\ =&\mathbb{E}_{x_0}\left[\left(1 - \exp\left(-t\left(x_0^2 + L^2\right)^{-(m+3)}\right)\right) \frac{\mathcal{M}_{\mathsf{I}_{\text{agg}}|x_0}(-t)\exp\left(-t\bar{\sigma}_{\text{n}}^2\right)}{t} \right]. \end{aligned} \tag{3.28}$$

Inserting (3.28) together with the density function $f_{x_0}(x_0)$ into (3.27) yields the following result:

$$\begin{aligned} \mathbb{E}[C] =& \frac{1}{2\ln(2)} \int_0^{\infty} 2\pi\lambda_{\text{a}} x_0 \exp\left(-\pi\lambda_{\text{a}} x_0^2\right) \int_0^{\infty} \mathcal{M}_{\mathsf{I}_{\text{agg}}|x_0}(-t) \\ &\times \left(1 - \exp\left(-t\left(x_0^2 + L^2\right)^{-(m+3)}\right)\right) \frac{\exp\left(-t\bar{\sigma}_{\text{n}}^2\right)}{t} \mathrm{d}t\mathrm{d}x_0. \end{aligned} \tag{3.29}$$

Comparing (3.29) with (3.23), it can be seen that the MGF-based approach is more efficient for the ergodic capacity calculation. In particular, it only requires a double integral of a real-valued function over the first quadrant space.

3.3.3 SIC Receiver

Due to the broadcasting nature of the VLC channel, SIC can enhance the performance of users in the network by decoding useful signals and interference sequentially. With this approach, the interference which has been successfully decoded can be subtracted from the original signal waveform, leading to an increment of the SINR. However, not all the interference can be successfully decoded. As a prerequisite for accurate SIC, interference with the strongest power should be decoded and canceled first because it preserves the highest SINR and therefore can

be more accurately decoded. In attocell networks, the channel gain is a decreasing function of the link distance. SIC receivers should first cancel the interference from the closest AP. Similar to signal detection, the performance of SIC heavily depends on the effective SINR: a higher SINR causes less residual interference. As a result, the exact amount of residual interference is a function of the SINR from each previous interference cancellation process. Unfortunately, it is difficult and mathematically intractable to use this exact model for the performance characterization of SIC in attocell networks. Instead, a closely related mathematical model to capture the idiosyncrasy of the SIC process is used [40], as depicted in Figure 3.2. In the following, the proposed MGF-based approach is reused to derive tractable results for the SIC case. In fact, this subsection can be viewed as a generalization of the analysis presented in the previous subsection.

From (3.6), the (unitless) normalized aggregate interference for the SIC receiver can be written as $\mathsf{I}_{\text{agg}} = \eta_{\text{I}}\mathsf{I}_{\text{n}} + \mathsf{I}_{\text{f}}$, where $\mathsf{I}_{\text{n}} = \sum_{x_i \in \Phi_{\text{a}} \cap \mathcal{B}(o,r_{\text{I}})\setminus\{x_0\}} (x_i^2 + L^2)^{-(m+3)}$ represents the normalized sum power of interference inside the cancellation region $\mathcal{B}(o, r_{\text{I}})$ before SIC, and $\mathsf{I}_{\text{f}} = \sum_{x_j \in \Phi_{\text{a}} \setminus \mathcal{B}(o,r_{\text{I}})\setminus\{x_0\}} (x_j^2 + L^2)^{-(m+3)}$ represents the normalized sum power of interference outside the cancellation region. It is straightforward to show that, when $x_0 > r_{\text{I}}$, the conditional MGF of the aggregate interference with SIC is the same as (3.10). When $x_0 \leq r_{\text{I}}$, the conditional MGF of the aggregate interference with SIC is:

$$\mathcal{M}_{\mathsf{I}_{\text{agg}}|x_0}(t) = \mathcal{M}_{\eta_{\text{I}}\mathsf{I}_{\text{n}}|x_0}(t)\mathcal{M}_{\mathsf{I}_{\text{f}}|x_0}(t), \tag{3.30}$$

where $\mathcal{M}_{\eta_{\text{I}}\mathsf{I}_{\text{n}}|x_0}(t)$ is the MGF of the normalized sum residual interference inside the cancellation region:

$$\begin{aligned}\mathcal{M}_{\eta_{\text{I}}\mathsf{I}_{\text{n}}|x_0}(t) = \exp\Bigg\{ -\pi\lambda_{\text{a}}\Bigg\{ & r_{\text{I}}^2 - x_0^2 + \left(x_0^2 + L^2\right)\exp\left(\eta_{\text{I}} t \left(x_0^2 + L^2\right)^{-(m+3)}\right) \\ & - \left(r_{\text{I}}^2 + L^2\right)\exp\left(\eta_{\text{I}} t \left(r_{\text{I}}^2 + L^2\right)^{-(m+3)}\right) \\ & - (-\eta_{\text{I}} t)^{\frac{1}{m+3}}\,\Gamma\left(\frac{m+2}{m+3}, -\eta_{\text{I}} t \left(x_0^2 + L^2\right)^{-(m+3)}\right) \\ & + (-\eta_{\text{I}} t)^{\frac{1}{m+3}}\,\Gamma\left(\frac{m+2}{m+3}, -\eta_{\text{I}} t \left(r_{\text{I}}^2 + L^2\right)^{-(m+3)}\right)\Bigg\}\Bigg\},\end{aligned} \tag{3.31}$$

and $\mathcal{M}_{\mathsf{I}_{\text{f}}|x_0}(t)$ is the MGF of the normalized sum interference outside the cancellation region,

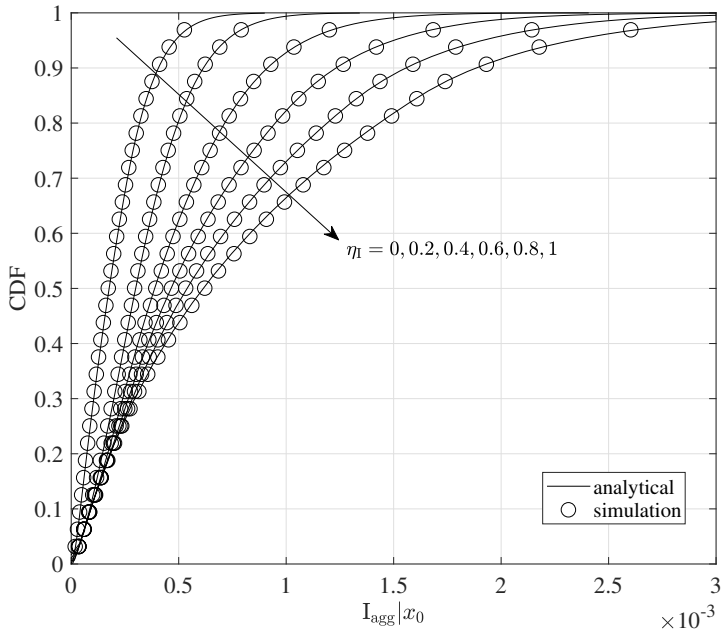

Figure 3.5: *Empirical and analytical CDFs of* $\mathrm{I}_{\mathrm{agg}}$ *conditioned on* x_0 *(with SIC). The network setup is illustrated in Figure 3.2, and the following parameters are used:* $\Psi_{1/2} = 60°$, $\lambda_{\mathrm{a}} = 0.1$, *and* $L = 2$ m.

given by:

$$\mathcal{M}_{\mathrm{I_f}|x_0}(t) = \exp\Bigg\{ -\pi\lambda_{\mathrm{a}}\Bigg\{ \left(r_{\mathrm{I}}^2 + L^2\right)\left(-1 + \exp\left(t\left(r_{\mathrm{I}}^2 + L^2\right)^{-(m+3)}\right)\right) + (-t)^{\frac{1}{m+3}}\left(\Gamma\left(\frac{m+2}{m+3}\right) - \Gamma\left(\frac{m+2}{m+3}, -t\left(r_{\mathrm{I}}^2 + L^2\right)^{-(m+3)}\right)\right)\Bigg\}\Bigg\}. \quad (3.32)$$

Based on the MGFs of the sum interference inside and outside the cancellation region, the PDF and CDF of the aggregate interference conditioned on $x_0 \leq r_{\mathrm{I}}$ can be obtained as

$$f_{\mathrm{I_{agg}}|x_0}(I) = \frac{1}{\pi}\int_0^{\infty} \Re\left\{\exp\left(-\jmath z I\right)\mathcal{M}_{\eta_{\mathrm{I}}\mathrm{I_n}|x_0}(\jmath z)\mathcal{M}_{\mathrm{I_f}|x_0}(\jmath z)\right\}\mathrm{d}z, \quad (3.33)$$

$$F_{\mathrm{I_{agg}}|x_0}(I) = \frac{1}{2} - \frac{1}{\pi}\int_0^{\infty} \Im\left\{\frac{\exp\left(-\jmath z I\right)\mathcal{M}_{\eta_{\mathrm{I}}\mathrm{I_n}|x_0}(\jmath z)\mathcal{M}_{\mathrm{I_f}|x_0}(\jmath z)}{z}\right\}\mathrm{d}z. \quad (3.34)$$

When $x_0 > r_{\mathrm{I}}$, $f_{\mathrm{I_{agg}}|x_0}(I)$ and $F_{\mathrm{I_{agg}}|x_0}(I)$ become the same as those derived for the nSIC case. To illustrate the accuracy of the derived MGFs, the empirical and analytical CDFs of the aggregate interference conditioned on x_0 are shown in Figure 3.5. It can be seen that the derived analytical results are quite accurate for various values of η_{I}, with $\eta_{\mathrm{I}} = 0$ representing the scenario of perfect SIC.

Following similar steps, the expectation of SINR^n can be calculated. To find the conditional MGF of the normalized aggregate interference plus noise, it requires knowledge of the relationship between distances x_0 and r_I. Specifically, given the radius of the interference cancellation region r_I, which is specified by the interference cancellation capability of the SIC receiver, the distance x_0 can either be larger or smaller than r_I. From the void probability of the PPP [112], it is known that $\mathbb{P}[x_0 \leq r_\mathrm{I}] = 1 - \exp(-\pi\lambda_\mathrm{a} r_\mathrm{I}^2)$ and $\mathbb{P}[x_0 > r_\mathrm{I}] = \exp(-\pi\lambda_\mathrm{a} r_\mathrm{I}^2)$. On the one hand, when $x_0 \leq r_\mathrm{I}$, the aggregate interference consists both of residual interference inside the cancellation region and the interference outside the cancellation region, *i.e.,* $\mathsf{I}_\mathrm{agg} = \eta_\mathrm{I}\mathsf{I}_\mathrm{n} + \mathsf{I}_\mathrm{f}$. In this scenario, the conditional MGF of the aggregate interference is $\mathcal{M}_{\mathsf{I}_\mathrm{agg}|x_0}(t) = \mathcal{M}_{\eta_\mathrm{I}\mathsf{I}_\mathrm{n}|x_0}(t)\mathcal{M}_{\mathsf{I}_\mathrm{f}|x_0}(t)$, and the integration region for x_0 is $[0, r_\mathrm{I}]$. On the other hand, when $x_0 > r_\mathrm{I}$, no interference can be canceled. Therefore, the aggregate interference and its MGF is the same as the one for the nSIC case. The integration region for x_0 in this scenario is $[r_\mathrm{I}, \infty]$. Combining the described integrations over two regions, the expectation of the n-th moment of the SINR of the typical SIC receiver can be obtained as:

$$\begin{aligned}\mathbb{E}\left[\mathsf{SINR}^n\right] =& \Gamma^{-1}(n) \int_0^{r_\mathrm{I}} 2\pi\lambda_\mathrm{a} x_0 \exp\left(-\pi\lambda_\mathrm{a} x_0^2\right) \left(x_0^2 + L^2\right)^{-(m+3)n} \\ &\times \int_0^\infty t^{n-1} \mathcal{M}_{\eta_\mathrm{I}\mathsf{I}_\mathrm{n}|x_0}(-t)\mathcal{M}_{\mathsf{I}_\mathrm{f}|x_0}(-t) \exp\left(-t\bar{\sigma}_\mathrm{n}^2\right) \mathrm{d}t\mathrm{d}x_0 \\ &+ \Gamma^{-1}(n) \int_{r_\mathrm{I}}^\infty 2\pi\lambda_\mathrm{a} x_0 \exp\left(-\pi\lambda_\mathrm{a} x_0^2\right) \left(x_0^2 + L^2\right)^{-(m+3)n} \\ &\times \int_0^\infty t^{n-1} \mathcal{M}_{\mathsf{I}_\mathrm{f}|x_0}(-t) \exp\left(-t\bar{\sigma}_\mathrm{n}^2\right) \mathrm{d}t\mathrm{d}x_0. \end{aligned} \tag{3.35}$$

Observe that (3.35) simplifies to (3.22) when the radius of the interference cancellation region becomes zero. Although the derived n-th moment of the SINR is not expressed in a closed form, it only involves a double integral of a closed-form function. Therefore, it can be computed efficiently with standard numerical methods. With the MGF of the aggregate interference, the ergodic capacity of the typical SIC receiver can be calculated as:

$$\begin{aligned}\mathbb{E}[C] =& \frac{1}{2\ln(2)} \int_0^{r_\mathrm{I}} 2\pi\lambda_\mathrm{a} x_0 \exp\left(-\pi\lambda_\mathrm{a} x_0^2\right) \int_0^\infty \mathcal{M}_{\eta_\mathrm{I}\mathsf{I}_\mathrm{n}|x_0}(-t)\mathcal{M}_{\mathsf{I}_\mathrm{f}|x_0}(-t) \\ &\times \left(1 - \exp\left(-t\left(x_0^2 + L^2\right)^{-(m+3)}\right)\right) \frac{\exp\left(-t\bar{\sigma}_\mathrm{n}^2\right)}{t} \mathrm{d}t\mathrm{d}x_0 \\ &+ \frac{1}{2\ln(2)} \int_{r_\mathrm{I}}^\infty 2\pi\lambda_\mathrm{a} x_0 \exp\left(-\pi\lambda_\mathrm{a} x_0^2\right) \int_0^\infty \mathcal{M}_{\mathsf{I}_\mathrm{f}|x_0}(-t) \\ &\times \left(1 - \exp\left(-t\left(x_0^2 + L^2\right)^{-(m+3)}\right)\right) \frac{\exp\left(-t\bar{\sigma}_\mathrm{n}^2\right)}{t} \mathrm{d}t\mathrm{d}x_0. \end{aligned} \tag{3.36}$$

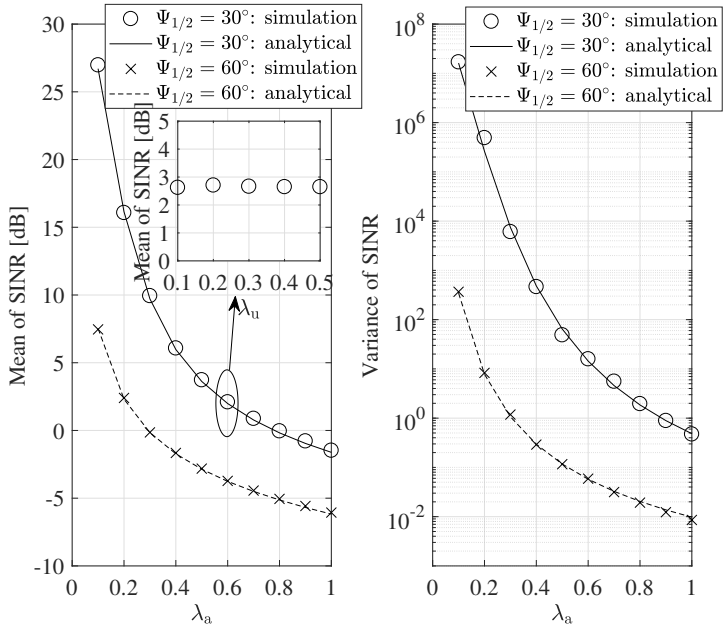

Figure 3.6: *Mean and variance of the SINR of a random user (nSIC receiver).*

3.4 Simulation Results

In this section, Monte Carlo simulations are carried out to substantiate the derived analytical results. The simulation setup is an indoor office of size $18 \times 14 \times 3.5$ m^3, as depicted in Figure 3.2. Unless otherwise specified, the following parameters are used for the simulation. The VLC APs are Lambertian light sources with a semiangle of $60°$, and they all transmit signals at a 1 W power level. Each user is equipped with a PD for VLC signal reception, which has a FOV of $90°$, an effective area of 1 cm^2 and a responsivity of 0.4 $\mathrm{A/W}$. The modulation bandwidth and the noise power spectral density (PSD) are set to 20 MHz and 10^{-22} A^2/Hz, respectively [4, 105]. The optical concentrator used at the receiver front-end has a reflective index of 1.5 and the optical filter has a unity gain.

Figure 3.6 shows the mean value and variance of the SINR for the nSIC receiver. The inner plot confirms Slivnyak's theorem in that the SINR statistics is independent of the user density. Therefore, results obtained for the typical user can reflect the spatially averaged results for all users in the network. It can be seen that the MGF-based analytical results closely match with the Monte Carlo simulations. The mean value of the SINR is simply the first moment of the SINR, *i.e.,* $\mathbb{E}[\mathsf{SINR}]$, while the variance of the SINR is computed from the second moment of the SINR minus its squared mean, *i.e.,* $\mathbb{E}\left[\mathsf{SINR}^2\right] - (\mathbb{E}[\mathsf{SINR}])^2$. Figure 3.6 also illustrates that both mean and variance of the SINR are decreasing functions of the AP density. Also, APs

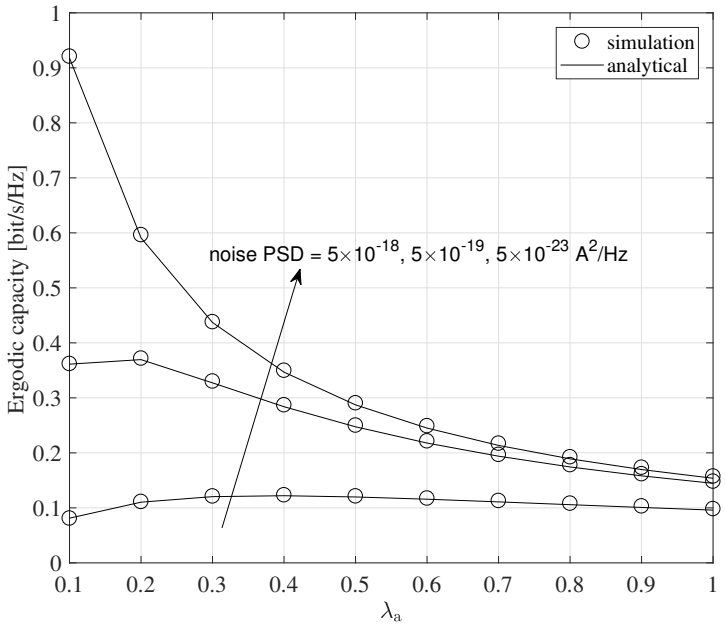

Figure 3.7: *Ergodic capacity of a random user (nSIC receiver) with different AP densities.*

with a narrower semiangle are shown to give a higher SINR.

Figure 3.7 illustrates the ergodic capacity function versus λ_{a} under different noise powers. It can be seen that the derived analytical results are quite accurate in all settings. In the interference-limited case, *i.e.,* when noise PSD is 5×10^{-23} A^2/Hz, the ergodic capacity is a monotonically decreasing function of the AP density. This is because, when the impact of the noise process can be ignored, a denser distribution of APs in the network results in a higher level of interference and hence a lower capacity. On the other hand, when the noise power is comparable to or stronger than the interference, the ergodic capacity function is no longer monotonic. In particular, the ergodic capacity becomes a concave function of the AP density. Taking noise PSD of 5×10^{-19} A^2/Hz as an example, it can be seen from Figure 3.7 that the ergodic capacity reaches the maximum at $\lambda_{\mathrm{a}} = 0.2$. This can be explained as follows. When $\lambda_{\mathrm{a}} < 0.2$, the ergodic capacity at the typical user is primarily limited by the noise process. As a result, enlarging the AP density increases the probability that the typical user can connect to a closer AP to improve the ergodic capacity. When λ_{a} exceeds threshold 0.2, the achievable capacity is mainly limited by the interference, rather than the noise process. Despite the fact the ergodic capacity function has different shapes under different noise powers, a lower noise variance always yields a higher capacity.

To further investigate the impact of noise on the network performance, Figure 3.8 shows the

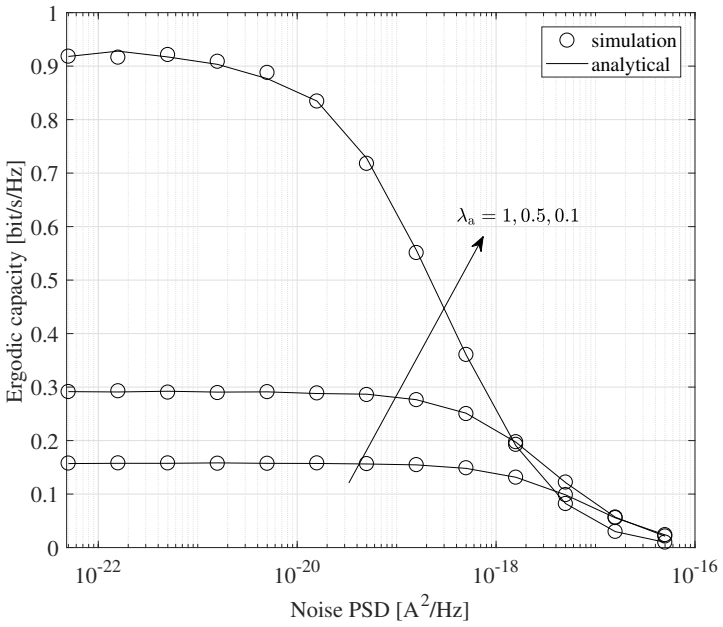

Figure 3.8: *Ergodic capacity of a random user (nSIC receiver) subject to different noise levels.*

ergodic capacity as a function of noise PSDs. It can be seen that the ergodic capacity function monotonically decreases as the noise power increases. However, the intersecting points indicate that there is no general conclusion on the impact of the AP density. Specifically, in a network with a denser distribution of APs, the ergodic capacity at the typical user is more immune to the impact of receiver noise. In contrast, in a sparse network, the change of noise power can have a strong influence on the link capacity.

Considering a typical user with interference cancellation capability, the mean value of the SINR is plotted against the AP density in Figure 3.9. It can be observed that imperfect interference cancellation greatly limits the achievable SINR. Specifically, given the radius of the interference cancellation region $r_{\mathrm{I}} = 4$ m and the AP density $\lambda_{\mathrm{a}} = 0.5$, perfect interference cancellation yields an average SINR of 16 dB. For an imperfect SIC receiver that is capable of canceling 80% of the interference power, the achieved average SINR is reduced by 12 dB. Therefore, it can be concluded that accurate interference cancellation plays an important role in improving the SINR performance, especially in a dense network with a large number of APs.

Figure 3.10 plots the ergodic capacity achieved at the typical user with SIC. Similar to the SINR results shown in Figure 3.9, Figure 3.10 shows that to achieve a high capacity gain, users are required to have a stronger interference cancellation capability. For example, given $\lambda_{\mathrm{a}} = 0.5$ and $r_{\mathrm{I}} = 4$ m, an ergodic capacity of 2.6 bit/s/Hz can be achieved with perfect

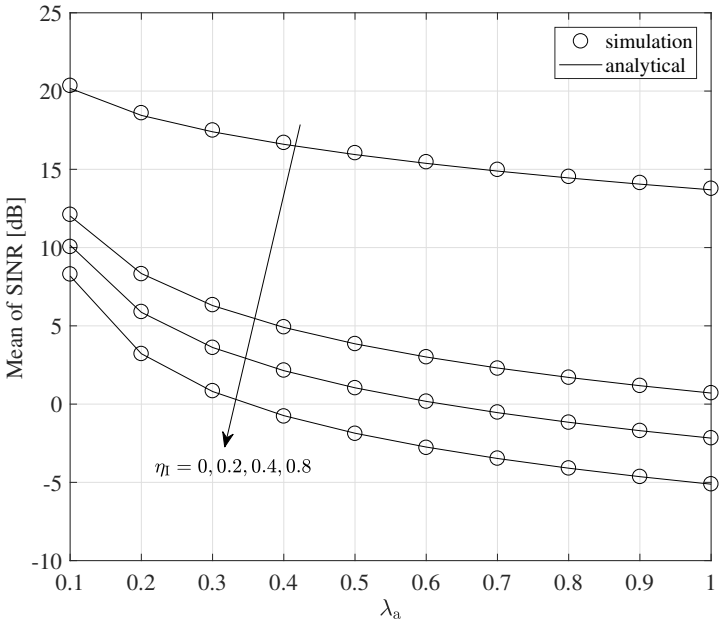

Figure 3.9: *Mean value of the SINR of a random user (SIC receiver).* $r_{\mathrm{I}} = 4$ m.

interference cancellation. For an imperfect SIC receiver that is capable of removing 80% of the interference, the achievable ergodic capacity is reduced to 0.8 bit/s/Hz. It is also interesting to note that, for perfect SIC, the ergodic function becomes concave. In this case, there exists an optimal λ_{a} yielding the highest ergodic capacity. This can be explained as follows. Suppose the density of APs is extremely low. Slightly increasing λ_{a} enhances the possibility of a random user connecting to a stronger AP. Although this also leads to a higher interference level, the dominant part of interference I_{n} is still cancellable. Further increasing λ_{a} beyond the optimal point primarily brings increment to interference I_{f}, which is not cancellable due to the limited SIC capability of mobile users.

Last but not least, Figure 3.11 shows the ergodic capacity function versus the SIC capability. Since η_{I} denotes the portion of the residual interference power, a smaller value of η_{I} corresponds to a receiver with a stronger interference cancellation capability. This explains why the ergodic capacity is a monotonically decreasing function of η_{I}. Note that $r_{\mathrm{I}} = 0$ corresponds to the nSIC case, which can be viewed as the benchmark for the SIC receiver. It can be seen from Figure 3.11 that, given noise PSD of 5×10^{-23} A^2/Hz and $\lambda_{\mathrm{a}} = 0.1$, the nSIC receiver achieves an ergodic capacity of 0.93 bit/s/Hz. For the SIC receiver with 4 meters interference cancellation radius and $\eta_{\mathrm{I}} = 0.1$, the ergodic capacity is doubled to around 1.9 bit/s/Hz. As η_{I} increases, less interference can be canceled and the ergodic capacity decreases.

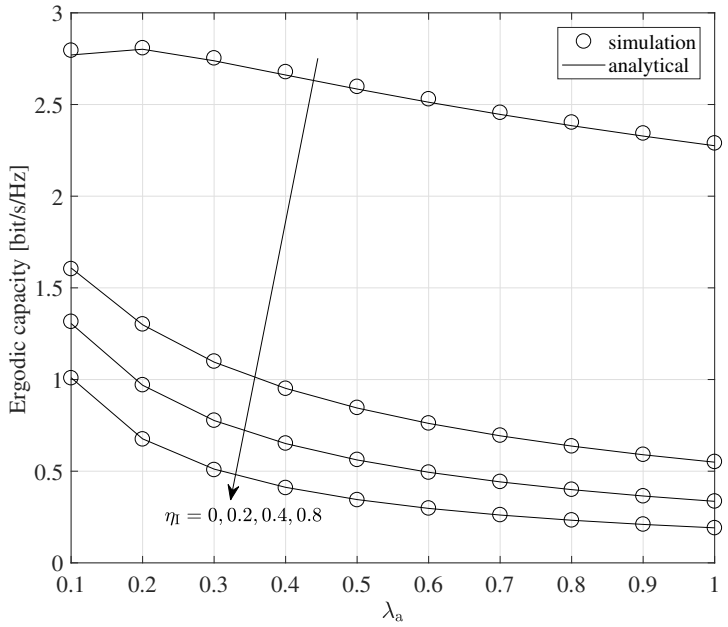

Figure 3.10: *Ergodic capacity of a random user (SIC receiver) with different AP densities.* $r_{\mathrm{I}} = 4$ m.

Note that the above presented results are derived from LOS channels. With multipath reflections and shadowing, the results would become more complicated. To elaborate more, multipath reflections enhance both the signal power and interference, given that there is no intersymbol interference (ISI) or ISI has already been mitigated through the use of cyclic prefix (CP) and equalization. Therefore, the actual SINR would fluctuate. Similarly, shadowing could block the LOS transmission of useful signals or reduce the amount of interference. A through investigation of these aspects deserve a dedicated study.

3.5 Summary

In this chapter, the signal, interference and SINR statistics in indoor attocell networks have been studied with the consideration of AP idleness. An AP is assumed to be idle if it is not associated with any users and hence does not generate interference to users inside the network. Motivated by this, a Bernoulli thinning process is applied to the original hexagonal model. This chapter begins by comparing the Bernoulli-thinned hexagonal model and the stochastic PPP model in terms of their rationale, modeling techniques and preliminary performance results. Monte Carlo simulations illustrate that the PPP model can yield similar results as generated by the Bernoulli-thinned hexagonal model. Moreover, the PPP model is more analytically tractable, allowing the

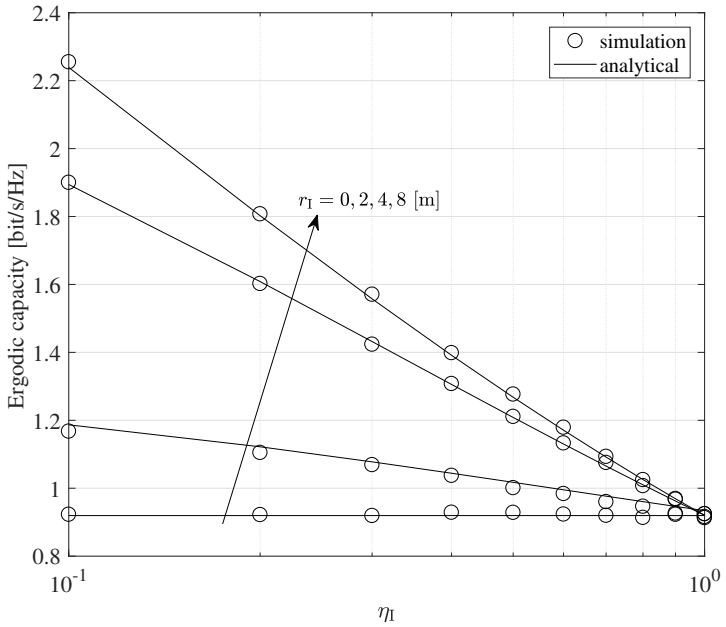

Figure 3.11: *Ergodic capacity of a random user (SIC receiver) with different SIC capabilities.* $\lambda_{\mathrm{a}} = 0.1$.

system performance to be characterized more efficiently. Moving on, the second part of this chapter presents an analytical framework for tractable computation of SINR statistics in attocell networks. The analytical framework is built upon the MGF approach and it is also applicable to networks with SIC. Based on the derived results, a number of network metrics have been evaluated. Among them, the coverage probability has been studied in detail against various network parameters. A simple analytical upper bound on the coverage probability has also been derived and given in a closed form. Finally, the accuracy of the proposed analytical framework is validated with extensive numerical results. The performance improvement brought by the SIC demonstrates that efficient interference mitigation/cancellation techniques are promising for future indoor attocell networks.

Chapter 4
Coordinated Multipoint Joint Transmission

4.1 Introduction

Following the trend of network densification [16, 17], visible light communication (VLC)-enabled networks are expected to achieve significant capacity gains and indoor data coverage from small-sized optical attocells [12]. The dense deployment of optical attocells unavoidably gives rise to inter-cell interference (ICI) when the available frequency spectrum is shared among multiple cells. Different from traditional orthogonal multiplexing techniques, this spectrum-sharing based approach aims to transmit and receive signals in the presence of interference in order to achieve higher network throughputs. Therefore, advanced interference mitigation techniques are key to unlocking the capacity of attocell networks by making full use of the available spectrum and improving its spectral efficiency. Towards this direction, emerging technologies such as fractional frequency reuse (FFR) [41, 114, 115], self-organizing interference coordination [116], successive interference cancellation (SIC) [37–41] and coordinated multipoint (CoMP) [17, 106, 117–120] have been proposed.

FFR was first proposed as an interference cancellation technique for orthogonal frequency division multiple access (OFDMA) networks [41]. Its principle is to partition the overall available spectrum into a number of narrow bands and allocate them in an intelligent way so that cell-edge users do not interfere with each other while cell-center users only receive a limited amount of interference from adjacent cells [41, 114, 115]. Although the total spectrum is limited, FFR is designed to improve the overall spectral efficiency of the network by maximizing the spatial reuse factor of each frequency band. In the implementation of FFR, there is an inherent trade-off between improving the rate and coverage performance of cell-edge users and maximizing the sum throughput of the network.

The self-organizing interference coordination uses a busy burst (BB) signaling approach for dynamic resource allocation [116]. In this approach, resources are partitioned into multiple

time frames. Users who intend to continue receiving data using the same resource in the next time frame are requested to broadcast a BB signal. From the received BB signals, access points (APs) in neighboring cells estimate the level of ICI that they could potentially cause to the user, provided that channel reciprocity holds. Based on this information, APs are able to decide whether or not to transmit in the next time frame without any central supervision.

SIC, first proposed in [37], is a multiuser detection technique that exploits the structure of ICI for interference mitigation [38–41]. The principle of SIC is to decode and cancel out interference signals in a sequential manner so as to enhance the effective signal-to-interference-plus-noise ratio (SINR). For example, the decoded interference can be re-encoded and accurately subtracted from the received signal using the channel state information (CSI). Such processes can be repeated for an arbitrary number of interfering nodes. Apart from its simplicity and amenability to implementation, SIC has been shown to generate near-capacity results with the availability of accurate CSI [38, 39].

CoMP is another emerging technology that is capable of mitigating ICI via AP cooperations [17, 106, 117–120]. The coordination and data exchange between APs are supported by a backbone network, which can be realized using a wired Ethernet or existing power lines, *i.e.,* via power line communication (PLC) [50, 121–123]. By making use of the shared information between cooperative APs, ICI can be effectively mitigated or even converted into useful signals. Since the cooperative APs can also be viewed as a virtual multiple-input multiple-output (MIMO) system, CoMP is also named cooperative MIMO. Based on the detailed coordination scheme, downlink CoMP can be classified into the following three main categories.

- Joint transmission (JT): In CoMP-JT, coordinated APs simultaneously transmit the same data to multiple users in a coherent or noncoherent manner. The transmitted data comprises appropriately weighted information signals that are intended for different users. Since the weighting factors are selected so that interference signals can be converted into useful signals, this scheme outperforms the non-coordinated case. However, successful JT requires the network to have a high backhaul bandwidth to exchange user data and CSI among APs with low latency.

- Dynamic point selection (DPS): Similar to JT, DPS also relies on sharing user data among APs. However, the appropriately weighted information signals are transmitted by a single AP at each time instance, and the serving AP is changed dynamically based on the

resource availability and channel conditions.

- Coordinated scheduling/beamforming (CS/CB): In CS/CB, only CSI is shared among the coordinated APs. As a result, user data is only available at one AP, but the scheduling and beamforming designs are done via the coordination among multiple APs. The beamforming coefficients are selected such that interfering APs are steered towards the null space of the interfered user.

This chapter discusses CoMP-JT as the interference mitigation technique for indoor attocell networks, whose realization can be classified into two categories: noncoherent JT and coherent JT [124–128]. Note that the noncoherent and coherent JT schemes discussed in this work are on the electrical domain, rather than on the optical domain. More specifically, in the optical domain, noncoherent transmission refers to the typical intensity modulation (IM) while coherent transmission refers to the scenario where both amplitude and phase of the signal are modulated. This infers that coherent detection of an optical signal requires a local oscillator so as to extract the phase information of the signal at the receiver, using either homodyne or heterodyne detection techniques [129]. On the other hand, in the electrical domain, noncoherent JT refers to the scenario where APs cooperatively transmit the same data without frame synchronization, thereby yielding an increment in the received signal power. Coherent JT in the electrical domain refers to the case where the transmit signals are synchronized based on the shared CSI to compensate for the time delay of multipath transmissions. In this case, the received electrical signals can be constructively combined in amplitude [124–128].

Successful realization of CoMP-JT demands the backhaul network to fulfill stringent capacity and latency requirements which are imposed by specific cooperation techniques. For example, achieving a higher downlink throughput requires even higher backhaul capacity which is capable of exchanging both data and signals for coordination. Also, the round-trip latency among cooperative APs may be limited to milliseconds so that the quality of service (QoS) is well maintained, especially when users have high mobilities.

The performance of noncoherent JT and coherent JT in radio frequency (RF)-based cellular networks has been analytically studied in [127] and [128], respectively. In both works, base stations (BSs) are assumed to be independently distributed according to a Poisson point process (PPP). Since the vertical distance of the communication link in cellular networks is typically much smaller than the horizontal distance, a planar network model is generally used [127, 128].

However, in attocell networks, the size of optical attocells is in the order of meters. This indicates that a three-dimensional (3D) network model taking into account both horizontal and vertical distances of the communication link is necessary.

In this chapter, the approximate distribution functions of the signal power and interference are studied through second-order moment matching. With this approach, analytical expressions for the coverage probability with noncoherent/coherent JT are derived into tractable forms. In the interference-limited scenario, analytical results for the coverage probability with noncoherent/coherent JT are further simplified into closed forms. It is shown that, for typical receiver noise levels, the SINR can be well approximated by the signal-to-interference ratio (SIR), based on which simpler closed-form results are derived. Also, this chapter investigates the impact of various key parameters on the network performance and studies the achievable performance gain of coherent JT over noncoherent JT. These findings are useful for studying the behaviors and trends of the network and providing guidelines for the design of practical attocell networks.

The remainder of this chapter is organized as follows. Section 4.2 describes the PPP model under investigation and formulates the SINR expression for noncoherent/coherent JT. In Section 4.3, the approximate distribution functions of the signal power and interference are investigated and used for the coverage probability analysis. Simulation results and discussions on the impact of various key parameters on the coverage performance are presented in Section 4.4. Finally, concluding remarks are given in Section 4.5.

4.2 System Model

Consider the downlink transmission of an indoor attocell network with full frequency reuse. As depicted in Figure 4.1, APs are attached to the room ceiling and their horizontal locations are modeled by a two-dimensional (2D) homogeneous PPP $\Phi_{\mathrm{a}} = \{x_i, i \in \mathbb{N}^+\} \subset \mathbb{R}^2$, with node density λ_{a}, where x_i is the horizontal distance between AP i and the origin. Users are assumed to be mobile on a fixed horizontal plane, for example, at desktop level, and their horizontal locations are modeled by another independent 2D homogeneous PPP. The vertical separation between APs and users is denoted by L. Based on the user-centric AP cooperation scheme [130], users are assumed to be served by a cluster of APs within a predefined cooperative region. Since APs that are close to a given user typically result in a high received signal strength (RSS), the cooperation region is defined as a 2D ball centered around the user with

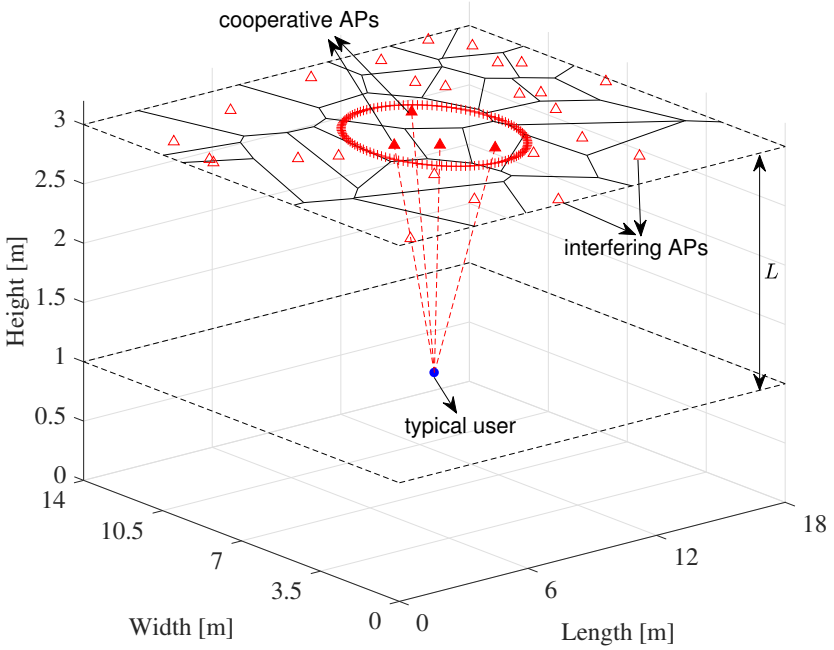

Figure 4.1: *CoMP-JT attocell network with Voronoi cells. APs inside ball $\mathcal{B}(o, r_{\mathrm{c}})$ are coordinated while APs outside ball $\mathcal{B}(o, r_{\mathrm{c}})$ act as the source of interference.*

radius r_{c}. Therefore, for the typical user located at the origin, the cooperation region can be written as $\mathcal{B}(o, r_{\mathrm{c}})$. Similarly, the region outside the cooperation ball is denoted by $\bar{\mathcal{B}}(o, r_{\mathrm{c}})$. The backhaul capacity required by CoMP-JT depends on parameters such as system bandwidth, number of users and size of the cooperative cells. In this work, finite backhaul capacity is modeled by limiting the cooperation cell size via the tunable parameter r_{c} while other models such as simplified scheduling and low-bit feedback are not considered. The analysis is focused on a *typical* user located at the origin because according to Slivnyak's theorem [45], this typical user reflects the spatially averaged performance of users in the network. Due to the homogeneity of Φ_{a}, the number of cooperative APs inside ball $\mathcal{B}(o, r_{\mathrm{c}})$ still follows a Poisson distribution, whose probability mass function (PMF) is:

$$\mathbb{P}\left[\sum_{x_i \in \Phi_{\mathrm{a}}} \mathbf{1}_{\mathcal{B}(o,r_{\mathrm{c}})}(x_i) = n\right] = \frac{\left(\pi\lambda_{\mathrm{a}} r_{\mathrm{c}}^2\right)^n}{n!} \exp\left(-\pi\lambda_{\mathrm{a}} r_{\mathrm{c}}^2\right), \tag{4.1}$$

where $\mathbf{1}_{\mathcal{B}(o,r_{\mathrm{c}})}(x_i)$ is the random counting measure of ball $\mathcal{B}(o, r_{\mathrm{c}})$, defined as:

$$\mathbf{1}_{\mathcal{B}(o,r_{\mathrm{c}})}(x_i) = \begin{cases} 1, & x_i \in \mathcal{B}(o, r_{\mathrm{c}}) \\ 0, & \text{otherwise} \end{cases}. \tag{4.2}$$

The same channel model in (3.4) is used. In the case of noncoherent JT, a user receives multiple copies of the same signal transmitted by a cluster of cooperative APs. In this scheme, accurate synchronizations are not required at the cooperative APs. At the receiver side, the received signals are combined by accumulating their powers [126, 127]. Therefore, noncoherent JT has lower implementation complexity and requires less backhaul capacity when compared to its coherent counterpart. The achieved SINR at the typical user under the noncoherent JT scheme can be formulated as:

$$\mathsf{SINR} = \frac{\sum\limits_{x_i \in \Phi_{\mathrm{a}} \cap \mathcal{B}(o, r_{\mathrm{c}})} \left(x_i^2 + L^2\right)^{-(m+3)}}{\sum\limits_{x_i \in \Phi_{\mathrm{a}} \cap \bar{\mathcal{B}}(o, r_{\mathrm{c}})} \left(x_i^2 + L^2\right)^{-(m+3)} + \bar{\sigma}_{\mathrm{n}}^2}, \tag{4.3}$$

where $\bar{\sigma}_{\mathrm{n}}^2 = \sigma_{\mathrm{n}}^2 / P_{\mathrm{tx}} \alpha^2$ represents the normalized noise power.

In the case of coherent JT, APs cooperate by transmitting the same data to each user in a synchronous manner, resembling a distributed transmitter array. As a result, the received signals are combined in amplitude, rather than in power. The achieved SINR at the typical user under the coherent JT scheme can be formulated as:

$$\mathsf{SINR} = \frac{\left(\sum\limits_{x_i \in \Phi_{\mathrm{a}} \cap \mathcal{B}(o, r_{\mathrm{c}})} \left(x_i^2 + L^2\right)^{-\frac{m+3}{2}} \right)^2}{\sum\limits_{x_i \in \Phi_{\mathrm{a}} \cap \bar{\mathcal{B}}(o, r_{\mathrm{c}})} \left(x_i^2 + L^2\right)^{-(m+3)} + \bar{\sigma}_{\mathrm{n}}^2}. \tag{4.4}$$

Note that the SINR expressions under noncoherent JT and coherent JT schemes are different only in the received signal power. Comparing (4.3) with (4.4), it is evident that coherent JT outperforms noncoherent JT in terms of the SINR because of the following inequality:

$$\left(\sum_{x_i \in \Phi_{\mathrm{a}} \cap \mathcal{B}(o, r_{\mathrm{c}})} \left(x_i^2 + L^2\right)^{-(m+3)/2} \right)^2 > \sum_{x_i \in \Phi_{\mathrm{a}} \cap \mathcal{B}(o, r_{\mathrm{c}})} \left(x_i^2 + L^2\right)^{-(m+3)}. \tag{4.5}$$

4.3 Coverage Probability Analysis

In this section, the analysis is focused on the coverage probability of a typical user in the network. It is defined as the probability that the received SINR exceeds a certain threshold T.

For both noncoherent and coherent JT schemes, the SINR expression can be written as:

$$\mathsf{SINR} = \frac{\mathsf{S}}{\mathsf{I}_{\mathrm{agg}} + \bar{\sigma}_{\mathrm{n}}^2}, \tag{4.6}$$

where S and $\mathsf{I}_{\mathrm{agg}}$ represent the (unitless) normalized received signal power and the normalized interference power at the typical user, respectively. For noncoherent JT, the normalized signal power is $\mathsf{S} = \sum_{x_i \in \Phi_{\mathrm{a}} \cap \mathcal{B}(o,r_{\mathrm{c}})} \left(x_i^2 + L^2\right)^{-(m+3)}$. For coherent JT, the normalized signal power is $\mathsf{S} = \left(\sum_{x_i \in \Phi_{\mathrm{a}} \cap \mathcal{B}(o,r_{\mathrm{c}})} \left(x_i^2 + L^2\right)^{-(m+3)/2}\right)^2$. For both noncoherent and coherent JT schemes, the normalized aggregate interference is $\mathsf{I}_{\mathrm{agg}} = \sum_{x_i \in \Phi_{\mathrm{a}} \cap \bar{\mathcal{B}}(o,r_{\mathrm{c}})} \left(x_i^2 + L^2\right)^{-(m+3)}$. Since S and $\mathsf{I}_{\mathrm{agg}}$ are functions of points located in two disjoint sets of the PPP, they are statistically independent. Therefore, the density function of the SINR can be obtained by studying the distribution functions of S and $\mathsf{I}_{\mathrm{agg}}$ separately.

4.3.1 Characteristic Functions of S and $\mathsf{I}_{\mathrm{agg}}$

For noncoherent JT, the exact probability density functions (PDFs) of S and $\mathsf{I}_{\mathrm{agg}}$ can be obtained from the inversion of their characteristic functions[1] [131]. More specifically, the characteristic function of S can be calculated as:

$$\begin{aligned}
&\mathcal{F}_{\mathsf{S}}(\omega) = \mathbb{E}_{\Phi_{\mathrm{a}}}\left[\exp\left(\jmath\omega\mathsf{S}\right)\right] \\
=&\mathbb{E}_n\left[\mathbb{E}_{\Phi_{\mathrm{a}}}\left[\exp\left(\jmath\omega\mathsf{S}\right)\middle|\, \Phi_{\mathrm{a}}(\mathcal{B}(o,r_{\mathrm{c}})) = n\right]\right] \\
=&\sum_{n=0}^{\infty} \mathbb{P}\left[\sum_{x_i \in \Phi_{\mathrm{a}}} \mathbf{1}_{\mathcal{B}(o,r_{\mathrm{c}})}(x_i) = n\right] \\
&\times \mathbb{E}_{\Phi_{\mathrm{a}}}\left[\prod_{x_i \in \Phi_{\mathrm{a}} \cap \mathcal{B}(o,r_{\mathrm{c}})} \exp\left(\jmath\omega\left(x_i^2 + L^2\right)^{-(m+3)}\right)\middle|\, \Phi_{\mathrm{a}}(\mathcal{B}(o,r_{\mathrm{c}})) = n\right] \\
=&\sum_{n=0}^{\infty} \frac{\left(\pi\lambda_{\mathrm{a}} r_{\mathrm{c}}^2\right)^n}{n!} \exp\left(-\pi\lambda_{\mathrm{a}} r_{\mathrm{c}}^2\right) \left(\int_0^{r_{\mathrm{c}}} f_{x \in \mathcal{B}(o,r_{\mathrm{c}})}(x) \exp\left(\jmath\omega\left(x^2 + L^2\right)^{-(m+3)}\right) \mathrm{d}x\right)^n,
\end{aligned} \tag{4.7}$$

where $\jmath = \sqrt{-1}$ and $f_{x \in \mathcal{B}(o,r_{\mathrm{c}})}(x)$ is the PDF of the distance of a point uniformly distributed inside ball $\mathcal{B}(o, r_{\mathrm{c}})$. Due to the homogeneity of the PPP, it is known that $f_{x \in \mathcal{B}(o,r_{\mathrm{c}})}(x) =$

[1] Note that the characteristic function and moment generating function (MGF) are related concepts. Chapter 3 uses the MGF because of its easiness to calculate the SINR moments. Characteristic functions, on the other hand, are more suitable to calculate the distribution of continuous variables.

$2x/r_{\mathrm{c}}^2$ for $x \leq r_{\mathrm{c}}$, and zero otherwise. By reversely applying the Taylor series expansion, the characteristic function of S can be obtained as:

$$\begin{aligned}\mathcal{F}_{\mathsf{S}}(\omega) =& \exp\left(\pi\lambda_{\mathrm{a}} r_{\mathrm{c}}^2 \left(\int_0^{r_{\mathrm{c}}} \frac{2x}{r_{\mathrm{c}}^2} \exp\left(\jmath\omega\left(x^2+L^2\right)^{-(m+3)}\right) \mathrm{d}x - 1\right)\right) \\ =& \exp\Bigg\{ -\pi\lambda_{\mathrm{a}} r_{\mathrm{c}}^2 + \frac{\pi\lambda_{\mathrm{a}}}{m+3}\Bigg\{ -L^2 E_{\frac{m+4}{m+3}}\left(-\jmath\omega L^{-2(m+3)}\right) \\ &+ \left(r_{\mathrm{c}}^2+L^2\right) E_{\frac{m+4}{m+3}}\left(-\jmath\omega\left(r_{\mathrm{c}}^2+L^2\right)^{-(m+3)}\right)\Bigg\}\Bigg\}, \end{aligned} \tag{4.8}$$

for $\omega \geq 0$, and $\mathcal{F}_{\mathsf{S}}(\omega) = \mathcal{F}_{\mathsf{S}}^*(-\omega)$ for $\omega < 0$. In (4.8), $E_n(z) = \int_1^\infty \exp(-zt)t^{-n}\mathrm{d}t$ is the exponential integral function [110].

On the other hand, the characteristic function of interference $\mathsf{I}_{\mathrm{agg}}$ can be calculated as:

$$\begin{aligned}\mathcal{F}_{\mathsf{I}_{\mathrm{agg}}}(\omega) =& \sum_{n=0}^{\infty} \mathbb{P}\left[\sum_{x_i\in\Phi_{\mathrm{a}}} \mathbf{1}_{\bar{\mathcal{B}}(o,r_{\mathrm{c}})}(x_i) = n\right] \\ &\times \mathbb{E}_{\Phi_{\mathrm{a}}}\left[\prod_{x_i\in\Phi_{\mathrm{a}}\cap\bar{\mathcal{B}}(o,r_{\mathrm{c}})} \exp\left(\jmath\omega\left(x_i^2+L^2\right)^{-(m+3)}\right) \middle| \Phi_{\mathrm{a}}(\bar{\mathcal{B}}(o,r_{\mathrm{c}})) = n\right] \\ =& \sum_{n=0}^{\infty} \frac{\left(\lambda_{\mathrm{a}}\mu(\bar{\mathcal{B}}(o,r_{\mathrm{c}}))\right)^n}{n!} \exp\left(-\lambda_{\mathrm{a}}\mu(\bar{\mathcal{B}}(o,r_{\mathrm{c}}))\right) \\ &\times \left(\int_{r_{\mathrm{c}}}^{\infty} f_{x\in\bar{\mathcal{B}}(o,r_{\mathrm{c}})}(x) \exp\left(\jmath\omega\left(x^2+L^2\right)^{-(m+3)}\right)\mathrm{d}x\right)^n, \end{aligned} \tag{4.9}$$

where $\mu(\bar{\mathcal{B}}(o,r_{\mathrm{c}}))$ is the standard Lebesgue measure of $\bar{\mathcal{B}}(o,r_{\mathrm{c}})$ and $f_{x\in\bar{\mathcal{B}}(o,r_{\mathrm{c}})}(x)$ is the PDF of the distance of a point uniformly distributed in $\bar{\mathcal{B}}(o,r_{\mathrm{c}})$ to the origin. Since $\bar{\mathcal{B}}(o,r_{\mathrm{c}})$ is an unbounded region, $\mathcal{F}_{\mathsf{I}_{\mathrm{agg}}}(\omega)$ can be calculated by first considering $\bar{\mathcal{B}}(o,r_{\mathrm{c}})$ as an annulus with inner radius r_{c} and outer radius $\bar{r}_{\mathrm{c}}$ and then letting $\bar{r}_{\mathrm{c}} \to \infty$:

$$\begin{aligned}\mathcal{F}_{\mathsf{I}_{\mathrm{agg}}}(\omega) =& \lim_{\bar{r}_{\mathrm{c}}\to\infty} \sum_{n=0}^{\infty} \frac{\left(\pi\lambda_{\mathrm{a}}\left(\bar{r}_{\mathrm{c}}^2 - r_{\mathrm{c}}^2\right)\right)^n}{n!} \exp\left(-\pi\lambda_{\mathrm{a}}\left(\bar{r}_{\mathrm{c}}^2 - r_{\mathrm{c}}^2\right)\right) \\ &\times \left(\int_{r_{\mathrm{c}}}^{\bar{r}_{\mathrm{c}}} \frac{2x}{\bar{r}_{\mathrm{c}}^2 - r_{\mathrm{c}}^2} \exp\left(\jmath\omega\left(x^2+L^2\right)^{-(m+3)}\right)\mathrm{d}x\right)^n \\ =& \lim_{\bar{r}_{\mathrm{c}}\to\infty} \exp\left(\pi\lambda_{\mathrm{a}}\left(\bar{r}_{\mathrm{c}}^2 - r_{\mathrm{c}}^2\right)\left(\int_{r_{\mathrm{c}}}^{\bar{r}_{\mathrm{c}}} \frac{2x}{\bar{r}_{\mathrm{c}}^2 - r_{\mathrm{c}}^2} \exp\left(\jmath\omega\left(x^2+L^2\right)^{-(m+3)}\right)\mathrm{d}x - 1\right)\right). \end{aligned} \tag{4.10}$$

Using a change of variable $t = \left(x^2+L^2\right)^{-(m+3)}$ and integration by parts, $\mathcal{F}_{\mathsf{I}_{\mathrm{agg}}}(\omega)$ can be

further simplified to:

$$\mathcal{F}_{\mathsf{I}_{\text{agg}}}(\omega) = \exp\left(\pi\lambda_{\text{a}}\jmath\omega\int_0^{\left(r_{\text{c}}^2+L^2\right)^{-(m+3)}}\left(t^{-\frac{1}{m+3}}-r_{\text{c}}^2-L^2\right)\exp\left(\jmath\omega t\right)\mathrm{d}t\right)$$

$$=\exp\left\{\pi\lambda_{\text{a}}\left(r_{\text{c}}^2+L^2\right)\left(1-\exp\left(\jmath\omega\left(r_{\text{c}}^2+L^2\right)^{-(m+3)}\right)\right)-\pi\lambda_{\text{a}}\left(-\jmath\omega\right)^{\frac{1}{m+3}}\Gamma\left(\frac{m+2}{m+3}\right)\right.$$

$$\left.+\,\pi\lambda_{\text{a}}\left(-\jmath\omega\right)^{\frac{1}{m+3}}\Gamma\left(\frac{m+2}{m+3},-\jmath\omega\left(r_{\text{c}}^2+L^2\right)^{-(m+3)}\right)\right\}, \tag{4.11}$$

for $\omega \geq 0$, and $\mathcal{F}_{\mathsf{I}_{\text{agg}}}(\omega) = \mathcal{F}^*_{\mathsf{I}_{\text{agg}}}(-\omega)$ for $\omega < 0$. In (4.11), $\Gamma(z) = \int_0^\infty \exp(-t)t^{z-1}\mathrm{d}t$ is the standard gamma function and $\Gamma(n,z) = \int_z^\infty \exp(-t)t^{n-1}\mathrm{d}t$ is the upper incomplete gamma function [110]. As can be seen from (4.8) and (4.11), the characteristic functions $\mathcal{F}_{\mathsf{S}}(\omega)$ and $\mathcal{F}_{\mathsf{I}_{\text{agg}}}(\omega)$ are both in complicated forms and no explicit expressions are available for the PDFs of S and I_{agg}. Therefore, numerical methods are required for the calculation of PDFs of S and I_{agg}. This can be achieved by performing the inverse Fourier transform or using the Gram-Charlier series expansion with infinite terms and Laguerre polynomials [132]. However, these two approaches are not pursued due to their high computation complexity and lack of insights into the distribution characteristics of S and I_{agg}.

It is interesting to note that for noncoherent JT, the characteristic function of $\mathsf{S}+\mathsf{I}_{\text{agg}}$, which represents the (unitless) normalized total receivable signal strength from all transmitting APs, can be treated as a special case of $\mathcal{F}_{\mathsf{S}}(\omega)$ when $r_{\text{c}} \to \infty$. This can also be viewed as the best-case scenario where all available APs cooperatively transmit without interference, yielding:

$$\mathcal{F}_{\mathsf{S}+\mathsf{I}_{\text{agg}}}(\omega) = \lim_{r_{\text{c}}\to\infty}\mathcal{F}_{\mathsf{S}}(\omega) = \exp\left(\pi\lambda_{\text{a}}\jmath\omega\int_0^\infty\left(t^{-\frac{1}{m+3}}-L^2\right)\exp\left(\jmath\omega t\right)\mathrm{d}t\right)$$

$$=\exp\left(-\pi\lambda_{\text{a}}\left(\Gamma\left(\frac{m+2}{m+3}\right)\left(-\jmath\omega\right)^{\frac{1}{m+3}}-L^2\right)\right), \tag{4.12}$$

in which the second step follows from a change of variable $t = \left(x^2+L^2\right)^{-(m+3)}$ and integration by parts. The inverse Fourier transform of $\mathcal{F}_{\mathsf{S}+\mathsf{I}_{\text{agg}}}(\omega)$ gives the PDF of $\mathsf{S}+\mathsf{I}_{\text{agg}}$, which can be obtained by following similar procedures as described in [131]:

$$f_{\mathsf{S}+\mathsf{I}_{\text{agg}}}(t) = \frac{\exp\left(\pi\lambda_{\text{a}}L^2\right)}{\pi t}\sum_{n=1}^{\infty}\frac{\Gamma\left(\frac{n}{m+3}+1\right)}{n!}\left(\pi\lambda_{\text{a}}\Gamma\left(\frac{m+2}{m+3}\right)t^{-\frac{1}{m+3}}\right)^n\sin\left(\frac{m+2}{m+3}n\pi\right). \tag{4.13}$$

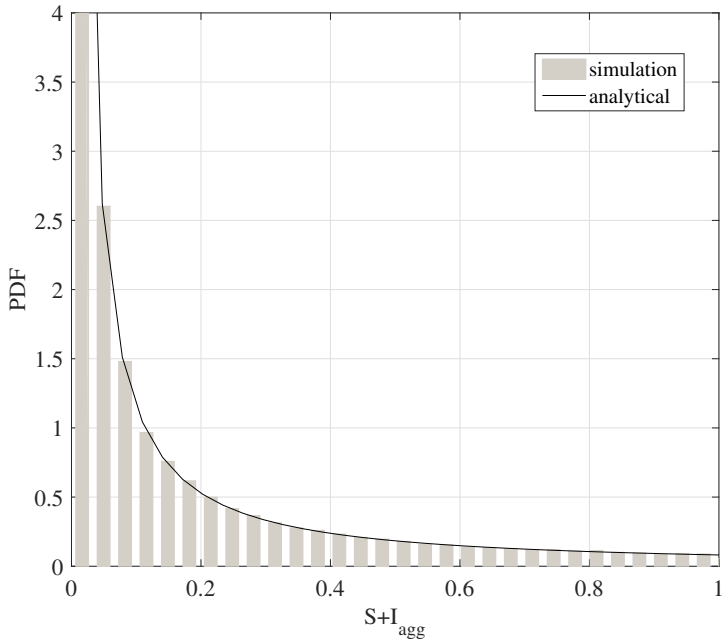

Figure 4.2: *PDF of* $\mathsf{S} + \mathsf{I}_{\mathrm{agg}}$ *for noncoherent JT. The parameters are* $\Psi_{1/2} = 60°$, $\lambda_{\mathrm{a}} = 0.1$, *and* $L = 1$ m.

In Figure 4.2, the analytical expression in (4.13) is compared with the empirical PDF of $\mathsf{S}+\mathsf{I}_{\mathrm{agg}}$ obtained from Monte Carlo simulations. The empirical data is obtained from $80,000$ realizations while the analytical expression is calculated by summing the first 100 terms of (4.13). It can be seen that the derived analytical expression closely matches the simulation results. Although the exact PDFs of the signal and interference cannot be obtained straightforwardly, existing works have shown that the Gamma distribution is a reasonable fit to the Poisson-field interference [127, 133]. Motivated by this, S and $\mathsf{I}_{\mathrm{agg}}$ are approximated as two independent Gamma-distributed random variables using the second-order moment matching method. The results are then used to approximate the coverage probability.

4.3.2 Noncoherent Joint Transmission

In this subsection, approximate distribution functions of S and $\mathsf{I}_{\mathrm{agg}}$ for noncoherent JT are derived. A Gamma random variable can be characterized by its shape parameter k and scale parameter θ. Considering the normalized signal power, its mean can be calculated from Camp-

bell's theorem [45]:

$$\begin{aligned}\mathbb{E}\left[\mathsf{S}\right] =&\mathbb{E}\left[\sum_{x_i\in\Phi_{\mathrm{a}}\cap\mathcal{B}(o,r_{\mathrm{c}})}\left(x_i^2+L^2\right)^{-(m+3)}\right]\\ =&2\pi\lambda_{\mathrm{a}}\int_0^{r_{\mathrm{c}}} x\left(x^2+L^2\right)^{-(m+3)}\mathrm{d}x\\ =&\frac{\pi\lambda_{\mathrm{a}}}{m+2}\left(L^{-2(m+2)}-\left(r_{\mathrm{c}}^2+L^2\right)^{-(m+2)}\right).\end{aligned} \tag{4.14}$$

The variance of S can be calculated as:

$$\begin{aligned}\mathrm{Var}\left[\mathsf{S}\right] =&\mathbb{E}\left[\mathsf{S}^2\right]-\left(\mathbb{E}\left[\mathsf{S}\right]\right)^2\\ =&\mathbb{E}\left[\sum_{x_i\in\Phi_{\mathrm{a}}\cap\mathcal{B}(o,r_{\mathrm{c}})}\left(x_i^2+L^2\right)^{-2(m+3)}\right]\\ =&2\pi\lambda_{\mathrm{a}}\int_0^{r_{\mathrm{c}}} x\left(x^2+L^2\right)^{-2(m+3)}\mathrm{d}x\\ =&\frac{\pi\lambda_{\mathrm{a}}}{2m+5}\left(L^{-2(2m+5)}-\left(r_{\mathrm{c}}^2+L^2\right)^{-(2m+5)}\right).\end{aligned} \tag{4.15}$$

Since a gamma distribution with shape parameter k_{S} and scale parameter θ_{S} has mean $k_{\mathsf{S}}\theta_{\mathsf{S}}$ and variance $k_{\mathsf{S}}\theta_{\mathsf{S}}^2$, k_{S} and θ_{S} can be obtained as follows:

$$k_{\mathsf{S}}=\frac{\left(\mathbb{E}[\mathsf{S}]\right)^2}{\mathrm{Var}[\mathsf{S}]}=\pi\lambda_{\mathrm{a}}\frac{2m+5}{(m+2)^2}\frac{\left(L^{-2(m+2)}-\left(r_{\mathrm{c}}^2+L^2\right)^{-(m+2)}\right)^2}{L^{-2(2m+5)}-\left(r_{\mathrm{c}}^2+L^2\right)^{-(2m+5)}}, \tag{4.16}$$

and

$$\theta_{\mathsf{S}}=\frac{\mathrm{Var}[\mathsf{S}]}{\mathbb{E}[\mathsf{S}]}=\frac{m+2}{2m+5}\frac{L^{-2(2m+5)}-\left(r_{\mathrm{c}}^2+L^2\right)^{-(2m+5)}}{L^{-2(m+2)}-\left(r_{\mathrm{c}}^2+L^2\right)^{-(m+2)}}. \tag{4.17}$$

Hence, the approximated PDF of S for noncoherent JT is:

$$f_{\mathsf{S}}(S)\approx\frac{\theta_{\mathsf{S}}^{-k_{\mathsf{S}}}}{\Gamma(k_{\mathsf{S}})}S^{k_{\mathsf{S}}-1}\exp\left(-\frac{S}{\theta_{\mathsf{S}}}\right). \tag{4.18}$$

Similarly, the mean and variance of the normalized aggregate interference can be calculated as

$$\mathbb{E}\left[\mathsf{I}_{\mathrm{agg}}\right]=\frac{\pi\lambda_{\mathrm{a}}}{m+2}\left(r_{\mathrm{c}}^2+L^2\right)^{-(m+2)}, \tag{4.19}$$

$$\mathrm{Var}\left[\mathsf{I}_{\mathrm{agg}}\right]=\frac{\pi\lambda_{\mathrm{a}}}{2m+5}\left(r_{\mathrm{c}}^2+L^2\right)^{-(2m+5)}. \tag{4.20}$$

With second-order moment matching, the distribution of I_{agg} for noncoherent JT can be approximated by

$$f_{\mathsf{I}_{\text{agg}}}(I) \approx \frac{\theta_{\mathsf{I}_{\text{agg}}}^{-k_{\mathsf{I}_{\text{agg}}}}}{\Gamma(k_{\mathsf{I}_{\text{agg}}})} I^{k_{\mathsf{I}_{\text{agg}}}-1} \exp\left(-\frac{I}{\theta_{\mathsf{I}_{\text{agg}}}}\right), \tag{4.21}$$

where the shape parameter and scale parameters are

$$k_{\mathsf{I}_{\text{agg}}} = \pi\lambda_{\text{a}} \frac{2m+5}{(m+2)^2} \frac{\left(r_{\text{c}}^2+L^2\right)^{-2(m+2)}}{\left(r_{\text{c}}^2+L^2\right)^{-(2m+5)}}, \tag{4.22}$$

$$\theta_{\mathsf{I}_{\text{agg}}} = \frac{m+2}{2m+5} \frac{\left(r_{\text{c}}^2+L^2\right)^{-(2m+5)}}{\left(r_{\text{c}}^2+L^2\right)^{-(m+2)}}. \tag{4.23}$$

Based on (4.18) and (4.21), the coverage probability can be approximated using properties of the gamma distribution:

$$\begin{aligned}
\mathbb{P}\left[\mathsf{SINR} > T\right] =& \mathbb{E}_{\mathsf{I}_{\text{agg}}}\left[\mathbb{P}\left[\mathsf{S} > T\left(\mathsf{I}_{\text{agg}}+\bar{\sigma}_{\text{n}}^2\right)\middle|\, \mathsf{I}_{\text{agg}}\right]\right] \\
\approx& \mathbb{E}_{\mathsf{I}_{\text{agg}}}\left[\frac{\Gamma\left(k_{\mathsf{S}}, \frac{T\left(\mathsf{I}_{\text{agg}}+\bar{\sigma}_{\text{n}}^2\right)}{\theta_{\mathsf{S}}}\right)}{\Gamma\left(k_{\mathsf{S}}\right)}\right] \\
\approx& \frac{\theta_{\mathsf{I}_{\text{agg}}}^{-k_{\mathsf{I}_{\text{agg}}}}}{\Gamma\left(k_{\mathsf{S}}\right)\Gamma\left(k_{\mathsf{I}_{\text{agg}}}\right)} \int_0^\infty I^{k_{\mathsf{I}_{\text{agg}}}-1} \exp\left(-\frac{I}{\theta_{\mathsf{I}_{\text{agg}}}}\right) \Gamma\left(k_{\mathsf{S}}, \frac{T\left(I+\bar{\sigma}_{\text{n}}^2\right)}{\theta_{\mathsf{S}}}\right) \mathrm{d}I.
\end{aligned} \tag{4.24}$$

Using the series expansion of the upper incomplete gamma function [110, (8.354.2)], (4.24) can be rewritten as:

$$\begin{aligned}
&\mathbb{P}\left[\mathsf{SINR} > T\right] \\
\approx& \frac{\theta_{\mathsf{I}_{\text{agg}}}^{-k_{\mathsf{I}_{\text{agg}}}}}{\Gamma\left(k_{\mathsf{S}}\right)\Gamma\left(k_{\mathsf{I}_{\text{agg}}}\right)} \int_0^\infty I^{k_{\mathsf{I}_{\text{agg}}}-1} \exp\left(-\frac{I}{\theta_{\mathsf{I}_{\text{agg}}}}\right) \left(\Gamma\left(k_{\mathsf{S}}\right) - \sum_{n=0}^{\infty} \frac{(-1)^n \left(\frac{T\left(I+\bar{\sigma}_{\text{n}}^2\right)}{\theta_{\mathsf{S}}}\right)^{k_{\mathsf{S}}+n}}{n!\left(k_{\mathsf{S}}+n\right)}\right) \mathrm{d}I \\
=& 1 - \frac{\theta_{\mathsf{I}_{\text{agg}}}^{-k_{\mathsf{I}_{\text{agg}}}}}{\Gamma\left(k_{\mathsf{S}}\right)\Gamma\left(k_{\mathsf{I}_{\text{agg}}}\right)} \sum_{n=0}^{\infty} \frac{(-1)^n}{n!\left(k_{\mathsf{S}}+n\right)} \int_0^\infty I^{k_{\mathsf{I}_{\text{agg}}}-1} \exp\left(-\frac{I}{\theta_{\mathsf{I}_{\text{agg}}}}\right) \left(\frac{T\left(I+\bar{\sigma}_{\text{n}}^2\right)}{\theta_{\mathsf{S}}}\right)^{k_{\mathsf{S}}+n} \mathrm{d}I.
\end{aligned} \tag{4.25}$$

With a change of variable $t = I/\bar{\sigma}_{\mathrm{n}}^2$, (4.25) can be further simplified to:

$$\mathbb{P}\left[\mathsf{SINR} > T\right] \approx 1 - \frac{\theta_{\mathsf{I}_{\mathrm{agg}}}^{-k_{\mathsf{I}_{\mathrm{agg}}}}}{\Gamma\left(k_{\mathsf{S}}\right)\Gamma\left(k_{\mathsf{I}_{\mathrm{agg}}}\right)} \sum_{n=0}^{\infty} \frac{(-1)^n}{n!\left(k_{\mathsf{S}}+n\right)} \left(\frac{T}{\theta_{\mathsf{S}}}\right)^{k_{\mathsf{S}}+n} \left(\bar{\sigma}_{\mathrm{n}}^2\right)^{k_{\mathsf{S}}+k_{\mathsf{I}_{\mathrm{agg}}}+n} \times \int_0^{\infty} t^{k_{\mathsf{I}_{\mathrm{agg}}}-1} \exp\left(-\frac{\bar{\sigma}_{\mathrm{n}}^2}{\theta_{\mathsf{I}_{\mathrm{agg}}}} t\right) (1+t)^{k_{\mathsf{S}}+n} \, \mathrm{d}t. \tag{4.26}$$

After applying [110, (9.211.4)], the integration in (4.26) can be interpreted as the integral representation of the confluent hypergeometric function with parameters $k_{\mathsf{I}_{\mathrm{agg}}}$, $k_{\mathsf{S}} + k_{\mathsf{I}_{\mathrm{agg}}} + n + 1$ and $\bar{\sigma}_{\mathrm{n}}^2/\theta_{\mathsf{I}_{\mathrm{agg}}}$. After some simplifications, the coverage probability can be written as:

$$\mathbb{P}\left[\mathsf{SINR} > T\right] \approx 1 - \frac{\theta_{\mathsf{I}_{\mathrm{agg}}}^{-k_{\mathsf{I}_{\mathrm{agg}}}}}{\Gamma\left(k_{\mathsf{S}}\right)} \sum_{n=0}^{\infty} \frac{(-1)^n}{n!\left(k_{\mathsf{S}}+n\right)} \left(\frac{T}{\theta_{\mathsf{S}}}\right)^{k_{\mathsf{S}}+n} \times \left(\bar{\sigma}_{\mathrm{n}}^2\right)^{k_{\mathsf{S}}+k_I+n} U\left(k_I, k_{\mathsf{S}} + k_{\mathsf{I}_{\mathrm{agg}}} + n + 1, \frac{\bar{\sigma}_{\mathrm{n}}^2}{\theta_{\mathsf{I}_{\mathrm{agg}}}}\right), \tag{4.27}$$

where $U(a,b,z) = \Gamma^{-1}(a) \int_0^{\infty} \exp(-zt)\, t^{a-1} (1+t)^{b-a-1} \, \mathrm{d}t$ is the confluent hypergeometric function [110]. Note that (4.27) can be significantly simplified if the communication link is interference-limited. More specifically, when $\bar{\sigma}_{\mathrm{n}}^2 = 0$, the coverage probability can be simplified to:

$$\mathbb{P}\left[\mathsf{SINR} > T\right] \approx \frac{\theta_{\mathsf{I}_{\mathrm{agg}}}^{-k_{\mathsf{I}_{\mathrm{agg}}}}}{\Gamma\left(k_{\mathsf{S}}\right)\Gamma\left(k_{\mathsf{I}_{\mathrm{agg}}}\right)} \int_0^{\infty} I^{k_{\mathsf{I}_{\mathrm{agg}}}-1} \exp\left(-\frac{I}{\theta_{\mathsf{I}_{\mathrm{agg}}}}\right) \Gamma\left(k_{\mathsf{S}}, \frac{TI}{\theta_{\mathsf{S}}}\right) \mathrm{d}I. \tag{4.28}$$

The integration in (4.28) can be further calculated as:

$$\begin{aligned} &\int_0^{\infty} I^{k_{\mathsf{I}_{\mathrm{agg}}}-1} \exp\left(-\frac{I}{\theta_{\mathsf{I}_{\mathrm{agg}}}}\right) \Gamma\left(k_{\mathsf{S}}, \frac{TI}{\theta_{\mathsf{S}}}\right) \mathrm{d}I \\ =&\frac{\Gamma\left(k_{\mathsf{S}}+k_I\right)\left(\frac{\theta_{\mathsf{S}}}{T}\right)^{k_{\mathsf{I}_{\mathrm{agg}}}}}{k_{\mathsf{I}_{\mathrm{agg}}}\left(1+\frac{\theta_{\mathsf{S}}}{\theta_{\mathsf{I}_{\mathrm{agg}}}T}\right)^{k_{\mathsf{S}}+k_{\mathsf{I}_{\mathrm{agg}}}}} {}_2F_1\left(1, k_{\mathsf{S}}+k_{\mathsf{I}_{\mathrm{agg}}}; k_{\mathsf{I}_{\mathrm{agg}}}+1; \frac{1}{1+\frac{\theta_{\mathsf{I}_{\mathrm{agg}}}}{\theta_{\mathsf{S}}}T}\right) \\ =&\frac{\Gamma\left(k_{\mathsf{S}}+k_{\mathsf{I}_{\mathrm{agg}}}\right)}{k_{\mathsf{I}_{\mathrm{agg}}}} \left(\frac{\theta_{\mathsf{S}}}{T}\right)^{k_{\mathsf{I}_{\mathrm{agg}}}} {}_2F_1\left(k_{\mathsf{I}_{\mathrm{agg}}}, k_{\mathsf{S}}+k_{\mathsf{I}_{\mathrm{agg}}}; k_{\mathsf{I}_{\mathrm{agg}}}+1; -\frac{\theta_{\mathsf{S}}}{\theta_{\mathsf{I}_{\mathrm{agg}}}T}\right), \end{aligned} \tag{4.29}$$

where ${}_2F_1(\cdot,\cdot;\cdot;\cdot)$ is the Gauss hypergeometric function [110]. In the above derivation, the first step follows from [110, (6.455.1)] and the second step is obtained with the use of Pfaff

transformation [110, (9.131.1)]. Inserting (4.29) into (4.28) yields

$$\mathbb{P}\left[\mathsf{SINR} > T\right] \approx \frac{\Gamma\left(k_{\mathsf{S}} + k_{\mathsf{I}_{\mathrm{agg}}}\right)}{k_{\mathsf{I}_{\mathrm{agg}}}\Gamma\left(k_{\mathsf{S}}\right)\Gamma\left(k_{\mathsf{I}_{\mathrm{agg}}}\right)} \left(\frac{\theta_{\mathsf{S}}}{\theta_{\mathsf{I}_{\mathrm{agg}}} T}\right)^{k_{\mathsf{I}_{\mathrm{agg}}}} \times {}_2F_1\left(k_{\mathsf{I}_{\mathrm{agg}}}, k_{\mathsf{S}} + k_{\mathsf{I}_{\mathrm{agg}}}; k_{\mathsf{I}_{\mathrm{agg}}} + 1; -\frac{\theta_{\mathsf{S}}}{\theta_{\mathsf{I}_{\mathrm{agg}}} T}\right), \tag{4.30}$$

Notice that the coverage probability in (4.30) depends on k_{S}, $k_{\mathsf{I}_{\mathrm{agg}}}$ and the ratio between θ_{S} and $\theta_{\mathsf{I}_{\mathrm{agg}}}$. When the communication link is interference-limited, (4.30) provides a more tractable result than (4.27) for the coverage probability computation. For the general case when $\bar{\sigma}_{\mathrm{n}}^2 \neq 0$, the coverage probability is more accurately characterized by (4.27), while (4.30) can be used as an analytical upper bound.

4.3.3 Coherent Joint Transmission

In this subsection, approximate distribution functions of the normalized signal power and interference for coherent JT are derived using a similar approach. Since the independence between S and $\mathsf{I}_{\mathrm{agg}}$ is still preserved, the coverage probability can also be computed using the PDFs of S and $\mathsf{I}_{\mathrm{agg}}$.

The interference expressions for noncoherent JT and coherent JT are the same, as are their distributions. Therefore, for coherent JT, $\mathsf{I}_{\mathrm{agg}}$ can also be approximated by a gamma distribution with shape parameter $k_{\mathsf{I}_{\mathrm{agg}}}$ and scale parameter $\theta_{\mathsf{I}_{\mathrm{agg}}}$ given by (4.22) and (4.23), respectively. For coherent JT, the expression for S is given as a sum squared. As a result, the gamma distribution is no longer accurate for modeling the distribution of S. To better understand the characteristics of S, the distribution of the signal amplitude $\mathsf{Y} = \sqrt{\mathsf{S}} = \sum_{x_i \in \Phi_{\mathrm{a}} \cap \mathcal{B}(o, r_{\mathrm{c}})} \left(x_i^2 + L^2\right)^{-(m+3)/2}$ is first studied. Since Y for coherent JT has a similar expression as S for noncoherent JT, it can also be approximated by a gamma distribution. The mean and variance of Y are found to be:

$$\mathbb{E}\left[\mathsf{Y}\right] = \frac{2\pi\lambda_{\mathrm{a}}}{m+1}\left(L^{-(m+1)} - \left(r_{\mathrm{c}}^2 + L^2\right)^{-\frac{m+1}{2}}\right), \tag{4.31}$$

$$\mathrm{Var}\left[\mathsf{Y}\right] = \frac{\pi\lambda_{\mathrm{a}}}{m+2}\left(L^{-2(m+2)} - \left(r_{\mathrm{c}}^2 + L^2\right)^{-(m+2)}\right). \tag{4.32}$$

Letting $\mathbb{E}\left[\mathsf{Y}\right] = k_{\mathsf{Y}}\theta_{\mathsf{Y}}$ and $\mathrm{Var}\left[\mathsf{Y}\right] = k_{\mathsf{Y}}\theta_{\mathsf{Y}}^2$, the shape parameter k_{Y} and scale parameter θ_{Y} for

the gamma distribution of Y are obtained as:

$$k_{\mathsf{Y}} = 4\pi\lambda_{\mathrm{a}}\frac{m+2}{(m+1)^2}\frac{\left(L^{-(m+1)} - \left(r_{\mathrm{c}}^2 + L^2\right)^{-\frac{m+1}{2}}\right)^2}{L^{-2(m+2)} - \left(r_{\mathrm{c}}^2 + L^2\right)^{-(m+2)}}, \tag{4.33}$$

$$\theta_{\mathsf{Y}} = \frac{(m+1)}{2(m+2)}\frac{L^{-2(m+2)} - \left(r_{\mathrm{c}}^2 + L^2\right)^{-(m+2)}}{L^{-(m+1)} - \left(r_{\mathrm{c}}^2 + L^2\right)^{-\frac{m+1}{2}}}. \tag{4.34}$$

Based on the property of gamma distribution, the cumulative distribution function (CDF) of S can be obtained as:

$$\mathbb{P}\left[\mathsf{S} < t\right] = \mathbb{P}\left[\mathsf{Y} < \sqrt{t}\right] \approx 1 - \frac{\Gamma\left(k_{\mathsf{Y}}, \frac{\sqrt{t}}{\theta_{\mathsf{Y}}}\right)}{\Gamma\left(k_{\mathsf{Y}}\right)}. \tag{4.35}$$

Calculating the derivative of the CDF yields the PDF of S:

$$f_{\mathsf{S}}(t) = \frac{\partial}{\partial t}\mathbb{P}\left[\mathsf{S} < t\right] \approx \frac{\theta_{\mathsf{Y}}^{-k_{\mathsf{Y}}}}{2\Gamma\left(k_{\mathsf{Y}}\right)} t^{\frac{k_{\mathsf{Y}}}{2}-1} \exp\left(-\frac{\sqrt{t}}{\theta_{\mathsf{Y}}}\right). \tag{4.36}$$

The PDF of S can also be written as a generalized gamma distribution:

$$f_{\mathsf{S}}(S) \approx \frac{p_{\mathsf{S}}}{a_{\mathsf{S}}^{d_{\mathsf{S}}}}\frac{S^{d_{\mathsf{S}}-1}}{\Gamma\left(\frac{d_{\mathsf{S}}}{p_{\mathsf{S}}}\right)} \exp\left(-\left(\frac{S}{a_{\mathsf{S}}}\right)^{p_{\mathsf{S}}}\right), \tag{4.37}$$

where the scale parameter and shape parameters are $a_{\mathsf{S}} = \theta_{\mathsf{Y}}^2$, $p_{\mathsf{S}} = k_{\mathsf{Y}}/2$ and $d_{\mathsf{S}} = 1/2$. Combining (4.21) and (4.37), the coverage probability for coherent JT can be calculated as:

$$\begin{aligned}
&\mathbb{P}\left[\mathsf{SINR} > T\right] = \mathbb{E}_{\mathsf{I}_{\mathrm{agg}}}\left[\mathbb{P}\left[\mathsf{S} > T\left(\mathsf{I}_{\mathrm{agg}} + \bar{\sigma}_{\mathrm{n}}^2\right) \middle| \mathsf{I}_{\mathrm{agg}}\right]\right] \\
\approx &\mathbb{E}_{\mathsf{I}_{\mathrm{agg}}}\left[\frac{\Gamma\left(\frac{d_{\mathsf{S}}}{p_{\mathsf{S}}}, \left(\frac{T\left(\mathsf{I}_{\mathrm{agg}}+\bar{\sigma}_{\mathrm{n}}^2\right)}{a_{\mathsf{S}}}\right)^{p_{\mathsf{S}}}\right)}{\Gamma\left(k_{\mathsf{Y}}\right)}\right] \\
\approx &\frac{\theta_{\mathsf{I}_{\mathrm{agg}}}^{-k_{\mathsf{I}_{\mathrm{agg}}}}}{\Gamma\left(k_{\mathsf{Y}}\right)\Gamma\left(k_{\mathsf{I}_{\mathrm{agg}}}\right)}\int_0^\infty I^{k_{\mathsf{I}_{\mathrm{agg}}}-1}\exp\left(-\frac{I}{\theta_{\mathsf{I}_{\mathrm{agg}}}}\right)\Gamma\left(k_{\mathsf{Y}}, \frac{\sqrt{T\left(I+\bar{\sigma}_{\mathrm{n}}^2\right)}}{\theta_{\mathsf{Y}}}\right)\mathrm{d}I.
\end{aligned} \tag{4.38}$$

By following similar steps as in (4.25) and (4.26), the coverage probability simplifies to:

$$\begin{aligned}
\mathbb{P}\left[\mathsf{SINR} > T\right] \approx 1 - &\frac{\theta_{\mathsf{I}_{\mathrm{agg}}}^{-k_{\mathsf{I}_{\mathrm{agg}}}}}{\Gamma\left(k_{\mathsf{Y}}\right)}\sum_{n=0}^{\infty}\frac{(-1)^n}{n!\left(k_{\mathsf{Y}}+n\right)}\left(\frac{\sqrt{T}}{\theta_{\mathsf{Y}}}\right)^{k_{\mathsf{S}}+n}\left(\bar{\sigma}_{\mathrm{n}}^2\right)^{\frac{k_{\mathsf{Y}}}{2}+k_{\mathsf{I}_{\mathrm{agg}}}+\frac{n}{2}} \\
&\times U\left(k_{\mathsf{I}_{\mathrm{agg}}}, \frac{k_Y}{2} + k_{\mathsf{I}_{\mathrm{agg}}} + \frac{n}{2} + 1, \frac{\bar{\sigma}_{\mathrm{n}}^2}{\theta_{\mathsf{I}_{\mathrm{agg}}}}\right).
\end{aligned} \tag{4.39}$$

The result can be further simplified if the communication link is interference-limited. More specifically, when $\bar{\sigma}_{\mathrm{n}}^2 = 0$, the coverage probability can be simplified using a change of variable $t = \sqrt{TI}/\theta_{\mathsf{Y}}$:

$$\begin{aligned}\mathbb{P}\left[\mathsf{SINR} > T\right] \approx & \frac{\theta_I^{-k_{\mathsf{I}_{\mathrm{agg}}}}}{\Gamma\left(k_{\mathsf{Y}}\right)\Gamma\left(k_{\mathsf{I}_{\mathrm{agg}}}\right)} \int_0^{\infty} I^{k_{\mathsf{I}_{\mathrm{agg}}}-1} \exp\left(-\frac{I}{\theta_{\mathsf{I}_{\mathrm{agg}}}}\right) \Gamma\left(k_{\mathsf{Y}}, \frac{\sqrt{TI}}{\theta_{\mathsf{Y}}}\right) \mathrm{d}I \\ = & \frac{2}{\Gamma\left(k_{\mathsf{Y}}\right)\Gamma\left(k_{\mathsf{I}_{\mathrm{agg}}}\right)} \left(\frac{\theta_{\mathsf{Y}}^2}{\theta_{\mathsf{I}_{\mathrm{agg}}} T}\right)^{k_{\mathsf{I}_{\mathrm{agg}}}} \int_0^{\infty} t^{2k_{\mathsf{I}_{\mathrm{agg}}}-1} \exp\left(-\frac{\theta_{\mathsf{Y}}^2}{\theta_{\mathsf{I}_{\mathrm{agg}}} T} t^2\right) \Gamma\left(k_{\mathsf{Y}}, t\right) \mathrm{d}t.\end{aligned} \tag{4.40}$$

After replacing the incomplete gamma function in (4.40) with a series representation [110, (8.354.2)], the coverage probability can be expressed as:

$$\begin{aligned}\mathbb{P}\left[\mathsf{SINR} > T\right] \approx & \frac{2}{\Gamma\left(k_{\mathsf{Y}}\right)\Gamma\left(k_{\mathsf{I}_{\mathrm{agg}}}\right)} \left(\frac{\theta_{\mathsf{Y}}^2}{\theta_{\mathsf{I}_{\mathrm{agg}}} T}\right)^{k_{\mathsf{I}_{\mathrm{agg}}}} \int_0^{\infty} t^{2k_{\mathsf{I}_{\mathrm{agg}}}-1} \exp\left(-\frac{\theta_{\mathsf{Y}}^2}{\theta_{\mathsf{I}_{\mathrm{agg}}} T} t^2\right) \\ & \times \left(\Gamma\left(k_{\mathsf{Y}}\right) - \sum_{n=0}^{\infty} \frac{(-1)^n}{n!\left(k_{\mathsf{Y}}+n\right)} t^{k_{\mathsf{Y}}+n}\right) \mathrm{d}t \\ = & 1 - \frac{2}{\Gamma\left(k_{\mathsf{Y}}\right)\Gamma\left(k_{\mathsf{I}_{\mathrm{agg}}}\right)} \left(\frac{\theta_{\mathsf{Y}}^2}{\theta_{\mathsf{I}_{\mathrm{agg}}} T}\right)^{k_{\mathsf{I}_{\mathrm{agg}}}} \sum_{n=0}^{\infty} \frac{(-1)^n}{n!\left(k_{\mathsf{Y}}+n\right)} \\ & \times \int_0^{\infty} t^{k_{\mathsf{Y}}+2k_{\mathsf{I}_{\mathrm{agg}}}+n-1} \exp\left(-\frac{\theta_{\mathsf{Y}}^2}{\theta_{\mathsf{I}_{\mathrm{agg}}} T} t^2\right) \mathrm{d}t \\ = & 1 - \frac{1}{\Gamma\left(k_{\mathsf{Y}}\right)\Gamma\left(k_{\mathsf{I}_{\mathrm{agg}}}\right)} \left(\frac{\sqrt{\theta_{\mathsf{I}_{\mathrm{agg}}} T}}{\theta_{\mathsf{Y}}}\right)^{k_{\mathsf{Y}}} \sum_{n=0}^{\infty} \frac{(-1)^n}{n!\left(k_{\mathsf{Y}}+n\right)} \left(\frac{\theta_{\mathsf{I}_{\mathrm{agg}}} T}{\theta_{\mathsf{Y}}^2}\right)^{\frac{n}{2}} \\ & \times \Gamma\left(\frac{k_{\mathsf{Y}}}{2} + k_{\mathsf{I}_{\mathrm{agg}}} + \frac{n}{2}\right).\end{aligned} \tag{4.41}$$

Interpreting the sum of the infinite series as two sums with odd and even indexes, (4.41) can be rewritten as:

$$\begin{aligned}\mathbb{P}\left[\mathsf{SINR} > T\right] \approx & 1 + \frac{1}{\Gamma\left(k_{\mathsf{Y}}\right)\Gamma\left(k_{\mathsf{I}_{\mathrm{agg}}}\right)} \left(\frac{\sqrt{\theta_{\mathsf{I}_{\mathrm{agg}}} T}}{\theta_{\mathsf{Y}}}\right)^{k_{\mathsf{Y}}} \\ & \times \left(\sum_{n=0}^{\infty} \left(\frac{\theta_{\mathsf{I}_{\mathrm{agg}}} T}{\theta_{\mathsf{Y}}^2}\right)^{n+\frac{1}{2}} \frac{\Gamma\left(\frac{k_{\mathsf{Y}}}{2} + k_{\mathsf{I}_{\mathrm{agg}}} + n + \frac{1}{2}\right)}{(2n+1)!\left(k_{\mathsf{Y}}+2n+1\right)} - \sum_{n=0}^{\infty} \left(\frac{\theta_{\mathsf{I}_{\mathrm{agg}}} T}{\theta_{\mathsf{Y}}^2}\right)^{n} \frac{\Gamma\left(\frac{k_{\mathsf{Y}}}{2} + k_{\mathsf{I}_{\mathrm{agg}}} + n\right)}{(2n)!\left(k_{\mathsf{Y}}+2n\right)}\right).\end{aligned} \tag{4.42}$$

Based on the following two identities: $(2n)! = n!4^n\Gamma\left(n+1/2\right)/\Gamma\left(1/2\right)$ and $(2n+1)! =$

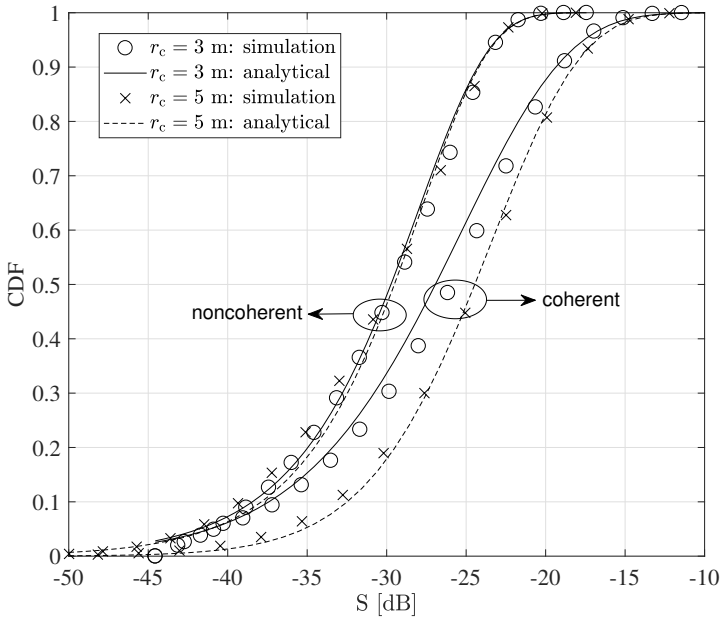

Figure 4.3: *Empirical and approximated CDFs of the (unitless) normalized signal power* S.

$2(n)!4^n\Gamma\left(n+3/2\right)/\Gamma\left(1/2\right)$, it follows that:

$$\mathbb{P}\left[\mathsf{SINR} > T\right] \approx 1 + \frac{1}{\Gamma\left(k_{\mathsf{Y}}\right)\Gamma\left(k_{\mathsf{I}_{\text{agg}}}\right)}\left(\frac{\sqrt{\theta_{\mathsf{I}_{\text{agg}}}T}}{\theta_{\mathsf{Y}}}\right)^{k_{\mathsf{Y}}}\sum_{n=0}^{\infty}\frac{\Gamma\left(\frac{1}{2}\right)}{2\Gamma\left(n+\frac{1}{2}\right)}\left(\frac{\theta_{\mathsf{I}_{\text{agg}}}T}{4\theta_{\mathsf{Y}}^2}\right)^n\frac{1}{n!} \times\left(\frac{\sqrt{\theta_{\mathsf{I}_{\text{agg}}}T}}{\theta_{\mathsf{Y}}}\frac{\Gamma\left(\frac{k_{\mathsf{Y}}}{2}+k_{\mathsf{I}_{\text{agg}}}+n+\frac{1}{2}\right)}{2\left(n+\frac{1}{2}\right)\left(\frac{k_{\mathsf{Y}}}{2}+n+\frac{1}{2}\right)}-\frac{\Gamma\left(\frac{k_{\mathsf{Y}}}{2}+k_{\mathsf{I}_{\text{agg}}}+n\right)}{\frac{k_{\mathsf{Y}}}{2}+n}\right). \quad (4.43)$$

Interpreting the infinite series in (4.43) as the generalized hypergeometric series, the coverage probability can be further simplified to:

$$\begin{aligned}\mathbb{P}\left[\mathsf{SINR} > T\right] \approx & 1 + \frac{1}{\Gamma\left(k_{\mathsf{Y}}\right)\Gamma\left(k_{\mathsf{I}_{\text{agg}}}\right)}\left(\frac{\sqrt{\theta_{\mathsf{I}_{\text{agg}}}T}}{\theta_{\mathsf{Y}}}\right)^{k_{\mathsf{Y}}}\left\{\frac{\sqrt{\theta_{\mathsf{I}_{\text{agg}}}T}\Gamma\left(\frac{k_{\mathsf{Y}}}{2}+k_{\mathsf{I}_{\text{agg}}}+\frac{1}{2}\right)}{\theta_{\mathsf{Y}}\left(k_{\mathsf{Y}}+1\right)}\right. \\ & \times {}_2F_2\left(\frac{k_{\mathsf{Y}}+1}{2}, \frac{k_{\mathsf{Y}}}{2}+k_{\mathsf{I}_{\text{agg}}}+\frac{1}{2}; \frac{3}{2}, \frac{k_{\mathsf{Y}}+3}{2}; \frac{\theta_{\mathsf{I}_{\text{agg}}}T}{4\theta_{\mathsf{Y}}^2}\right) \\ & \left.-\frac{\Gamma\left(\frac{k_{\mathsf{Y}}}{2}+k_{\mathsf{I}_{\text{agg}}}\right)}{k_{\mathsf{Y}}}{}_2F_2\left(\frac{k_{\mathsf{Y}}}{2}+k_{\mathsf{I}_{\text{agg}}}, \frac{k_{\mathsf{Y}}}{2}; \frac{1}{2}, \frac{k_{\mathsf{Y}}}{2}+1; \frac{\theta_{\mathsf{I}_{\text{agg}}}T}{4\theta_{\mathsf{Y}}^2}\right)\right\}, \quad (4.44)\end{aligned}$$

where ${}_2F_2(\cdot,\cdot;\cdot,\cdot;\cdot)$ is the generalized hypergeometric series [110]. It can be seen that the coverage probability in (4.44) depends on k_{Y}, $k_{\mathsf{I}_{\text{agg}}}$ and the ratio between $\sqrt{\theta_{\mathsf{I}_{\text{agg}}}}$ and θ_{Y}. When the communication link is dominated by interference, evaluating the coverage probability of a

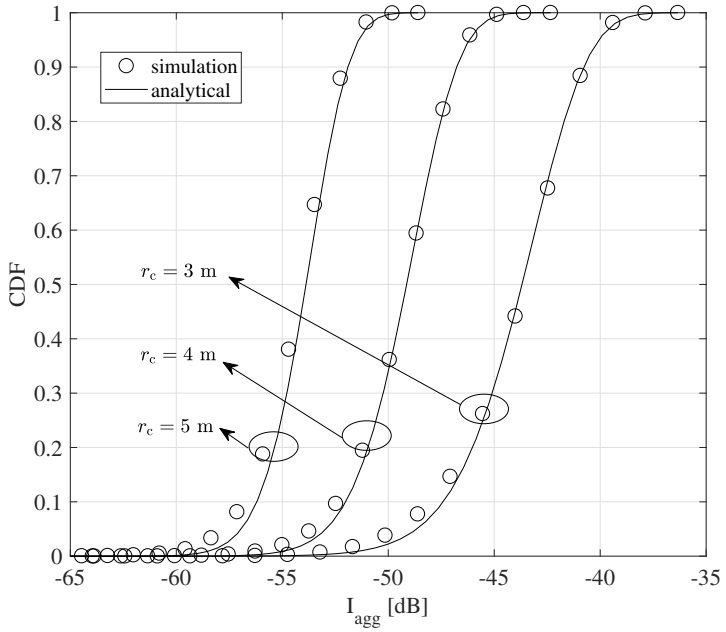

Figure 4.4: *Empirical and approximated CDFs of the (unitless) normalized interference* $\mathsf{I}_{\mathrm{agg}}$.

typical user using (4.44) is more analytically tractable. For the general case when $\bar{\sigma}_{\mathrm{n}}^2 \neq 0$, the coverage probability can be more accurately computed with (4.39), while (4.44) serves as an analytical upper bound.

4.4 Simulation Results

In this section, Monte Carlo simulations are presented to validate the theoretical results derived in Section 4.3. For the simulation setup, an indoor office of size $18 \times 14 \times 3.5$ m^3 is considered, as depicted in Figure 4.1. If not otherwise specified, the following parameters are assumed. The VLC APs have a semiangle of 60° and 1 W signal power. The PD used at the receiver side has a FOV of 90°, an effective detection area of 1 cm^2 and a responsivity of 0.4 $\mathrm{A/W}$. The vertical separation between users and VLC APs is set to 2 m. The modulation bandwidth and the noise power spectral density (PSD) are assumed to be 20 MHz and 10^{-22} A^2/Hz, respectively [4, 105]. The impact of receiver noise on the network performance is investigated in a latter part of this section. At the receiver front-end, assume the optical concentrator has a reflective index of 1.5 and the optical filter has a unity gain. The density of interfering APs is assumed to be 0.1.

Figure 4.3 compares the approximated CDF of the normalized signal power with its empirical

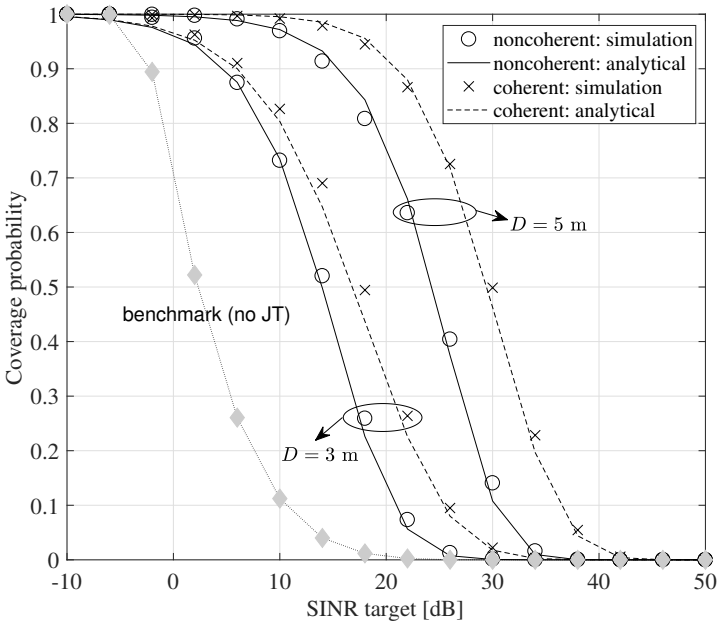

Figure 4.5: *Coverage probabilities for noncoherent and coherent JT schemes.*

CDF obtained through simulations. It can be seen that for noncoherent JT the signal power is well modeled by the gamma distribution, while for coherent JT the signal power is well approximated by the generalized gamma distribution. When the cooperation radius increases from 3 m to 5 m, only a slight improvement on the received signal power is observed for noncoherent JT. This is because signals transmitted from APs that are further away from the user are more severely attenuated. However, for coherent JT, signals transmitted by APs within the cooperation region are constructively accumulated in amplitude. Therefore, when the cooperation radius for coherent JT increases from 3 m to 5 m, $2-5$ dB improvement on the normalized signal power is observed. Figure 4.3 also shows that coherent JT outperforms its noncoherent counterpart in terms of the received signal power, but it requires more stringent signal synchronization and a higher implementation cost.

In Figure 4.4, the empirical and approximated CDFs of the normalized interference power are compared. Since the interference has the same expression for both JT schemes, it is not explicitly distinguished in this context. It is shown in Figure 4.4 that the gamma approximation of the interference power is reasonably accurate, with only slight deviations in the lower tail. As the cooperation radius is increased from 3 m to 5 m, the normalized interference power is reduced by $8-10$ dB. Therefore, combining the results shown in Figure 4.3 and Figure 4.4, It can be concluded that the main benefit of increasing the cooperation radius is the reduction of

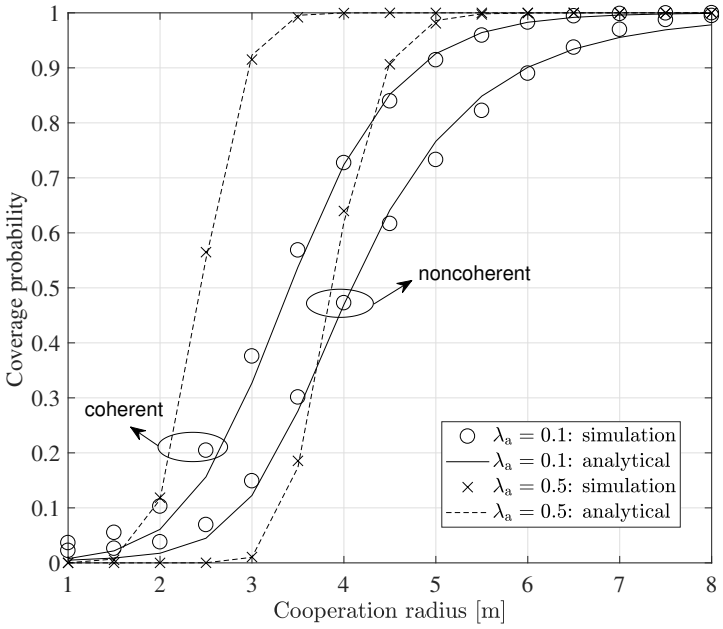

Figure 4.6: *Coverage probabilities for noncoherent and coherent JT schemes with different sizes of the cooperation region ($T = 20$ dB).*

interference level rather than the enhancement of useful signal power.

With different values of the target SINR, the coverage probability for noncoherent and coherent JT schemes are compared in Figure 4.5. Benchmark results representing the case without CoMP-JT are also shown. It can be seen that for both JT schemes, the derived analytical results closely match the simulation results. It is also observed that increasing the cooperation radius can significantly enhance the coverage probability of a typical user. For example, when the SINR target is 20 dB, increasing the cooperation radius from 3 m to 5 m helps improve the coverage probability from 0.15 to 0.76 for noncoherent JT and from 0.33 to 0.92 for coherent JT. Figure 4.5 also shows that coherent JT always yields a higher coverage probability than noncoherent JT, due to the accumulation in signal amplitude rather than in signal power. Furthermore, the gap between the coverage probabilities for noncoherent and coherent JT expands as the the cooperation radius is increased.

In Figure 4.6, the coverage probabilities for noncoherent and coherent JT schemes are investigated with different sizes of the cooperation region. It is shown that for both JT schemes, the coverage probability increases as the cooperation radius increases. Notice that, for small cooperation regions, the coverage probability is higher when the density of APs is smaller. On the other hand, for large cooperation regions, the coverage probability is higher when the den-

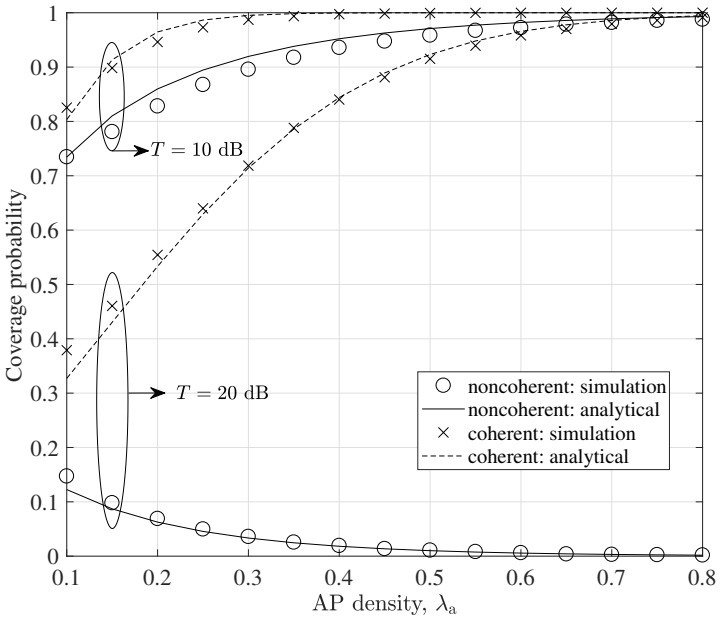

Figure 4.7: *Coverage probabilities for noncoherent and coherent JT schemes with different densities of APs ($r_c = 3$ m).*

sity of APs is larger. It is also shown that coherent JT gives a higher coverage probability than noncoherent JT, especially when the density of APs is large.

Figure 4.7 investigates how the coverage probability of a typical user scales with the density of APs in the network. It can be seen that for a small value of the SINR target ($T = 10$ dB), the coverage probabilities for both JT schemes increase as the density of APs gets larger. However, for a large value of the SINR target ($T = 20$ dB), the coverage probabilities for the two JT schemes scale differently with respect to AP density. More specifically, the coverage probability for noncoherent JT monotonically decreases with an increase in the density of APs, while the coverage probability for coherent JT monotonically increases as the density of APs is increased. The fundamental change of behavior of noncoherent JT when $T = 20$ dB is due to its limited capability to achieve the required SINR target. In this scenario, increasing the density of APs primarily gives rise to the aggregate interference level, leading to a poorer coverage performance as illustrated in Figure 4.7. As a result, in comparison with noncoherent JT, the benefit of coherent JT becomes more significant when the target SINR is set at a higher value.

The derived analytical results are applicable to arbitrary receiver noise levels. In Figure 4.8, the effect of receiver noise on the coverage probability is investigated. It can be seen from Figure 4.8 that the analytical results are generally accurate across all receiver noise levels. For

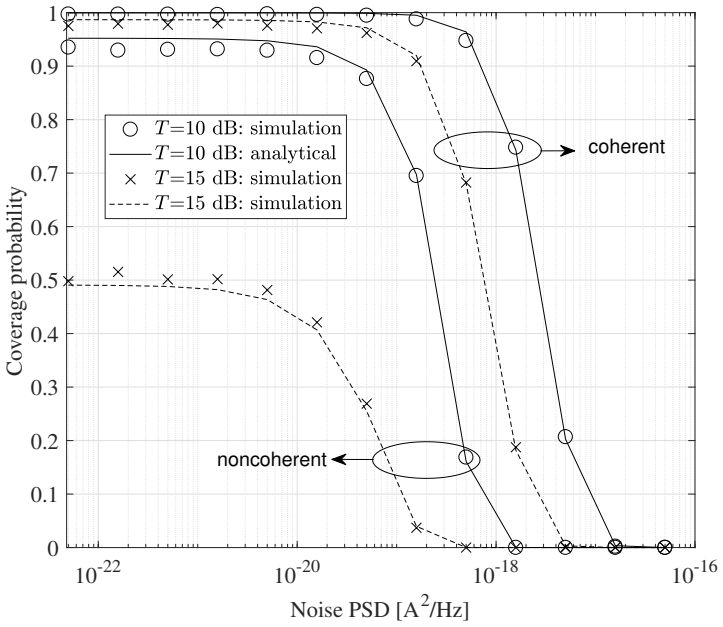

Figure 4.8: *Impact of receiver noise on the coverage probability for noncoherent and coherent JT schemes ($r_{\mathrm{c}} = 3$ m, $\lambda_{\mathrm{a}} = 0.4$).*

noise PSD less than 5×10^{-22} A^2/Hz, the coverage probability remains constant because the communication link is interference-limited. As the noise power continues to increase, the coverage probability starts to decrease until it reaches zero. Therefore, for typical receiver noise PSD of 10^{-22} A^2/Hz [4, 105], assuming that the communication link is interference-limited is reasonable and it can significantly simplify the coverage probability analysis for both noncoherent and coherent JT schemes.

4.5 Summary

In this chapter, the characteristic functions of the signal and interference in a cooperative attocell network have been investigated. The derived characteristic functions allow the PDFs of signal and interference to be obtained through the Fourier inversion theorem. However, the characteristic functions are in complicated forms and no explicit expressions for the PDFs are available. Motivated by this, a tractable method to approximate the coverage analysis is then presented. For both noncoherent JT and coherent JT, analytical expressions for the coverage probability have been derived and further simplified into closed forms when the communication link is interference-limited. The accuracy of the proposed analytical model has been validated through extensive Monte Carlo simulations. Also, the coverage performance of the network

has been comprehensively investigated with various parameters. Results show that, although coherent JT requires more stringent signal synchronization and has a higher implementation cost than noncoherent JT, it gives superior coverage performance to users in the network, especially when the network is densely deployed with APs. Furthermore, the performance gain of coherent JT over its noncoherent counterpart is found to be more significant when the network has high SINR demands.

Chapter 5
Non-Orthogonal Multiple Access

5.1 Introduction

As a wireless broadband technology, it is essential that visible light communication (VLC) can efficiently support multiple users with simultaneous network access. Chapter 3 and Chapter 4 focused on inter-cell interference (ICI) and studied the performance of a random user in optical attocell networks assuming full frequency reuse. This chapter investigates an efficient multiple access (MA) technique for intra-cell interference mitigation. Traditional MA techniques include frequency division multiple access (FDMA), time division multiple access (TDMA) and code division multiple access (CDMA). However, these techniques cannot provide sufficient resource reuse. A transmission scheme using discrete-sequence optical code division multiple access (OCDMA) was proposed in [134], where optical orthogonal codes (OOCs) are used to encode the data in the time domain by turning the light-emitting diodes (LEDs) on and off. As a default extension from orthogonal frequency division multiplexing (OFDM), orthogonal frequency division multiple access (OFDMA) [25, 26] enables resources to be reused at the subcarrier level and it has been widely implemented in the long-term evolution (LTE) downlink. For the long-term evolution advanced (LTE-A) uplink, a modified version of OFDMA named single carrier frequency division multiple access (SC-FDMA) [135] is used due to its low peak-to-average power ratio (PAPR). In [116], self-organizing interference management for the OFDMA-based VLC systems using busy burst (BB) signaling was evaluated in an aircraft cabin. Compared to the static resource partitioning, the BB approach was shown to improve the fairness and spectral efficiency of the system. By exploiting different color bands in visible light, a color-clustered MA scheme was proposed in [136], where multiple users are clustered into separate color clusters: red, green and blue (RGB). In [137], CDMA is combined with color-shift keying (CSK) for MA, in which data is transmitted imperceptibly through the variation in the color emitted by RGB LEDs.

To further enlarge the system capacity and provide enhanced user experience, especially for users at the cell edge, non-orthogonal multiple access (NOMA) has recently been proposed

as a promising solution for the fifth generation (5G) wireless networks [30, 31, 33]. Different from orthogonal multiple access (OMA) concepts, where users are allocated with exclusive time-frequency (TF) resources, NOMA uses power-domain multiplexing to realize MA. Specifically, signals for multiple users are superposed in the power domain so that all of the users can share the same TF resources during signal transmission. After the signal is broadcast through the channel, successive interference cancellation (SIC) is carried out at the receiver side for signal detection. As a result, channel state information (CSI) is required. The concept of NOMA can be related to the special case of superposition coding (SC) developed for broadcast channels [38]. According to the principle of NOMA, users with poor channel conditions are allocated more signal power to decode their own messages while users with good channel conditions are allocated less power but employ SIC to decode and remove the messages intended for other users with poorer channel conditions before decoding their own messages.

The implementation of NOMA in a coordinated two-point radio frequency (RF) system has recently been studied in [138], in which Alamouti codes are employed to improve the data rate of cell-edge users without degrading the performance of cell-center users. With a fixed power allocation (FPA) strategy, the performance of NOMA has been investigated and analytically characterized for the cellular downlink in [139]. The problem of user pairing on the performance of NOMA in RF systems has recently been studied in [140]. From a fairness standpoint, the power allocation problem was investigated in [141] in terms of the CSI. The optimization problems were solved through the proposed low-complexity polynomial algorithms therein. In [142], the application of multiuser beamforming has been adapted to NOMA with the aim of maximizing the system throughput. The design of uplink NOMA was proposed in [143], where a low-complexity scheduling algorithm was developed to achieve the proportional fairness. In the same work, fractional frequency reuse (FFR) was applied to further enhance the performance of cell-edge users. A cooperative transmission scheme for NOMA has been proposed in [144], where users with good channel conditions are used as relays to improve the reception reliability for users with poor channel conditions.

Recently, the application of NOMA has also been studied in VLC systems. Due to the fundamental differences between the VLC and RF channels, applying NOMA to VLC requires careful reconsideration [145, 146]. In [147], a gain-ratio power allocation (GRPA) strategy was proposed for multiuser VLC systems, whose performance was analyzed using a random walk mobility model to simulate the movements of indoor users. It was shown in [147] that the

system sum rate can be further enhanced by adaptively tuning the semiangle of LEDs and the field-of-view (FOV) of photodiodes (PDs). In [148], the performance of NOMA was compared with OFDMA in a VLC system with illumination constraints, and its superior performance was shown. In the following, a theoretical framework is provided for analyzing the performance of NOMA in a VLC system and characterizing its performance gain over OMA. Moving on, the new framework is used to devise effective user pairing strategies to improve the system throughput. The results confirm the superiority of NOMA over conventional OMA techniques and suggest that NOMA is an appealing technology for future attocell networks.

The rest of this chapter is organized as follows. The system model for an attocell downlink with the implementation of NOMA is introduced in Section 5.2. The performance of NOMA is evaluated in Section 5.3 for two different scenarios. In Section 5.4, the achievable performance gain of NOMA over OMA techniques is analytically quantified. Simulation results are presented and discussed in Section 5.5. Finally, conclusions are drawn in Section 5.6.

5.2 System Model

Consider the downlink transmission model, where LEDs are located in the ceiling and K users are uniformly distributed within a circular area. This model is an extension of the point-to-point (P2P) VLC system to accommodate multiple users. In the analysis, users are assumed to be static or quasi-static so that their CSI is not outdated until the next channel estimation. Focus on a single attocell whose radius is r_{e} and the vertical distance from the LED to the receiver plane is denoted by L. In a polar coordinate system, the location of user k can be represented by (r_k, φ_k), where r_k represents its horizontal separation from the LED and φ_k represents its polar angle from the reference axis. A complete VLC channel consists not only the line-of-sight (LOS) link but also the diffuse components which are caused by light reflections from interior surfaces. However, previous work has reported that in a typical indoor environment without shadowing the strongest diffuse component is at least 7 dB (electrical) lower than the weakest LOS component [105]. For these reasons, only the LOS link is considered in the theoretical analysis. For completeness, simulation results based on a complete VLC channel considering the wideband nature of VLC and shadowing effects are also presented.

Without loss of generality, assume that users are ordered based on their channel qualities: $h_1 \leq \cdots \leq h_k \leq \cdots \leq h_K$, where h_k denotes the direct current (DC) channel gain of the LOS link

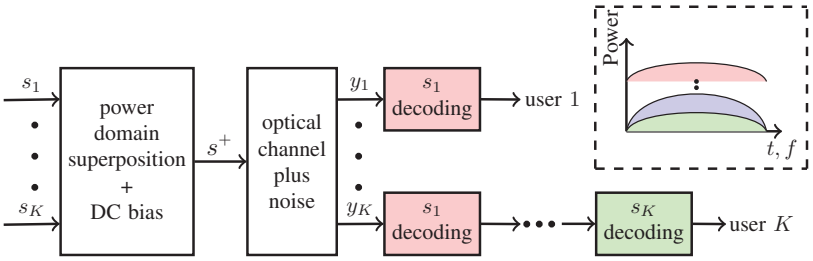

Figure 5.1: *Illustration of NOMA principle.*

for the k-th user. The principle of NOMA is illustrated in Figure 5.1, where the bipolar message signals for different users are superposed in the power domain. To obtain a unipolar signal, a DC bias is added before signal transmission. Assume the electrical-to-optical conversion factor is unity. After going through the optical channel and with the addition of noise, SIC is carried out at the receiver side before information decoding. According to this principle, the superposed signal to be transmitted at the LED is given by:

$$s^+ = \sum_{i=1}^{K} a_i \sqrt{P_{\text{tx}}} s_i + I_{\text{DC}}, \tag{5.1}$$

where P_{tx} represents the electrical signal power of the LED; I_{DC} is the DC bias added to the LED to ensure the positive instantaneous intensity; s_i is the modulated message signal intended for the i-th user; and a_i represents the power allocation coefficient for the i-th user. The message signal for each user is assumed to be zero mean with unity variance. Due to the total power constraint, power allocation coefficients should satisfy:

$$\sum_{i=1}^{K} a_i^2 = 1. \tag{5.2}$$

In NOMA, users with poorer channel qualities are allocated more signal power. This implies that $a_1 \geq \cdots a_k \geq \cdots \geq a_K$. After removing the DC term, the received signal at the k-th user is given by:

$$y_k = \sqrt{P_{\text{tx}}} h_k \left(\underbrace{\sum_{j=1}^{k-1} a_j s_j}_{\text{SIC}} + \underbrace{a_k s_k}_{\text{signal}} + \underbrace{\sum_{i=k+1}^{K} a_i s_i}_{\text{interference}} \right) + z_k, \tag{5.3}$$

where z_k denotes the real-valued Gaussian noise with zero mean and variance σ_{n}^2. SIC is carried out at the k-th user to remove the message signal for the other users with poorer channel con-

ditions (the "SIC" term in (5.3)). The messages for users with higher channel gains are treated as noise (the "interference" term in (5.3)). Assuming unity optical-to-electrical conversion, the achievable data rate per bandwidth[1] for the k-th user is given by:

$$R_k = \begin{cases} \frac{1}{2}\log_2\left(1+\frac{(h_k a_k)^2}{\sum\limits_{i=k+1}^{K}(h_k a_i)^2+\frac{1}{\rho}}\right), & k=1,\cdots,K-1 \\ \frac{1}{2}\log_2\left(1+\rho(h_k a_k)^2\right), & k=K \end{cases}, \tag{5.4}$$

in unit of bit per channel use (bpcu), where $\rho = P_{\text{tx}}/\sigma_{\text{n}}^2$ represents the transmit signal-to-noise ratio (SNR) and the scaling factor $1/2$ is due to the Hermitian symmetry. Note that (5.4) is conditioned on the event that the k-th user can successfully decode the message for the j-th user ($\forall j \leq k$). Denote $R_{k\to j}$ as the rate for the k-th user to detect the message intended for the j-th user and $\tilde{R}_j$ as the target data rate for successful message detection at the j-th user. The above condition can be expressed as:

$$R_{k\to j} = \begin{cases} \frac{1}{2}\log_2\left(1+\frac{(h_k a_j)^2}{\sum\limits_{i=j+1}^{K}(h_k a_i)^2+\frac{1}{\rho}}\right) \geq \tilde{R}_j, & j\leq k, j\neq K \\ \frac{1}{2}\log_2\left(1+\rho(h_k a_j)^2\right) \geq \tilde{R}_j, & j=k=K \end{cases}. \tag{5.5}$$

If (5.5) is satisfied, it is assumed that perfect SIC can be performed in the decoding chain without error propagations.

5.3 Performance Evaluation

In this section, analytical results for the performance analysis of NOMA are presented, which lay the foundation for studying the impact of user pairing in the next section.

According to (3.4), the channel gain for the k-th user is $h_k = \alpha\left(r_k^2+L^2\right)^{-(m+3)/2}$. Define a function $h = u(r) = \alpha(r^2+L^2)^{-(m+3)/2}$. It is evident that h is a monotonically decreasing function with respect to r. Therefore, the probability density function (PDF) of the unordered

[1]For brevity, this is called data rate in the remaining part of this chapter.

channel gain can be calculated using the "change of variable" method:

$$f_{h_k}(h) = \left| \frac{\partial}{\partial h} u^{-1}(h) \right| \cdot f_{r_k}\left(u^{-1}(h)\right), \tag{5.6}$$

where u^{-1} denotes the inverse function of u and $f_{r_k}(r) = 2r/r_{\mathrm{e}}^2$ is the PDF of variable r_k following the uniform distribution. Consequently, the PDF of the unordered variable h_k^2 can be obtained as:

$$f_{h_k^2}(t) = \frac{1}{r_{\mathrm{e}}^2} \frac{1}{m+3} \alpha^{\frac{2}{m+3}} t^{-\frac{1}{m+3}-1}, \tag{5.7}$$

for $t \in [\kappa_{\min}, \kappa_{\max}]$, where $\kappa_{\min}$ and $\kappa_{\max}$ are given as $\kappa_{\min} = \alpha^2/(r_{\mathrm{e}}^2 + L^2)^{m+3}$ and $\kappa_{\max} = \alpha^2/L^{2(m+3)}$. Integrating (5.7) over $[\kappa_{\min}, \kappa_{\max}]$, the cumulative distribution function (CDF) of the unordered variable h_k^2 can therefore be obtained as:

$$F_{h_k^2}(t) = -\frac{1}{r_{\mathrm{e}}^2} \alpha^{\frac{2}{m+3}} t^{-\frac{1}{m+3}} + \frac{L^2}{r_{\mathrm{e}}^2} + 1. \tag{5.8}$$

Using order statistics [149], the PDF of the ordered variable h_k^2, denoted by $f'_{h_k^2}(t)$, can be readily obtained as:

$$\begin{aligned} f'_{h_k^2}(t) &= \frac{K!}{(k-1)!\,(K-k)!} F_{h_k^2}(t)^{k-1} \left(1 - F_{h_k^2}(t)\right)^{K-k} f_{h_k^2}(t) \\ &= \frac{\Omega}{m+3} \frac{K!}{(k-1)!\,(K-k)!} \left(-\Omega t^{-\frac{1}{m+3}} + \frac{L^2}{r_{\mathrm{e}}^2} + 1\right)^{k-1} \left(\Omega t^{-\frac{1}{m+3}} - \frac{L^2}{r_{\mathrm{e}}^2}\right)^{K-k} t^{-\frac{1}{m+3}-1}, \end{aligned} \tag{5.9}$$

where $\Omega = \alpha^{2/(m+3)}/r_{\mathrm{e}}^2$. Note that (5.9) is obtained assuming that the total number of users is fixed and known. If K is unknown but follows a certain point process, for example, the Poisson point process (PPP), (5.9) becomes a conditional PDF on K. The final result should be obtained by further averaging the conditional PDF with respect to all possible realizations of K. For non-uniform user distributions, the results can be obtained in a similar way by plugging the specific distribution function into (5.6).

5.3.1 Case I: Guaranteed Quality of Service

Consider the case that each user has a target data rate, which is determined by its quality of service (QoS) requirement. In this case, user outage probability is an important metric. Service satisfaction at the k-th user requires successful detection of messages not only for this user itself

but also for other users with poorer channel conditions. If this constraint is met, the sum rate of the system is simply $\sum_{k=1}^{K} \tilde{R}_k$. Therefore, the sum rate is not of interest in this case. Instead, the analysis is focused on the outage probability at each user, which is defined as the probability that the achievable rate is below the QoS target. Based on (5.5), the outage probability at the k-th user can be expressed as:

$$\begin{aligned} \mathrm{P}_k^{\mathrm{out}} =& 1 - \mathbb{P}\left[R_{k\to j} \geq \tilde{R}_j,\ \forall j \leq k\right] \\ =& 1 - \mathbb{P}\left[h_k^2 \geq \varepsilon_j,\ \forall j \leq k\right], \end{aligned} \tag{5.10}$$

where the threshold ε_j is given by:

$$\varepsilon_j = \begin{cases} \frac{\beta_j}{\rho\left(a_j^2 - \beta_j \sum\limits_{i=j+1}^{K} a_i^2\right)}, & j \neq K \\ \frac{\beta_j}{\rho a_K^2}, & j = K \end{cases}, \tag{5.11}$$

in which $\beta_j = 2^{\tilde{R}_j} - 1$ denotes the required signal-to-interference-plus-noise ratio (SINR) at the j-th user for successful message detection. Note that (5.10) is obtained based on the following condition:

$$a_j^2 > \beta_j \sum_{i=j+1}^{K} a_i^2. \tag{5.12}$$

If power allocation coefficients do not satisfy (5.12), the user outage probability would always be one. Define a new threshold $\varepsilon_k^* = \min\{\max\{\varepsilon_1, \cdots, \varepsilon_k, \kappa_{\min}\}, \kappa_{\max}\}$. Using order statistics[149], the outage probability of the k-th user can be obtained as:

$$\begin{aligned} \mathrm{P}_k^{\mathrm{out}} =& 1 - \mathbb{P}\left[h_k^2 \geq \varepsilon_k^*\right] \\ =& \sum_{i=k}^{K} \frac{K!}{i!\,(K-i)!} F_{h_k^2}(\varepsilon_k^*)^i \left(1 - F_{h_k^2}(\varepsilon_k^*)\right)^{K-i}. \end{aligned} \tag{5.13}$$

System coverage probability is defined as the probability that all of the users in the system can achieve reliable detection, which is given by:

$$\mathrm{P}^{\mathrm{cov}} = \prod_{k=1}^{K} (1 - \mathrm{P}_k^{\mathrm{out}}), \tag{5.14}$$

assuming that the outage event at each user is independent.

5.3.2 Case II: Opportunistic Best-Effort Service

Consider the case where data rates for different users are opportunistically allocated based on their channel conditions, *i.e.,* $\tilde{R}_j = R_j$. In this scenario, it can be readily verified that the condition in (5.5) always holds and all of the users can be served with zero outage probability but with different data rates. The following theorem gives a closed-form expression for the achievable sum rate.

Theorem 1 *For arbitrary power allocation strategies, the ergodic sum rate of NOMA with uniformly distributed users is given by:*

$$\begin{aligned} R^{\mathrm{NOMA}} =& \frac{\Omega}{m+3} \sum_{k=1}^{K-1} \sum_{p=0}^{k-1} \sum_{q=0}^{K-k} \left\{ \frac{K!}{p!\,(k-1-p)!\,q!\,(K-k-q)!} \left(\frac{L^2}{r_{\mathrm{e}}^2}+1\right)^{k-1-p} \right. \\ & \left. \times \left(\frac{L^2}{r_{\mathrm{e}}^2}\right)^{K-k-q} (-1)^{p+K-k-q} \Omega^{p+q} \left(\varpi_1(\kappa_{\max}) - \varpi_1(\kappa_{\min})\right) \right\} + \frac{\Omega}{m+3} \\ & \times \sum_{l=0}^{K-1} \left(\frac{K!}{l!\,(K-1-l)!} \left(\frac{L^2}{r_{\mathrm{e}}^2}+1\right)^{K-1-l} (-\Omega)^l \left(\varpi_2(\kappa_{\max}) - \varpi_2(\kappa_{\min})\right) \right), \end{aligned} \tag{5.15}$$

where $\varpi_1(\kappa)$ *is defined as:*

$$\begin{aligned} \varpi_1(\kappa) =& \frac{\kappa^{-\frac{p+q+1}{m+3}}}{2\left(\frac{p+q+1}{m+3}\right)^2 \ln(2)} \left\{ -\frac{p+q+1}{m+3} \ln\left(1 + \frac{(\tau_k - \tau_{k+1})\kappa}{\tau_{k+1}\kappa + \frac{1}{\rho}}\right) \right. \\ & - {}_2F_1\left(1, -\frac{p+q+1}{m+3}; -\frac{p+q+1}{m+3}+1; -\rho\tau_{k+1}\kappa\right) \\ & \left. + {}_2F_1\left(1, -\frac{p+q+1}{m+3}; -\frac{p+q+1}{m+3}+1; -\rho\tau_k\kappa\right) \right\}, \end{aligned} \tag{5.16}$$

in which $\tau_k = \sum_{i=k}^{K} a_i^2$, $\tau_{k+1} = \sum_{i=k+1}^{K} a_i^2$ *and* ${}_2F_1(\cdot,\cdot;\cdot;\cdot)$ *denotes the Gauss hypergeometric function. In* (5.15), $\varpi_2(\kappa)$ *is defined as:*

$$\begin{aligned} \varpi_2(\kappa) =& \frac{\kappa^{-\frac{l+1}{m+3}}}{2\left(\frac{l+1}{m+3}\right)^2 \ln(2)} \left\{ -1 - \frac{l+1}{m+3} \ln\left(1 + \rho a_K^2 \kappa\right) \right. \\ & \left. + {}_2F_1\left(1, -\frac{l+1}{m+3}; -\frac{l+1}{m+3}+1; -\rho a_K^2\kappa\right) \right\}. \end{aligned} \tag{5.17}$$

The proof of Theorem 1 can be found in Appendix A. Theorem 1 demonstrates that unlike OMA, the capacity of NOMA can be enhanced with an increase in the total number of users in the system. However, this performance gain is achieved at the cost of increased computation complexity caused by the SIC process at the receivers. The ergodic sum rate of an OFDMA-based system is stated in the following corollary.

Corollary 1 *The ergodic sum rate of an OFDMA-based attocell with uniformly deployed users is:*

$$R^{\mathrm{OFDMA}} = \frac{\Omega}{m+3} \sum_{k=1}^{K} \sum_{p=0}^{k-1} \sum_{q=0}^{K-k} \left\{ \frac{K!\, b_k}{p!\,(k-1-p)!\,q!\,(K-k-q)!} \times \left(\frac{L^2}{r_{\mathrm{e}}^2}+1\right)^{k-1-p} \times \left(\frac{L^2}{r_{\mathrm{e}}^2}\right)^{K-k-q} (-1)^{p+K-k-q} \Omega^{p+q} \left(\varpi_3(\kappa_{\max}) - \varpi_3(\kappa_{\min})\right) \right\}, \tag{5.18}$$

where $\varpi_3(\kappa)$ is defined as:

$$\varpi_3(\kappa) = \frac{\kappa^{-\frac{p+q+1}{m+3}}}{2\left(\frac{p+q+1}{m+3}\right)^2 \ln(2)} \left\{ -1 - \frac{p+q+1}{m+3} \ln\left(1+\frac{\upsilon_k}{b_k}\rho\kappa\right) + {}_2F_1\left(1, -\frac{p+q+1}{m+3}; -\frac{p+q+1}{m+3}+1; -\frac{\upsilon_k}{b_k}\rho\kappa\right) \right\}, \tag{5.19}$$

where b_k is the fraction of bandwidth occupied by the k-th user and υ_k is the fraction of the power allocated to the k-th user.

The total bandwidth constraint requires that $\sum_{k=1}^{K} b_k = 1$ while the total power constraint requires that $\sum_{k=1}^{K} \upsilon_k = 1$. The derivation of Corollary 1 can follow similar steps as the derivation of R^{NOMA} shown in Appendix A. Combining Theorem 1 and Corollary 1, the ergodic sum rate gain of NOMA over OFDMA can be obtained.

5.4 Impact of User Pairing

Selecting a subset of users to perform NOMA can effectively reduce the computation complexity of the system. This results in a hybrid MA scheme which consists of a combination of NOMA and OMA techniques. As the performance of such a hybrid system is highly dependent on the user selection strategy, this section studies the effect of user pairing on the system

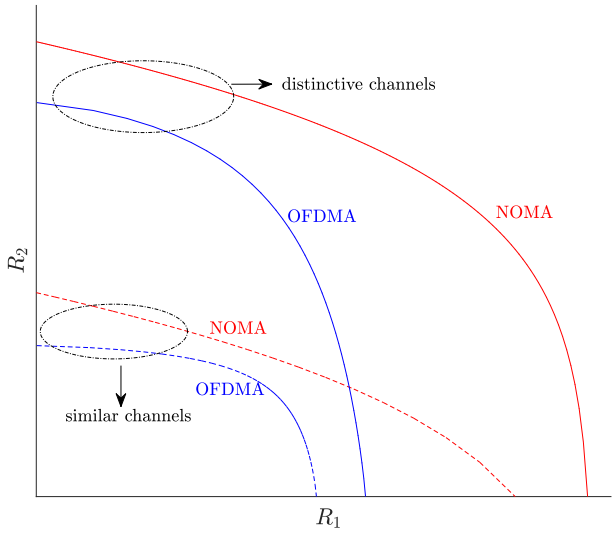

Figure 5.2: *Compare capacity regions between NOMA and OFDMA ($\upsilon_1 = \upsilon_2$) in a two-user scenario.*

performance. In order to obtain simple but insightful results, the entity of users is divided into groups and each group consists of two users. However, it can be readily extended to the case where an arbitrary number of users are selected and paired to perform NOMA. From a qualitative point of view, the capacity region for NOMA and OFDMA in a two-user scenario is illustrated in Figure 5.2. The results of NOMA are plotted by varying the power multiplexing coefficients while the results of OFDMA are obtained by varying the bandwidth coefficients. It can be seen that a higher performance gain can be obtained if two users with more distinctive channel conditions are paired to perform NOMA. This finding will be quantitatively validated in the following.

Assume that the i-th user and the j-th user ($i \leq j$) in the system are selected to perform NOMA so that $a_i^2 + a_j^2 = 1$. According to OFDMA, each user is allocated a fraction of the orthogonal subcarriers. Therefore the achieved data rate for each user is $\bar{R}_k = \frac{1}{2} b_k \log_2 \left(1 + \frac{\upsilon_k}{b_k} \rho h_k^2\right)$, where $k = \{i, j\}$.

5.4.1 Impact of User Pairing on Individual Rates

In this subsection, the impact of user pairing on individual data rates is studied. For arbitrary power allocation strategies, the probability that both users can achieve higher individual rates in NOMA than in OFDMA is given by the following theorem.

Theorem 2 *Assume that the i-th and the j-th user ($i < j$) are paired together to perform NOMA. A necessary condition for NOMA to achieve higher individual rates than OFDMA ($b_i = b_j, \upsilon_i = \upsilon_j$) is $a_{\mathrm{th1}} < a_j < a_{\mathrm{th2}}$, where*

$$a_{\mathrm{th1}} = \sqrt{\frac{-1+\sqrt{1+\rho\kappa_{\max}}}{\rho\kappa_{\max}}}, \tag{5.20}$$

$$a_{\mathrm{th2}} = \sqrt{\frac{-1+\sqrt{1+\rho\kappa_{\min}}}{\rho\kappa_{\min}}}. \tag{5.21}$$

If the above condition is met, the probability that NOMA can achieve higher individual rates than OFDMA is:

$$\begin{aligned}
&\mathbb{P}\left[R_i > \bar{R}_i, R_j > \bar{R}_j\right] \\
&= \sum_{l=0}^{K-j}\sum_{p=0}^{i-1}\sum_{q=0}^{j-1-i}\left\{\frac{(-1)^{K-i-l+p-q+1}\Omega^{j+l+p}}{(j-i+l-q)(p+q+1)}\frac{K!}{l!\,(K-j-l)!\,p!\,(i-1-p)!\,q!\,(j-1-i-q)!}\right. \\
&\left.\times\left(\frac{L^2}{r_{\mathrm{e}}^2}+1\right)^{i-1-p}\left(\frac{L^2}{r_{\mathrm{e}}^2}\right)^{K-j-l}\left(\varsigma^{\star-\frac{p+q+1}{m+3}}-\kappa_{\min}{}^{-\frac{p+q+1}{m+3}}\right)\left(\kappa_{\max}{}^{-\frac{j-i+l-q}{m+3}}-\varsigma^{\star-\frac{j-i+l-q}{m+3}}\right)\right\},
\end{aligned} \tag{5.22}$$

where $\varsigma^\star = \min\{\max\{\varsigma, \kappa_{\min}\}, \kappa_{\max}\}$ and $\varsigma = (1-2a_j^2)/\rho a_j^4$.

The proof of Theorem 2 can be found in Appendix B. Theorem 2 demonstrates that given the appropriate power allocation coefficients, NOMA is nearly certain to outperform OFDMA if two users with distinct channel qualities are paired together.

5.4.2 Impact of User Pairing on the Sum Rate

In this subsection, the impact of user pairing on the ergodic sum rate is studied. The following theorem states that the ergodic sum rate gain of NOMA over OFDMA is upper-bounded in high SNR regimes. Also, this upper-bound remains unchanged for different power allocation strategies.

Theorem 3 *Assuming that the i-th user and the j-th user ($i < j$) are paired to perform NOMA ($a_i^2 + a_j^2 = 1$), as ρ increases, the sum rate gain of NOMA over OFDMA first decreases then*

increases until it is upper-bounded in high SNR regimes. This upper bound is given by:

$$\begin{aligned}
&\mathbb{E}\left[R_i + R_j - \bar{R}_i - \bar{R}_j\right] \leq \frac{1}{2}\left(b_i \log_2\left(\frac{b_i}{\upsilon_i}\right) + b_j \log_2\left(\frac{b_j}{\upsilon_j}\right)\right) \\
&+ \frac{1-b_j}{2\ln(2)} \sum_{p=0}^{j-1} \sum_{q=0}^{K-j} \left\{ \frac{K!(-1)^{p+K-j-q}\Omega^{p+q+1}}{p!\,(j-1-p)!\,q!\,(K-j-q)!} \left(\frac{L^2}{r_{\mathrm{e}}^2}+1\right)^{j-1-p} \left(\frac{L^2}{r_{\mathrm{e}}^2}\right)^{K-j-q} \right. \\
&\left. \times \left(\varpi_4(\kappa_{\max}) - \varpi_4(\kappa_{\min})\right) \right\} \\
&- \frac{b_i}{2\ln(2)} \sum_{p=0}^{i-1} \sum_{q=0}^{K-i} \left\{ \frac{K!(-1)^{p+K-i-q}\Omega^{p+q+1}}{p!\,(i-1-p)!\,q!\,(K-i-q)!} \left(\frac{L^2}{r_{\mathrm{e}}^2}+1\right)^{i-1-p} \left(\frac{L^2}{r_{\mathrm{e}}^2}\right)^{K-i-q} \right. \\
&\left. \times \left(\varpi_4(\kappa_{\max}) - \varpi_4(\kappa_{\min})\right) \right\}. \qquad (5.23)
\end{aligned}$$

where

$$\varpi_4(\kappa) = -\frac{\kappa^{-\frac{p+q+1}{m+3}}\left(m+3+(p+q+1)\ln(\kappa)\right)}{(p+q+1)^2}. \qquad (5.24)$$

The proof can be found in Appendix C. Theorem 3 gives the upper bound of the ergodic sum rate gain of NOMA over OFDMA for arbitrary i and j ($i < j$). However, it is of more interest to evaluate how the performance gain varies against i and j. The following corollary states that the optimum sum rate gain is achieved if two users with the most distinctive channel conditions are paired together to perform NOMA.

Corollary 2 *If the i-th user and the j-th user ($i < j$) are paired to perform NOMA, the sum rate gain of NOMA over OFDMA achieves the maximum by pairing the two users with the most distinctive channel conditions, i.e., $i = 1$ and $j = K$. In high SNR regimes, this maximum gain is upper-bounded by:*

$$\begin{aligned}
&\mathbb{E}\left[R_1 + R_K - \bar{R}_1 - \bar{R}_K\right] \\
\leq &\frac{1}{2}\left(b_1 \log_2\left(\frac{b_1}{\upsilon_1}\right) + b_K \log_2\left(\frac{b_K}{\upsilon_K}\right)\right) + \frac{1}{4\ln(2)} \sum_{l=0}^{K-1} \left\{ \frac{K!}{l!\,(K-1-l)!}\Omega^{l+1} \right. \\
&\left. \times \left(\varpi_5(\kappa_{\max}) - \varpi_5(\kappa_{\min})\right) \left((-1)^l \left(\frac{L^2}{r_{\mathrm{e}}^2}+1\right)^{K-1-l} - (-1)^{K-1-l} \left(\frac{L^2}{r_{\mathrm{e}}^2}\right)^{K-1-l} \right) \right\}, \qquad (5.25)
\end{aligned}$$

Parameter name, notation	value
Vertical distance of the link, L	2.15 m
Cell radius, r_{e}	3.6 m
Total number of users, K	10
LED semiangle, $\Psi_{1/2}$	60°
Transmit signal power, P_{tx}	0.25 W
Receiver FOV, Ψ_{FOV}	60°
Effective receiver responsivity, η	0.4 A/W
PD detection area, A_{PD}	1 cm^2
Reflective index, n_{c}	1.5
Optical filter gain, G_{f}	1
Signal bandwidth, B	20 MHz
Noise PSD	10^{-21} A^2/Hz

Table 5.1: *NOMA: simulation setup and parameters.*

where

$$\varpi_5(\kappa) = -\frac{\kappa^{-\frac{l+1}{m+3}}\left(m+3+(l+1)\ln(\kappa)\right)}{(l+1)^2}. \tag{5.26}$$

The proof is provided in Appendix D.

5.5 Simulation Results

The aim of this section is to substantiate the derived analytical results with Monte Carlo simulations and investigate the system performance against various parameters. If not otherwise specified, the parameters used for the simulation setup are summarized in Table 5.1.

Successfully implementation of NOMA requires users to have distinctive channel conditions. The probability mass function (PMF) of the electrical channel gain of a random user uniformly distributed inside the cell is shown in Figure 5.3. Results show that the channel of a cell-center user can be five times larger than that of a cell-edge user, assuming the same receiver configuration[2]. In practice, users may hold their receiving devices with random orientations. In these scenarios, their channel differences can be further enlarged, which permit the use of NOMA to bring additional performance gains.

[2]Note that RF users may have more distinctive channel conditions due to multipath fading, which is absent in VLC channels.

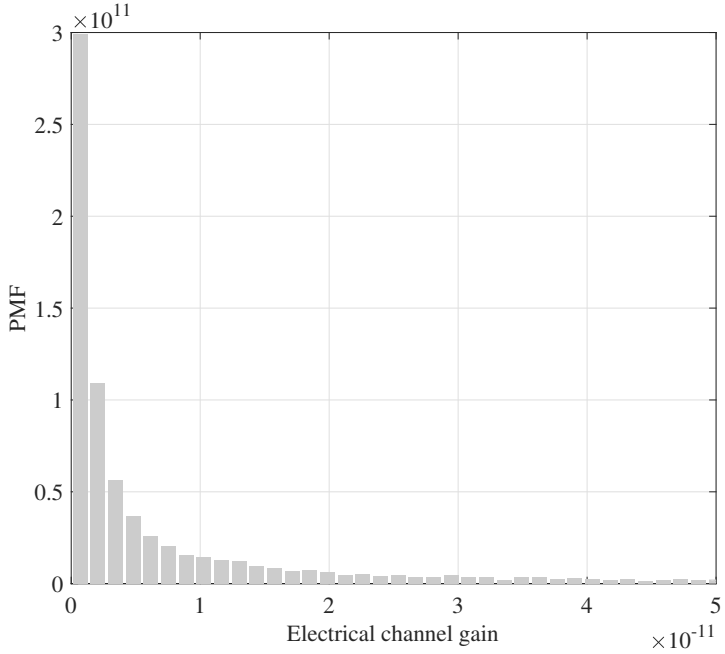

Figure 5.3: *PMF of the (electrical) channel gain.*

5.5.1 Analytical Framework

Figure 5.4 shows the system coverage probability for different power allocation coefficients in a two-user scenario. Along the following discussions on the two-user scenario, the user closer to the LED is referred to as the *near* user and the user further away from the LED is referred to as the *far* user. It can be seen that the analytical results are consistent with the simulation results, and an optimum set of power allocation coefficients for achieving the maximum coverage probability exists. For a low target data rate, the system coverage probability is nearly 100%, given that the power allocation coefficients are optimally chosen. As the target data rate increases, the achievable maximum coverage probability decreases. Also, it can be seen that a larger coverage probability can be achieved by pairing two users with more distinctive channel conditions. An interesting finding is that when the target data rate for both users increases, more signal power should be allocated to the *far* user in order to achieve the optimal coverage probability.

An exhaustive search (ES) method is used to find the optimum power allocation coefficients. Specifically, a lookup table is formed, in which the system coverage probability is saved for each systematic search of the power coefficients. After this, the optimum pair of power coefficients is found by referring to the lookup table and selecting the one that gives the highest

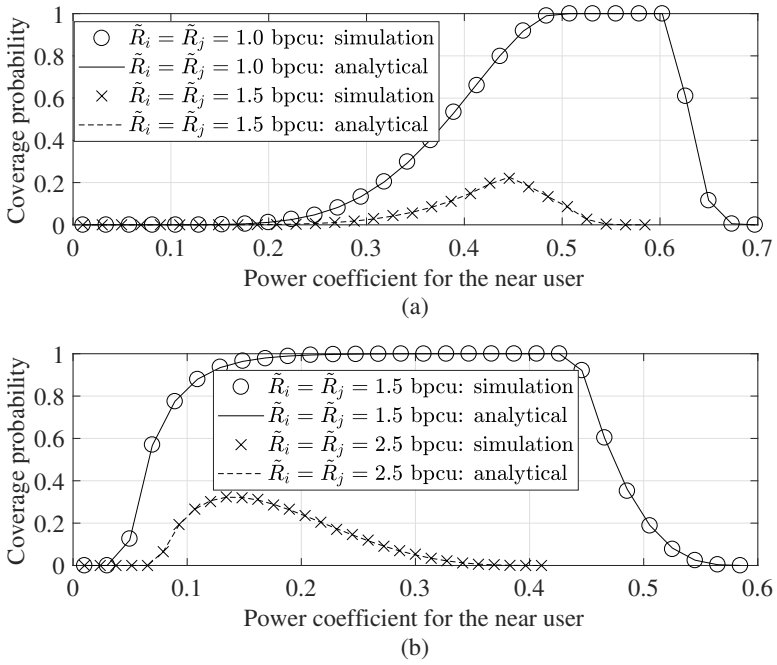

Figure 5.4: *System coverage probability for different power allocation coefficients: (a)* $i = 1$ *and* $j = 2$ *(similar channels); (b)* $i = 1$ *and* $j = 10$ *(distinctive channels).*

coverage probability. Figure 5.5 shows the maximum achievable coverage probability as a function of the target data rate. As expected, the maximum coverage probability decreases as the target data rate increases. Compared with OFDMA, NOMA is shown to be able to provide a higher coverage probability, and this performance gain can be further enlarged by pairing two users with more distinctive channel conditions. For example, when $i = 1$ and $j = 10$, NOMA can provide 2.2 bpcu data rate for both users with 90% coverage probability while OFDMA can only provide 0.7 bpcu data rate for both users with the same coverage probability.

In Figure 5.6, the probability that NOMA achieves higher individual rates than OFDMA is evaluated. It can be seen that the developed analytical results match closely with computer simulations. For a fixed number of users, it is shown that pairing users with more distinctive channel conditions can achieve higher data rates. Such performance gain is supported by the SIC process, which greatly improves the SINR by canceling out a portion of interference. Figure 5.6 also shows that NOMA is more beneficial when implemented in dense networks, where efficient user selection and pairing algorithms can bring additional performance gains. To enlarge the channel difference among users, angle diversity (AD) and wavelength division multiplexing are possible solutions.

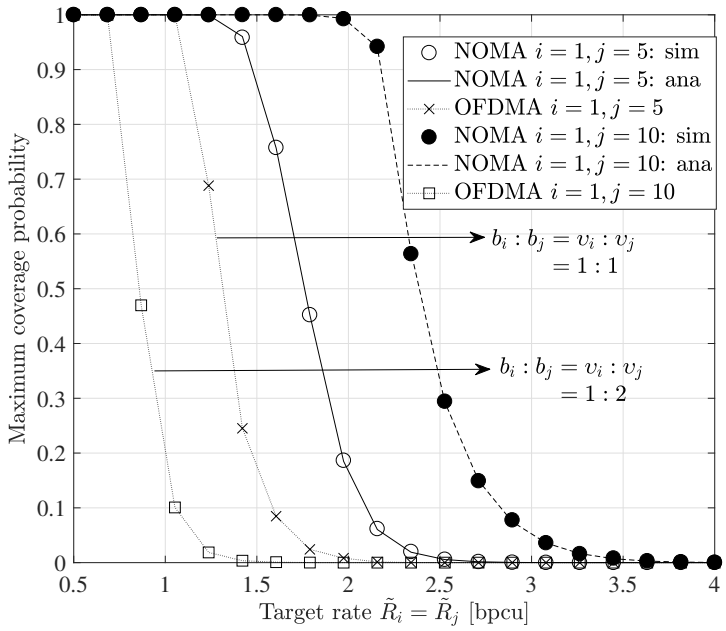

Figure 5.5: *System maximum coverage probability for different target data rates.*

In Figure 5.7, the ergodic sum rate gain of NOMA over OFDMA is shown as a function of the transmit SNR. Note that fixed resource allocation schemes are assumed for both NOMA and OFDMA. Although the network performance can be improved further with more efficient resource allocation algorithms, they are not the focus in this thesis. It can be seen that the derived theoretical bound shows good consistency with simulation results. Also, Figure 5.7 demonstrates that, as the transmit SNR ρ increases, the sum rate gain of NOMA over OFDMA first decreases until reaching a minimum. As ρ continues to increase, the sum rate gain increases until it reaches the upper bound. This trend is consistent with Theorem 3. Also, it can be concluded that the performance gain of NOMA over OFDMA is enlarged at high transmit SNR values.

5.5.2 Multipath Reflections and Shadowing Effect

One of the advantages of VLC is that when the LOS is blocked by opaque objects, signal transmission is still possible via the diffuse links but with a lower data rate. The performance evaluation presented in Section 5.3 is based on the LOS link because the LOS link is the dominant part of VLC channels, and it is mathematically intractable to include diffuse links in the channel model. To evaluate the performance of NOMA inside a VLC network with multipath reflections and shadowing, simulation-based results are provided in the following. Denote the

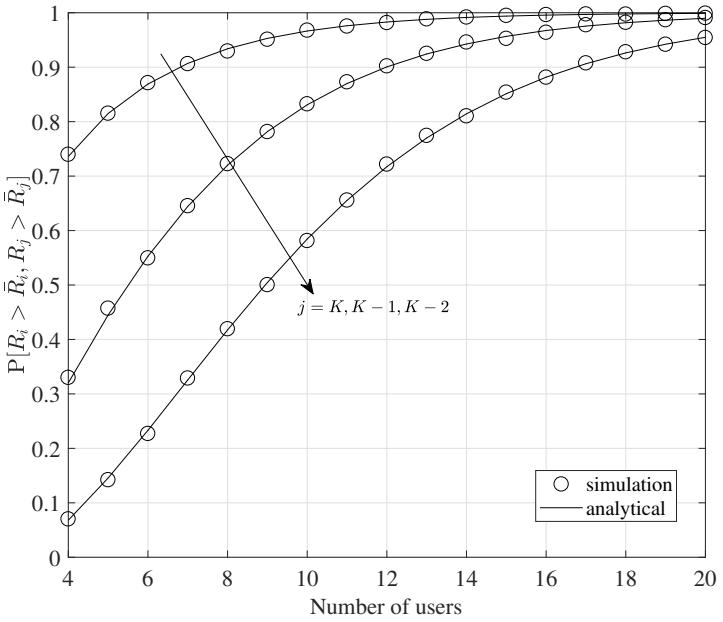

Figure 5.6: *Probability of NOMA achieving higher individual data rates than OFDMA ($i = 1$, $a_i^2 = 9/10$ and $a_j^2 = 1/10$).*

LOS blockage event as X, whose probability mass function can be modeled by the Bernoulli distribution, given by:

$$\Pr[X = \chi] = \begin{cases} p, & \chi = 1 \\ 1 - p, & \chi = 0 \end{cases}, \tag{5.27}$$

where p is the probability that the LOS is blocked. When $\chi = 0$, the VLC channel consists both the LOS and diffuse components, with the dominant part being the LOS link. When $\chi = 1$, the LOS link is blocked with probability p. In this case, signals are transmitted via the diffuse links.

Different from narrowband infrared (IR) wireless communication, VLC uses a wide spectrum, which ranges from 380 nm to 780 nm. This means that the wavelength-dependent power spectral density of LEDs and the reflectance of indoor reflectors should be considered when modeling the VLC channel. Detailed analysis on this topic can be found in Chapter 2. It has been reported that the received signal power from multipath reflections and the root-mean-square (RMS) delay spread in VLC are generally smaller than those in IR systems [6]. In the following, the performance of NOMA is studied in a more realistic scenario where multipath reflections and LOS blockage are considered. Specifically, a room of size $5 \times 5 \times 3$ m^3 is considered. The LED is located at the center of the ceiling while receivers are randomly distributed

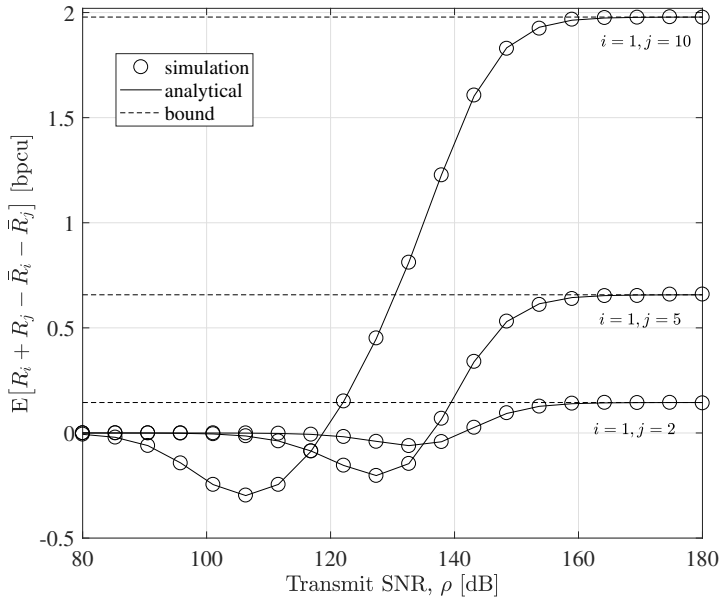

Figure 5.7: *Ergodic sum rate gain of NOMA over OFDMA ($b_i : b_j = \upsilon_i : \upsilon_j = 1 : 2$).*

in the room. Monte Carlo simulations are carried out and the system performance is evaluated over $1,000$ independent trials. The channel impulse response is simulated using the recursive algorithm reported in [6], as given in (2.10). It can be seen from Figure 5.8 that the performance of NOMA in a VLC system degrades when the LOS blockage probability increases. However, due to the existence of multipath reflections in indoor VLC, signal transmission is still possible even if the LOS link is totally blocked. For example, in a VLC network occupied by 10 users, a sum rate of 4.3 bpcu can be achieved when the LOS link is unblocked. If the VLC links are subject to human blockages with a probability of 50%, the average sum rate drops by 1 bpcu. In the worst-case scenario where the LOS links are completely blocked, signal transmissions are still possible via multipath reflections but a low data rate is provided.

5.6 Summary

In this chapter, a theoretical framework for analyzing the performance of NOMA in an attocell downlink has been presented. Different from Chapter 3 and Chapter 4, which mainly deal with the ICI, this chapter is focused on intra-cell interference mitigation using NOMA. Since the results presented in this chapter do not rely on any particular network geometry, they can be applied to either traditional deterministic network models or stochastic models such as the PPP. In a single attocell deployment, the performance of NOMA has been analytically evaluated

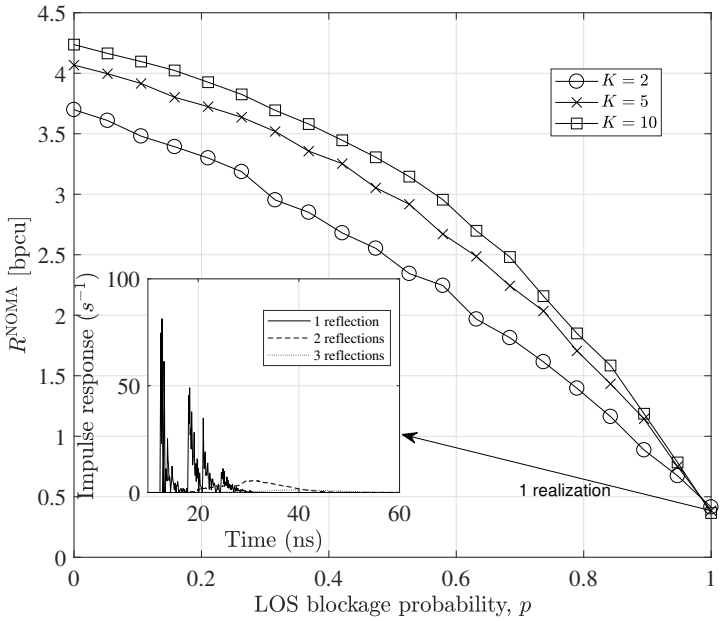

Figure 5.8: *Ergodic sum rate of NOMA with LOS blockage and shadowing.*

and compared with the traditional OMA technique. For the guaranteed QoS provision, closed-form expressions for the system coverage probability are derived. To provide the opportunistic best-effort service to users with different channel qualities, the ergodic sum rate expression are derived. Results show that, compared with OMA, NOMA can offer a high performance gain by utilizing power-domain multiplexing, and this performance gain can be further enlarged by pairing users with more distinctive channel conditions.

Although the theoretical framework is built upon the LOS link, simulation results taking into account multipath reflections and shadowing effects are also presented. Both analytical and simulation results have demonstrated that NOMA can serve as an efficient intra-cell interference mitigation technique for future attocell networks. With the presence of multiple APs and hence potential ICI, merging NOMA with ICI-mitigation techniques are worth investigating further.

Chapter 6
Physical-Layer Security in the Multiuser Environment

In a wired network, transmitting and receiving devices are connected via dedicated cables. Therefore, receivers that are not physically connected are unable to access the network. In contrast, in optical attocell networks utilizing visible light communication (VLC), the broadcast nature of visible light enables simultaneous wireless data to be delivered to multiple users. Despite the fact that wireless communications have removed the physical constraints on user connectivity, allowing users to be mobile, the broadcast environment inevitably makes wireless communications vulnerable to malicious eavesdropping and information interception. Following previous chapters that deal with data coverage, this chapter investigates security vulnerabilities of attocell networks that are imposed by unauthorized eavesdroppers.

6.1 Introduction

Despite their differences, both wired and wireless networks share the same Open Systems Interconnect (OSI) model, which characterizes and standardizes communication functionalities of a typical telecommunication system. The OSI model describes seven layers of interaction of an information system, containing fundamental function areas that are generally required for data transfer between nodes in a distributed environment. From top to bottom, it includes the application layer, the presentation layer, the session layer, the transport layer, the network layer, the data link layer and the physical layer [150]. The description of each OSI layer can be found in Table 6.1. Looking down from the top-level application perspective, data is created and communicated down the stack layer by layer. When the original data traverses through each layer, additional information such as the layer-added content is also included until the represented data reaches the bottom physical layer. At that point, a physical medium such as radio or visible light is used to send out the data. Within the OSI model, every layer has its own security characteristics and vulnerabilities [151]. However, by reviewing the flow of information through the model, it can be seen that all the six layers above are dependent on the

OSI layer	Protocol data unit (PDU)	Layer description	Security control methods
Application (7)	Data	User applications, *e.g.,* web browser and Telnet	Application monitoring
Presentation (6)	Data	Data conversion and translation	Separation of user input and program control functions
Session (5)	Data	Session establishment, sync and termination (log on/off)	Password encryption
Transport (4)	Segment	Flow control to ensure error-free transmission between layers 1-3	Strict firewall rules
Network (3)	Packet	Routing and switching information between networks	Broadcast monitoring and route policy control
Data link (2)	Frame	Data frame establishment and defining rules for medium access	Medium access control (MAC) address filtering
Physical (1)	Bit	Transmission medium, *e.g.,* radio and visible light	Video/audio surveillance and biometric authentication

Table 6.1: *OSI Layers and the corresponding security control methods*

physical layer to deliver the information between nodes. As a result, the physical-layer security is critical for all information security assets, which is the focus of this chapter.

The physical layer is responsible for the actual encoding and transmission of data. The definition of physical-layer security can be widened to include all physical items such as the communication media, transmitting and receiving devices, information feed and power cables. Among them, hardware devices can be securely stored, but wireless communication media is prone to security breaches due to its broadcast nature. In theory, as long as the an eavesdropper is within the coverage area of the access point (AP), the transmitted data can be overheard.

From an information-theoretic point of view, the physical-layer security was pioneered by Wyner for proposing the wiretap channel [152]: a channel in which an eavesdropper receives a degraded version of the transmitted signal. The degraded wiretap channel was later extended to the non-degraded broadcast channel by Csiszár and Körner [153]. In their seminal work, it is shown that perfect secrecy can be achieved as long as the legitimate user has a less degraded channel than the eavesdropper. The secrecy capacity is derived as the difference be-

tween the information capacities for the two users. Typical security enhancement techniques that are implemented at upper layers of the communication chain include password protection and user admission control. Physical-layer security enhancement, on the other hand, exploits the randomness of noise and wireless communication channels to limit the amount of legitimate information to be detected by unauthorized eavesdroppers [152, 153].

Different from point-to-point (P2P) communication, studying the secrecy performance in a large-scale wireless network requires not only the knowledge of locations of legitimate users but also the knowledge of locations of eavesdropping users that may interact with legitimate users. Initial works that characterize the secrecy performance in multiuser wireless networks rely on the secrecy graph model to study the node connectivity [154, 155] and the maximum secrecy capacity [156] from an information-theoretic perspective. Following these works, the secrecy capacity per source-destination pair was investigated in [157] by characterizing the secrecy capacity scaling law in a wireless network. Moving from network information theory, recent works have evaluated the secrecy performance in multiuser wireless networks using mathematical tools from stochastic geometry [158, 159]. It should be noted that the works in [152–159] are all focused on radio frequency (RF) based wireless networks.

Due to these fundamental differences between RF and VLC (see Chapter 2), results on the secrecy capacity obtained for RF networks cannot be directly applied to optical attocell networks. By considering one transmitter, one legitimate user and one eavesdropper in a VLC system, lower and upper bounds on the secrecy capacity of the amplitude-constrained Gaussian wiretap channel were recently studied in [160], with the use of the derived capacity lower and upper bounds in [161]. In the same work [160], beamforming was also utilized to improve the secrecy capacity for the multiple-input single-output (MISO) VLC channel. Following this, the optimal beamformer design problem subject to amplitude constraints was further studied in [14]. The secrecy performance in a single-cell VLC system was studied in [162]. However, the randomness of legitimate users as well as eavesdroppers and, more importantly, the interactions among them, have not been fully characterized when analyzing the secrecy performance in multiuser attocell networks.

This chapter aims to characterize the secrecy performance in an indoor attocell network by considering the unique properties of the VLC channel as well as the network layout differing from typical RF networks. The proposed approach is built upon a stochastic model with two independent random topologies for APs and mobile users. Specifically, the VLC APs are modeled by a

two-dimensional (2D) homogeneous Poisson point process (PPP) in the ceiling while the locations of users, which include both legitimate users and eavesdroppers, are modeled by another independent 2D homogeneous PPP at the user plane. To separate eavesdroppers from legitimate users, the locations of random eavesdroppers are obtained from a thinned PPP. The remainder of this chapter is organized as follows. Section 6.2 formulates the information-theoretic secrecy capacity expression as a preliminary. The secrecy outage probability and the ergodic secrecy capacity with/without AP cooperation are derived in Section 6.3. The analysis on the secrecy performance is extended in Section 6.4 by implementing a disk-shaped protected zone. Simulation results and discussions are provided in Section 6.5. Finally, concluding remarks are given in Section 6.6.

6.2 Preliminaries

Consider a downlink transmission scenario of an attocell network with the presence of both legitimate users and eavesdroppers inside an indoor space. The VLC APs are vertically fixed, since they are attached to the room ceiling, and their horizontal positions are modeled by a 2D homogeneous PPP Φ_{a} with density λ_{a}. Similarly, mobile users are assumed to be at a fixed height and their horizontal positions are modeled by another independent 2D homogeneous PPP Φ_{u} with density λ_{u}. The vertical distance between the AP plane and the user plane is denoted by L. Among all of the users, the presence of malicious eavesdroppers could compromise the transmission privacy of legitimate links due to the broadcast nature of the VLC channel. Since eavesdroppers are typically disguised as legitimate users, it is uncertain whether a random user $u \in \Phi_{\mathrm{u}}$ is a legitimate user or an eavesdropper. Therefore, it is assumed that u is an eavesdropper with probability p_{e} and that u is a legitimate user with probability $1 - p_{\mathrm{e}}$. This thinned realization of Φ_{u} gives the point process for eavesdroppers, Φ_{e}, which is also a homogeneous PPP whose density can be found as $\lambda_{\mathrm{e}} = p_{\mathrm{e}}\lambda_{\mathrm{u}}$ [45]. Furthermore, it is assumed that eavesdroppers do not collude with each other so that each eavesdropper needs to decode the transmitted information messages individually. The same channel model given in (3.4) is used. Considering the communication link from an AP $x \in \Phi_{\mathrm{a}}$ to an eavesdropper $e \in \Phi_{\mathrm{e}}$, the received optical power can be written as:

$$P_{\mathrm{rx}}(x, e) = \frac{\alpha}{(||e - x||^2 + L^2)^{\frac{m+3}{2}}} P_{\mathrm{o}}, \tag{6.1}$$

where P_{o} denotes the radiated optical power of the AP. Similarly, the received signal power at the legitimate user can be written as $P_{\mathrm{rx}}(x, o)$, with o representing the origin is the location of the typical user of interest. Based on the information-theoretic capacity of VLC systems [65], the secrecy capacity of a VLC link can be calculated from [163]:

$$C_{\mathrm{s}} = \left[C_{\mathrm{b}} - C_{\mathrm{e}}\right]^{+}, \tag{6.2}$$

where $[a]^{+} = \max\{a, 0\}$, C_{b} is the channel capacity of the legitimate link and C_{e} is the channel capacity of the eavesdropping link. As legitimate users and eavesdroppers may use different grades of receivers, for example, photodiodes (PDs) with different detection areas, bandwidths and field-of-views (FOVs), they are subject to different levels of ambient noise and are capable of detecting signals from various incident angles and with different amplifying gains. The effect of choosing different FOV receivers is discussed in Section 6.5 while the impact of receivers with different detection areas and amplifying gains can be accounted for in the system model by assigning different noise variances at the legitimate user and the eavesdropper. Based on this, σ^2_{nb} and σ^2_{ne} are denoted as the noise variance at the legitimate user and the noise variance at the eavesdropper, respectively.

6.3 Secrecy Capacity

6.3.1 Nearest Access Point Association

Without AP cooperation, the nearest AP is assumed to serve a mobile user in the network in order to maximize the information rate of the communication link. Based on (3.4), the capacity of the legitimate link can be written as $C_{\mathrm{b}} = \max_{x \in \Phi_{\mathrm{a}}} \frac{1}{2} \log_2(1 + P^2_{\mathrm{rx}}(x, o)/\sigma^2_{\mathrm{nb}}) = \frac{1}{2} \log_2(1 + P^2_{\mathrm{rx}}(x_0, o)/\sigma^2_{\mathrm{nb}})$, where x_0 represents the location of the nearest AP to the origin. Since it is assumed that eavesdroppers do not collude, the secrecy performance of the legitimate user is limited by the eavesdropper with the highest signal-to-noise ratio (SNR). Therefore, the secrecy capacity at the typical legitimate user is formulated as:

$$\begin{aligned} C_{\mathrm{s}} &= \left[\frac{1}{2}\log_2\left(1 + \frac{P^2_{\mathrm{rx}}(x_0, o)}{\sigma^2_{\mathrm{nb}}}\right) - \frac{1}{2}\log_2\left(1 + \frac{P^2_{\mathrm{rx}}(x_0, e^*(x_0))}{\sigma^2_{\mathrm{ne}}}\right)\right]^{+} \\ &= \left[\frac{1}{2}\log_2\left(\frac{P^2_{\mathrm{rx}}(x_0, o) + \sigma^2_{\mathrm{nb}}}{P^2_{\mathrm{rx}}(x_0, e^*(x_0)) + \sigma^2_{\mathrm{ne}}}\right) + \log_2\left(\frac{\sigma_{\mathrm{ne}}}{\sigma_{\mathrm{nb}}}\right)\right]^{+} \end{aligned}$$

$$\approx \left[\log_2\left(\frac{P_{\mathrm{rx}}(x_0,o)}{P_{\mathrm{rx}}(x_0,e^*(x_0))}\right)+\log_2\left(\frac{\sigma_{\mathrm{ne}}}{\sigma_{\mathrm{nb}}}\right)\right]^+ \tag{6.3}$$

where $e^*(x_0)$ denotes the horizontal distance from AP x_0 to the nearest eavesdropper. The approximation made in the last step is based on the fact that the received signal power is generally much larger than the noise variance in a VLC system utilizing existing luminaries as APs [104, 164]. It is shown in (6.3) that a nonnegative secrecy capacity can only be achieved when the legitimate user achieves a higher SNR than the strongest eavesdropper. In the case that the eavesdropper receives signals from a less-degraded link than the legitimate user, the achievable secrecy capacity drops to zero. It can also be seen from (6.3) that when the legitimate user and the eavesdropper use different grades of receivers, the achievable secrecy capacity at the legitimate user is offset by a constant, whose value is proportional to the logarithm of $\sigma_{\mathrm{ne}}/\sigma_{\mathrm{nb}}$. Therefore, without loss of generality, $\sigma_{\mathrm{nb}}=\sigma_{\mathrm{ne}}$ is assumed in the following analysis. Given that the legitimate user is connected to AP x, the general solution for $e^*(x)$ can be obtained by finding the location of the eavesdropper $e\in\Phi_{\mathrm{e}}$ that receives the strongest signal power:

$$e^*(x)=\arg\max_{e\in\Phi_{\mathrm{e}}} P_{\mathrm{rx}}(x,e)=\arg\min_{e\in\Phi_{\mathrm{e}}}||e-x||, \tag{6.4}$$

where the second step is obtained based on the monotonic property of (6.1).

According to (6.3), it can be shown that $C_{\mathrm{s}}\geq 0$. Therefore, the cumulative distribution function (CDF) of the secrecy capacity can be calculated from:

$$\begin{aligned} F_{C_{\mathrm{s}}}(v) =& \mathbb{P}\left[C_{\mathrm{s}}\leq v\right] \\ =& \mathbb{P}\left[\frac{P^2_{\mathrm{rx}}(x_0,o)}{P^2_{\mathrm{rx}}(x_0,e^*(x_0))}\leq 4^v\right] \\ =& \mathbb{P}\left[||e^*(x_0)-x_0||\leq\sqrt{\beta x_0^2+(\beta-1)L^2}\right], \end{aligned} \tag{6.5}$$

where $\beta=4^{v/(m+3)}$ is an auxiliary variable. Since the legitimate user is served by the nearest AP, the probability density function (PDF) of x_0 is [165]:

$$f_{x_0}(x_0)=2\pi\lambda_{\mathrm{a}}x_0\exp\left(-\pi\lambda_{\mathrm{a}}x_0^2\right). \tag{6.6}$$

When conditioned on distance x_0, (6.5) represents the probability that no eavesdroppers exist within a disk, which is centered at x_0 and has a radius of $\sqrt{\beta x_0^2+(\beta-1)L^2}$. Therefore, the

void probability of PPP [166] can be applied to further simplify the calculation of (6.5), yielding

$$\begin{aligned} F_{C_\mathrm{s}}(v) =& \mathbb{E}_{x_0}\left[\mathbb{P}\left[||e^*(x_0)-x_0|| \leq \sqrt{\beta x_0^2+(\beta-1)L^2}\middle| x_0\right]\right] \\ =& \int_0^\infty \mathbb{P}\left[||e^*(x_0)-x_0|| \leq \sqrt{\beta x_0^2+(\beta-1)L^2}\middle| x_0\right] f_{x_0}(x_0)\mathrm{d}x_0 \\ =& \int_0^\infty \left(1-\exp\left(-\pi\lambda_\mathrm{e}\left(\beta x_0^2+(\beta-1)L^2\right)\right)\right) 2\pi\lambda_\mathrm{a} x_0 \exp\left(-\pi\lambda_\mathrm{a} x_0^2\right)\mathrm{d}x_0 \\ =& 1-\frac{1}{1+\frac{\lambda_\mathrm{e}}{\lambda_\mathrm{a}}\beta}\exp\left(-\pi\lambda_\mathrm{e}\left(\beta-1\right)L^2\right). \end{aligned} \tag{6.7}$$

After plugging $\beta = 4^{v/(m+3)}$ into (6.7), the secrecy capacity distribution is found as:

$$F_{C_\mathrm{s}}(v) = 1-\frac{1}{1+\frac{\lambda_\mathrm{e}}{\lambda_\mathrm{a}}4^{\frac{v}{m+3}}}\exp\left(-\pi\lambda_\mathrm{e}\left(4^{\frac{v}{m+3}}-1\right)L^2\right), \tag{6.8}$$

for $v \geq 0$, and zero otherwise. The above result assumes that the legitimate user is connected to the nearest AP. Consider the case that the legitimate user is connected to the n-th nearest AP. Using the distance distribution of the legitimate user to the n-th nearest AP [165]:

$$f_{x_n}(x_n) = \frac{2(\pi\lambda_\mathrm{a}x_n^2)^n}{x_n\Gamma(n)}\exp\left(-\pi\lambda_\mathrm{a}x_n^2\right), \tag{6.9}$$

the CDF of the secrecy capacity when the legitimate user is connected to the n-th nearest AP can be calculated as:

$$F_{C_\mathrm{s}}(v) = 1-\left(\frac{1}{1+\frac{\lambda_\mathrm{e}}{\lambda_\mathrm{a}}4^{\frac{v}{m+3}}}\right)^n\exp\left(-\pi\lambda_\mathrm{e}\left(4^{\frac{v}{m+3}}-1\right)L^2\right), \tag{6.10}$$

for $v \geq 0$, and zero otherwise. The secrecy outage probability, denoted by p_so, is defined as the probability that the secrecy capacity is below a target secrecy rate $\bar{C}_\mathrm{s}$. Mathematically, it is formulated as:

$$p_\mathrm{so} = \mathbb{P}\left[C_\mathrm{s} \leq \bar{C}_\mathrm{s}\right] = F_{C_\mathrm{s}}(\bar{C}_\mathrm{s}). \tag{6.11}$$

Letting λ_a approach infinity, a lower bound on the secrecy capacity can be obtained:

$$p_\mathrm{so}^\mathrm{LB} = \lim_{\lambda_\mathrm{a}\to\infty} p_\mathrm{so} = 1-\exp\left(-\pi\lambda_\mathrm{e}\left(4^{\frac{\bar{R}_\mathrm{s}}{m+3}}-1\right)L^2\right). \tag{6.12}$$

Reviewing (6.8) and (6.12), it can be concluded that installing more VLC APs can help decrease the secrecy outage probability of a typical legitimate user. However, when the density of APs

reaches a certain level, further increasing the density of APs is not meaningful since it can no longer enhance the secrecy performance. In other words, it is impossible for a legitimate user in the network to simultaneously achieve a target secrecy rate $\bar{C}_{\rm s}$ and have an outage probability lower than $p_{\rm so}^{\rm LB}(\bar{C}_{\rm s})$. Given a target secrecy rate $\bar{C}_{\rm s}$ and a target outage probability $\bar{p}_{\rm so} > p_{\rm so}^{\rm LB}(\bar{C}_{\rm s})$, this requirement can be achieved by installing more APs in the network so that the density of APs satisfies $\lambda_{\rm a} \geq \lambda_{\rm e}\left(1-\bar{p}_{\rm so}\right)4^{\bar{C}_{\rm s}/(m+3)}\big/\left(\bar{p}_{\rm so}-p_{\rm so}^{\rm LB}(\bar{C}_{\rm s})\right)$. It is also interesting to note that reducing the semiangle of the LED, or equivalently increasing its Lambertian order, helps improve the secrecy performance of the network.

From the distribution function of $C_{\rm s}$, the ergodic secrecy capacity can be calculated from a single integration:

$$\begin{aligned}\mathbb{E}[C_{\rm s}] =& \int_0^\infty \left(1-F_{C_{\rm s}(v)}\right){\rm d}v \\ =& \frac{m+3}{\ln(4)}\int_1^\infty \frac{1}{\beta\left(1+\frac{\lambda_{\rm e}}{\lambda_{\rm a}}\beta\right)}\exp\left(-\pi\lambda_{\rm e}\left(\beta-1\right)L^2\right){\rm d}\beta \\ =& \frac{m+3}{\ln(4)}\left(\int_1^\infty \frac{\exp\left(-\pi\lambda_{\rm e}\left(\beta-1\right)L^2\right)}{\beta}{\rm d}\beta - \int_1^\infty \frac{\exp\left(-\pi\lambda_{\rm e}\left(\beta-1\right)L^2\right)}{\beta+\frac{\lambda_{\rm a}}{\lambda_{\rm e}}}{\rm d}\beta\right).\end{aligned} \tag{6.13}$$

After applying [110, (3.351.5)], the first integration in (6.13) can be calculated as:

$$\int_1^\infty \frac{\exp\left(-\pi\lambda_{\rm e}\left(\beta-1\right)L^2\right)}{\beta}{\rm d}\beta = -\exp\left(\pi\lambda_{\rm e}L^2\right){\rm Ei}\left(-\pi\lambda_{\rm e}L^2\right), \tag{6.14}$$

where ${\rm Ei}(a) = -\int_{-a}^{\infty}\exp(-t)/t{\rm d}t$ is the exponential integral function [110]. After applying [110, (3.352.2)], the second integration in (6.13) can be calculated as:

$$\int_1^\infty \frac{\exp\left(-\pi\lambda_{\rm e}\left(\beta-1\right)L^2\right)}{\beta+\frac{\lambda_{\rm a}}{\lambda_{\rm e}}}{\rm d}\beta = -\exp\left(\pi(\lambda_{\rm e}+\lambda_{\rm a})L^2\right){\rm Ei}\left(-\pi(\lambda_{\rm e}+\lambda_{\rm a})L^2\right). \tag{6.15}$$

Plugging (6.14) and (6.15) into (6.13) yields

$$\mathbb{E}[C_{\rm s}] = \frac{m+3}{\ln(4)}\left(\exp\left(\pi(\lambda_{\rm e}+\lambda_{\rm a})L^2\right){\rm Ei}\left(-\pi(\lambda_{\rm e}+\lambda_{\rm a})L^2\right) - \exp\left(\pi\lambda_{\rm e}L^2\right){\rm Ei}\left(-\pi\lambda_{\rm e}L^2\right)\right). \tag{6.16}$$

Based on the equality $\lim_{\lambda_{\rm a}\to\infty}\exp\left(\pi(\lambda_{\rm e}+\lambda_{\rm a})L^2\right){\rm Ei}\left(-\pi(\lambda_{\rm e}+\lambda_{\rm a})L^2\right) = 0$, the upper

bound on the secrecy capacity can be obtained as

$$C_{\mathrm{s}}^{\mathrm{UB}} = \lim_{\lambda_{\mathrm{a}} \to \infty} \mathbb{E}[C_{\mathrm{s}}] = \frac{m+3}{\ln(4)} \left(-\exp\left(\pi \lambda_{\mathrm{e}} L^2\right) \mathrm{Ei}\left(-\pi \lambda_{\mathrm{e}} L^2\right)\right). \tag{6.17}$$

It can be seen that increasing the density of VLC APs can help enhance the ergodic secrecy capacity of the network. However, when the density of APs exceeds a certain level, installing more APs can not enhance the ergodic secrecy capacity any further. While satisfying the illumination requirement, using LEDs with a smaller semiangle can increase the secrecy capacity of a typical user. Specifically, it can be seen from (6.16) and (6.17) that a linear relationship exists between the ergodic secrecy capacity and the Lambertian order m. Given the choice of LEDs, the maximum ergodic secrecy capacity can not exceed the upper bound given in (6.17). To achieve a target ergodic secrecy rate $\bar{C}_{\mathrm{s}}$, whose value is smaller than $C_{\mathrm{s}}^{\mathrm{UB}}$, the density of APs needs to exceed λ_{a}^{*}, where λ_{a}^{*} is the numerical solution for λ_{a} to equation $\exp\left(\pi(\lambda_{\mathrm{e}}+\lambda_{\mathrm{a}})L^2\right) \mathrm{Ei}\left(-\pi(\lambda_{\mathrm{e}}+\lambda_{\mathrm{a}})L^2\right) = \ln(4)\bar{C}_{\mathrm{s}}/(m+3) + \exp\left(\pi\lambda_{\mathrm{e}}L^2\right) \mathrm{Ei}\left(-\pi\lambda_{\mathrm{e}}L^2\right)$.

6.3.2 Optimal Access Point Association

Due to the randomness of eavesdroppers, it is not always optimal to serve the legitimate user with the nearest AP. For example, if the eavesdropper is close to the nearest AP around the legitimate user but far away from the second nearest AP around the legitimate user, selecting the second nearest AP to serve the legitimate user may yield a higher secrecy rate. Therefore, with the cooperation among APs, the secrecy performance of legitimate users can be further enhanced. However, it should be noted that selecting the optimal AP to serve legitimate users requires knowledge of the location information of all eavesdroppers at the central controller. This can be achieved, for example, with indoor sensing and localization technologies. Despite the additional implementation and computation complexity, this optimal scheme yields an enhanced secrecy rate. It is useful for network designers to quantify the secrecy performance provided by the nearest AP and optimal AP and to decide which scheme is more suitable for practical implementations. When the optimal AP is selected to serve the legitimate user, the secrecy capacity is formulated as:

$$C_{\mathrm{s}} = \left[\max_{x \in \Phi_{\mathrm{a}}} \left\{ \frac{1}{2} \log_2 \left(\frac{P_{\mathrm{rx}}^2(x,o)}{P_{\mathrm{rx}}^2(x,e^*(x))} \right) \right\} \right]^{+}. \tag{6.18}$$

Due to the intractability of the secrecy capacity expression in (6.18), the distribution function of C_{s} is hard to obtain. In the following, two analytical bounds on the CDF of the secrecy capacity are provided. With the cooperation of APs, the CDF of the secrecy rate can be calculated using the probability generating functional (PGFL) of the PPP [45]:

$$\begin{aligned}
F_{C_{\mathrm{s}}}(v) =& \mathbb{P}\left[\max_{x\in\Phi_{\mathrm{a}}}\left\{\frac{1}{2}\log_2\left(\frac{P_{\mathrm{rx}}^2(x,o)}{P_{\mathrm{rx}}^2(x,e^*(x))}\right)\right\}\leq v\right] \\
=& \mathbb{P}\left[\frac{1}{2}\log_2\left(\frac{P_{\mathrm{rx}}^2(x,o)}{P_{\mathrm{rx}}^2(x,e^*(x))}\right)\leq v, \forall x\in\Phi_{\mathrm{a}}\right] \\
=& \mathbb{E}_{\Phi_{\mathrm{e}}}\left[\mathbb{E}_{\Phi_{\mathrm{a}}}\left[\prod_{x\in\Phi_{\mathrm{a}}}\mathbf{1}\left(||e-x||\leq\sqrt{\beta l^2+(\beta-1)L^2}\right)\right]\right] \\
=& \mathbb{E}_{\Phi_{\mathrm{e}}}\left[\exp\left(-\lambda_{\mathrm{a}}\int_{\mathbb{R}^2}\mathbf{1}\left[||e-x||>\sqrt{\beta l^2+(\beta-1)L^2}\Big|\, x\right]\mathrm{d}x\right)\right],
\end{aligned} \tag{6.19}$$

where $\mathbf{1}(\mathcal{A})=1$ with event $\mathcal{A}$ being true, and zero otherwise. Based on Jensen's inequality, the lower bound can be calculated as:

$$\begin{aligned}
F_{C_{\mathrm{s}}}(v) \geq& \exp\left(-2\pi\lambda_{\mathrm{a}}\int_0^\infty \mathbb{P}\left[||e-x||>\sqrt{\beta x^2+(\beta-1)L^2}\Big|\, x\right]x\mathrm{d}x\right) \\
=& \exp\left(-\frac{\lambda_{\mathrm{a}}}{\lambda_{\mathrm{e}}}4^{-\frac{v}{m+3}}\exp\left(-\pi\lambda_{\mathrm{e}}\left(4^{\frac{v}{m+3}}-1\right)L^2\right)\right).
\end{aligned} \tag{6.20}$$

The upper bound can be obtained from the following inequality:

$$\left[\max_{x\in\Phi_{\mathrm{a}}}\left\{\log_2\left(\frac{P_{\mathrm{rx}}^2(x,o)}{P_{\mathrm{rx}}^2(x,e^*(x))}\right)\right\}\right]^+ \geq \left[\log_2\left(\frac{P_{\mathrm{rx}}^2(x_0,o)}{P_{\mathrm{rx}}^2(x_0,e^*(x_0))}\right)\right]^+. \tag{6.21}$$

In other words, choosing the nearest AP to serve the legitimate user is sub-optimal, which gives an upper bound on the CDF of the secrecy capacity, as given in (6.8). Based on the upper bound on the CDF of the secrecy rate, a lower bound on the ergodic secrecy capacity can be obtained, as given in (6.16). An upper bound on the ergodic secrecy capacity can be obtained by integrating the complement of the CDF of C_{s}:

$$\begin{aligned}
\mathbb{E}[C_{\mathrm{s}}] =& \int_0^\infty \left(1-F_{C_{\mathrm{s}}(v)}\right)\mathrm{d}v \\
\leq& \frac{m+3}{\ln(4)}\int_1^\infty\left(1-\exp\left(-\frac{\lambda_{\mathrm{a}}}{\lambda_{\mathrm{e}}\beta}\exp\left(-\pi\lambda_{\mathrm{e}}\left(\beta-1\right)L^2\right)\right)\right)\frac{1}{\beta}\mathrm{d}\beta.
\end{aligned} \tag{6.22}$$

Because of the nested exponential function in (6.22), a closed-form expression is not available. However, (6.22) can be efficiently calculated using numerical methods.

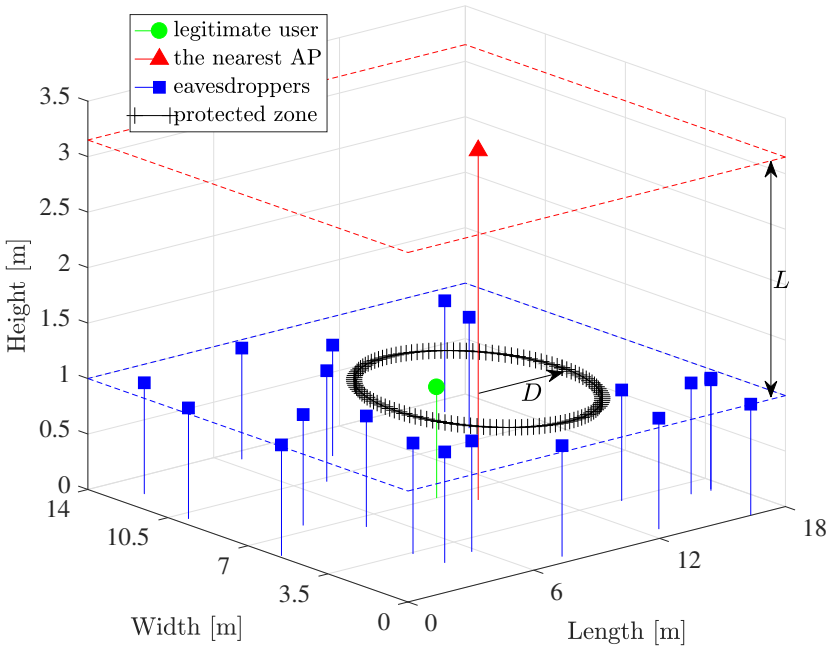

Figure 6.1: *Random network model with a secrecy protected zone. In this model, each VLC AP has a disk-shaped protected zone, which is centered around the AP and has a radius of D on the user plane. For simplicity, only the protected zone around the nearest AP is drawn.*

6.4 Secrecy Enhancement with a Protected Zone

In order to further enhance the secrecy performance of legitimate users in attocell networks, a strategy named the "protected zone" [167] can be implemented. As depicted in Figure 6.1, a protected zone is an eavesdropper-free area allowing only legitimate users to enter. If any eavesdropper enters the protected zone, such behavior will be made aware to the AP, which will then notify the legitimate user and temporarily stop the communication. A practical implementation of the protected zone in indoor attocell networks can be achieved with motion sensors that are already built in modern energy-saving lighting devices. It is acknowledged that there might be means to break the suggested enforcement of the protected zone, for example, by disguising as legitimate users. However, a deeper investigation of this aspect is outside the scope of this work. A secrecy protected zone can be completely described by its center, *i.e.,* its associated AP, and a security radius D. The security radius is defined as the smallest horizontal distance between the AP and any eavesdroppers that are undetectable.

Given that the horizontal distance between the nearest AP to the legitimate user is x_0, the PDF of the horizontal distance between this AP and the nearest eavesdropper outside the protected

zone can be calculated using the void probability of PPP [166]:

$$f_{||e^*(x_0)-x_0||}(v) = 2\pi\lambda_{\mathrm{e}} v \exp\left(-\pi\lambda_{\mathrm{e}}(v^2 - D^2)\right), \tag{6.23}$$

for $v \geq D$, and zero otherwise. Since the protected zone has a radius D, the minimum distance between the nearest eavesdropper and the AP is D. Therefore, the location of the nearest eavesdropper is

$$e^*(x_0) = \arg \min_{e\in\Phi_{\mathrm{e}}, e\notin\mathcal{B}(x_0,D)} ||e - x_0||, \tag{6.24}$$

where $\mathcal{B}(x_0, D)$ denotes the disk-shaped area centered at x_0 with radius D. Due to the exclusive region in (6.24), the derivation of the CDF of the enhanced secrecy rate needs to be separated into two scenarios. On the one hand, when $\sqrt{(\beta-1)L^2} \geq D$, *i.e.,* $v \geq \frac{m+3}{2}\log_2\left(D^2/L^2+1\right)$, the CDF of the enhanced secrecy rate can be calculated as:

$$\begin{aligned} F_{C_{\mathrm{s}}}(v) =& \int_0^\infty \left(1 - \exp\left(-\pi\lambda_{\mathrm{e}}\left(\beta x_0^2 + (\beta-1)L^2 - D^2\right)\right)\right) 2\pi\lambda_{\mathrm{a}} x_0 \exp\left(-\pi\lambda_{\mathrm{a}} x_0^2\right) \mathrm{d}x_0, \\ =& 1 - \frac{\exp\left(-\pi\lambda_{\mathrm{e}}\left(\left(4^{\frac{v}{m+3}} - 1\right)L^2 - D^2\right)\right)}{1 + \frac{\lambda_{\mathrm{e}}}{\lambda_{\mathrm{a}}} 4^{\frac{v}{m+3}}} \end{aligned} \tag{6.25}$$

On the other hand, when $\sqrt{(\beta-1)L^2} < D$, *i.e.,* $0 \leq v < \frac{m+3}{2}\log_2\left(D^2/L^2+1\right)$, the CDF of the enhanced secrecy capacity can be calculated as:

$$\begin{aligned} & F_{C_{\mathrm{s}}}(v) \\ =& \int_{\sqrt{\frac{D^2-(\beta-1)L^2}{\beta}}}^\infty 2\pi\lambda_{\mathrm{a}} x_0 \exp\left(-\pi\lambda_{\mathrm{a}} x_0^2\right) \left(1 - \exp\left(-\pi\lambda_{\mathrm{e}}\left(\beta x_0^2 + (\beta-1)L^2 - D^2\right)\right)\right) \mathrm{d}x_0 \\ &+ \int_0^{\sqrt{\frac{D^2-(\beta-1)L^2}{\beta}}} 2\pi\lambda_{\mathrm{a}} x_0 \exp\left(-\pi\lambda_{\mathrm{a}} x_0^2\right) \mathbb{P}\left[e^*(x_0) \in \mathcal{B}(x_0, D)\right] \mathrm{d}x_0, \end{aligned} \tag{6.26}$$

where the critical point $x_0 = \sqrt{(D^2 - (\beta-1)L^2)/\beta}$ is found by solving $\sqrt{\beta x_0^2 + (\beta-1)L^2} = D$. Since $e^*(x_0) \notin \mathcal{B}(x_0, D)$, it follows that $\mathbb{P}\left[e^*(x_0) \in \mathcal{B}(x_0, D)\right] = 0$. As a result, the second integration in (6.26) reduces to zero. Calculating the first integration in (6.26) yields

$$F_{C_{\mathrm{s}}}(v) = \frac{\exp\left(-\pi\lambda_{\mathrm{a}}\left(D^2 - \left(4^{\frac{v}{m+3}} - 1\right)L^2\right)4^{-\frac{v}{m+3}}\right)}{1 + \frac{\lambda_{\mathrm{a}}}{\lambda_{\mathrm{e}}} 4^{-\frac{v}{m+3}}}, \tag{6.27}$$

for $0 \leq v < \frac{m+3}{2}\log_2\left(D^2/L^2+1\right)$. It can be seen from (6.25) and (6.27) that the radius of the protected zone has a strong impact on the secrecy performance. On the one hand, if the radius of the protected zone is small enough so that the target secrecy rate satisfies $\bar{C}_\mathrm{s} \geq \frac{m+3}{2}\log_2\left(D^2/L^2+1\right)$, given a fixed density of eavesdroppers, the secrecy outage probability is lower bounded by:

$$p_\mathrm{so}^\mathrm{LB} = 1 - \exp\left(-\pi\lambda_\mathrm{e}\left(\left(4^{\frac{\bar{C}_\mathrm{s}}{m+3}}-1\right)L^2 - D^2\right)\right), \tag{6.28}$$

which is obtained when the density of the APs approaches infinity. On the other hand, if the radius of the protected zone is large enough so that the target secrecy rate satisfies $\bar{C}_\mathrm{s} < \frac{m+3}{2}\log_2\left(D^2/L^2+1\right)$, increasing the density of VLC APs can efficiently reduce the secrecy outage probability. The worst-case scenario of the secrecy outage probability is upper bounded by:

$$p_\mathrm{so}^\mathrm{UB} = \exp\left(-\pi\lambda_\mathrm{a}\left(D^2 - \left(4^{\frac{\bar{C}_\mathrm{s}}{m+3}}-1\right)L^2\right)4^{-\frac{\bar{C}_\mathrm{s}}{m+3}}\right), \tag{6.29}$$

which is obtained by letting λ_e approach infinity. Moreover, for legitimate users to achieve a target secrecy rate $\bar{C}_\mathrm{s}$ with a target secrecy outage probability $\bar{p}_\mathrm{so}$, network designers can set up the protected zone with radius no smaller than D^*, where $D^* = ((4^{\bar{C}_\mathrm{s}/(m+3)}-1)L^2 + (\ln(1-\bar{p}_\mathrm{so}) + \ln(1+4^{\bar{C}_\mathrm{s}/(m+3)}\lambda_\mathrm{e}/\lambda_\mathrm{a}))/\pi\lambda_\mathrm{e})^{1/2}$ for $\bar{p}_\mathrm{so} \geq 1-(1+4^{\bar{C}_\mathrm{s}/(m+3)}\lambda_\mathrm{e}/\lambda_\mathrm{a})^{-1}$, and $D^* = ((4^{\bar{C}_\mathrm{s}/(m+3)}-1)L^2 - (\ln\bar{p}_\mathrm{so} + \ln(1+4^{-\bar{C}_\mathrm{s}/(m+3)}\lambda_\mathrm{a}/\lambda_\mathrm{e}))4^{\bar{C}_\mathrm{s}/(m+3)}/\pi\lambda_\mathrm{a})^{1/2}$ for $\bar{p}_\mathrm{so} < 1-(1+4^{\bar{C}_\mathrm{s}/(m+3)}\lambda_\mathrm{e}/\lambda_\mathrm{a})^{-1}$. Also, it is evident that a more stringent secrecy requirement with a larger $\bar{C}_\mathrm{s}$ and/or a smaller $\bar{p}_\mathrm{so}$ requires the implementation of a larger secrecy protected zone.

The enhanced ergodic capacity can be calculated by integrating the complement of the CDF. Since the CDF has different expressions at different regions, the integration should be separated into two parts:

$$\begin{aligned}\mathbb{E}[C_\mathrm{s}] =& \frac{m+3}{\ln(4)}\int_1^{\frac{D^2}{L^2}+1}\left(1 - \frac{\exp\left(\frac{-\pi\lambda_\mathrm{a}\left(D^2-(\beta-1)L^2\right)}{\beta}\right)}{1+\frac{\lambda_\mathrm{a}}{\lambda_\mathrm{e}}\frac{1}{\beta}}\right)\frac{1}{\beta}\mathrm{d}\beta \\ &+ \frac{m+3}{\ln(4)}\int_{\frac{D^2}{L^2}+1}^{\infty}\frac{\exp\left(-\pi\lambda_\mathrm{e}\left((\beta-1)L^2 - D^2\right)\right)}{\beta+\frac{\lambda_\mathrm{e}}{\lambda_\mathrm{a}}\beta^2}\mathrm{d}\beta,\end{aligned} \tag{6.30}$$

where for simplicity the variable of integration has been changed from v to β. The first integra-

tion in (6.30) can be simplified to:

$$\int_1^{\frac{D^2}{L^2}+1}\left(1-\frac{\exp\left(\frac{-\pi\lambda_{\mathrm{a}}\left(D^2-(\beta-1)L^2\right)}{\beta}\right)}{1+\frac{\lambda_{\mathrm{a}}}{\lambda_{\mathrm{e}}}\frac{1}{\beta}}\right)\frac{1}{\beta}\mathrm{d}\beta$$

$$=\ln\left(\frac{D^2}{L^2}+1\right)+\exp\left(\pi\lambda_{\mathrm{a}}L^2\right)\int_1^{\frac{D^2}{L^2}+1}\frac{\exp\left(-\frac{\pi\lambda_{\mathrm{a}}\left(L^2+D^2\right)}{\beta}\right)}{\beta+\frac{\lambda_{\mathrm{a}}}{\lambda_{\mathrm{e}}}}\mathrm{d}\beta, \tag{6.31}$$

in which the integration part can be obtained as:

$$\begin{aligned}\int_1^{\frac{D^2}{L^2}+1}\frac{\exp\left(-\frac{\pi\lambda_{\mathrm{a}}\left(L^2+D^2\right)}{\beta}\right)}{\beta+\frac{\lambda_{\mathrm{a}}}{\lambda_{\mathrm{e}}}}\mathrm{d}\beta =&\mathrm{Ei}\left(-\pi\lambda_{\mathrm{a}}L^2\right)-\mathrm{Ei}\left(-\pi\lambda_{\mathrm{a}}\left(L^2+D^2\right)\right)\\&+\exp\left(\pi\lambda_{\mathrm{e}}\left(L^2+D^2\right)\right)\mathrm{Ei}\left(-\pi(\lambda_{\mathrm{a}}+\lambda_{\mathrm{e}})\left(L^2+D^2\right)\right)\\&-\exp\left(\pi\lambda_{\mathrm{e}}\left(L^2+D^2\right)\right)\mathrm{Ei}\left(-\pi\lambda_{\mathrm{a}}L^2-\pi\lambda_{\mathrm{e}}\left(L^2+D^2\right)\right).\end{aligned} \tag{6.32}$$

Similarly, the second integration in (6.30) can be simplified to:

$$\begin{aligned}&\int_{\frac{D^2}{L^2}+1}^{\infty}\frac{\exp\left(-\pi\lambda_{\mathrm{e}}\left(\left(\beta-1\right)L^2-D^2\right)\right)}{\beta+\frac{\lambda_{\mathrm{e}}}{\lambda_{\mathrm{a}}}\beta^2}\mathrm{d}\beta\\&=\exp\left(\pi\lambda_{\mathrm{e}}\left(L^2+D^2\right)\right)\left(\int_{\frac{D^2}{L^2}+1}^{\infty}\frac{\exp\left(-\pi\lambda_{\mathrm{e}}\beta L^2\right)}{\beta}\mathrm{d}\beta-\int_{\frac{D^2}{L^2}+1}^{\infty}\frac{\exp\left(-\pi\lambda_{\mathrm{e}}\beta L^2\right)}{\beta+\frac{\lambda_{\mathrm{a}}}{\lambda_{\mathrm{e}}}}\mathrm{d}\beta\right).\end{aligned} \tag{6.33}$$

With the application of [110, (3.352.2)], the two integrations in (6.33) can be simplified to:

$$\int_{\frac{D^2}{L^2}+1}^{\infty}\frac{\exp\left(-\pi\lambda_{\mathrm{e}}\beta L^2\right)}{\beta}\mathrm{d}\beta=-\mathrm{Ei}\left(-\pi\lambda_{\mathrm{e}}\left(L^2+D^2\right)\right), \tag{6.34}$$

and

$$\int_{\frac{D^2}{L^2}+1}^{\infty}\frac{\exp\left(-\pi\lambda_{\mathrm{e}}\beta L^2\right)}{\beta+\frac{\lambda_{\mathrm{a}}}{\lambda_{\mathrm{e}}}}\mathrm{d}\beta=-\exp\left(\pi\lambda_{\mathrm{a}}L^2\right)\mathrm{Ei}\left(-\pi\lambda_{\mathrm{e}}L^2\left(\frac{\lambda_{\mathrm{a}}}{\lambda_{\mathrm{e}}}+\frac{D^2}{L^2}+1\right)\right). \tag{6.35}$$

Combining (6.31) – (6.35) yields the following closed-form expression for the ergodic secrecy

Parameter	value
Room dimensions	$18 \times 14 \times 3.5$ m^3
Height of VLC APs	3.15 m
Height of mobile users	1 m
LED semiangle	30°
Transmit signal power of the AP	1 W
Receiver detection area	1 cm^2
Receiver responsivity	0.4 A/W
Reflective index of the optical concentrator	1.5
Optical filter gain	1
Receiver FOV	90°
Bandwidth	40 MHz
Noise PSD	10^{-21} A^2/Hz

Table 6.2: *Physical-layer security: simulation setup and parameters.*

capacity expression:

$$\begin{aligned}\mathbb{E}[C_{\rm s}] =& \frac{m+3}{\ln(4)}\left(-\exp\left(\pi\lambda_{\rm e}\left(L^2+D^2\right)\right)\mathrm{Ei}\left(-\pi\lambda_{\rm e}\left(L^2+D^2\right)\right)+\ln\left(\frac{D^2}{L^2}+1\right)\right)\\ &+\frac{m+3}{\ln(4)}\exp\left(\pi\lambda_{\rm a}L^2\right)\Big\{\mathrm{Ei}\left(-\pi\lambda_{\rm a}L^2\right)-\mathrm{Ei}\left(-\pi\lambda_{\rm a}\left(L^2+D^2\right)\right)\\ &+\exp\left(\pi\lambda_{\rm e}\left(L^2+D^2\right)\right)\mathrm{Ei}\left(-\pi(\lambda_{\rm a}+\lambda_{\rm e})\left(L^2+D^2\right)\right)\Big\}. \end{aligned} \tag{6.36}$$

Note that the above ergodic secrecy capacity expression simplifies to (6.16) when $D = 0$. Also, it is shown in (6.36) that the ergodic secrecy capacity scales linearly with the Lambertian order m, regardless of the size of the protected zone. Given the choice of LEDs, the density of APs and the density of eavesdroppers, a target ergodic secrecy capacity $\bar{C}_{\rm s}$ can be achieved through the implementation of a protected zone with radius D^*, where D^* is the numerical solution for D by letting (6.36) equal $\bar{C}_{\rm s}$. Since the expression in (6.36) monotonically increases with respect to D, the numerical solution for D^* is unique.

6.5 Simulation Results

In this section, a MATLAB implementation is used to validate the derived results. Simulation results are obtained by averaging $20,000$ realizations of Monte Carlo simulations. A typical office of size $18 \times 14 \times 3.5$ m^3 is considered, as illustrated in Figure 6.1. If not otherwise specified, the network parameters used for the simulation setup are described in Table 6.2.

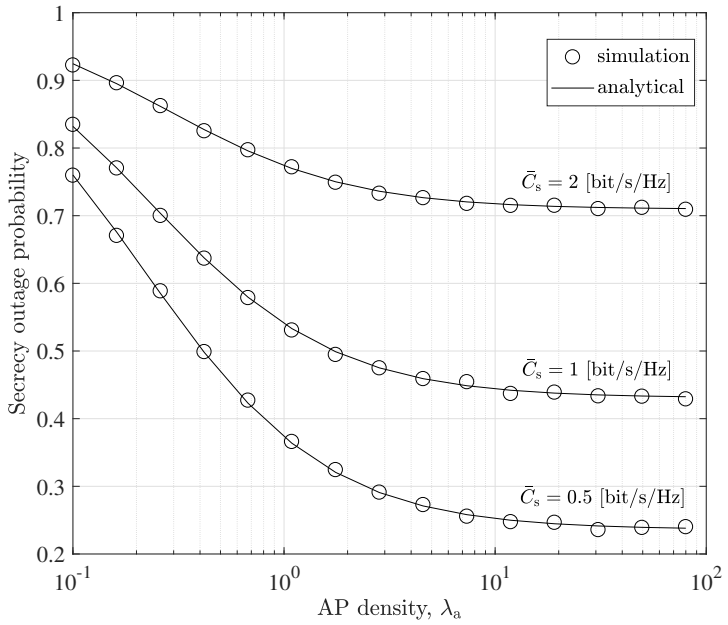

Figure 6.2: *Secrecy outage probability versus AP density. The legitimate user is served by the nearest AP in its vicinity.* $\lambda_e = 0.2$.

First, consider the scenario where the legitimate user is served by the nearest AP without implementation of the secrecy protected zone. In this case, malicious eavesdroppers can be horizontally as close as possible to the AP that serves the legitimate user. By fixing the density of eavesdroppers ($\lambda_e = 0.2$), the secrecy outage probability at the typical legitimate user is evaluated for different values of the AP density, as shown in Figure 6.2. It can be seen that, when λ_a is small, increasing the density of VLC APs can efficiently reduce the secrecy outage probability at the legitimate user. However, when λ_a is large, further increasing the density of VLC APs only slightly reduces the secrecy outage probability. For example, given that the target secrecy rate is $\bar{C}_s = 1$ bit/s/Hz, increasing λ_a from 0.1 to 1 causes the secrecy outage probability to drop by 0.3. In comparison, when λ_a is increased from 1 to 10, the secrecy outage probability only drops by 0.1. Also, it is shown that a lower bound on the secrecy outage probability exists even if the density of VLC APs approaches infinity. This result is in agreement with (6.12). In Figure 6.3, the ergodic secrecy capacity is plotted against the density of APs. It is shown that the ergodic secrecy capacity at the legitimate user drops when the density of eavesdroppers increases. Given a fixed density of eavesdroppers, increasing the density of VLC APs can efficiently enhance the ergodic secrecy capacity when λ_a is small. However, the ergodic secrecy capacity of the legitimate user tends to saturate at high AP densities. As a result, increasing the density of VLC APs when λ_a is large does not bring a significant incrementation to the ergodic

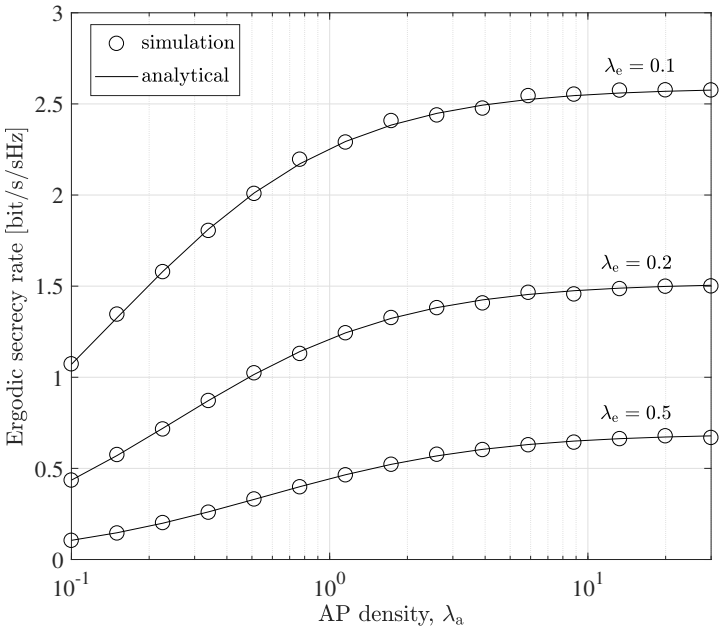

Figure 6.3: *Ergodic secrecy capacity versus AP density. The legitimate user is served by the nearest AP in its vicinity.*

secrecy capacity. Instead, increasing the density of APs when λ_a is small is more meaningful.

Second, consider the scenario where the legitimate user is served by the optimal AP when APs are cooperated in the network. For the typical legitimate user, the optimal AP is not necessarily the nearest one, depending on the locations of potential eavesdroppers. With the cooperation among VLC APs, the optimal AP that brings the highest secrecy rate to the legitimate user is selected. In the Monte Carlo simulation, the optimal AP is found out through the exhaustive search (ES) method. In Figure 6.4, the secrecy outage probability is plotted against different eavesdropper densities, and it can be seen that the simulation results are well bounded by the derived analytical results. On the one hand, by assuming that the optimal AP is the nearest one, the secrecy rate of the legitimate user is underestimated. As a result, this assumption leads to an upper bound on the secrecy outage probability. On the other hand, the lower bound on the secrecy outage probability is obtained from Jensen's inequality, as described in (6.20). Comparing the lower bound with the upper bound, it can be seen that the lower bound is closer to the simulation results. It is also shown in Figure 6.4 that both theoretical bounds on the secrecy outage probability are reasonably tight when the eavesdropper density is large. In Figure 6.5, the ergodic secrecy capacity of the legitimate user is computed for different values of the eavesdropper density. It should be noted that assuming that the optimal AP is the nearest one gives the lower bound on the ergodic secrecy capacity in Figure 6.5, which corresponds to

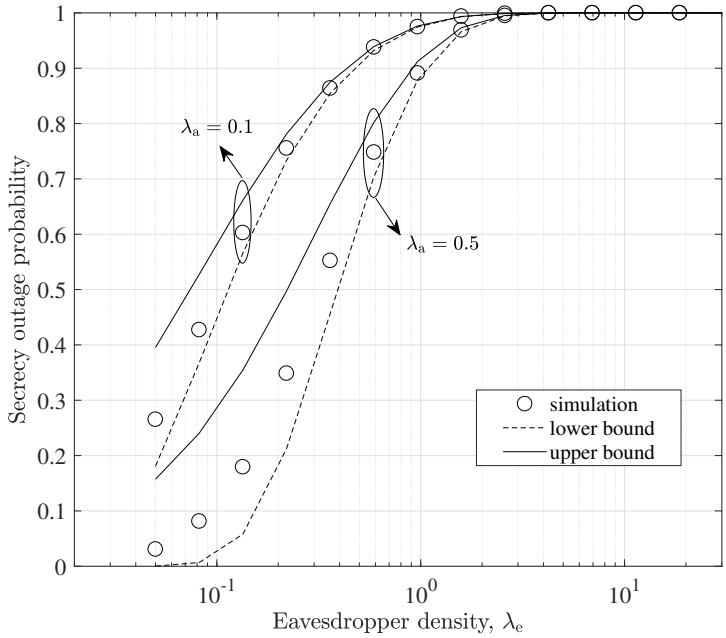

Figure 6.4: *Secrecy outage probability versus eavesdropper density. The legitimate user is served by the optimal AP.* $\bar{C}_s = 0.5$ bit/s/Hz.

the upper bound on the secrecy outage probability in Figure 6.4. Again, both analytical bounds become tighter as the eavesdropper density increases. Based on the results shown in Figure 6.4 and Figure 6.5, it can be concluded that the optimal AP that maximizes the secrecy performance of the legitimate user is not necessarily the nearest one. To investigate further, the probability mass function (PMF) of the index of the optimal AP that maximizes the secrecy capacity of the legitimate user is shown in Figure 6.6. Index i relates to the i-th nearest neighboring AP to the legitimate user. For example, index 1 corresponds to the nearest AP, index 2 corresponds to the second nearest AP, and so on. It is shown in Figure 6.6 that, when compared to other neighboring APs, the nearest AP is most likely the optimal one. However, it is also possible that the optimal AP is the second nearest or the third nearest, *etc.* Figure 6.6 also shows that with a smaller value of λ_a, it is more likely that the nearest AP is the optimal one, which therefore explains why the analytical bounds are tighter for smaller values of λ_a, as observed in Figure 6.4 and Figure 6.5.

Third, consider the scenario where the legitimate user is served by the nearest AP in its vicinity, with the implementation of a secrecy protected zone. It is assumed that any malicious eavesdroppers inside the protected zone can be detected by the AP so that these eavesdroppers do not cause any secrecy information loss at the legitimate user. As a result, the secrecy information loss at the legitimate user is caused by eavesdroppers outside the protected zone only. In Fig-

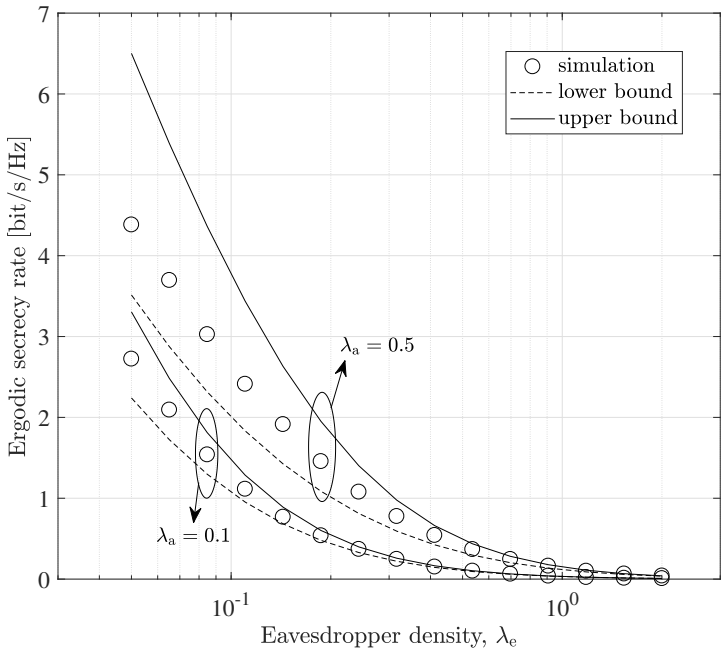

Figure 6.5: *Ergodic secrecy capacity versus eavesdropper density. The legitimate user is served by the optimal AP.*

ure 6.7, the secrecy outage probability is plotted against the density of VLC APs. It is shown that, for a given target secrecy rate, the secrecy outage probability decreases as the AP density increases. However, when λ_{a} is large, further increasing the density of VLC APs only slightly reduces the secrecy outage probability. Also, it is shown that a lower bound on the secrecy outage probability exists when λ_{a} approaches infinity. After implementing a secrecy protected zone, the secrecy outage probability is reduced significantly. More specifically, when $\lambda_{\mathrm{a}} = 1$, $\lambda_{\mathrm{e}} = 0.2$ and the target secrecy rate is $\bar{C}_{\mathrm{s}} = 2$ bit/s/Hz, implementing a secrecy protected zone with radius $D = 1$ m reduces the secrecy outage probability by 0.2. If the secrecy protected zone has a radius of $D = 2$ m, the secrecy outage probability can be reduced to nearly zero. It is also shown in Figure 6.7 that, with a sufficiently large protected area, the secrecy outage probability is no longer bounded at the lower end, *i.e.,* increasing the density of VLC APs can efficiently reduce the secrecy outage probability to zero. Figure 6.8 sets $\lambda_{\mathrm{a}} = 0.5$ and evaluates the impact of the eavesdropper density on the secrecy outage probability. It can be seen that, without the protected zone, the secrecy outage probability can be as large as one if the eavesdropper density is sufficiently high. However, with the implementation of a protected zone, the worst-case scenario of the secrecy outage probability can be limited below a certain level. For example, when the target secrecy rate is $\bar{C}_{\mathrm{s}} = 2$ bit/s/Hz and the protected zone has a radius of $D = 2$ m, the worst-case secrecy outage probability at the legitimate user does not exceed

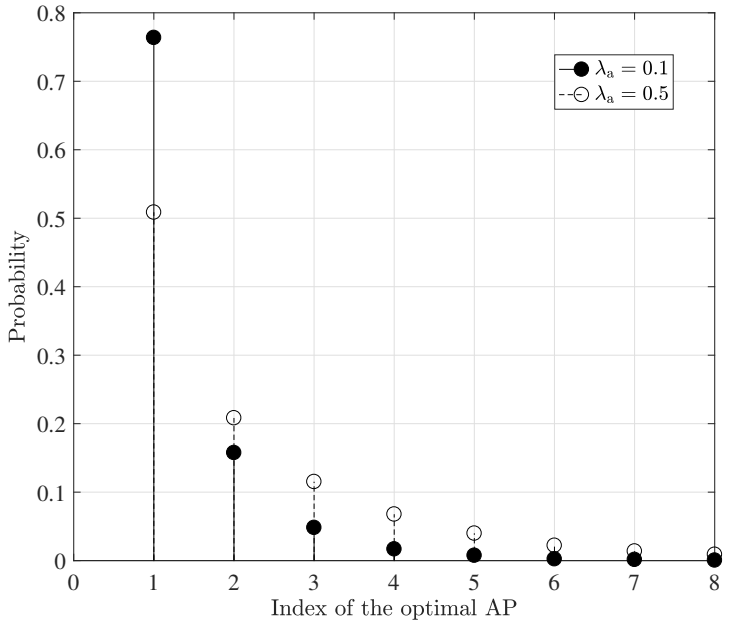

Figure 6.6: *PMF of the index of the optimal AP.* $\lambda_e = 0.2$.

0.12, regardless of the eavesdropper density. To further investigate the impact of the protected zone, Figure 6.9 shows the ergodic secrecy capacity against the radius of the protected zone while fixing the eavesdropper density to $\lambda_e = 0.2$. The slope of the curve shows that a very small protected area brings only marginal improvement on the secrecy performance. However, by further increasing the size of the protected zone, the secrecy performance at the legitimate user can be enhanced significantly. Specifically, when $\lambda_a = 1$ and $\Psi_{1/2} = 30°$, increasing the radius of the protected zone from 0 to 1 m increases the ergodic secrecy capacity by 0.6 bit/s/Hz. In contrast, increasing the radius of the protected zone from 1 to 2 m can increase the ergodic secrecy capacity by 1.9 bit/s/Hz. In Figure 6.9, it is also shown that using more directional LEDs, *i.e.,* LEDs with a smaller semiangle, enhances the secrecy performance at the legitimate user. However, the actual choice of LEDs should also take practical illumination requirements into consideration.

Note that the above obtained results assume full FOV detectors. As nonimaging concentrators typically exhibit a trade-off between gain and FOV, reducing the FOV would give rise to the concentrator gain (see (2.5)). Therefore, legitimate users can enhance the secrecy capacity by employing narrow FOV detectors as long as the VLC link falls within the FOV. There is a similar trade-off at eavesdroppers. Eavesdroppers employing a wide FOV are capable of intercepting VLC signals coming from a wide area, but the amount of interceptable information

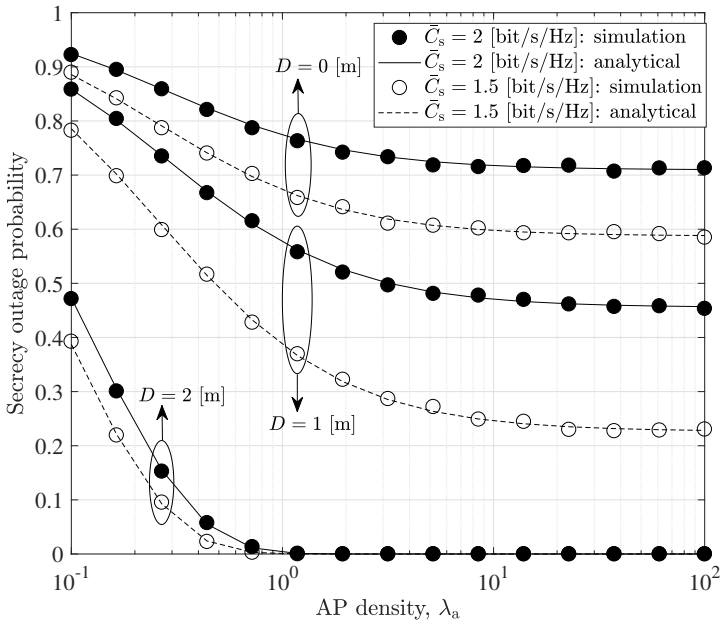

Figure 6.7: *Secrecy outage probability versus AP density. The legitimate user is served by the nearest AP in its vicinity, and eavesdroppers are outside the protected zone with radius D. $\lambda_e = 0.2$.*

is reduced. To better understand this trade-off, the impact of detector FOV on the secrecy capacity is investigated and the simulation results are shown in Figure 6.10. It can be seen that there is an optimal FOV that maximizes the ergodic secrecy capacity. To elaborate more, when the detector FOV is small, increasing FOV enhances the achievable rate of the legitimate link but limits the possibility of eavesdropping to a certain degree, thereby contributing to the secrecy improvement. However, further increasing FOV beyond the optimal point degrades the secrecy performance because the legitimate link is now more prone to eavesdropping. With given simulation parameters, Figure 6.10 shows that detectors with $15 \sim 20^\circ$ FOV are ideal.

6.6 Summary

In this chapter, the physical-layer security in a PPP-based indoor attocell network has been investigated. With the use of mathematical tools from stochastic geometry, analytically tractable expressions for the secrecy outage probability, the ergodic secrecy capacity and their lower and upper bounds are derived. The analytical results are substantiated with extensive Monte Carlo simulations. Moreover, impacts of AP cooperation and the implementation of a secrecy protected zone on the secrecy performance have also been investigated. Results show that co-

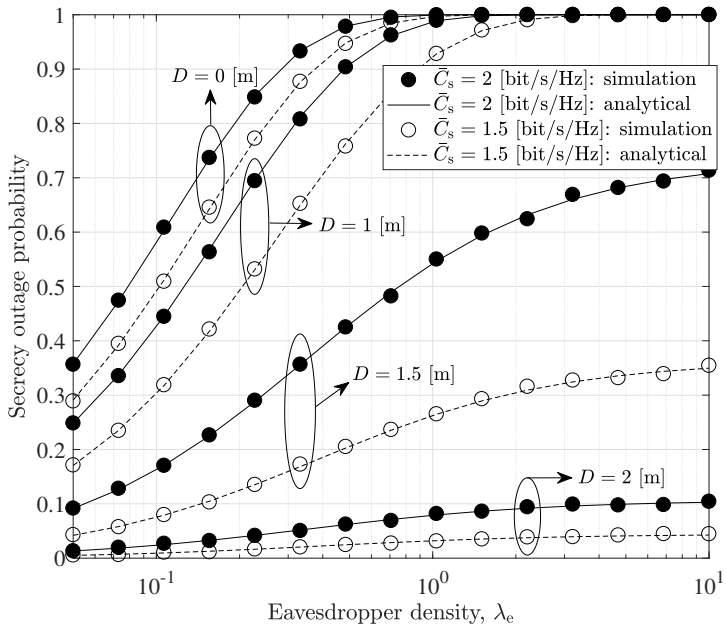

Figure 6.8: *Secrecy outage probability versus eavesdropper density. The legitimate user is served by the nearest AP in its vicinity, and eavesdroppers are outside the protected zone with radius D. $\lambda_a = 0.5$.*

operating neighboring APs can enhance the secrecy performance of attocell networks, but only to a limited extent. Instead, building a secrecy protected zone around APs can significantly improve the network secrecy performance.

With the cooperation of APs, a virtual MISO system can be formed, allowing advanced optical beamforming techniques to be implemented for securer communication. Nevertheless, unearthing the optimal beamformer is no easy task, whose complexity becomes more significant with an increased number of cooperative APs. Moreover, the beamformer design has to take into consideration of the nonnegativity constraint of optical signals, which could further scale up the computing overhead. As the optimal beamformer design requires knowledge of channel state information (CSI) for not only legitimate users but also eavesdroppers, this knowledge may range from partial and statistical CSI to a complete lack of CSI, especially when there is no feedback from passive eavesdroppers.

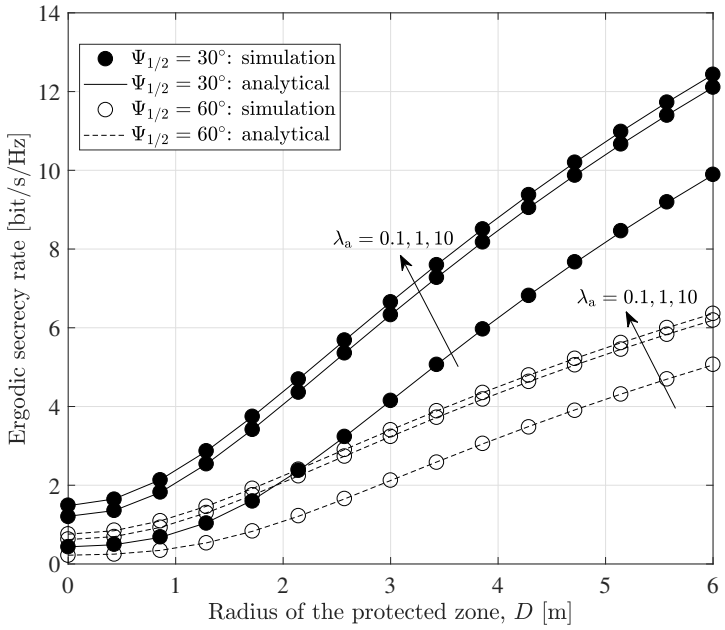

Figure 6.9: *Ergodic secrecy capacity versus the radius of the protected zone. The legitimate user is served by the nearest AP in its vicinity.* $\lambda_e = 0.2$.

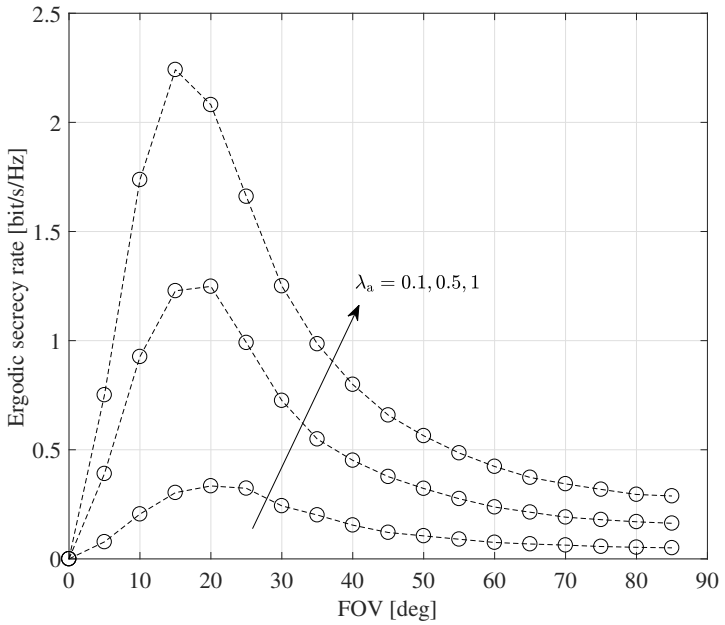

Figure 6.10: *Impact of detector FOV on the secrecy capacity. The legitimate user is served by the nearest AP in its vicinity.* $\lambda_e = 0.2$.

Chapter 7

Conclusions, Limitations and Future Research

7.1 Summary and Conclusions

Indoor attocell networks are usually modeled by placing the access points (APs), typically in the form of light-emitting diodes (LEDs), on a hexagonal grid, with mobile users either deterministically placed or randomly distributed inside the network. Although these models are straightforward to set up, they are by no means tractable and therefore require extensive computer-aided simulations to evaluate the network performance. Also, these models inherently overlook the idleness of APs. Idle APs represent the LEDs that either are inactive or operate in the illumination mode only (without signal transmission). From this point of view, a random thinning process built upon the hexagonal model is more accurate. In this thesis, a stochastic Poisson point process (PPP) model has been proposed to evaluate the performance of indoor attocell networks utilizing visible light communication (VLC) because it can yield close results to the thinned hexagonal model while being significantly more tractable.

Based on the PPP model, fundamental performance metrics of attocell networks have been studied in detail. Specifically, an analytical framework based on the moment generating function (MGF) has been proposed to facilitate accurate characterizations of the signal, interference and signal-to-interference-plus-noise ratio (SINR). The SINR distribution is then utilized to derive the link coverage probability and ergodic capacity. Unlike point-to-point (P2P) VLC, attocell networking is fundamentally limited by the role of interference rather than noise. Since interference is essentially unwanted signals that are intended for other users, it can be used to enhance the link performance if efficiently exploited. This leads to an advanced interference mitigation technique called the successive interference cancellation (SIC), which is capable of decoding interfering signals in order of descending signal powers and subtracting the decoded interfering signal to enhance the SINR. The analytical framework has also been extended to include practical SIC, whose operation is imperfect and leaves residual interference.

The performance of an attocell network can be optimized by selecting optical receivers with low noise figures and implementing interference mitigation techniques. Although the first approach is effective in improving the overall performance, it is costly since the receiver components are often the most expensive part of the communication link. In contrast, the second approach is more attractive and practical because it enhances the network performance with a reasonable amount of implementation overhead. Therefore, interference mitigation techniques have been the focus of this thesis. In general, interference in an attocell network can be classified into two categories: inter-cell interference (ICI) and intra-cell interference. ICI exists in most networks and it originates from APs that are transmitting signals to other users on the same communication resource. Intra-cell interference originates when the AP inside an attocell multiplexes signals for a number of users for transmission on the same communication resource. Examples of this kind are code division multiplexing and power domain multiplexing.

To address the ICI problem in attocell networks, the coordinated multipoint (CoMP) with joint transmission (JT) has been investigated. CoMP-JT aims to reduce the ICI level by cooperating a cluster of APs. Through cooperation, user signals and the channel state information (CSI) are mutually shared via backhaul communications. In this way, ICI can be effectively converted into useful signals to enhance the SINR. Depending on the specifically implemented JT scheme, interference-converted signals can be added in a coherent or noncoherent manner. For coherent JT, signals are preprocessed based on the CSI, *i.e.,* using zero-forcing precoding, so that the received signals are coherently constructed in amplitude. For noncoherent JT, signals are transmitted without joint frame alignment so that the received signal power is combined. For both JT schemes, the exact probability density functions (PDFs) of the signal power and interference have been derived by inverting their characteristic functions. However, the derived characteristic functions are in completed forms and no explicit expressions for the PDFs are available. Motivated by this, the distribution functions for the signal power and interference are approximated with second-order moment matching. It has been shown that, for noncoherent JT, the signal power and interference can both be modeled by gamma distributions. For coherent JT, it has been shown that the signal power and interference can be approximated by a generalized gamma distribution and a gamma distribution, respectively. The approximated distributions of signal power and interference allow the link coverage probability to be derived straightforwardly. Combing analytical results and simulations, it has been shown that, although coherent JT requires more stringent signal synchronization and has higher implementation cost than the noncoherent counterpart, it yields superior coverage performance. Moreover, the per-

formance gain of coherent JT over noncoherent JT is more evident for attocell networks with a dense deployment of APs and high SINR requirements.

Although intra-cell interference can be avoided with the use of orthogonal multiple access (OMA) schemes, they lead to a limited network throughput, especially when there are a large number of users at the cell edge. To achieve higher network throughputs, non-orthogonal multiple access (NOMA) has been proposed in this thesis as an effective technique to mitigate the intra-cell interference. The benefits of NOMA originate from power-domain multiplexing at the transmitter side and SIC at the receiver side. Specifically, although the received signal at each user contains unwanted signal copies that are intended for other users, the dominant part of intra-cell interference can be mitigated by SIC so that it does not noticeably degrade the SINR. This work has provided a theoretical framework for the performance evaluation of NOMA and characterized its throughput gain over the traditional OMA technique. Results reveal that the performance gain of NOMA can be further enlarged with appropriate user selection and pairing algorithms. In fact, it is advantageous to pair users with distinctive channel conditions because this allows unwanted signals to be more effectively removed in the SIC process.

Along with interference and multiuser access, another important performance indicator of optical attocell networks is information security. Although the network security can be linked to all seven layers of the Open Systems Interconnect (OSI) model, the top six layers all rely on the bottom physical layer to deliver the information. Therefore, the physical-layer security is critical for all information security assets and it is the focus of the last part of this thesis. Compared to traditional radio frequency (RF) wireless networks, VLC-based attocell networks are inherently more secure because the transmitted signal does not penetrate through opaque walls and hence can be well confined within the room where it originates. Moreover, compared to RF channels, VLC channels have a higher path-loss exponent. As a result, given that all other parameters remain the same, the eavesdropped signal in VLC would experience a severer attenuation than that in RF. To quantify the secrecy performance of attocell networks, the information-theoretic secrecy capacity has been investigated. Using mathematical tools from stochastic geometry, analytical expressions for the secrecy outage probability, the ergodic secrecy capacity, as well as their lower and upper bounds, have been derived and simplified into tractable forms. Furthermore, two secrecy enhancement techniques, namely AP cooperation and eavesdropper-free protected zones, have been proposed and included into the analytical framework. Results show that AP cooperation can enhance the secrecy performance of attocell

networks, but the gain is limited. The implementation of eavesdropper-free protected zones, on the other hand, is more effective and it can significantly improve the network security.

Through modeling and characterizing the role of interference, this thesis shows that interference is one of the bottlenecks that fundamentally limit the performance of optical attocell networks. By classifying interference into two categories according to its origination, this thesis has suggested two powerful interference mitigation techniques: CoMP and NOMA. CoMP aims at reducing the level of ICI by exploiting the spatial diversity among the distributed APs. Therefore, it is most applicable to attocell networks with a dense deployment of optical APs. NOMA, on the other hand, offers throughput gains by utilizing the spatial diversity of the multiuser channel. As a result, significant performance gains are expected for attocell networks with sparsely distributed mobile users. On the physical layer, VLC is expected to provide higher information securities as visible light can be more easily confined and managed than radio waves. In this regard, physical secrecy enhancement measures are promising solutions for future optical attocell networks.

7.2 Limitations and Future Research

In this thesis, the analytical frameworks proposed to evaluate optical attocell networks are based on the stochastic PPP model. This is an idealized model, where no restrictions are added upon neighboring APs. However, there exist practical modeling restrictions on the total number of APs and their locations. In this sense, the development of a refined model that more accurately reflects practical scenarios can be the subject of future work. Towards this direction, it is of interest to build an analytical framework upon the thinned hexagonal model, in which the hexagons represent physical locations of LED luminaries and the thinning process captures the activeness of APs.

In Chapter 2, a complete VLC channel model including the line-of-sight (LOS) and diffuse links has been studied via a recursive approach. Although the model captures the wavelength-dependent multipath dispersion characteristics of VLC, it is mathematically intractable and its computation relies on computer simulations. Therefore, the analysis presented in this thesis is focused on the LOS link because it is the dominate part of the VLC channel and it allows tractable analytical results to be derived. A tractable yet accurate VLC channel model may be studied in future work. Also, the attocell network under investigation is configured in an

empty space without any obstructions or objects while a real environment may contain multiple interiors. In this case, the channel model becomes more complicated and is subject to random shadowing. In addition, this thesis assumes a vertical receiver orientation in the link setup. This assumption is made to simplify the user-AP association rule, according to which the user is guaranteed to receive signals with the highest power from the nearest AP. When receiver devices are subject to random orientations, the channel model would become more involved and the result of user-AP association would also change. Future works on this subject may relax these assumptions. For example, instead of assuming a vertical receiver orientation, a probabilistic model capturing the orientation profile of mobile users can be developed.

At the receiver front-end, optical compound parabolic concentrators (CPCs) are used in order to enhance the effective detection area of photodiodes (PDs). This is a cost-effective method because an off-the-shelf PD with a large detection area is very expensive. Compared to a bare PD, which has a full filed-of-view (FOV), a CPC limits the FOV to a certain angle. Light rays whose incident angle is greater than the FOV is blocked. Intuitively, using CPCs with a smaller FOV can enhance the channel gain and limit the interference level. However, it complicates the modeling of interfering APs. In this thesis, a wide FOV of 90° is assumed. A generalization on this subject is worth investigating further.

In Chapter 3 and Chapter 5, SIC has been utilized as an interference mitigation technique to address the inter-cell interference (ICI) and intra-cell interference, respectively. In Chapter 3, the SIC capability is characterized by a simplified model, which assumes that the interference generated by APs inside a disk-shaped area is cancellable. However, the performance of practical SIC depends on the interference demodulation and remodulation processes, and only interference whose equivalent SINR exceeds a certain threshold is cancellable. Also, residual interference exists in SIC because interference demodulation and remodulation processes are subject to errors and imperfections. A linear relationship is used in Chapter 3 to model the residual interference, which may be inaccurate for real-world systems. Similarly, the performance of NOMA studied in Chapter 5 assumes perfect SIC. However, the performance of practical NOMA-based attocell networks may subject to certain degradations.

In Chapter 4, CoMP-JT has been investigated as an ICI mitigation technique for optical attocell networks, whose operation relies on the cooperation and data exchange among APs. It has been assumed in the analysis that the backhaul link can provide error-free coordination and data exchange. However, the backhaul link in practical applications has delivery latency and limited

capacity. The latency affects the duration for which the CSI remains valid, depending on user mobilities. In fact, apart from the feedback scheduling delay, additional backhaul latency can be caused by hardware limitations and the necessary time required for signal processing. The second limiting factor is the backhaul capacity, which should be much larger than the downlink delivery rate because not only the CSI but also the user data need to be shared among cooperative APs. Furthermore, the AP cooperation scheme is based on a static clustering approach. Hence, it has the drawback that the coordinated APs are not optimized for individual users.

It has been shown in Chapter 5 that when two users are selected for NOMA, the optimum network throughput can be achieved by pairing two users with the most distinctive channel conditions. On this topic, it would be interesting to study a more general case, where a multiplicity of users (more than two) are clustered for NOMA. Although the proposed analytical framework can be used to evaluate the performance of NOMA with arbitrary power allocation coefficients, it does not shed light on the optimal power allocation algorithm that maximizes the network throughput or user fairness. Moreover, the study of NOMA is restricted to a single attocell for the purpose of mitigating intra-cell interference. Future works may include the investigation of more advanced techniques that are capable of mitigating the ICI and intra-cell interference simultaneously. Towards this directions, multiple-input and multiple-out (MIMO) and optical beamforming techniques are worth investigating.

The physical-layer security discussed in Chapter 6 only considers wiretapping of a standalone eavesdropper. However, practical attocell networks may also be vulnerable to more harmful jamming attacks, in which malicious users may generate disrupting signals to prevent legitimate users from accessing the network. To avoid this kind of attack, spectrum sensing techniques can be further investigated as a means of jamming signal detection and prevention. Moreover, the analysis presented in Chapter 6 assumes that eavesdroppers do not collude. In the presence of colluding eavesdroppers, they are able to exchange and combine the information received to facilitate joint signal detection. In this case, the network secrecy performance would be degraded further. Future works may also include artificial-noise-aided secrecy enhancement techniques, which allow APs to generate specific interfering signals as artificial noise to degrade the performance of eavesdroppers. Since additional communication resources are utilized for artificial noise, this approach unavoidably reduces the achievable data rate of legitimate users.

The interference mitigation techniques discussed in this thesis implicitly assume the knowledge of perfect CSI at the transmitter. However, in practice, channel uncertainty may arise due to user

location uncertainties, noisy channel estimations, erroneous and/or outdated CSI feedbacks. In these scenarios, the estimated channel vector at AP i, denoted by $\hat{\mathbf{h}}_i$, can be modeled by [168]:

$$\hat{\mathbf{h}}_i = \mathbf{h}_i + \boldsymbol{\epsilon}_i, \tag{7.1}$$

where $\mathbf{h}_i$ is the true channel coefficient vector at AP i and $\boldsymbol{\epsilon}_i$ is the channel estimation error vector. Note that vectors $\hat{\mathbf{h}}_i$, $\mathbf{h}_i$ and $\boldsymbol{\epsilon}_i$ all have the same size, which is equivalent to the number of users. Noisy CSI can be modeled by considering $\boldsymbol{\epsilon}_i$ as a Gaussian distribution with zero mean while outdated CSI can be modeled by bounding the Euclidean norm of $\boldsymbol{\epsilon}_i$ [168]. Since the discussed interference mitigation techniques all depend on CSI, re-evaluating the network performance with CSI uncertainties can be future work.

In this thesis, VLC APs are assumed to be single-LED luminaires. Transmit diversity can be achieved when using multi-LED transmitters to form a multiple-input single-output (MISO) system[1]. However, a densely packed multi-LED transmitter in the form an LED array may not offer a high diversity gain due to the absence of multipath fading in VLC channels. To overcome this issue, techniques such as multi-color LED transmitters can be investigated because PDs have different responsivities at different wavelengths, thereby offering different channel gains.

Last but not least, the studies conducted in this thesis are based on analytical evaluations and computer simulations, where some idealized assumptions are made to facilitate the process. In this regard, experimental validations are necessary to verify the accuracy and practicality of the obtained results. In doing so, important findings may be revealed and the presented work with practical modifications would be more meaningful towards the implementation of future optical attocell networks.

[1]The CoMP-JT schemes discussed in Chapter 4 can be viewed as a virtual MISO system.

Appendix A

Ergodic Sum Rate of NOMA (Theorem 1)

According to (5.4), the ergodic sum rate of NOMA can be calculated as:

$$\begin{aligned} R^{\text{sum}} &= \sum_{k=1}^{K} \mathbb{E}\left[R_k\right] \\ &= \sum_{k=1}^{K-1} \underbrace{\int_{\kappa_{\min}}^{\kappa_{\max}} \frac{1}{2}\log_2\left(1+\frac{a_k^2 t}{t\sum\limits_{i=k+1}^{K} a_i^2+\frac{1}{\rho}}\right) f'_{h_k^2}(t)\,dt}_{Q_k} + \underbrace{\int_{\kappa_{\min}}^{\kappa_{\max}} \frac{1}{2}\log_2\left(1+\rho a_K^2 t\right) f'_{h_K^2}(t)\,dt}_{Q_K}, \end{aligned} \tag{A.1}$$

where Q_k denotes the ergodic data rate for the k-th user, $k \in \{1, \cdots, K-1\}$, and Q_K denotes the ergodic data rate for the K-th user. Applying binomial expansion, Q_K can be written as:

$$\begin{aligned} Q_K = \frac{\Omega K}{2(m+3)} \sum_{l=0}^{K-1} \Bigg\{ &\frac{(K-1)!}{l!\,(K-1-l)!}(-\Omega)^l \left(\frac{L^2}{r_{\text{e}}^2}+1\right)^{K-1-l} \\ &\times \int_{\kappa_{\min}}^{\kappa_{\max}} \log_2\left(1+\rho a_K^2 t\right) t^{-\frac{l+1}{m+3}-1} \mathrm{d}t \Bigg\}. \end{aligned} \tag{A.2}$$

Integrating by parts, the integration in (A.2) can be rewritten as:

$$\begin{aligned} &\int \log_2\left(1+\rho a_K^2 t\right) t^{-\frac{l+1}{m+3}-1} \mathrm{d}t \\ =& -\frac{m+3}{l+1}\log_2\left(1+\rho a_K^2 t\right) t^{-\frac{l+1}{m+3}} + \frac{1}{\ln(2)}\frac{m+3}{l+1}\int \frac{\rho a_K^2}{1+\rho a_K^2 t} t^{-\frac{l+1}{m+3}} \mathrm{d}t \end{aligned} \tag{A.3}$$

After applying the geometric series, the integration in (A.3) can be calculated as:

$$\begin{aligned}
&\int \frac{\rho a_K^2}{1+\rho a_K^2 t} t^{-\frac{l+1}{m+3}} \mathrm{d}t = \int \left(1 - \sum_{n=0}^{\infty} \left(-\rho a_K^2 t\right)^n\right) t^{-\frac{l+1}{m+3}-1} \mathrm{d}t \\
=& - \int \left(\left(-1 + \sum_{n_1=0}^{\infty} \frac{-\frac{l+1}{m+3}(-\rho a_K^2 t)^{n_1}}{-\frac{l+1}{m+3}+n_1} \right) + \left(\sum_{n_2=0}^{\infty} \frac{n_2(-\rho a_K^2 t)^{n_2}}{-\frac{l+1}{m+3}+n_2} \right) \right) t^{-\frac{l+1}{m+3}-1} \mathrm{d}t \\
=& \frac{m+3}{l+1} \left(-1 + \sum_{n=0}^{\infty} \frac{-\frac{l+1}{m+3}\left(-\rho a_K^2 t\right)^n}{-\frac{l+1}{m+3}+n} \right) t^{-\frac{l+1}{m+3}} \\
=& \frac{m+3}{l+1} \left(-1 + \sum_{n=0}^{\infty} \frac{(1)_n \left(-\frac{l+1}{m+3}\right)_n}{\left(-\frac{l+1}{m+3}+1\right)_n} \frac{\left(-\rho a_K^2 t\right)^n}{n!} \right) t^{-\frac{l+1}{m+3}},
\end{aligned} \tag{A.4}$$

where $(\cdot)_n$ represents the Pochhammer symbol. After replacing the power series in (A.4) with the Gaussian hypergeometric function, the expression for Q_K is obtained, as shown in (5.15). In a similar way, the expression for Q_k can be obtained by applying the quotient rule of the logarithmic function.

Appendix B

Probability of NOMA Achieving Higher Individual Rates than OFDMA (Theorem 2)

The probability that NOMA achieves higher individual data rates than OFDMA can be calculated from:

$$\begin{aligned}&\mathbb{P}\left[R_i > \bar{R}_i, R_j > \bar{R}_j\right]\\ =&\mathbb{P}\left[\underbrace{1+\frac{h_i^2 a_i^2}{h_i^2 a_j^2+\frac{1}{\rho}} > \left(1+\frac{\upsilon_i}{b_i}\rho h_i^2\right)^{b_i}}_{\mathrm{E}_i}, \underbrace{1+\rho h_j^2 a_j^2 > \left(1+\frac{\upsilon_j}{b_j}\rho h_j^2\right)^{b_j}}_{\mathrm{E}_j}\right].\end{aligned} \tag{B.1}$$

Note that the joint PDF of h_i^2 and h_j^2 can be obtained as [149]:

$$f_{h_i^2,h_j^2}(u,v) = \omega f_{h_k^2}(u) f_{h_k^2}(v) F_{h_k^2}(u)^{i-1}\left(1-F_{h_k^2}(v)\right)^{K-j}\left(F_{h_k^2}(v)-F_{h_k^2}(u)\right)^{j-1-i}, \tag{B.2}$$

where $\omega = K!\left((i-1)!\,(j-1-i)!\,(K-j)!\right)^{-1}$. After further simplification, the probability of events E_i and E_j can be written as:

$$\mathbb{P}\left[\mathrm{E}_i\right] = \mathbb{P}\left[h_i^2 < \varsigma\right], \tag{B.3}$$

$$\mathbb{P}\left[\mathrm{E}_j\right] = \mathbb{P}\left[h_j^2 > \varsigma\right]. \tag{B.4}$$

Therefore, the probability that NOMA achieves higher individual rates than OFDMA can be computed as:

$$\begin{aligned}&\mathbb{P}\left[R_i > \bar{R}_i, R_j > \bar{R}_j\right]\\ =&\omega \int_{\varsigma^\star}^{\kappa_{\max}} \underbrace{f_{h_k^2}(v)\left(1-F_{h_k^2}(v)\right)^{K-j}}_{\Xi_1(v)} \left\{ \underbrace{\int_{\kappa_{\min}}^{\varsigma^\star} f_{h_k^2}(u) F_{h_k^2}(u)^{i-1}\left(F_{h_k^2}(v)-F_{h_k^2}(u)\right)^{j-1-i} du}_{\Xi_2(v)} \right\} dv,\end{aligned} \tag{B.5}$$

where $\Xi_1(v)$ can be calculated using the binomial expansion:

$$\Xi_1(v) = \frac{1}{m+3}\sum_{l=0}^{K-j}\frac{(K-j)!}{l!\,(K-j-l)!}\Omega^{l+1}\left(-\frac{L^2}{r_{\mathrm{e}}^2}\right)^{K-j-l} v^{-\frac{l+1}{m+3}-1}. \tag{B.6}$$

Again applying the binomial expansion, the inner integration in (B.5) can be obtained as:

$$\begin{aligned}\Xi_2(v) =& \sum_{p=0}^{i-1}\sum_{q=0}^{j-1-i}\left\{\frac{1}{p+q+1}\frac{(i-1)!\,(j-1-i)!}{p!\,(i-1-p)!\,q!\,(j-1-i-q)!}\Omega^{p+j-1}(-1)^{p+j-i-q}\right.\\ &\left.\times\left(\varsigma^{\star-\frac{p+q+1}{m+3}}-\kappa_{\min}{}^{-\frac{p+q+1}{m+3}}\right)\left(\frac{L^2}{r_{\mathrm{e}}^2}+1\right)^{i-1-p} v^{-\frac{j-1-i-q}{m+3}}\right\}.\end{aligned} \tag{B.7}$$

Combining (B.5)–(B.7), Theorem 2 is proved.

Appendix C
An Upper Bound on the Sum Rate Gain of NOMA over OFDMA (Theorem 3)

The sum rate gain of NOMA over OFDMA can be formulated as:

$$\begin{aligned}\mathbb{E}\left[R_i + R_j - \bar{R}_i - \bar{R}_j\right] =& \frac{1}{2}\int_{\kappa_{\min}}^{\kappa_{\max}} \left(\log_2\left(1 + \frac{a_i^2 t}{a_j^2 t + \frac{1}{\rho}}\right) - b_i \log_2\left(1 + \frac{\upsilon_i}{b_i}\rho t\right)\right) f'_{h_i^2}(t)\mathrm{d}t \\ &+ \frac{1}{2}\int_{\kappa_{\min}}^{\kappa_{\max}} \left(\log_2\left(1 + \rho a_j^2 t\right) - b_j \log_2\left(1 + \frac{\upsilon_j}{b_j}\rho t\right)\right) f'_{h_j^2}(t)\mathrm{d}t.\end{aligned} \tag{C.1}$$

It can be seen from (C.1) that $\mathbb{E}\left[R_i + R_j - \bar{R}_i - \bar{R}_j\right] \approx 0$ when ρ approximates zero. According to Leibniz integral rule, it follows that

$$\begin{aligned}\frac{\partial \mathbb{E}\left[R_i + R_j - \bar{R}_i - \bar{R}_j\right]}{\partial \rho} =& \frac{1}{2\ln(2)}\int_{\kappa_{\min}}^{\kappa_{\max}} \left(\frac{t}{1+\rho t} - \frac{a_j^2 t}{1+\rho a_j^2 t} - \frac{b_i t}{\frac{b_i}{\upsilon_i} + \rho t}\right) f'_{h_i^2}(t)\mathrm{d}t \\ &+ \frac{1}{2\ln(2)}\int_{\kappa_{\min}}^{\kappa_{\max}} \left(\frac{a_j^2 t}{1+\rho a_j^2 t} - \frac{b_j t}{\frac{b_j}{\upsilon_j} + \rho t}\right) f'_{h_j^2}(t)\mathrm{d}t.\end{aligned} \tag{C.2}$$

As ρ increases, the derivative of $\mathbb{E}\left[R_i + R_j - \bar{R}_i - \bar{R}_j\right]$ first drops below zero and then increases to a positive value. Therefore, the trend of the sum rate gain of NOMA over OFDMA is proved. In high SNR regimes, it is straightforward to show:

$$\lim_{\rho\to\infty} \mathbb{E}\left[R_i\right] = \lim_{\rho\to\infty} \int_{\kappa_{\min}}^{\kappa_{\max}} \frac{1}{2}\log_2\left(1 + \frac{a_i^2 t}{a_j^2 t + \frac{1}{\rho}}\right) f'_{h_i^2}(t)\mathrm{d}t = \frac{1}{2}\log_2\left(1 + \frac{a_i^2}{a_j^2}\right) = -\log_2 a_j. \tag{C.3}$$

The data rate for the j-th user participated in NOMA can be divided into two parts:

$$\mathbb{E}\left[R_j\right] = \underbrace{\int_{\kappa_{\min}}^{\kappa_{\max}} b_i \log_2\sqrt{1+\rho a_j^2 t} f'_{h_j^2}(t)\mathrm{d}t}_{\mathrm{N}_1} + \underbrace{\int_{\kappa_{\min}}^{\kappa_{\max}} b_j \log_2\sqrt{1+\rho a_j^2 t} f'_{h_j^2}(t)\mathrm{d}t}_{\mathrm{N}_2}. \tag{C.4}$$

In high SNR regimes, the difference between N_2 and $\mathbb{E}\left[\bar{R}_j\right]$ can be calculated as:

$$\begin{aligned}\lim_{\rho\to\infty}\left(\mathrm{N}_2-\mathbb{E}\left[\bar{R}_j\right]\right)=&\lim_{\rho\to\infty}\frac{1}{2}b_j\int_{\kappa_{\min}}^{\kappa_{\max}}\log_2\frac{1+\rho a_j^2 t}{1+\frac{\upsilon_j}{b_j}\rho t}f'_{h_j^2}(t)\mathrm{d}t\\ =&b_j\log_2 a_j+\frac{1}{2}b_j\log_2\left(\frac{b_j}{\upsilon_j}\right).\end{aligned}\tag{C.5}$$

Applying integration by parts, N_1 in high SNR regimes can be calculated as:

$$\lim_{\rho\to\infty}\mathrm{N}_1=b_i\log_2 a_j+\lim_{\rho\to\infty}\frac{b_i}{2}\log_2\left(1+\rho\kappa_{\min}\right)+\frac{b_i}{2\ln(2)}\int_{\kappa_{\min}}^{\kappa_{\max}}\frac{1}{t}\left(1-F'_{h_j^2}(t)\right)\mathrm{d}t,\tag{C.6}$$

where $F'_{h_j^2}(t)$ represents the CDF of the order variable h_k^2. The integration in (C.6) can be simplified to:

$$\begin{aligned}\int_{\kappa_{\min}}^{\kappa_{\max}}\frac{1}{t}\left(1-F'_{h_j^2}(t)\right)\mathrm{d}t=&\sum_{p=0}^{j-1}\sum_{q=0}^{K-j}\left\{\frac{K!(-1)^{p+K-j-q}\Omega^{p+q+1}}{p!\,(j-1-p)!\,q!\,(K-j-q)!}\left(\frac{L^2}{r_{\mathrm{e}}^2}+1\right)^{j-1-p}\right.\\ &\left.\times\left(\frac{L^2}{r_{\mathrm{e}}^2}\right)^{K-j-q}\left(\varpi_4(\kappa_{\max})-\varpi_4(\kappa_{\min})\right)\right\}-\ln(\kappa_{\min}).\end{aligned}\tag{C.7}$$

In a similar way, $\bar{R}_i$ in high SNR regimes can be calculated as:

$$\begin{aligned}\lim_{\rho\to\infty}\mathbb{E}\left[\bar{R}_i\right]=&\lim_{\rho\to\infty}\frac{b_i}{2}\log_2\left(1+\frac{\upsilon_i}{b_i}\rho\kappa_{\min}\right)-\frac{b_i}{2\ln(2)}\ln(\kappa_{\min})\\ &+\frac{b_i}{2\ln(2)}\sum_{p=0}^{i-1}\sum_{q=0}^{K-i}\left\{\frac{K!}{p!\,(i-1-p)!\,q!\,(K-i-q)!}(-1)^{p+K-i-q}\Omega^{p+q+1}\right.\\ &\left.\times\left(\frac{L^2}{r_{\mathrm{e}}^2}+1\right)^{i-1-p}\left(\frac{L^2}{r_{\mathrm{e}}^2}\right)^{K-i-q}\left(\varpi_4(\kappa_{\max})-\varpi_4(\kappa_{\min})\right)\right\}.\end{aligned}\tag{C.8}$$

Combining (C.3)–(C.8), Theorem 3 is proved.

Appendix D
Optimal User Pairing in NOMA and Its Sum Rate Gain over OFDMA (Corollary 2)

The proof is divided into two parts. First, it is shown that the maximum sum rate gain is achieved when $i = 1$ and $j = K$. Second, it derives the expression of the maximum sum rate gain shown in (5.25). For the first part, it is equivalent to prove the following:

$$\lim_{\rho\to\infty} \mathbb{E}\left[R_{i+1} + R_j - \bar{R}_{i+1} - \bar{R}_j\right] < \lim_{\rho\to\infty} \mathbb{E}\left[R_i + R_j - \bar{R}_i - \bar{R}_j\right], \tag{D.1}$$

for $\forall i < K$, and

$$\lim_{\rho\to\infty} \mathbb{E}\left[R_i + R_{j+1} - \bar{R}_i - \bar{R}_{j+1}\right] > \lim_{\rho\to\infty} \mathbb{E}\left[R_i + R_j - \bar{R}_i - \bar{R}_j\right], \tag{D.2}$$

for $\forall j < K$. The expression in (D.1) is equivalent to

$$\lim_{\rho\to\infty} \mathbb{E}\left[R_{i+1} - R_i - \bar{R}_{i+1} + \bar{R}_i\right] < 0. \tag{D.3}$$

From (C.3), it can be shown that $\lim_{\rho\to\infty} \mathbb{E}\left[R_{i+1}\right] = \lim_{\rho\to\infty} \mathbb{E}\left[R_i\right]$. Therefore, in order to prove (D.1), it is equivalent to prove:

$$\begin{aligned}
&\lim_{\rho\to\infty} \mathbb{E}\left[R_{i+1} - R_i - \bar{R}_{i+1} + \bar{R}_i\right] < 0 \Longrightarrow \lim_{\rho\to\infty} \mathbb{E}\left[\bar{R}_i - \bar{R}_{i+1}\right] < 0 \\
\Longrightarrow &\int_{\kappa_{\min}}^{\kappa_{\max}} \frac{1}{t}\left(1 - F'_{h_i^2}(t)\right) \mathrm{d}t < \int_{\kappa_{\min}}^{\kappa_{\max}} \frac{1}{t}\left(1 - F'_{h_{i+1}^2}(t)\right) \mathrm{d}t \\
\Longrightarrow &F'_{h_i^2}(t) > F'_{h_{i+1}^2}(t).
\end{aligned} \tag{D.4}$$

As $F'_{h_i^2}(t)$ represents the CDF of the i-th largest variable h_i^2, it is obvious that (D.4) is true. To this end, (D.1) is proved. The proof of (D.2) can be conducted in a similar way. For the second part, the expression of (5.25) can be obtained by setting $i = 1$ and $j = K$ in (5.23).

Appendix E
List of Publications

The following articles have resulted from the work presented in this thesis.

E.1 Journal Papers

L. Yin, W. O. Popoola, X. Wu, and H. Haas, "Performance evaluation of non-orthogonal multiple access in visible light communication," *IEEE Trans. Commun.*, vol. 64, no. 12, pp. 5162–5175, Dec. 2016.

L. Yin and H. Haas, "Coverage analysis of multiuser visible light communication networks," *IEEE Trans. Wireless Commun.*, vol. 17, no. 3, pp. 1630–1643, Mar. 2018.

L. Yin and H. Haas, "Physical-layer security in multiuser visible light communication networks," *IEEE J. Sel. Areas Commun.,* vol. 36, no. 1, pp. 162-174, Jan. 2018.

L. Yin and H. Haas, "Joint transmission in multiuser visible light communication networks," *IEEE Trans. Mobile Comput.,* (*major revision, Mar. 2018*).

E.2 Book Chapters

L. Yin and H. Haas, "Application of non-orthogonal multiple access to visible light communication networks," in *Multiple Access Techniques for 5G wireless Networks and Beyond*, Springer, (*to appear*).

E.3 Conference Papers

L. Yin, X. Wu, and H. Haas, "SDMA grouping in coordinated multi-point VLC systems," in *Proc. IEEE Summer Topicals Meeting Series (SUM),* Nassau, Bahamas, July 2015, pp. 169-170.

L. Yin, X. Wu, and H. Haas, "Indoor visible light positioning with angle diversity transmitter," in *Proc. IEEE Vehicular Technology Conference (VTC)*, Boston, MA, Sept. 2015, pp. 1–5.

L. Yin, X. Wu, and H. Haas, "On the performance of non-orthogonal multiple access in visible light communication," in *Proc. IEEE 26th Annual Symposium on Personal, Indoor and Mobile Radio Communications (PIMRC)*, Hong Kong, China, Sept. 2015, pp. 1376–1381.

L. Yin, X. Wu, H. Haas, and L. Hanzo, "Low-complexity SDMA user-grouping for the CoMP-VLC downlink," in *Proc. IEEE Global Communications Conference (GLOBECOM),* San Diego, CA, Dec. 2015, pp. 1-6.

L. Yin, M. S. Islim, and H. Haas, "LiFi: Transforming fibre into wireless," in *Proc. SPIE Broadband Access Communication Technologies XI,* San Francisco, CA, Jan. 2017, pp. 1-9.

E.4 Contributed Papers

H. Haas, L. Yin, Y. Wang, and C. Chen, "What is LiFi?" *J. Lightw. Technol.*, vol. 34, no. 6, pp. 1533–1544, Mar. 2016.

M. F. Leitao, C. Foucher, M. Islim, L. Yin, B. Guilhabert, A. Krysa, S. Videv, E. Xie, E. Gu, H. Haas, N. Laurand, and M. D. Dawson, "Laser-excited 580nm AlGaInP nanomembrane for visible light communications," in *Light, Energy and the Environment*. Optical Society of America, 2016, p. JW4A.2.

K. Rae, C. Foucher, B. Guilhabert, M. S. Islim, L. Yin, D. Zhu, R. A. Oliver, D. J. Wallis, H. Haas, N. Laurand, and M. D. Dawson, "InGaN LEDs integrated onto colloidal quantum dot functionalized ultra-thin glass," Opt. Express, vol. 25, no. 16, pp. 19179-19184, July 2017.

M. F. Leitao, M. S. Islim, L. Yin, S. Viola, S. Watson, A. Kelly, X. Li, D. Yu, H. Zeng, S. Videv, H. Haas, E. Gu, N. Laurand, and M. D. Dawson, "MicroLED-pumped perovskite quantum dot color converter for visible light communications," in *Proc. IEEE Photonics Conference (IPC),* Orlando, FL, USA, Oct. 2017, pp. 69-70.

References

[1] Vishay, *Power SMD LED PLCC-2*. [Online]. Available: http://www.vishay.com/docs/81273/vlmw33.pdf

[2] First Sensor, *PC0.55-5t THD PIN Photo Diode #501289*. [Online]. Available: http://www.first-sensor.com/cms/upload/datasheets/PC0.55-5t_THD_501289_501290.pdf

[3] A. J. C. Moreira, R. T. Valadas, and A. M. de Oliveria Duarte, "Optical interference produced by artifical light," *Wireless Networks*, vol. 3, no. 2, pp. 131–140, May 1997.

[4] T. Komine and M. Nakagawa, "Fundamental analysis for visible-light communication system using LED lights," *IEEE Trans. Consum. Electron.*, vol. 50, no. 1, pp. 100–107, Feb. 2004.

[5] P. Djahani and J. M. Kahn, "Analysis of infrared wireless links employing multibeam transmitters and imaging diversity receivers," *IEEE Trans. Commun.*, vol. 48, no. 12, pp. 2077–2088, Dec. 2000.

[6] K. Lee, H. Park, and J. R. Barry, "Indoor channel characteristics for visible light communications," *IEEE Commun. Lett.*, vol. 15, no. 2, pp. 217–219, Feb. 2011.

[7] "Cisco visual networking index: Global mobile data traffic forecast update, 2016-2021," White Paper, Cisco, Mar. 2017.

[8] Y. Tanaka, S. Haruyama, and M. Nakagawa, "Wireless optical transmissions with white colored LED for wireless home links," in *Proc. 11th IEEE International Symposium on Personal Indoor and Mobile Radio Communications (PIMRC)*, London, UK, Sept. 2000, pp. 1325–1329.

[9] H. T. Friis, "A note on a simple transmission formula," *Proceedings of the IRE*, vol. 34, no. 5, pp. 254–256, May 1946.

[10] "Status of IEEE 802.11 light communication SG," Meeting Update, Jan. 2018, accessed 3 May 2018. [Online]. Available: http://www.ieee802.org/11/Reports/lcsg_update.htm

[11] IEEE Std. 802.15.7-2011, *IEEE Standard for Local and Metropolitan Area Networks, Part 15.7: Short-Range Wireless Optical Communication Using Visible Light*, IEEE Std., 2011.

[12] H. Haas, "High-speed wireless networking using visible light," *SPIE Newsroom*, Apr. 2013.

[13] S. M. Kim and S. M. Kim, "Performance improvement of visible light communications using optical beamforming," in *Proc. Fifth International Conference on Ubiquitous and Future Networks (ICUFN),*, Da Nang, Vietnam, July 2013, pp. 362–365.

[14] A. Mostafa and L. Lampe, "Optimal and robust beamforming for secure transmission in MISO visible-light communication links," *IEEE Trans. Signal Process.*, vol. 64, no. 24, pp. 6501–6516, Dec. 2016.

[15] I. Stefan, H. Burchardt, and H. Haas, "Area spectral efficiency performance comparison between VLC and RF femtocell networks," in *Proc. IEEE International Conference on Communications (ICC)*, Budapest, June 2013, pp. 3825–3829.

[16] N. Bhushan, J. Li, D. Malladi, R. Gilmore, D. Brenner, A. Damnjanovic, R. T. Sukhavasi, C. Patel, and S. Geirhofer, "Network densification: The dominant theme for wireless evolution into 5G," *IEEE Commun. Mag.*, vol. 52, no. 2, pp. 82–89, Feb. 2014.

[17] V. Jungnickel, K. Manolakis, W. Zirwas, B. Panzner, V. Braun, M. Lossow, M. Sternad, R. Apelfrojd, and T. Svensson, "The role of small cells, coordinated multipoint, and massive MIMO in 5G," *IEEE Commun. Mag.*, vol. 52, no. 5, pp. 44–51, May 2014.

[18] V. Chandrasekhar, J. G. Andrews, and A. Gatherer, "Femtocell networks: A survey," *IEEE Commun. Mag.*, vol. 46, no. 9, pp. 59–67, Sept. 2008.

[19] J. G. Andrews, S. Buzzi, W. Choi, S. Hanly, A. Lozano, A. C. K. Soong, and J. C. Zhang, "What will 5G be?" *IEEE J. Sel. Areas Commun.*, vol. 32, no. 6, pp. 1065–1082, June 2014.

[20] M. Jaber, M. A. Imran, R. Tafazolli, and A. Tukmanov, "5G backhaul challenges and emerging research directions: A survey," *IEEE Access*, vol. 4, pp. 1743–1766, May 2016.

[21] H. Haas, L. Yin, Y. Wang, and C. Chen, "What is LiFi?" *J. Lightw. Technol.*, vol. 34, no. 6, pp. 1533–1544, Mar. 2016.

[22] A. M. Vegni and T. D. C. Little, "Handover in VLC systems with cooperating mobile devices," in *Proc. International Conference on Computing, Networking and Communications (ICNC)*, Maui, HI, USA, Jan. 2012, pp. 126–130.

[23] D. Tse and P. Viswanath, *Fundamentals of Wireless Communication*. New York, NY, USA: Cambridge University Press, 2005.

[24] A. J. Viterbi, *CDMA: Principles of Spread Spectrum Communication*. Redwood City, CA, USA: Addison Wesley Longman Publishing Co., Inc., 1995.

[25] R. v. Nee and R. Prasad, *OFDM for Wireless Multimedia Communications*, 1st ed. Norwood, MA, USA: Artech House, Inc., 2000.

[26] Y. G. Li and G. L. Stuber, *Orthogonal Frequency Division Multiplexing for Wireless Communications*, 1st ed. Boston, MA, USA: Springer US, 2006.

[27] C. Y. Wong, R. S. Cheng, K. B. Letaief, and R. D. Murch, "Multiuser OFDM with apaptive subcarrier, bit, and power allocation," *IEEE J. Sel. Areas Commun.*, vol. 17, no. 10, pp. 1747–1758, Oct. 1999.

[28] L. Dai, B. Wang, Y. Yuan, S. Han, C.-L. I, and Z. Wang, "Non-orthogonal multiple access for 5G: Solutions, challenges, opportunities, and future research trends," *IEEE Commun. Mag.*, vol. 53, no. 9, pp. 74–81, Sept. 2015.

[29] Y. Liu, Z. Qin, M. Elkashlan, Z. Ding, A. Nallanathan, and L. Hanzo, "Nonorthogonal multiple access for 5G and beyond," *Proc. IEEE*, vol. 105, no. 12, pp. 2347–2381, Dec. 2017.

[30] Y. Saito, Y. Kishiyama, A. Benjebbour, T. Nakamura, A. Li, and K. Higuchi, "Non-orthogonal multiple access (NOMA) for cellular future radio access," in *Proc. IEEE Vehicular Technology Conference (VTC Spring)*, Dresden, Germany, June 2013, pp. 1–5.

[31] Y. Saito, A. Benjebbour, Y. Kishiyama, and T. Nakamura, "System level performance evaluation of downlink non-orthogonal multiple access (NOMA)," in *Proc. IEEE Annual Symposium on Personal, Indoor and Mobile Radio Communications (PIMRC)*, London, UK, Sept. 2013, pp. 611–615.

[32] A. Benjebbovu, A. Li, Y. Saito, Y. Kishiyama, A. Harada, and T. Nakamura, "System-level performance of downlink NOMA for future LTE enhancements," in *Proc. IEEE Globecom Workshops (GC Wkshps)*, Atlanta, GA, USA, Dec. 2013, pp. 66–70.

[33] A. Benjebbour, Y. Saito, Y. Kishiyama, A. Li, A. Harada, and T. Nakamura, "Concept and practical considerations of non-orthogonal multiple access (NOMA) for future radio access," in *Proc. International Symposium on Intelligent Signal Processing and Communication Systems*, Naha, Japan, Nov. 2013, pp. 770–774.

[34] H. Nikopour and H. Baligh, "Sparse code multiple access," in *Proc. IEEE 24th Annual International Symposium on Personal, Indoor, and Mobile Radio Communications (PIMRC)*, London, UK, Sept. 2013, pp. 332–336.

[35] M. Taherzadeh, H. Nikopour, A. Bayesteh, and H. Baligh, "SCMA codebook design," in *Proc. IEEE 80th Vehicular Technology Conference (VTC2014-Fall)*, Vancouver, BC, Canada, Sept. 2014, pp. 1–5.

[36] S. Chen, B. Ren, Q. Gao, S. Kang, S. Sun, and K. Niu, "Pattern division multiple access – a novel nonorthogonal multiple access for fifth-generation radio networks," *IEEE Trans. Veh. Technol.*, vol. 66, no. 4, pp. 3185–3196, Apr. 2017.

[37] T. Cover, "Broadcast channels," *IEEE Trans. Inf. Theory*, vol. 18, no. 1, pp. 2–14, Jan. 1972.

[38] T. M. Cover and J. A. Thomas, *Elements of Information Theory*, 2nd ed. New York: Wiley-Interscience, 2006.

[39] J. G. Andrews, "Interference cancellation for cellular systems: A contemporary overview," *IEEE Wireless Commun.*, vol. 12, no. 2, pp. 19–29, Apr. 2005.

[40] S. P. Weber, J. G. Andrews, X. Yang, and G. de Veciana, "Transmission capacity of wireless *ad hoc* networks with successive interference cancellation," *IEEE Trans. Inf. Theory*, vol. 53, no. 8, pp. 2799–2814, Aug. 2007.

[41] G. Boudreau, J. Panicker, N. Guo, R. Chang, N. Wang, and S. Vrzic, "Interference coordination and cancellation for 4G networks," *IEEE Commun. Mag.*, vol. 47, no. 4, pp. 74–81, Apr. 2009.

[42] J. B. Carruthers and J. M. Kahn, "Angle diversity for nondirected wireless infrared communication," *IEEE Trans. Commun.*, vol. 48, no. 6, pp. 960–969, June 2000.

[43] L. Yin, X. Wu, and H. Haas, "Indoor visible light positioning with angle diversity transmitter," in *Proc. IEEE Vehicular Technology Conference (VTC)*, Boston, MA, Sept. 2015, pp. 1–5.

[44] Z. Chen and H. Haas, "Space division multiple access in visible light communications," in *Proc. IEEE International Conference on Communications (ICC)*, London, UK, June 2015, pp. 5115–5119.

[45] D. Stoyan, W. Kendall, and J. Mecke, *Stochastic Geometry and Its Applications*, 2nd ed. John Wiley and Sons, 1996.

[46] A. Baddeley, I. Bárány, R. Schneider, and W. Weil, *Stochastic Geometry*, ser. Lecture Notes in Mathematics. Springer-Verlag Berlin Heidelberg, 2007.

[47] H. ElSawy, E. Hossain, and M. Haenggi, "Stochastic geometry for modeling, analysis, and design of multi-tier and cognitive cellular wireless networks: A survey," *IEEE Commun. Surveys Tuts.*, vol. 15, no. 3, pp. 996–1019, Third Quarter 2013.

[48] M. Haenggi, *Stochastic Geometry for Wireless Networks*, 1st ed. New York, NY, USA: Cambridge University Press, 2012.

[49] F. Baccelli and B. Błaszczyszyn, "Stochastic geometry and wireless networks: Volume I theory," *Foundations and Trends in Networking*, vol. 3, no. 3-4, pp. 249–449, Jan. 2010.

[50] T. Komine and M. Nakagawa, "Integrated system of white LED visible-light communication and power-line communication," *IEEE Trans. Consum. Electron.*, vol. 49, no. 1, pp. 71–79, 2003.

[51] J. C. Maxwell, *A Treatise on Electricity and Magnetism*, 1st ed. Oxford, UK: Clarendon Press, 1873.

[52] J. G. Andrews, F. Baccelli, and R. K. Ganti, "A tractable approach to coverage and rate in cellular networks," *IEEE Trans. Commun.*, vol. 59, no. 11, pp. 3122–3134, Nov. 2011.

[53] M. Afshang and H. S. Dhillon, "Fundamentals of modeling finite wireless networks using binomial point process," *IEEE Trans. Wireless Commun.*, vol. 16, no. 5, pp. 3355–3370, May 2017.

[54] M. Haenggi, "Mean interference in hard-core wireless networks," *IEEE Commun. Lett.*, vol. 15, no. 8, pp. 792–794, Aug. 2011.

[55] R. K. Ganti and M. Haenggi, "Interference and outage in clustered wireless *ad hoc* networks," *IEEE Trans. Inf. Theory*, vol. 55, no. 9, pp. 4067–4086, Aug. 2009.

[56] J.-S. Ferenc and Z. Néda, "On the size distribution of poisson voronoi cells," *Phy. A Stat. Mech. Appl.*, vol. 385, no. 2, pp. 518–526, Nov. 2007.

[57] C. H. Chang, C. Y. Li, H. H. Lu, C. Y. Lin, J. H. Chen, Z. W. Wan, and C. J. Chen, "A 100-Gb/s multiple-input multiple-output visible laser light communication system," *J. Lightw. Technol.*, vol. 32, no. 24, pp. 4723–4729, Oct. 2014.

[58] D. Tsonev, S. Videv, and H. Haas, "Towards a 100 Gb/s visible light wireless access network," *Opt. Express*, vol. 23, no. 2, pp. 1627–1637, Jan. 2015.

[59] M. F. Leitao, C. Foucher, M. Islim, L. Yin, B. Guilhabert, A. Krysa, S. Videv, E. Xie, E. Gu, H. Haas, N. Laurand, and M. D. Dawson, "Laser-excited 580nm AlGaInP nanomembrane for visible light communications," in *Light, Energy and the Environment*. Optical Society of America, 2016, p. JW4A.2.

[60] J. Kahn and J. Barry, "Wireless infrared communications," *Proc. IEEE*, vol. 85, no. 2, pp. 265–298, Feb. 1997.

[61] E. Schubert, *Light-Emitting Diodes*. Cambridge: Cambridge University Press, 2006.

[62] T. Q. Khanh, P. Bodrogi, Q. T. Vinh, and H. Winkler, *LED Lighting: Technology and Perception*. Weinheim: Wiley-VCH Verlag GmbH & Co. KGaA, 2014.

[63] W. O. Popoola, "Impact of VLC on light emission quality of white LEDs," *J. Lightw. Technol.*, vol. 34, no. 10, pp. 2526–2532, May 2016.

[64] H. Elgala, R. Mesleh, and H. Haas, "An LED model for intensity-modulated optical communication systems," *IEEE Photon. Technol. Lett.*, vol. 22, no. 11, pp. 835–837, 2010.

[65] S. Dimitrov and H. Haas, "Information rate of OFDM-based optical wireless communication systems with nonlinear distortion," *J. Lightw. Technol.*, vol. 31, no. 6, pp. 918–929, Mar. 2013.

[66] S. Pimputkar, J. S. Speck, S. P. DenBaars, and S. Nakamura, "Prospects for LED lighting," *Nature Photon.*, vol. 3, pp. 180–182, 2009.

[67] F. R. Gfeller and U. Bapst, "Wireless in-house data communication via diffuse infrared radiation," *Proc. IEEE*, vol. 67, no. 11, pp. 1474–1486, Nov. 1979.

[68] I. Moreno and C.-C. Sun, "Modeling the radiation pattern of LEDs," *Opt. Express*, vol. 16, no. 3, pp. 1808–1819, Jan. 2008.

[69] F. M. Mims, *Siliconnections: Coming of Age in the Electronic Era*. New York: McGraw-Hill, 1986.

[70] P. Dietz, W. Yerazunis, and D. Leigh, "Very low-cost sensing and communication using bidirectional LEDs," in *Proc. UbiComp*, A. Dey, A. Schmidt, and J. McCarthy, Eds., vol. 2864. Seattle, Washington: Springer, Berlin, Heidelberg, Oct. 2003, pp. 175–191.

[71] D. Giustiniano, N. O. Tippenhauer, and S. Mangold, "Low-complexity visible light networking with LED-to-LED communication," in *Proc. IFIP Wireless Days*, Dublin, Nov. 2012, pp. 1–8.

[72] S. Schmid, G. Corbellini, S. Mangold, and T. R. Gross, "LED-to-LED visible light communication networks," in *Proc. Fourteenth ACM International Symposium on Mobile Ad Hoc Networking and Computing (MobiHoc)*, Bangalore, India, July 2013, pp. 1–10.

[73] B. E. A. Saleh and M. C. Teich, *Fundamentals of Photonics*, 2nd ed. New York: John Wiley & Sons, Inc, 1991.

[74] Z. Ghassemlooy, W. Popoola, and S. Rajbhandari, *Optical Wireless Communications: System and Channel Modelling with MATLAB*, 1st ed. Boca Raton: CRC Press, 2012.

[75] K. Phang and D. A. Johns, "A CMOS optical preamplifier for wireless infrared communications," *IEEE Trans. Circuits Syst. II, Analog Digit. Signal Process.*, vol. 46, no. 7, pp. 852–859, July 1999.

[76] S. D. Personick, "Receiver design for digital fiber optic communications systems, I and II," *Bell Syst. Techn. J.*, vol. 52, no. 6, pp. 843–886, July - Aug. 1973.

[77] J. B. Johnson, "Thermal agitation of electricity in conductors," *Phys. Rev.*, vol. 32, no. 1, pp. 97–109, July 1928.

[78] D. Tsonev, H. Chun, S. Rajbhandari, J. McKendry, S. Videv, E. Gu, M. Haji, S. Watson, A. Kelly, G. Faulkner, M. Dawson, H. Haas, and D. O'Brien, "A 3-Gb/s single-LED OFDM-based wireless VLC link using a gallium nitride μLED," *IEEE Photon. Technol. Lett.*, vol. 26, no. 7, pp. 637–640, Apr. 2014.

[79] H. Chun, S. Rajbhandari, G. Faulkner, and D. O'Brien, "Effectiveness of blue-filtering in WLED based indoor visible light communication," in *Proc. 3rd International Workshop in Optical Wireless Communications (IWOW)*, Funchal, Portugal, Sept. 2014, pp. 60–64.

[80] X. Ning, R. Winston, and J. O'Gallagher, "Dielectric totally internally reflecting concentrators," *Appl. Opt.*, vol. 26, no. 2, pp. 300–305, Jan. 1987.

[81] J. Barry, J. Kahn, W. Krause, E. Lee, and D. Messerschmitt, "Simulation of multipath impulse response for indoor wireless optical channels," *IEEE J. Sel. Areas Commun.*, vol. 11, no. 3, pp. 367–379, Apr. 1993.

[82] J. B. Carruthers and J. M. Kahn, "Modeling of nondirected wireless infrared channels," *IEEE Trans. Commun.*, vol. 45, no. 10, pp. 1260–1268, Oct. 1997.

[83] J. B. Carruthers and P. Kannan, "Iterative site-based modeling for wireless infrared channels," *IEEE Trans. Antennas Propag.*, vol. 50, no. 5, pp. 759–765, May 2002.

[84] V. Jungnickel, V. Pohl, S. Nonnig, and C. V. Helmolt, "A physical model of the wireless infrared communication channel," *IEEE J. Sel. Areas Commun.*, vol. 20, no. 3, pp. 631–640, Aug. 2002.

[85] F. Miramirkhani and M. Uysal, "Channel modeling and characterization for visible light communications," *IEEE Photon. J.*, vol. 7, no. 6, pp. 1–16, Dec. 2015.

[86] G. Forney, "Maximum-likelihood sequence estimation of digital sequences in the presence of intersymbol interference," *IEEE Trans. Inf. Theory*, vol. 18, no. 3, pp. 363–378, May 1972.

[87] C. Douillard, M. Jézéquel, C. Berrou, A. Picart, P. Didier, and A. Glavieux, "Iterative correction of intersymbol interference: Turbo-equalization," *Eur. Trans. Telecomm.*, vol. 6, no. 5, pp. 507–511, Sept. 1995.

[88] D. Falconer, S. L. Ariyavisitakul, A. Benyamin-Seeyar, and B. Eidson, "Frequency domain equalization for single-carrier broadband wireless systems," *IEEE Commun. Mag.*, vol. 40, no. 4, pp. 58–66, Apr. 2002.

[89] S. Rajagopal, R. D. Roberts, and S. K. Lim, "IEEE 802.15.7 visible light communication: Modulation schemes and dimming support," *IEEE Commun. Mag.*, vol. 50, no. 3, pp. 72–82, Mar. 2012.

[90] M. Z. Afgani, H. Haas, H. Elgala, and D. Knipp, "Visible light communication using OFDM," in *Proc. International Conference on Testbeds and Research Infrastructures for the Development of Networks and Communities (TRIDENTCOM)*, Barcelona, Spain, Mar. 2006, pp. 1–6.

[91] H. Elgala, R. Mesleh, H. Haas, and B. Pricope, "OFDM visible light wireless communication based on white LEDs," in *Proc. IEEE Vehicular Technology Conference (VTC) - Spring*, Dublin, Ireland, Apr. 2007, pp. 2185–2189.

[92] J. Armstrong, "OFDM for optical communications," *J. Lightw. Technol.*, vol. 27, no. 3, pp. 189–204, Feb. 2009.

[93] H. E. Levin, "A complete and optimal data allocation method for practical discrete multitone systems," in *Proc. IEEE Global Telecommunications Conference (GLOBECOM)*, vol. 1, San Antonio, TX, USA, Nov. 2001, pp. 369–374.

[94] T. Komine, J. H. Lee, S. Haruyama, and M. Nakagawa, "Adaptive equalization system for visible light wireless communication utilizing multiple white LED lighting equipment," *IEEE Trans. Wireless Commun.*, vol. 8, no. 6, pp. 2892–2900, June 2009.

[95] L. Wu, Z. Zhang, J. Dang, and H. Liu, "Adaptive modulation schemes for visible light communications," *J. Lightw. Technol.*, vol. 33, no. 1, pp. 117–125, Jan. 2015.

[96] J. B. Carruthers and J. M. Kahn, "Multiple-subcarrier modulation for nondirected wireless infrared communication," *IEEE J. Sel. Areas Commun.*, vol. 14, no. 3, pp. 538–546, Apr. 1996.

[97] J. Armstrong and A. J. Lowery, "Power efficient optical OFDM," *Electron. Lett.*, vol. 42, no. 6, pp. 370–372, Mar. 2006.

[98] J. Armstrong and B. J. C. Schmidt, "Comparison of asymmetrically clipped optical OFDM and DC-biased optical OFDM in AWGN," *IEEE Commun. Lett.*, vol. 12, no. 5, pp. 343–345, May 2008.

[99] R. Mesleh, H. Elgala, and H. Haas, "On the performance of different OFDM based optical wireless communication systems," *IEEE/OSA J. Opt. Commun. Netw.*, vol. 3, no. 8, pp. 620–628, Aug. 2011.

[100] M. Rosenblatt, "A central limit theorem and a strong mixing condition," *Proc. Natl. Acad. Sci.*, vol. 42, no. 1, pp. 43–47, Jan. 1956.

[101] S. Dimitrov, S. Sinanovic, and H. Haas, "Clipping noise in OFDM-based optical wireless communication systems," *IEEE Trans. Commun.*, vol. 60, no. 4, pp. 1072–1081, Apr. 2012.

[102] D. Tsonev, S. Sinanovic, and H. Haas, "Complete modeling of nonlinear distortion in OFDM-based optical wireless communication," *J. Lightw. Technol.*, vol. 31, no. 18, pp. 3064–3076, Sept. 2013.

[103] J. J. Bussgang, "Crosscorrelation functions of amplitude-distorted gaussian signals," Research Laboratory of Electronics, Massachusetts Institute of Technology, Cambridge, MA, Tech. Rep. 216, Mar. 1952.

[104] J. Grubor, S. Randel, K. D. Langer, and J. Walewski, "Broadband information broadcasting using LED-based interior lighting," *J. Lightw. Technol.*, vol. 26, no. 24, pp. 3883–3892, Dec. 2008.

[105] L. Zeng, D. O'Brien, H. Minh, G. Faulkner, K. Lee, D. Jung, Y. J. Oh, and E. T. Won, "High data rate multiple input multiple output (MIMO) optical wireless communications using white LED lighting," *IEEE J. Sel. Areas Commun.*, vol. 27, no. 9, pp. 1654–1662, Dec. 2009.

[106] H. Ma, L. Lampe, and S. Hranilovic, "Coordinated broadcasting for multiuser indoor visible light communication systems," *IEEE Trans. Commun.*, vol. 63, no. 9, pp. 3313–3324, Sept. 2015.

[107] D. Bykhovsky and S. Arnon, "Multiple access resource allocation in visible light communication systems," *J. Lightw. Technol.*, vol. 32, no. 8, pp. 1594–1600, Feb. 2014.

[108] L. Yin and H. Haas, "Coverage analysis of multiuser visible light communication networks," *IEEE Trans. Wireless Commun.*, vol. 17, no. 3, pp. 1630–1643, Mar. 2017.

[109] C. Chen, D. A. Basnayaka, and H. Haas, "Downlink performance of optical attocell networks," *J. Lightw. Technol.*, vol. 34, no. 1, pp. 137–156, Jan. 2016.

[110] I. S. Gradshteyn and I. M. Ryzhik, *Tables of Integrals, Series, and Products*, 7th ed. Academic Press, 2007.

[111] J. Gil-Peaez, "Note on the inversion theorem," *Biometrika*, vol. 38, no. 3-4, pp. 481–482, Dec. 1951.

[112] H. R. Thompson, "Distribution of distance to nth neighbour in a population of randomly distributed individuals," *Ecology*, vol. 37, no. 2, pp. 391–394, Apr. 1956.

[113] N. Cressie, A. S. Davis, J. L. Folks, and G. E. Policello, "The moment-generating function and negative integer moments," *J. Amer. Stat.*, vol. 35, no. 3, pp. 148–150, Aug. 1981.

[114] T. D. Novlan, R. K. Ganti, A. Ghosh, and J. G. Andrews, "Analytical evaluation of fractional frequency reuse for OFDMA cellular networks," *IEEE Trans. Wireless Commun.*, vol. 10, no. 12, pp. 4294–4305, Dec. 2011.

[115] C. Chen, S. Videv, D. Tsonev, and H. Haas., "Fractional frequency reuse in DCO-OFDM-based optical attocell networks," *J. Lightw. Technol.*, vol. 33, no. 19, pp. 3986–4000, Oct. 2015.

[116] B. Ghimire and H. Haas, "Self-organising interference coordination in optical wireless networks," *EURASIP J. Wireless Commun. Netw.*, vol. 1, no. 131, Apr. 2012.

[117] R. Irmer, H. Droste, P. Marsch, M. Grieger, G. Fettweis, S. Brueck, H.-P. Mayer, L. Thiele, and V. Jungnickel, "Coordinated multipoint: Concepts, performance, and field trial results," *IEEE Commun. Mag.*, vol. 49, no. 2, pp. 102–111, Feb. 2011.

[118] S. Bassoy, H. Farooq, M. A. Imran, and A. Imran, "Coordinated multi-point clustering schemes: A survey," *IEEE Commun. Surveys Tuts.*, vol. 19, no. 2, pp. 743–764, Second Quarter 2017.

[119] M. Kashef, M. Abdallah, K. Qaraqe, H. Haas, and M. Uysal, "Coordinated interference management for visible light communication systems," *J. Opt. Commun. Netw.*, vol. 7, no. 11, pp. 1098–1108, Nov. 2015.

[120] X. Li, F. Jin, R. Zhang, J. Wang, Z. Xu, and L. Hanzo, "Users first: User-centric cluster formation for interference-mitigation in visible-light network," *IEEE Trans. Wireless Commun.*, vol. 15, no. 1, pp. 39–53, Jan. 2016.

[121] H. C. Ferreira, L. Lampe, J. Newbury, and T. G. Swart, Eds., *Power Line Communications: Theory and Applications for Narrowband and Broadband Communications over Power Lines*. Hoboken, NJ, USA: Wiley, 2010.

[122] T. Komine, S. Haruyama, and M. Nakagawa, "Performance evaluation of narrowband OFDM on integrated system of power line communication and visible light wireless communication," in *Proc. International Symposium on Wireless Pervasive Computing*, Phuket, Thailand, Jan. 2006, pp. 1–6.

[123] H. Ma, L. Lampe, and S. Hranilovic, "Integration of indoor visible light and power line communication systems," in *Proc. IEEE 17th International Symposium on Power Line Communications and Its Applications*, Johannesburg, South Africa, Mar. 2013, pp. 291–296.

[124] 3rd Generation Partnership Project (3GPP), "Coordinated multi-point operation for LTE physical layer aspects," , Sophia-Antipolis, France, Tech. Rep. TR 36.819, Sept. 2011.

[125] H. Taoka, S. Nagata, K. Takeda, Y. Kakishima, X. She, and K. Kusume, "MIMO and CoMP in LTE-advanced," *NTT Docomo Tech. J.*, vol. 12, no. 2, pp. 20–28, Sept. 2010.

[126] D. Lee, H. Seo, B. Clerckx, E. Hardouin, D. Mazzarese, S. Nagata, and K. Sayana, "Coordinated multipoint transmission and reception in LTE-Advanced: Deployment scenarios and operational challenges," *IEEE Commun. Mag.*, vol. 50, no. 2, pp. 148–155, Feb. 2012.

[127] R. Tanbourgi, S. Singh, J. G. Andrews, and F. K. Jondral, "A tractable model for noncoherent joint-transmission base station cooperation," *IEEE Trans. Wireless Commun.*, vol. 13, no. 9, pp. 4959–4973, Sept. 2014.

[128] G. Nigam, P. Minero, and M. Haenggi, "Coordinated multipoint joint transmission in heterogeneous networks," *IEEE Trans. Commun.*, vol. 62, no. 11, pp. 4143–4146, Nov. 2014.

[129] K. Kikuchi, "Fundamentals of coherent optical fiber communications," *J. Lightw. Technol.*, vol. 34, no. 1, pp. 157–179, Jan. 2016.

[130] R. Zhang, J. Wang, Z. Wang, Z. Xu, C. Zhao, and L. Hanzo, "Visible light communications in heterogeneous networks: Paving the way for user-centric design," *IEEE Wireless Commun.*, vol. 22, no. 2, pp. 8–16, Apr. 2015.

[131] E. S. Sousa and J. A. Silvester, "Optimum transmission ranges in a direct-sequence spread-spectrum multihop packet radio network," *IEEE J. Sel. Areas Commun.*, vol. 8, no. 5, pp. 762–771, June 1990.

[132] N. L. Bowers Jr., "Expansion of probability density functions as a sum of gamma densities with applications in risk theory," *Trans. Soc. Actuaries*, vol. 18, no. 52, pp. 125–147, 1966.

[133] M. Haenggi and R. K. Ganti, "Interference in large wireless networks," *Found. Trends Netw.*, vol. 3, no. 2, pp. 127–248, Feb. 2009.

[134] M. F. Guerra-Medina, O. Gonzalez, B. Rojas-Guillama, J. A. Martin-Gonzalez, F. Delgado, and J. Rabadan, "Ethernet-OCDMA system for multi-user visible light communciations," *Electron. Lett.*, vol. 48, no. 4, pp. 227–228, Feb. 2012.

[135] H. G. Myung, J. Lim, and D. J. Goodman, "Single carrier FDMA for uplink wireless transmission," *IEEE Veh. Technol. Mag.*, vol. 1, no. 3, pp. 30–38, Sept. 2006.

[136] K. Bandara and Y. H. Chung, "Novel colour-clustered multiuser visible light communication," *Trans. Emerging Tel. Tech.*, vol. 25, no. 6, pp. 579–590, May 2014.

[137] S. H. Chen and C. W. Chow, "Color-shift keying and code-division multiple-access transmission for RGB-LED visible light communications using mobile phone camera," *IEEE Photon. J.*, vol. 6, no. 6, pp. 1–6, Dec. 2014.

[138] J. Choi, "Non-orthogonal multiple access in downlink coordinated two-point systems," *IEEE Commun. Lett.*, vol. 18, no. 2, pp. 313–316, Feb. 2014.

[139] Z. Ding, Z. Yang, P. Fan, and H. V. Poor, "On the performance of non-orthogonal multiple access in 5G systems with randomly deployed users," *IEEE Signal Process. Lett.*, vol. 21, no. 12, pp. 1501–1505, Dec. 2014.

[140] Z. Ding, P. Fan, and H. V. Poor, "Impact of user pairing on 5G nonorthogonal multiple-access downlink transmissions," *IEEE Trans. Veh. Technol.*, vol. 65, no. 8, pp. 6010–6023, Sept. 2016.

[141] S. Timotheou and I. Krikidis, "Fairness for non-orthogonal multiple access in 5G systems," *IEEE Signal Process. Lett.*, vol. 22, no. 10, pp. 1647–1651, Apr. 2015.

[142] B. Kim, S. Lim, H. Kim, S. Suh, J. Kwun, S. Choi, C. Lee, S. Lee, and D. Hong, "Non-orthogonal multiple access in a downlink multiuser beamforming system," in *Proc. IEEE Military Communication Conference (MILCOM)*, San Diego, CA, Nov. 2013, pp. 1278–1283.

[143] X. Chen, A. Benjebbour, A. Li, and A. Harada, "Multi-user proportional fair scheduling for uplink non-orthogonal multiple access," in *Proc. IEEE Vehicular Technology Conference (VTC Spring)*, Seoul, Korea, May 2014, pp. 1–5.

[144] Z. Ding, M. Peng, and H. V. Poor, "Cooperative non-orthogonal multiple access in 5G systems," *IEEE Commun. Lett.*, vol. 19, no. 8, pp. 1462–1465, June 2015.

[145] L. Yin, X. Wu, and H. Haas, "On the performance of non-orthogonal multiple access in visible light communication," in *Proc. IEEE 26th Annual Symposium on Personal, Indoor and Mobile Radio Communications (PIMRC)*, Hong Kong, China, Sept. 2015, pp. 1376–1381.

[146] L. Yin, W. O. Popoola, X. Wu, and H. Haas, "Performance evaluation of non-orthogonal multiple access in visible light communication," *IEEE Trans. Commun.*, vol. 64, no. 12, pp. 5162–5175, Dec. 2016.

[147] H. Marshoud, V. M. Kapinas, G. K. Karagiannidis, and S. Muhaidat, "Non-orthogonal multiple access for visible light communications," *IEEE Photon. J.*, vol. 28, no. 1, pp. 51–54, Jan. 2016.

[148] R. C. Kizilirmak, C. R. Rowell, and M. Uysal, "Non-orthogonal multiple access (NOMA) for indoor visible light communications," in *Proc. International Workshop on Optical Wireless Communications (IWOW)*, Istanbul, Turkey, Sept. 2015, pp. 98–101.

[149] H. A. David and H. N. Nagaraja, *Order Statistics*, 3rd ed. New York: John Wiley, 2003.

[150] H. Zimmermann, "OSI reference model - the ISO model of architecture for open systems interconnection," *IEEE Trans. Commun.*, vol. 28, no. 4, pp. 425–432, Apr. 1980.

[151] Y. Zou, J. Zhu, X. Wang, and L. Hanzo, "A survey on wireless security: Technical challenges, recent advances, and future trends," *Proc. IEEE*, vol. 104, no. 9, pp. 1727–1765, Sept. 2016.

[152] A. D. Wyner, "The wire-tap channel," *Bell Syst. Tech. J.*, vol. 54, no. 8, pp. 1355–1387, Oct. 1975.

[153] I. Csiszár and J. Körner, "Broadcast channels with confidential messages," *IEEE Trans. Inf. Theory*, vol. 24, no. 3, pp. 339–348, May 1978.

[154] M. Haenggi, "The secrecy graph and some of its properties," in *Proc. IEEE Int. Symp. Inf. Theory*, Toronto, ON, July 2008, pp. 539–543.

[155] P. C. Pinto, J. Barros, and M. Z. Win, "Secure communication in stochastic wireless networks - Part I: Connectivity," *IEEE Trans. Inf. Forensics Security*, vol. 7, no. 1, pp. 125–138, Feb. 2012.

[156] ——, "Secure communication in stochastic wireless networks - Part II: Maximum rate and collusion," *IEEE Trans. Inf. Forensics Security*, vol. 7, no. 1, pp. 139–147, Feb. 2012.

[157] O. O. Koyluoglu, C. E. Koksal, and H. E. Gamal, "On secrecy capacity scaling in wireless networks," *IEEE Trans. Inf. Theory*, vol. 58, no. 5, pp. 3000–3015, May 2012.

[158] X. Zhou, R. K. Ganti, J. G. Andrews, and A. Hjorungnes, "On the throughput cost of physical layer security in decentralized wireless networks," *IEEE Trans. Wireless Commun.*, vol. 10, no. 8, pp. 2764–2775, Aug. 2011.

[159] H. Wang, X. Zhou, and M. C. Reed, "Physical layer security in cellular networks: A stochastic geometry approach," *IEEE Trans. Wireless Commun.*, vol. 12, no. 6, pp. 2776–2787, June 2013.

[160] A. Mostafa and L. Lampe, "Physical-layer security for MISO visible light communication channels," *IEEE J. Sel. Areas Commun.*, vol. 33, no. 9, pp. 1806–1818, Sept. 2015.

[161] A. Lapidoth, S. M. Moser, and M. A. Wigger, "On the capacity of free-space optical intensity channels," *IEEE Trans. Inf. Theory*, vol. 55, no. 10, pp. 4449–4461, Oct. 2009.

[162] G. Pan, J. Ye, and Z. Ding, "On secure VLC systems with spatially random terminals," *IEEE Commun. Lett.*, vol. 21, no. 3, pp. 492–495, Mar. 2016.

[163] S. Leung-Yan-Cheong and M. Hellman, "The gaussian wire-tap channel," *IEEE Trans. Inf. Theory*, vol. 24, no. 4, pp. 451–456, July 1978.

[164] L. Hanzo, H. Haas, S. Imre, D. O'Brien, M. Rupp, and L. Gyongyosi, "Wireless myth, realities, and futures: From 3G/4G to optical and quantum wireless," *Proc. IEEE*, vol. 100, no. Special Centennial Issue, pp. 1853–1888, May 2012.

[165] M. Haenggi, "On distances in uniform random networks," *IEEE Trans. Inf. Theory*, vol. 51, no. 10, pp. 3584–3586, Oct. 2005.

[166] S. Srinivasa and M. Haenggi, "Distance distributions in finite uniformly random networks: Theory and applications," *IEEE Trans. Veh. Technol.*, vol. 59, no. 2, pp. 940–949, Feb. 2010.

[167] N. Romero-Zurita, D. McLernon, M. Ghogho, and A. Swami, "PHY layer security based on protected zone and artificial noise," *IEEE Signal Process. Lett.*, vol. 20, no. 5, pp. 487–490, May 2013.

[168] M. B. Shenouda and T. N. Davidson, "On the design of linear transceivers for multiuser systems with channel uncertainty," *IEEE J. Sel. Areas Commun.*, vol. 26, no. 6, pp. 1015–1024, Aug. 2008.